Refining current design methods for vertical borehole heat exchangers considering complex ground conditions

by

Yunting Guo

A thesis submitted in partial fulfillment of the requirements for the degree of

Doctor of Philosophy

in

Mining Engineering

Department of Civil and Environmental Engineering
University of Alberta

Abstract

Ground source heat pump systems (GSHP), exploiting shallow geothermal energy, have been receiving increasing interest for space heating and cooling due to their high energy efficiency and low greenhouse gas emissions. A core component of the GSHP system is the ground heat exchanger (GHE) that is in contact with the ground. Accurate heat transfer analysis of the GHE is vital for optimizing the design and operation of GSHP systems. Among the different types of GHEs, the vertical borehole heat exchanger (BHE) is widely used, and various simulation and design tools have been developed for BHEs in the past two decades.

However, current BHE design methods have limitations as they rely on certain assumptions and fail to account for real ground conditions such as groundwater flow, multilayered ground conditions, and ground surface conditions. It has been proved that these conditions have a significant impact on the long-term thermal performance of vertical BHEs, and ignoring them can lead to inefficient GSHP systems. To address these issues, this thesis aims to refine the current design method by considering these ground conditions in the heat transfer analysis for BHEs.

The refined BHE design method takes into account non-uniform heat transfer rates in multilayered ground conditions. The variation in heat transfer rates is influenced by inhomogeneous ground thermal properties and the presence of groundwater flow. When groundwater flow is absent, conventional solutions assuming uniform heat transfer rates may overpredict ground temperatures in certain layers by up to 50.82%. The effect of inhomogeneous ground thermal properties further strengthens the variation in heat transfer rates and temperatures along the borehole. Additionally, when groundwater flow is present, the heat transfer rate in the aquifer can be approximately 21.69% higher than the average rate. The influence of the aquifer was examined, showing that heat

transfer in the aquifer strengthens with an increase in flow velocity. The study also examines the influence of ground surface conditions, particularly in the case of short boreholes over a long period of time. The difference in boundary conditions may lead to an underestimation of up to 26.3% for a 15-meter BHE after about 35.8 years. The refined design method considers the synergistic effect of the circulating fluid and the ground surface condition in analytical solutions, extending the impact of the ground surface boundary to greater depths. For example, at the bottom of a 70-meter borehole, the underestimation caused by using a constant ground surface temperature remains significant at 6.85%.

In summary, the refined BHE design method offers improved computational time and accuracy, making it a promising tool for designing vertical BHEs. It enhances the understanding and capabilities of current design methods, leading to more effective and efficient applications of shallow geothermal energy in GSHP systems.

Preface

This thesis is an original work by Yunting Guo under the supervision of Dr. Wei Victor Liu. Some of the research conducted for this thesis has been published or submitted for consideration towards publication.

Chapter 2 of this thesis has been accepted as Guo, Y., Hu, X., Banks, J., & Liu, W. V. Considering buried depth for vertical borehole heat exchangers in a borehole field with groundwater flow—An extended solution. *Energy and Buildings*, *235*, 110722. © Elsevier. (2021).

Chapter 3 of this thesis has been submitted for peer review as Guo, Y., Zhao, J., & Liu, W. V. Effects of varying heat transfer rates for U-shaped borehole heat exchangers in layered subsurface with groundwater flow. *Applied Thermal Engineering*. Unpublished © Elsevier. (under review).

Chapter 4 of this thesis has been accepted as Guo, Y., Huang, G., & Liu, W. V. A new semi-analytical solution addressing varying heat transfer rates for U-shaped vertical borehole heat exchangers in multilayered ground. *Energy*, *274*, 127373. © Elsevier. (2023).

Chapter 5 of this thesis has been submitted for peer review as Guo, Y., Zhao, J., & Liu, W. V. A new semi-analytical solution for U-shaped vertical borehole heat exchangers in multilayered ground with third-type boundary condition. *International Journal of Thermal Sciences*. Unpublished © Elsevier. (under review).

Chapter 6 of this thesis has originally written by Yunting Guo and have never been published before.

In this thesis, I was responsible for conceptualization, methodology, coding, results analysis, and manuscript composition. Dr. Wei Victor Liu was the supervisory author and contributed to

resources, supervision, and manuscript composition. Dr. Jonathan Banks shared the corresponding authorship in Chapter 2 and assisted with resources and manuscript edits. Dr. Xincheng Hu, Dr. Guangping Huang, and Jian Zhao were involved in manuscript edits in Chapter 2, Chapter 4, and Chapters 3 and 5, respectively.

Acknowledgement

I am profoundly grateful to all those who have contributed to the successful completion of this doctoral thesis.

First and foremost, I would like to express my heartfelt gratitude to my advisor, Dr. Wei Victor Liu, whose encouragement, support, and mentorship have been invaluable throughout this research endeavor. His insightful feedback and guidance have had a profound impact on both the quality of this thesis and my overall development as a researcher.

I would also like to express my gratitude to my colleagues, Dr. Alex Hu, Dr. Guangping Huang, and Jian Zhao, who have been a source of inspiration, collaboration, and support. Their camaraderie and intellectual discussions have been instrumental in shaping my research perspectives.

Special thanks go to my family for their unconditional support and endless love. I also wish to give many thanks to all my friends who enriched my life.

Additionally, I want to dedicate this work to my beloved, Jingwen (Jane) Wang, for her constant understanding, belief in my abilities, and unwavering love. She is the light that brightens my darkest days. Her presence in my life has provided me with the strength to overcome challenges and stay committed to this academic pursuit.

Finally, I want to express my sincere appreciation to all those whose names might not be mentioned here but have played a part, big or small, in this long journey. Their collective contributions have been invaluable.

Contents

List of Tables

List of Figures

Nomenclature

A	albedo	
B	borehole spacing	[m]
c	specific heat capacity	[$Jkg^{-1}K^{-1}$]
d	shank spacing	[m]
D	depth	[m]
$E_1(X)$	exponential integral function	
$erf(X)$	error function	
$erfc(X)$	complementary error function	
Fo	Fourier number	
g	g-function	
G	Green's function	
h	surface heat transfer coefficient	[$Wm^{-2}K^{-1}$]
H	borehole length	[m]
I_0	modified zero order Bessel function of the first kind	
k	thermal conductivity	[$Wm^{-1}K^{-1}$]
L	ground layer thickness	[m]

M	mass flow rate	[kgs^{-1}]
Pe	Peclet number	
q_l	heat transfer rate	[Wm^{-1}]
q_v	vertical heat flux	[Wm^{-2}]
Δq	incremental heat flux	
Q	heat load	[W]
r, r'	radial coordinate	[m]
$R_1^{\Delta}, R_2^{\Delta}, R_{12}^{\Delta}$	delta-circuit thermal resistance	[mKW^{-1}]
S	incident solar radiation	[Wm^{-2}]
t, t', τ	time	[s]
t_s	steady-state time	[s]
T	temperature	[°C]
T_0, T_i	undisturbed ground temperature	[°C]
ΔT	temperature variation	[°C]
U	$= u_d \rho_w c_w / \rho c$	[ms^{-1}]
u_d	groundwater velocity	[ms^{-1}]
V	circulating fluid flow rate	[m^3s^{-1}]

ΔX	non-dimensional distance in the x-direction	
x, x', y, y', z, z'	axial coordinate	[m]
α	thermal diffusivity	[m^2s^{-1}]
$\beta_1, \beta_2, \beta_{12}$	dimensionless thermal conductance	
$\varepsilon \Delta R$	net long-wave radiation	[Wm^{-2}]
Θ	dimensionless temperature	
λE	latent heat flux	[Wm^{-2}]
ρ	density	[kgm^{-3}]
ψ	influence function	

Subscripts

A	analytical solution
amb	ambient air
b	borehole
C	COMSOL result
down	downward-flowing fluid
E	contribution of heat generation
eff	effective properties

f	circulating fluid
g	grout
I	bottommost layer
in	fluid inlet
o	pipe outer wall
out	fluid outlet
p	pipe
par	parallel to bedding planes
per	perpendicular to bedding planes
up	upward-flowing fluid
U	contribution of upper surface boundary
V	contribution of lower surface boundary
w	water
r, x, y, z	directions

List of Abbreviations

BHE	Borehole heat exchanger
COP	Coefficient of performance
CQ	Constant heat transfer rate
FE	Finite element
FLS	Finite line source
GHE	Ground heat exchanger
GLD	Ground Loop Design
GSHP	Ground source heat pump
IGSHPA	International Ground Source Heat Pump Association
MAE	Mean absolute error
MAPE	Mean absolute percent error
MFLS	Moving finite line source
MFLSD	Moving finite line source with buried depth (D)
MVQ	Multilayered ground with varying heat transfer rates (Q)
RMSD	Root mean square deviation

Chapter 1. Introduction

1.1. Research background

In recent years, the mining industry has made commitments to reduce its carbon footprint, aiming for net-zero carbon emissions [1]. Presently, the mining sector is characterized by its substantial energy demands, a significant portion of which is fulfilled through the combustion of fossil fuels [2]. This reliance on fossil fuels is often driven by limited electrical grid capacity and infrastructure [3]. Notably, in Canada, the mining industry stands as the largest energy consuming and greenhouse gas emitting industrial sector [4]. Many mining activities continually require heat related energy, such as for ore processing, temperature control in offices, workshops, living quarters, equipment garages, and heating the intake air in underground mines to prevent shaft icing in cold climates. In this regard, geothermal systems that harness the heat from the Earth emerged as a viable solution [5]. By tapping into geothermal resources, these systems offer a more sustainable and energy-efficient alternative to conventional fossil fuel-based heating and cooling methods.

Ground source heat pump (GSHP) systems are the common method for harnessing geothermal energy. These systems have gained popularity in residential and commercial buildings due to their high energy efficiency and low greenhouse gas emissions [6]. Well-designed systems often exhibit a coefficient of performance (COP) of about four or more, delivering at least four units of heating or cooling output for one unit of energy input into running the heat pumps (usually electricity) [7]. As illustrated in Figure 1-1, this type of system generally contains distribution systems, the heat pump, and the ground heat exchanger [8]. An essential challenge in GSHP applications is the

accurate sizing of the ground heat exchanger to meet the projected heat demand throughout its operational lifespan, which can span several decades.

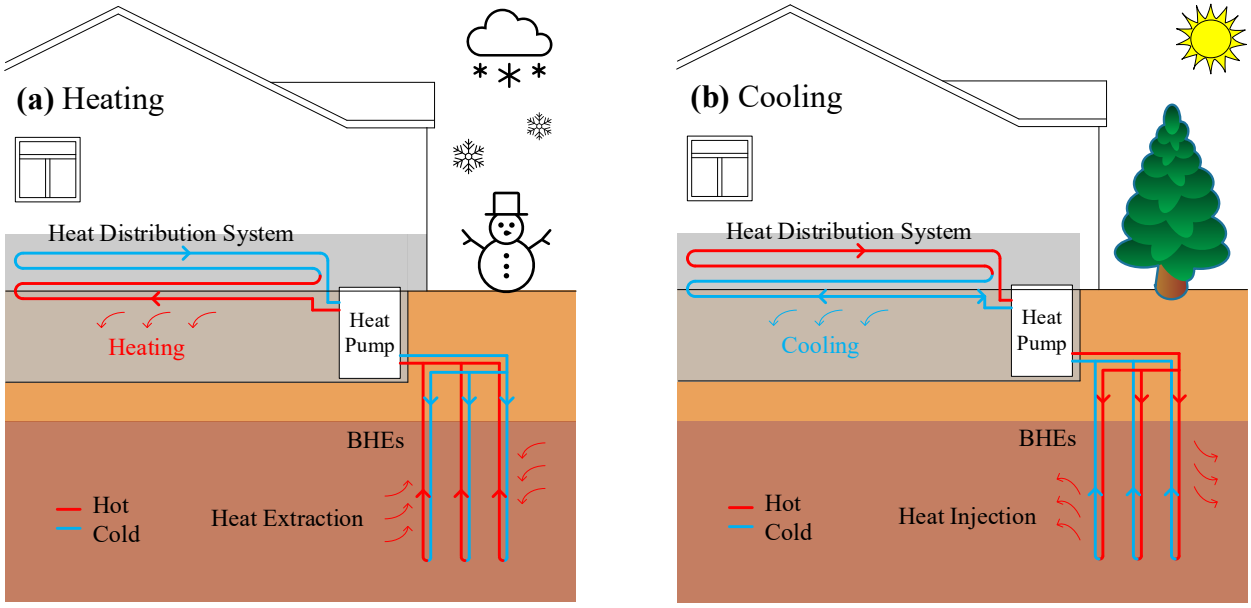

Figure 1-1. Schematics of BHEs system for space (a) heating and (b) cooling.

The vertical borehole heat exchanger (BHE) is one of the most common types of ground heat exchanger. In the residential sector of Quebec, Canada, for instance, vertical BHEs hold an 83% market dominance [9]. A BHE refers to a closed-loop pipe assembly installed in a vertical borehole, as shown in Figure 1-2. Different configurations of pipes can be found in vertical boreholes, including U-shaped, parallel double U-shaped, spiral-shaped, and coaxial [10]. The U-shaped pipe is particularly popular due to its simplicity and cost-effectiveness [11]. The space between the borehole wall and the pipes is usually backfilled with silica sand-based grout [12]. In this design, a fluid, typically a water and antifreeze mixture, is circulated to facilitate heat transfer between the heat pump and the ground [13, 14]. The active BHE is buried at some depth (D)

below the ground surface. The length (H) of the borehole typically ranges from 15 m to 150 m, which is strongly depending upon prevailing geological conditions [15, 16].

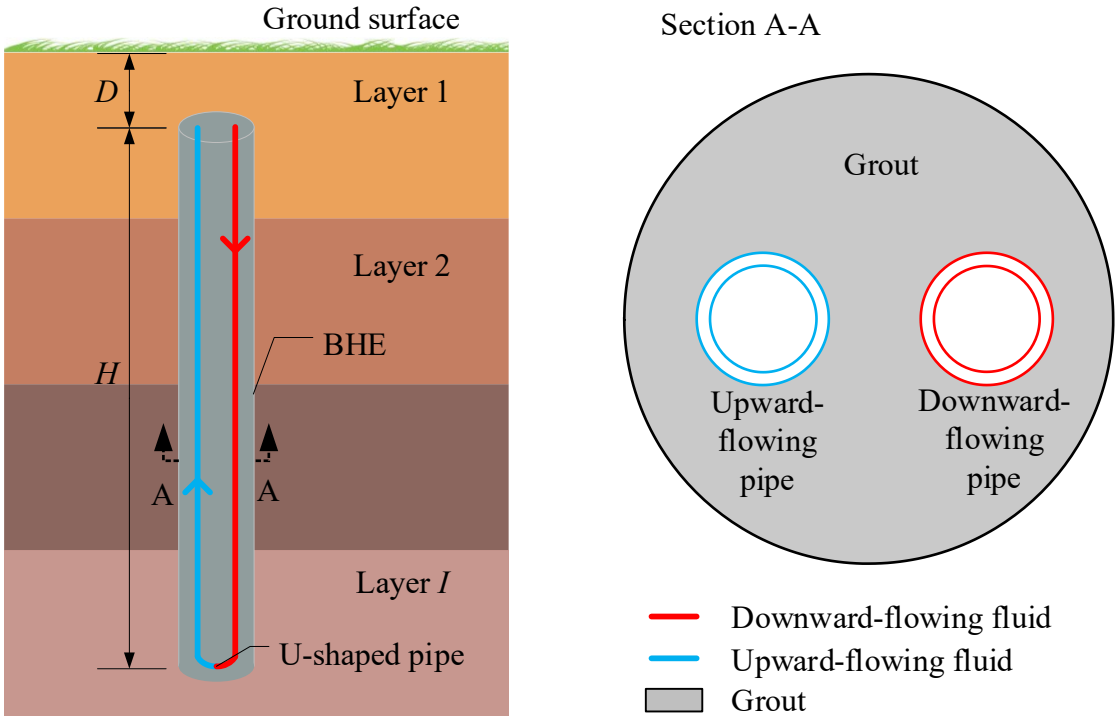

Figure 1-2. Schematic diagram of a BHE with a single U-shaped pipe.

The proper sizing of a BHE system is a primary challenge during the design phase. If the BHE is oversized, it can considerably increase upfront costs due to the additional drilling and materials for longer BHEs. It also increased electricity consumption for operating the larger system [17]. Conversely, an undersized ground heat exchanger will fail to effectively convey an adequate amount of heat to the heat pump during heating mode or disperse enough heat to the ground during cooling mode. Consequently, the heat pump will consume more electricity to achieve the desired heating and cooling output, resulting in a lower COP. Furthermore, in cold climates, an undersized design will lead to the heat circulating fluid operates with temperatures below 0 °C. This can lead

to the ground temperature dropping below the freezing point, causing freeze-thaw cycles in the sediments. When these cycles occur in cohesive sediments, they have the potential to disrupt vertical deformability and natural consolidation processes, ultimately resulting in notable and irreversible settlements [18]. In general, an improperly sized BHE can lead to an inefficient GSHP system, resulting in higher financial expenses and reduced environmental benefits. In more severe scenarios, inadequate sizing of a BHE may even contribute to irrecoverable settlements. Therefore, it is crucial to establish a proper method for sizing the BHE.

1.2. Literature review

Over the last two decades, several simulation and design tools [19-22] have been developed for sizing BHEs. Figure 1-3 presents a general flowchart outlining the common simulation process. The simulation proceeded with predicting the long-term thermal behaviour of the BHE using non-dimensional thermal response factors, commonly referred to as *g*-functions [23]. This *g*-function method was originally introduced by Eskilson [23]. It started with assessing the ground temperature regime due to a single BHE. Eskilson achieved this by solving the radial-axial transient heat conduction problem in a semi-infinite medium, treating the BHE as a line heat source, through a numerical finite-difference approach. Practically, a BHE can be assumed as a line heat source due to their substantial aspect ratios, which depths ranging from 15 to 150 m and diameters ranging from 0.1 to 0.15 m. Then, Eskilson's *g*-functions [23] for a BHE field containing multiple boreholes were determined by spatially superimposing the temperature responses contributed by each individual BHE within the field. Since the numerical simulation can be time-consuming and computationally intensive, a relatively large data set of pre-computed *g*-functions for different borehole geometries and borehole field configurations was generated and integrated

into BHE design tools, such as GLHEPRO [19], Earth Energy Designer (EED) [20], eQuest [21] and EnergyPlus [22].

For a specific borehole geometry, a *g*-function gives the temperature change (ΔT) from its undisturbed value (T_i), averaged over the borehole wall surface, due to a unit heat flow rate (q_l) applied at that borehole wall surface [23, 24],

$$\frac{\Delta T}{q_l/2\pi k_s} = g\left(\frac{t}{t_s}, \frac{r_b}{H}, \frac{B}{H}\right) \tag{1-1}$$

where k_s [$Wm^{-1}K^{-1}$] is the ground thermal conductivity, q_l [Wm^{-1}] is the heat transfer rate per unit length and *g* denotes the *g*-function. A *g*-function depends on three non-dimensional parameters: (r_b/H) is the ratio of the borehole radius over the borehole length; (B/H) is the ratio of the borehole spacing over the borehole length; and (t/t_s) is the non-dimensional time where $t_s = \frac{H^2}{9\alpha}$ is the steady-state time, and α [m^2s^{-1}] is the ground thermal diffusivity. The *g*-function reflects the capacity of the BHEs to avoid excessive heat accumulation or dissipation in the ground spanning several decades, making it a crucial metric for gauging BHE performance. For instance, in heating-dominated scenarios, a higher *g*-function value signifies a more substantial reduction in ground temperatures due to heat extraction. Consequently, the lower ground temperature leads to reduced heat transfer efficiency for the system during later stages.

Besides Eskilson's *g*-functions [23] , Ground Loop Design (GLD) [25] also employed an analytical solution known as the finite line source (FLS) solution [26]. Apart from the one employed by GLD,

there are various expressions of FLS solutions available in the literature [23, 27-29], all of which are theoretically identical to each other. The FLS solution provides analytical *g*-functions by solving the same radial-axial transient heat conduction problem described by Eskilson [23], based on Kelvin's theory [30] of a heat source. Kelvin's theory [30] takes the solution for an instantaneous point source in an infinite body as the fundamental solution and then derives the solution for a continuous line heat source by integrating the fundamental solution with respect to time and space variables [31].

Once the *g*-functions have been determined, either numerically or analytically, the temperature evolution at the borehole wall in response to time-varying heating and cooling loads can be predicted through the well-known Duhamel's theorem [32],

$$\Delta T(t) = \frac{1}{2\pi k_s} \frac{\partial}{\partial \tau} \int_0^t \frac{Q(t)}{H} g\left(\frac{t-\tau}{t_s}, \frac{r_b}{H}, \frac{B}{H}\right) d\tau \tag{1-2}$$

where Q [W] is the time-varying heating and cooling load. For a given borehole wall temperature, the circulating fluid temperature can be determined through a static heat transfer analysis for the region within the borehole. Numerous models for this specific region have been comprehensively reviewed in studies conducted by Lamarche et al. [33] and Javed and Spitler [17].

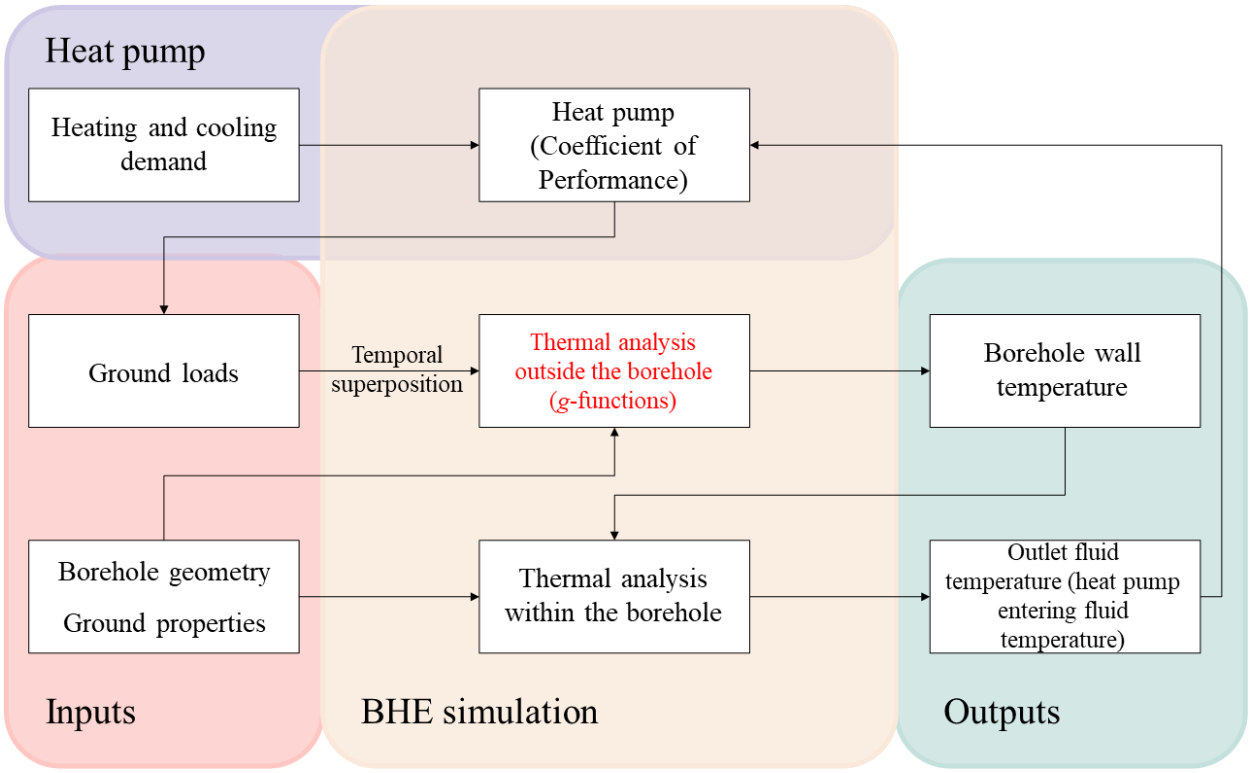

Figure 1-3. The flowchart of the common BHE simulation process.

Both Eskilson's *g*-functions and FLS solutions are widely used in BHE simulations. However, it is essential to recognize that these methods involve simplifications that can have significant impacts on the long-term thermal performance of BHE systems. Some of these simplifications include, but are not limited to,

a. ignorance of the buried depth *D*,

b. ignorance of groundwater advection,

c. homogeneity assumption of the ground,

d. a uniform distribution of the temperature or heat transfer rate over the borehole length,

e. and a constant ground surface temperature.

Relevant literature relating to each of the simplifications is reviewed below.

1.2.1 Buried depth

The buried depth (D) represents the distance from the ground surface to the starting point of the active BHE, where the horizontal connecting piping is buried [34]. In many anlytical solutions [27, 28, 35, 36], this distance was taken as zero, meaning that the effect of buried depth is ignored. However, the buried depth is crucial for accurate BHE system design, particularly in regions with cold climates. In cold regions, horizontal connecting piping is normally buried deeper to prevent the risk of freeze-thaw cycles in seasonally frozen ground [37]. As the depth increases, the thermal resistance of the ground layer above the BHE increases, which reduces the heat flow between the ground surface and the BHE [38]. To address the effect of buried depth, Claesson and Javed [29] proposed an analytical solution for the BHE including the buried depth term. Later, Cimmino et al. [38] and Bandos et al. [39] examined the effect of buried depth from 0 to infinity (∞). Their results indicated that the temperature variation caused by buried depth is particularly noticeable in the case of short boreholes for a longer period of time, and it becomes more significant for a field of multiple short boreholes [38, 39]. In our previous study [40], it found the average non-dimensional temperature for a 50-metre borehole increased by about 3.55% as buried depth increased from 0 m to 8 m. For a 10 × 10 borehole field, Cimmino et al. [38] demonstrated that the steady-state value increased by about 33% as the D/H ratio enlarged from 0 to 0.2.

In summary, neglecting the buried depth in BHE design can lead to an overprediction of the exploitable heat from the ground, resulting in an undersized BHE design. Therefore, considering the actual buried depth is crucial for accurate BHE design and optimal system performance.

1.2.2 Groundwater flow

Current design methods for BHEs typically consider pure conductive heat transfer around BHEs, disregarding the influence of groundwater flow. However, extensive studies [41-47] have shown that groundwater flow can considerably enhance the thermal performance of BHE systems. Wang et al. [47] conducted an in-situ experiment to investigate the impact of groundwater flow on BHE performance. The study showed that the groundwater flow strengthened the heat injection and heat extraction of the BHE on average by 9.8% and 12.9%, respectively. Angelotti et al. [42] created a three-dimensional model and studied the energy performance of a BHE under different groundwater velocities. Simulations demonstrated that the heat extraction rate was raised by 22%, 76%, and 105%, respectively, as the groundwater velocity increased from 0 m/s to 10^{-6} m/s, 5×10^{-6} m/s, and 10^{-7} m/s. These findings indicate that the groundwater flow enhances the heat transfer between the BHE and its surrounding ground, which is beneficial to the long-term performance of the BHE system.

In the last two decades, abundant analytical solutions [35, 36, 48-53] have been developed and proposed to evaluate the influence of groundwater flow on BHEs based on the moving line source (MLS) theory [31]. However, it is important to note that in these solutions, the buried depth (D) has been neglected, which may limit their accuracy in certain scenarios.

1.2.3 Stratified ground

Stratified ground refers to the geological condition where the ground consists of multiple layers with different thermal properties. In BHE design methods, the ground is usually treated as a homogenous body with an effective value of thermal conductivity, overlooking the influence of stratified ground [41]. In real installations, BHE systems often pass through multiple geologic layers with different thermal conductivities [54-56]. For instance, in the Hastings Lake Community Hall site (Alberta, Canada), geoscience information revealed that the thermal conductivities of sediments and rocks in the area tested within a range of 0.62 to 3.22 $Wm^{-1}K^{-1}$ [56]. Ignoring the stratified nature of the ground can lead to inaccuracies in BHE system simulations. Perego et al. [57] conducted a study on a GSHP system installed in highly heterogeneous alluvials in Italy. The study showed that by ignoring stratifications the simulation underestimated the ground temperature change by as much as 25%. Furthermore, the aquifer, a geological body consisting of water-bearing permeable rock and soil, is another important layer in stratified ground conditions. The presence of an aquifer introduces additional influence on the thermal behaviour of BHE systems due to the groundwater flow.

As for the thermal behaviour of a BHE in the multilayered ground, several analytical solutions [58-61] have been proposed over the last decade. Abdelaziz et al. [58] approached the problem by employing the principle of superposition. In this approach, a BHE was partitioned into distinct line heat source segments, corresponding to boundaries of underlying ground layers. By aggregating the contributions of these segments, the temperature change at an observation point within the ground was evaluated. For analysis simplification, the region between each line heat source segment and the observation point was treated as a homogeneous body with effective thermal and

physical properties. However, it is important to note that this solution is not derived from the governing equation, which can lead to an error of up to 15% when the thermal properties vary significantly Nevertheless, maybe due to its simplicity, this approach has also been adopted by many other studies [62-65] to account for the multilayered ground conditions. In contrast to assuming homogeneity, Pan et al. [59] used the integral-transformation method and proposed a cylindrical source solution describing the thermal behaviour of the BHE within multiple ground layers. Additionally, Zhou et al. [60] used Green's function method and derived solutions for two ground layers, and the same research group currently extended the capabilities of these solutions to accommodate more layers [66]. Considering the actual geologic layers and thermal properties of the ground is crucial for more accurate BHE system design and simulation, particularly when an aquifer is present. Analytical solutions that consider multilayered ground conditions can offer valuable insights into the thermal behaviour of BHE systems for specific geological settings.

1.2.4 Non-uniform heat transfer rate along the borehole length

In BHE design methods, a uniform temperature [23] or a constant heat transfer rate [26] was prescribed at the borehole wall surface. However, in reality, the heat transfer rate is non-uniformly distributed along the borehole depth, and the distribution changes during the operation. The non-uniformity of the heat transfer rate has been noted by a few researchers. For instance, Jia et al. [67] examined the heat transfer rate along a coaxial BHE in a homogeneous condition. Their analytical and numerical results demonstrated that the heat transfer rate varied by about 20% between the top and bottom areas of a 100-metre BHE. To consider the axial variation, Cimmino [68] proposed a solution that incorporated the borehole thermal resistance into the FLS solution. Their findings demonstrated that results from the constant heat transfer rate assumption overestimated the thermal

response factor by 25.8%, while results from the uniform temperature assumption underestimated it by 18.6% in the case of a large field of 10-by-10 boreholes.

This variation can be further intensified in the layered ground. Deng and Fedler [69] measured and simulated the heat transfer rates in a triple-layer soil system comprising coarse sand, clay, and fine sand. They found that the coarse sand and fine sand dissipated over 62% and 27% more heat than the clay, respectively, during 24 hours of operation [69]. Similarly, Luo et al. [70] examined the thermal performance of a BHE in the ground with five bedded layers, including an upper unsaturated layer, three middle layers containing groundwater flow, and a lower aquiclude. Their results showed that the heat transfer efficacy in the lower aquiclude was about 25.9% lower than that in the three middle layers. Neglecting the heat transfer rate variation may result in overestimating the temperature for the layers with lower thermal conductivity, as found in a sandbox experiment and simulation by Li et al. [71], where the constant heat transfer rate overpredicted the clay temperature by up to 76.6%. However, as of now, there is no established analytical or semi-analytical solution for BHEs in stratified ground that considers the non-uniform distribution of the heat transfer rate along the borehole length.

1.2.5 Ground surface boundary condition

Current design methods and most analytical solutions [27-29, 35, 58-61, 68, 72] for BHEs implemented a homogenous boundary condition of the first-type (or Dirichlet) at the ground surface, where the ground surface temperature remains unchanged at its initial temperature. This homogenous boundary condition is mathematically simple but unrealistic in practice since the ground surface temperature varies over time. The seasonal and daily temperature oscillations at the ground surface (i.e., the non-homogenous boundary condition) can be accounted for by

utilizing the superposition principle, as shown in the study by Bandos et al. [26]. The significance of time-independent ground surface temperature has been highlighted by Bidarmaghz et al. [73]. Specifically, the results indicated that the length could be reduced by approximately 11% and 6% for borehole lengths of 30 m and 50 m due to the temperature fluctuations at the ground surface. However, it is rather difficult to implement this time-independent temperature as the boundary condition in practice, as ground temperature measurements are often limited in duration and availability. As an alternative approach, the third-type (or Robin) boundary condition has gained more attention in BHE modelling in recent years [74-78]. The third-type boundary condition was implemented with a surface energy balance equation [79-81] to describe the heat exchange between the ambient and the ground surface. The surface energy balance equation requires meteorological data that is more accessible and well-monitored compared to ground temperature measurements. In the last decade, the third-type boundary condition has been implemented in a few analytical solutions [50-53, 82]. However, these solutions are only available for the homogeneous ground, which may limit their accuracy in certain geological conditions. There has been no previous work on the BHE that considers the ground surface condition in the multilayered ground.

1.3. Research objective

The overall objective of the present study is to refine the current BHE design method. To achieve this objective, the study addresses several research gaps through four specific sub-objectives, which are as follows:

(1) Develop an analytical solution for a BHE field with groundwater flow, considering the impact of buried depth (D).

(2) Investigate the effect of non-uniform heat transfer rate on a U-shaped BHE in the multilayered ground with aquifers.

(3) Develop a semi-analytical solution for BHEs in stratified ground conditions, considering the non-uniform distribution of heat transfer rate along the borehole length.

(4) Incorporate ground surface boundary conditions into BHE design and simulation by using the third-type (Robin) boundary condition with a surface energy balance equation.

By addressing these four sub-objectives (shown in Figure 1-4), particularly in scenarios involving groundwater flow, multilayered ground conditions, and non-uniform heat transfer rates, the study aims to refine the current BHE design methods, as depicted in Figure 1-5. The findings of the study aim to provide valuable insights and improve understanding of BHE systems. The refined method will contribute to more efficient and reliable BHE systems for geothermal applications.

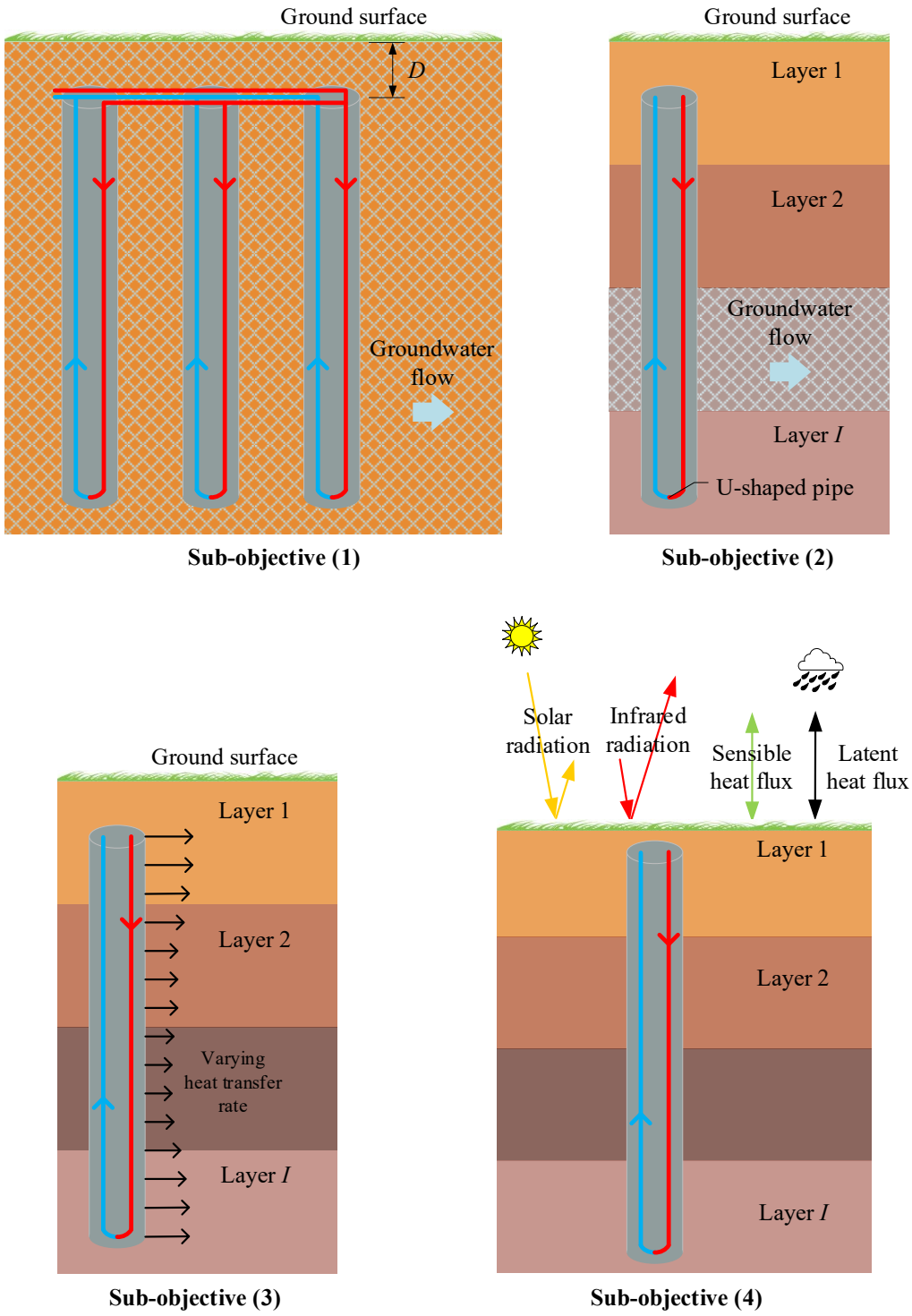

Figure 1-4. Schematic diagrams of ground conditions considered in four sub-objectives.

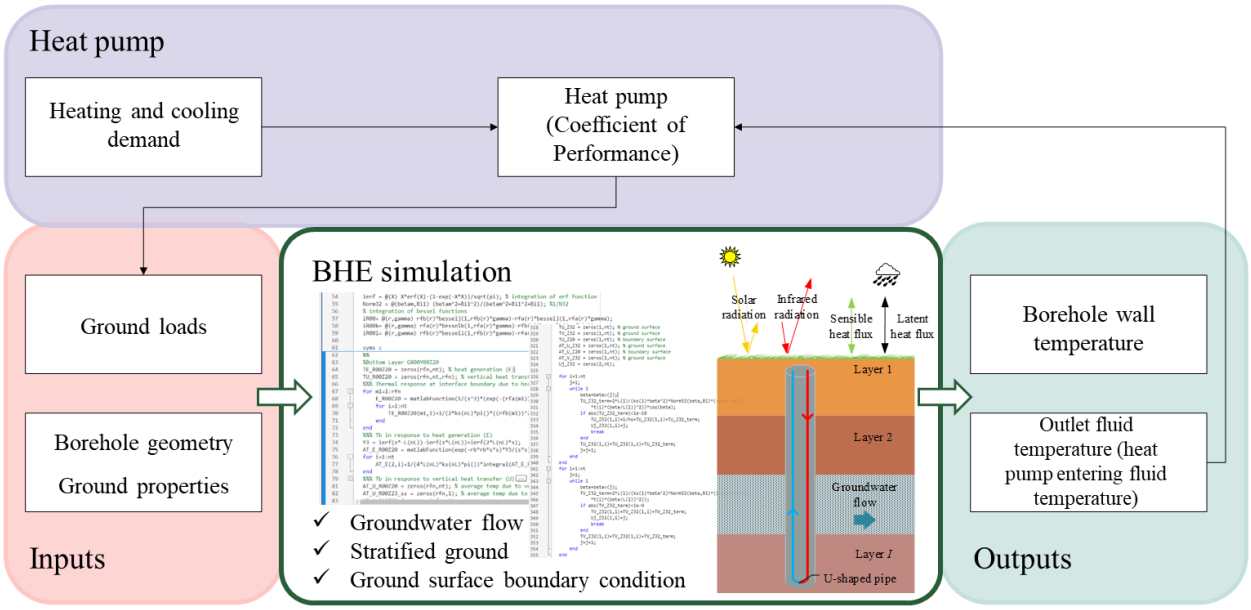

Figure 1-5. The illustration of the refined BHE simulation method.

1.4. Thesis structure

The study aims to refine the current BHE design methods by considering the effects of buried depth, groundwater flow, multilayered ground conditions, non-uniform heat transfer rates, and ground surface conditions. As shown in Figure 1-6, the thesis is organized according to the objectives of this study and presented in six chapters.

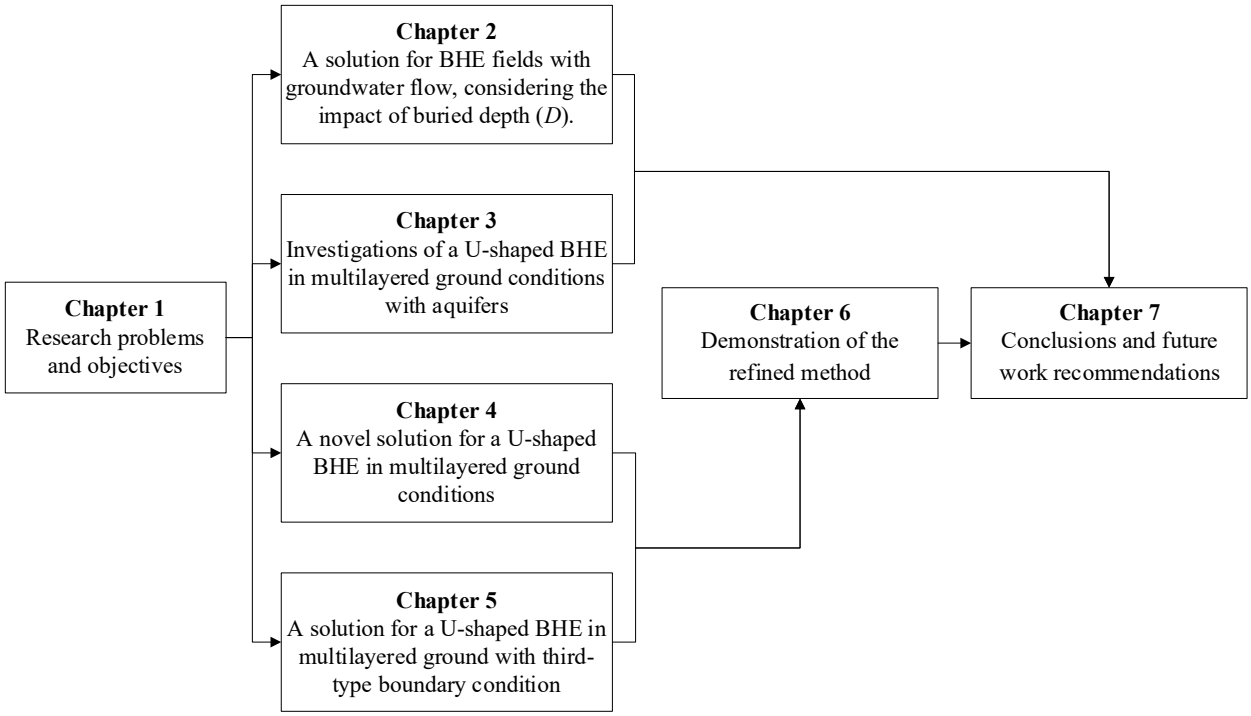

Figure 1-6. A flow chart showing the outline of this thesis.

Chapter 1 provides an introduction to BHEs, followed by a concise literature review of complex ground conditions. The objectives of this work are also presented.

Chapter 2 presents a solution for a BHE field with groundwater flow. The solution for a BHE field was obtained by spatially superposing the solution for a single BHE. A sensitivity analysis was carried out to evaluate the effect of the buried depth on heat transfer in BHE fields with groundwater flow. The results indicated that neglecting the buried depth leads to an over-prediction of exploitable heat. This over-prediction is exacerbated by an increasing number of boreholes in borehole fields or a decreasing Peclet number.

Chapter 3 investigates the effects of the non-uniform heat transfer rate for a U-shaped BHE in a layered subsurface with aquifers. A two-way coupling scheme was proposed to analyze the simultaneous heat transfer processes occurring inside and outside the borehole. The solution derived from this scheme is referred to as the MVQ solution, representing multilayered ground with varying heat transfer rates. For the specific parameters considered in this study, the heat transfer rate in the aquifer was about 21.69% more than the average rate. Furthermore, the influence of the aquifer is examined, showing that heat transfer in the aquifer strengthens with an increase in flow velocity. This highlights the importance of the MVQ solution for accurate thermal performance predictions of BHEs with aquifers.

Chapter 4 introduces a novel solution for analyzing the heat transfer outside a BHE in a layered subsurface. The proposed solution was integrated with the two-way coupling scheme, referred to as the MVQ solution, which considers non-uniform heat transfer rates. A comparison between the MVQ solution and an equivalent three-dimensional finite element (FE) model built in COMSOL Multiphysics showed a maximum mean absolute percentage error (MAPE) of less than 2.50%. In contrast, established analytical solutions that assume uniform heat transfer rates might potentially overpredict ground temperatures in certain layers by up to 50.82%. A parameter study revealed that inhomogeneous ground thermal properties strengthen the variation in heat transfer rates along the borehole length. Consequently, the MVQ solution is deemed essential for accurate thermal performance predictions of BHEs in multilayered ground conditions.

Chapter 5 extends the MVQ solution to consider the influence of the ground surface conditions. The extended solution incorporated a third-type boundary condition with a surface energy balance. Verification with an exact solution in a homogeneous ground yields a maximum error of

approximately 0.2%, showcasing its superior prediction accuracy. A systematic comparison revealed that using a constant ground surface temperature generally underestimates temperature changes in the ground, particularly for short BHE systems for a longer time. The underestimation may be up to 26.3% for a short 15-metre borehole. Additionally, the circulating fluid can transmit the impact of the ground surface condition to greater depths. The results indicated that at the bottom of a 70-metre borehole, the underestimation caused by using a constant ground surface temperature remains significant at 6.85%. These findings emphasize the indispensability of the MVQ solution.

Chapter 6 demonstrates the refined method utilizing the MVQ solution to the design of a BHE. The investigation focused on assessing the thermal performance of a BHE within a commercial building over a 10-year operational span while incorporating monthly heating and cooling loads. The refined method revealed that incorporating the multilayered ground configuration in the design phase could lead to a reduction in the depth of the BHE by approximately 14.3% for BHEs designed to be 70 metres deep under the conditions investigated in this study.

Chapter 7 concludes the major findings from this work lists the major limitations of this work and suggests a direction for further study. Further research on the BHE system is also recommended.

Chapter 2. Considering buried depth for vertical borehole heat exchangers in a borehole field with groundwater flow—an extended solution

This chapter has been accepted as **Guo, Y.**, Hu, X., Banks, J., & Liu, W. V. Considering buried depth for vertical borehole heat exchangers in a borehole field with groundwater flow—An extended solution. *Energy and Buildings*, *235*, 110722.

Nomenclature

B	borehole spacing	[m]
c	specific heat capacity	[$Jkg^{-1}K^{-1}$]
D	buried depth	[m]
d	$= \frac{D}{H}$	
$erf(X)$	error function	
Fo	Fourier number	
H	borehole length	[m]
I_0	modified zero order Bessel function of the first kind	
k	thermal conductivity	[$Wm^{-1}K^{-1}$]
n	number of observations	
N	number of boreholes in a borehole field	
Pe	Peclet number	
q_l	heat flow rate per unit length of the borehole	[Wm^{-1}]

Greek symbols

r, r'	radial distance to the source	[m]
r_b	radius of the borehole	[m]
R	$= \frac{r}{H}$	
s	$= \frac{1}{\sqrt{4\alpha(t-t')}}$	
t, t'	time	[s]
t_s	steady-state time	[s]
T	temperature	[°C]
T_0	undisturbed ground temperature	[°C]
ΔT	temperature variation	[°C]
U	$= \frac{u_d \rho_w c_w}{\rho c}$	[ms^{-1}]
u_d	groundwater velocity	[ms^{-1}]
ΔX	non-dimensional distance in the x-direction	
X, Y	arguments of functions	
x, y, z, z'	coordinates	[m]

α	thermal diffusivity	[m^2s^{-1}]	ρ	density	[kgm^{-3}]
φ	cylindrical coordinate		Θ	$= \frac{2\pi k \Delta T}{q_l}$	

Subscripts

A	analytical model	*w*	water
C	3D-FE COMSOL model	*b*	borehole

Superscripts

$\bar{}$	$= \frac{1}{H}\int_0^H \cdots \, dz'$ integral mean

2.1. Introduction

A ground source heat pump (GSHP) is a heat pump system that conveys heat to or from the ground [83]. By using a GSHP, low-temperature geothermal energy can be utilized to provide space heating and cooling [56]. GSHP systems have been receiving escalating interest due to their high energy efficiency, low electricity consumption, and potential to reduce greenhouse gas emissions [84]. Up until the end of 2013, the total installed capacity and the annual energy use of GSHP systems in Canada were estimated at 1,449 MWt and 11,111 TJ/year, respectively, and approximately 120,000 units had been installed nationwide [9, 85]. Among these installations, the vertical GSHP system is one of the most-used types, which occupies around 26% of the market [85].

The major component of a vertical GSHP system is a set of borehole heat exchangers (BHEs) buried in the ground (see Figure 2-1) [86]. A BHE normally contains a single (or double) U-tube placed in a vertical borehole [15]. The space between the borehole wall and the U-tube is usually grouted or backfilled [10]. In the tube, a working fluid (usually a water and antifreeze mixture) is circulated to collect/discharge heat from/to the ground, acting as a heat sink/source [10, 28]. A primary design parameter for a BHE is the borehole length. A longer length of the borehole generally provides an increase in heat extraction/injection [87]; however, the drilling costs also increase with the depth drilled [88]. For this reason, the heat exchanger normally comprises a borehole field in the order of 10-100 boreholes in non-residential applications [45]. These boreholes are normally connected to a single heat pump, and their size is designed to satisfy the intended heat demand of the project during the life cycle of the system (usually decades) [89, 90].

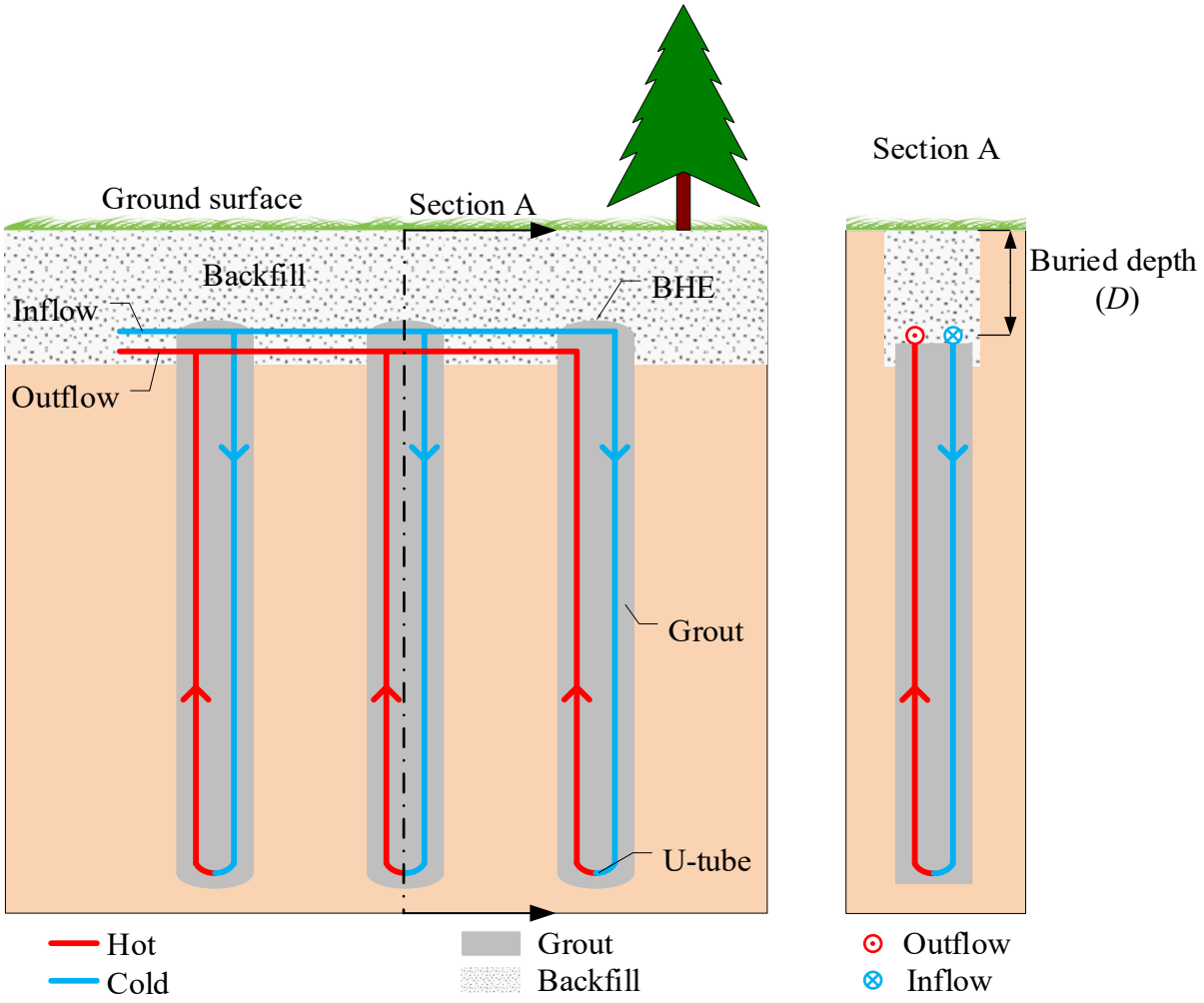

Figure 2-1. Schematic of borehole heat exchangers (BHEs) in heat extraction mode. Buried depth (*D*) represents the depth at which the horizontal connecting piping is buried.

To determine the size of the BHEs, computer simulations are usually used for predicting the long-term temperature evolution of the working fluid and the surrounding ground over the expected lifetime of the BHE system (usually up to 30 years) [91-93]. For analyzing the long-term heat transfer process in the surrounding ground, a simulation method was proposed by Eskilson [23] involving the use of non-dimensional thermal response factors, also known as *g*-functions. They have been employed commonly in BHE design tools, such as GLHEPRO [19] and Earth Energy

Designer (EED) [20]. For a specific borehole field configuration, the g-function gives the relationship between the temperature variation (ΔT) at the borehole wall from its undisturbed value (T_0) and the time-constant heat flux (q_l) applied at that borehole wall surface [23, 24],

$$\Delta T = T_b - T_0 = \frac{q_l}{2\pi k} \times g\left(\frac{t}{t_s}, \frac{r_b}{H}, \frac{B}{H}\right), \tag{2-1}$$

where T_b [K] is the borehole wall temperature, T_0 [K] is the undisturbed ground temperature, q_l [Wm^{-1}] is the rate of heat production or withdrawal per unit length, and k [$Wm^{-1}K^{-1}$] is the ground thermal conductivity. As shown in Equation (2-1), the g-function depends on three non-dimensional parameters: (r_b/H) is the ratio of the borehole radius over the borehole length; (B/H) is the ratio of the borehole spacing over the borehole length; and (t/t_s) is the non-dimensional time where $t_s = \frac{H^2}{9\alpha}$ is the steady-state time, and α [m^2s^{-1}] is the ground thermal diffusivity [23]. Eskilson's g-function [23] was developed using a numerical finite-difference approach that considered the transient radial-axial heat transfer in a single borehole. For a borehole field (a field containing multiple boreholes), g-functions were computed by superimposing the numerical solutions for each borehole in space to obtain the thermal response from the borehole field [23, 49, 94]. Because computing g-functions numerically is time-consuming and computationally intensive, a relatively large data set of g-functions was pre-computed for different borehole geometries and configurations and was embedded in the BHE design tools [29].

Eskilson's *g*-functions [23], however, were computed considering the pure conductive heat transfer around BHEs and ignoring the effect of groundwater advection. In general, the effect of groundwater flow is beneficial to the thermal performance of the BHEs. Chiasson et al. [45] compared the thermal performance of a 4 × 4 borehole field designed using pure heat conduction procedures with that of one simulated by the numerical finite-element model with groundwater flow. Comparisons indicated that the borehole fields were generally overdesigned by neglecting the groundwater flow. Wang et al. [47] investigated the effect of groundwater flow in an in situ experiment of a single BHE. It was shown that the groundwater flow enhanced the heat injection and heat extraction of the BHE on average by 9.8% and 12.9%, respectively, compared with the numerical results of a pure conductive scenario. In this regard, Sutton et al. [48], Diao et al. [49], Molina-Giraldo et al. [35], and Tye-Gingras and Gosselin [36] developed analytical solutions for transient heat transfer around BHEs with groundwater flow based on the moving line source (MLS) theory [31]. Coupled with a suitable spatial superposition scheme, *g*-functions have been computed based on these analytical solutions over a large range of time scales, borehole geometries, and borehole configurations [23, 94]. However, a significant design parameter buried depth (D), has been neglected in these MLS solutions.

For grouted boreholes, the buried depth can represent the depth at which the horizontal connecting piping is buried [34]. Horizontal connecting piping is normally buried deeper in cold regions than in warm regions to avoid the associated risk of freeze-thaw cycles in seasonally frozen ground [37]. As the buried depth increases, the thermal resistance of the ground layer above the boreholes increases, which diminishes the heat flow between the ground surface and the BHEs [38]. Cimmino et al. [38] showed that the steady-state value of one *g*-function decreases by about 25% as the non-dimensional buried depth (D/H) reduces from 0.2 to 0 for a 10 × 10 borehole field.

According to the design procedures set forth by ASHRAE (American Society of Heating, Refrigerating and Air-Conditioning Engineers) design procedures [95], the total length of boreholes depends on three parameters (i.e., effective ground thermal resistance for an annual pulse, a peak short-term pulse, and a peak daily pulse) that can be obtained from the *g*-function. It means that a 25% under-prediction of the *g*-function can lead to an over-prediction of the rate of heat exploitation (See Equation (2-1)) and can result in an undersized design by as much as 25%. To address the effect of buried depth, Claesson and Javed [29] proposed an analytical solution for the transient heat transfer around BHEs including the term buried depth (*D*). Later, the effect of buried depth from 0 to infinity (∞) was examined based on analytical solutions proposed by Cimmino et al. [38] and proposed by Bandos et al. [39]. Their results showed that the temperature variation caused by buried depth is relatively small for a single deep borehole; however, it becomes conspicuous for a field of multiple short boreholes [38, 39].

In general, neglecting the buried depth leads to an over-prediction of the exploitable heat from the ground, resulting in an under-sizing of the BHE design. In our previous study [40], the buried depth has been integrated into a new analytical solution—the moving finite line source solution considering buried depth (MFLSD) for one single borehole. However, until now, no research has been conducted on the use of the MFLSD solution in borehole fields (containing multiple boreholes) in common commercial (non-residential) applications. To this end, the objective of the present study is to extend the previous MFLSD solution from one single borehole to a borehole field and investigate the effect of buried depth in a borehole field with groundwater flow. The results can help in the BHEs system designing in commercial (non-residential) applications.

2.2. Methodology

The principle of superposition was employed to extend the MFLSD solution from a single borehole to a borehole field. Firstly, the MFLSD solution for a single borehole was briefly introduced. Secondly, three spatial superposition models (i.e., in cases M1, M2, and M3) were introduced, referring to three different boundary conditions. The three boundary conditions concept was originally proposed by Cimmino and Bernier [96]. M1 was then employed with the MFLSD solution for borehole fields. After that, the MFLSD solution for borehole fields was numerically verified with a three-dimensional (3D) finite element (FE) model constructed in COMSOL Multiphysics. For the verification, test cases were designed based on a real GeoExchange system project [97] in Edmonton, Canada. Finally, a parametric study was conducted to examine the effect of buried depth in three different simple rectangle configurations. The same borehole configuration has been used by many other researchers for BHE modelling [38, 49, 89, 98]. The MFLSD solution, spatial superposition models, and the 3D-FE COMSOL model are described below.

2.2.1 Simplifications and the MFLSD solution

For practical purposes, seven simplifications (S1 to S7) had been made to develop the MFLSD solution for a single borehole [40]. Carried over to this study, these assumptions are consistent with the work of Eskilson [23] or the work of Tye-Gingras and Gosselin [36]:

S1: The borehole can be treated as a line source because the radius of the borehole (e.g., r_b = 0.045 m) is very small when compared with its length (e.g., H = 70 m) [31].

S2: The ground surrounding the borehole is a homogeneous saturated porous media possessing mean thermal properties (i.e., mean thermal conductivity and mean thermal diffusivity) [23]. These mean values can be obtained from in situ thermal response tests [99, 100].

S3: The ground temperature is simplified using the (homogeneous) undisturbed ground temperature (T_0) that is approximated as the mean temperature along the borehole [23].

S4: The ground surface temperature fluctuation is neglected. The interface between ambient air and the ground surface is maintained at a constant temperature, which is equal to the undisturbed ground temperature [23].

S5: The groundwater is parallel to the ground in the x-direction with a uniform Darcy velocity u_d, resulting in an effective thermal transfer velocity $U = \frac{u_d \rho_w c_w}{\rho c}$ [ms^{-1}]. Herein, ρc [Jm^{-3}K^{-1}] is the volumetric heat capacity of the bulk porous medium, and $\rho_w c_w$ [Jm^{-3}K^{-1}] is the volumetric heat capacity of the groundwater [49].

S6: Local thermal equilibrium (LTE) is considered (i.e., the groundwater temperature is the same as the ground temperature at any point), which is a commonly used hypothesis for heat transfer in porous media [101]. At a macroscopic scale, LTE is valid because the temperatures of water and solids vary slowly in time and space, and the difference between them is minimal [102].

S7: All thermal and hydraulic properties are not affected by temperatures [36]. This assumption can be justified by the small ground temperature variation over the system's lifespan. In the design, the ground temperature variation is controlled at the minimum possible level to utilize geothermal energy efficiently [86].

Based on these assumptions, the heat transfer problem is seen as a line source with a finite length H moving with a speed of U in a homogeneous saturated porous media. If the line source starts releasing heat continuously at time zero, the MFLSD solution [40] gives the average temperature variation over the borehole length at any later time (t), at any radius (r), and at any azimuth (φ),

$$\overline{\Delta T} = \frac{q_l}{4\pi k} exp\left(\frac{rU}{2\alpha} cos(\varphi)\right) \int_{\frac{1}{\sqrt{4\alpha t}}}^{\infty} exp\left(-\frac{U^2}{16\alpha^2 s^2} - r^2 s^2\right) \frac{Fun(Hs,Ds)}{Hs^2} ds, \qquad (2\text{-}2)$$

where

$$Fun(X,Y) = 2ierf(X) + 2ierf(X+2Y) - ierf(2X+2Y) - ierf(2Y), \qquad (2\text{-}3)$$

$$ierf(X) = \int_0^X erf(Y)\, dY = Xerf(X) - \frac{1}{\sqrt{\pi}}\left(1 - e^{-X^2}\right), \qquad (2\text{-}4)$$

and $erf(X) = 1 - \frac{2}{\sqrt{\pi}} \int_X^{\infty} e^{-t^2}\, dt$ is the error function in mathematics.

The average temperature variation, Equation (2-2), can be integrated over the borehole circumference at the borehole radius (where $r = r_b$),

$$\overline{\Delta T} = \frac{q_l}{4\pi k} I_0\left(\frac{rU}{2\alpha}\right) \int_{\frac{1}{\sqrt{4\alpha t}}}^{\infty} exp\left(-\frac{U^2}{16\alpha^2 s^2} - r^2 s^2\right) \frac{Fun(Hs,Ds)}{Hs^2} ds, \quad (2\text{-}5)$$

where $I_0(X)$ is a modified zero-order Bessel function of the first kind.

Both Equations (2-2) and (2-5) can be non-dimensionalized to reduce the number of independent variables. The following non-dimensional variables are introduced: $\overline{\Theta_{MFLSD}} = 2\pi k \Delta T / q_l$, $R_b = r_b/H$, $d = D/H$, Fourier number $Fo = \alpha t / H^2$, and Peclet number $Pe = UH/\alpha$. It is worth noting that the non-dimensional variable $\overline{\Theta_{MFLSD}}$ has an identical physical meaning with the *g*-function. In order to distinguish the analytical and numerical *g*-functions, the analytical *g*-functions are denoted by $\overline{\Theta}(R_b, Fo, Pe, d)$. Equations (2-2) and (2-5) can be expressed in non-dimensional forms as

$$\overline{\Theta_{MFLSD}}(R_b, \varphi, Fo, Pe, d) = \frac{1}{2} exp\left(\frac{R_b Pe}{2} cos(\varphi)\right) \int_{\frac{1}{\sqrt{4Fo}}}^{\infty} exp\left(-\frac{Pe^2}{16s^2} - {R_b}^2 s^2\right) \frac{Fun(s,d\cdot s)}{s^2} ds, \quad (2\text{-}6)$$

$$\overline{\Theta_{MFLSD}}(R_b, Fo, Pe, d) = \frac{1}{2} I_0\left(\frac{R_b Pe}{2}\right) \int_{\frac{1}{\sqrt{4Fo}}}^{\infty} exp\left(-\frac{Pe^2}{16s^2} - {R_b}^2 s^2\right) \frac{Fun(s,d\cdot s)}{s^2} ds. \quad (2\text{-}7)$$

2.2.2 Principle of superposition for borehole fields

In non-residential applications, a BHE system normally comprises a borehole field containing multiple boreholes. Since multiple boreholes use the same ground resource, adjacent boreholes then influence the ground temperature distribution of each other after a few months (the process is

also known as thermal interaction) [10]. Accounting for this thermal interaction, *g*-functions for borehole fields are normally calculated by spatial superposition of single borehole solutions [23, 28, 36]. The principle of superposition can also be employed with the MFLSD solution [40] due to the linear relationship between the temperature variation (ΔT) and heat flux (q_l) (above-mentioned in the assumption S7). By employing the spatial superposition for the MFLSD solution, the temperature variation of a certain borehole *i* is calculated by superimposing all the response factors contributed by all boreholes in the borehole field [36],

$$\overline{\Delta T_i} = \frac{q_{l_i}}{2\pi k}\overline{\Theta_{MFLSD}} + \sum_{\forall j \neq i}\frac{q_{l_j}}{2\pi k}\overline{\Theta_{ji}}, \tag{2-8}$$

where $\overline{\Theta_{ji}}$ is the thermal effect of borehole *j* on borehole *i* in a non-dimensional form, and it can be obtained from

$$\overline{\Theta_{ji}} = \frac{1}{2}\cdot exp\left(\frac{\Delta X_{ji} Pe}{2}\right)\cdot I_0\left(\frac{R_b Pe}{2}\right)\cdot \int_{\frac{1}{\sqrt{4Fo}}}^{\infty} exp\left(-\frac{Pe^2}{16s^2} - {R_{ji}}^2 s^2\right)\cdot \frac{Fun(s,d\cdot s)}{s^2}\,ds, \tag{2-9}$$

with

$$\Delta X_{ji} = \frac{1}{H}\left|x_j - x_i\right|, \quad R_{ji} = \frac{1}{H}\sqrt{\left(x_j - x_i\right)^2 + \left(y_j - y_i\right)^2}, \tag{2-10}$$

where R_{ji} is the non-dimensional distance between the borehole i and the borehole j, and ΔX_{ji} is the non-dimensional distance between the borehole i and the borehole j in the x-direction.

Superimposing single borehole solutions, the heat flux (q_l) of boreholes can be assumed to be constant in time, as in case Model 1 (M1), or to vary in time and space, as in cases M2 and M3 (Table 2-1) [96]. Note that M1 and M2 all can be coupled with the MFLSD solution directly, and M3 cannot. These three spatial superposition models are under different boundary conditions along and between boreholes as briefly described below.

Table 2-1. Different models and boundary conditions for spatial superposition.

Models	Boundary condition (BC) along a single borehole	BC between boreholes	Reference
M1	The heat flux is constant along the borehole.	The heat flux is evenly distributed among the boreholes.	[28, 36]
M2	The heat flux is constant along the borehole.	The heat flux varies to keep the same average borehole wall temperature for all boreholes.	[38, 103]
M3	The heat flux varies to keep the borehole temperature uniformly distributed along the borehole.	The heat flux varies to keep the same average borehole wall temperature for all boreholes.	[96, 104]

M1 assumes that the heat flux is evenly distributed among the boreholes [28, 29]. Due to this assumption, Equation (2-8) can be simplified to calculate the non-dimensional temperature response of a certain borehole *i* in the borehole field,

$$\overline{\Theta_i} = \overline{\Theta_{MFLSD}} + \sum_{\forall j \neq i} \overline{\Theta_{ji}}. \tag{2-11}$$

Finally, the *g*-function is obtained by averaging the non-dimensional temperature response of all the boreholes in the borehole field,

$$\overline{\Theta_N} = \frac{1}{N} \sum_{i=1}^{N} \overline{\Theta_i}, \tag{2-12}$$

where *N* is the number of boreholes in a borehole field.

M2 is based on the assumption that the average borehole wall temperature is the same for all boreholes in the field [38]. In case M2, the heat flux is constant along each borehole from top to bottom; however, it is different between boreholes and varies over time. Guided by a method proposed by Cimmino et al. [38], the temporal superposition is imposed to account for the time-varying heat flux. The time-varying heat flux is more conveniently treated as stepwise values on an hourly basis because the heating and cooling demands are typically presented using annual hourly values [105]. With stepwise heat fluxes, the ground temperature variation at the end of the

n^{th} hour can be computed as a temporal superposition of the response from each of the preceding heat loads [105],

$$\overline{\Delta T}(t_n) = \sum_{i=1}^{n} \frac{q_l(t_i)}{2\pi k} \overline{\Theta_{MFLSD}}(t_i - t_{i-1}). \quad (2\text{-}13)$$

A more efficient theoretical approach for this heat conduction problem is to decompose the heat fluxes into a series of heat flux increments and superimpose the response of each heat flux increment [106],

$$\overline{\Delta T}(t_n) = \sum_{i=1}^{n} \frac{q_l{}'(t_i)}{2\pi k} \overline{\Theta_{MFLSD}}(t_n - t_i), \quad (2\text{-}14)$$

where $q_l{}'(t_i) = q_l(t_i) - q_l(t_{i-1})$ is the incremental heat load between two successive heat fluxes.

Equation (2-14) consists of the linear convolution sum of two discrete sequences, where one sequence is the incremental heat load ($q_l{}'$), and the other is the thermal response function (*g*-function). Marcotte and Pasquier [107] proposed to solve the linear convolution sum efficiently using the fast Fourier transform (FFT) algorithms via the circular convolution theorem. Specifically, the linear convolution sum of the two discrete sequences can be found by taking an FFT of each sequence, multiplying pointwise in the frequency domain, and then performing an inverse FFT [108],

$$2\pi k\overline{\Delta T} = \mathfrak{I}^{-1}\left[\mathfrak{I}(q_l{}')\mathfrak{I}\left(\overline{\Theta_{MFLSD}}\right)\right], \tag{2-15}$$

where, in the discrete case, $\mathfrak{I}$ denotes the FFT, and $\mathfrak{I}^{-1}$ denotes the inverse-FFT.

For two sequences of length n, each sequence must be padded with zeros to extend the length to $2n$-1 to ensure that the circular convolution and the linear convolution can coincide.

According to Equation (2-15), Equation (2-9) can be Fourier transformed into the frequency domain,

$$\mathfrak{I}\left(2\pi k\overline{\Delta T}\right) = \sum_{t_i \le t} \mathfrak{I}\left(q_{l_i}{}'\right)\mathfrak{I}\left(\overline{\Theta_{MFLSD}}\right) + \sum_{j=1\ \&\ j\neq i}^{N} \sum_{t_i \le t} \mathfrak{I}\left(q_{l_j}{}'\right)\mathfrak{I}\left(\overline{\Theta_{j\to i}}\right). \tag{2-16}$$

In addition, the constant total heat flux (q_t) is equal to the sum of the heat fluxes of every borehole in the field. Due to the linearity of the Fourier transform, the constant total heat flux in the frequency domain becomes

$$\mathfrak{I}(q_t{}') = \sum_{i=1}^{N} \mathfrak{I}\left(q_{l_i}{}'\right). \tag{2-17}$$

Equations (2-16) and (2-17) form a system of linear equations,

$$\begin{bmatrix} 0 \\ 0 \\ \vdots \\ 0 \\ \Im(q_t{}') \end{bmatrix} = \begin{bmatrix} \Im(\overline{\Theta_{MFLSD}}) & \Im(\overline{\Theta_{2\to1}}) & \cdots & \Im(\overline{\Theta_{N\to1}}) & -1 \\ \Im(\overline{\Theta_{1\to2}}) & \Im(\overline{\Theta_{MFLSD}}) & \cdots & \Im(\overline{\Theta_{N\to2}}) & -1 \\ \vdots & \vdots & \ddots & \vdots & \vdots \\ \Im(\overline{\Theta_{1\to N}}) & \Im(\overline{\Theta_{2\to N}}) & \cdots & \Im(\overline{\Theta_{MFLSD}}) & -1 \\ 1 & 1 & 1 & 1 & 0 \end{bmatrix} \begin{bmatrix} \Im(q_{l_1}{}') \\ \Im(q_{l_2}{}') \\ \vdots \\ \Im(q_{l_N}{}') \\ \Im(2\pi k\overline{\Delta T}) \end{bmatrix}. \quad (2\text{-}18)$$

The solution of the system of linear equations gives the heat flux in each borehole. The resulting non-dimensional temperature response $\overline{\Theta_{MFLSD}} = 2\pi k\Delta T/q_t/N$ becomes the analytical g-function.

M3 bears the assumption that the borehole temperature is uniformly distributed along the borehole and is equal for all boreholes [96]. This was assumed because the boreholes are connected in parallel with the same inlet fluid temperature in common real installations. This assumption was imposed on Eskilson's numerical model [23], and the same assumption was also considered in a semi-analytical model proposed by Cimmino and Bernier [96]. In the semi-analytical model, each borehole is separated into several segments. Each borehole segment is modelled by a line source of finite length, and a finite line source solution proposed by Cimmino and Bernier [96] accounts for the wall temperature variation of a segment caused by other segments. The average wall temperature is kept the same for all segments by varying the heat flux in each segment. As the number of segments increases, the result becomes closer to Eskilson's g-function; however, there is also an increase in calculation time. For instance, the calculation time is about 13 times greater for M3 (using 12 segments) than it is for M2 [96].

Among these three cases, M1 has gained the most interest in the literature [28, 29, 36, 49]. M1 was therefore employed in this study. A few studies have shown that the results of M2 are generally in good agreement with the results of M1 and M3 for small borehole fields [38, 103]; therefore, M2 was used for verification in this study. However, M3 was not employed in this study. Since the MFLSD solution is for the average wall temperature of an entire borehole and does not account for thermal interaction between borehole segments, the MFLSD solution cannot be coupled with the M3 directly.

2.2.3 Borehole fields

Employing spatial superposition for the MFLSD solution, the *g*-function can be computed for borehole fields comprising multiple boreholes in arbitrary configurations. In this study, three simple rectangle arrays (i.e., 3 × 2 [38, 49, 98, 109], 4 × 4 [45, 68, 89, 110], 10 × 10 [68, 96] borehole field) with an equal borehole spacing (B) were used because they have been commonly used in the literature. According to the design procedures set forth by ASHRAE [95], a borehole spacing from 6 m to 8 m is recommended to reduce the thermal interaction between individual boreholes. In Figure 2-2, a 3 × 2 borehole field is presented to show the concept.

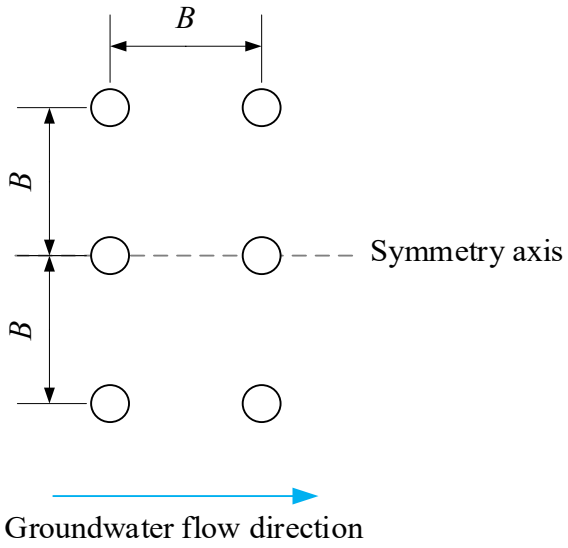

Figure 2-2. Schematic diagram of a 3 × 2 borehole field. *B* represents the borehole spacing that is the centre-to-centre distance between adjacent boreholes.

2.2.4 A real case scenario used for verification

For the verification of the *g*-function from the MFLSD solution for borehole fields, test cases were designed based on a real GeoExchange system project [97] in Edmonton, Canada. In the project, boreholes were designed with a length of 70 m and a radius of about 0.046 m; they were equally spaced at a distance of B = 7.6 m. A borehole spacing from 6 m to 8 m is recommended by the design procedures set forth by ASHRAE [95]. These two values (6 m and 8 m) of borehole spacing were also selected for the verification.

The thermal properties of the ground were acquired from an in situ thermal conductivity test [97]. The tested undisturbed ground temperature (T_0) is 6 °C, the thermal conductivity (k) is 1.59 $Wm^{-1}K^{-1}$, and the thermal diffusivity of the borehole (α) is 6.944 × 10^{-7} m^2s^{-1}. The volumetric heat capacity of the bulk porous medium (ρc) is 2.290 × 10^6 $Jm^{-3}K^{-1}$. A transient study was set for a sufficiently long time, from ~20 hours (about $Fo = 10^{-5}$) to ~ 100 years (or $Fo = 0.5$). For 100-year

continuous simulations, the heat injection rate was kept at q_l = 56 Wm^{-1}, which is the expected peak load on the U-tubes for the project.

Table 2-2. Parameters used in the calculations [97].

Parameter	**Value**
Length of the borehole (H)	70 m
Borehole radius (r_b)	0.04595 m
Thermal conductivity of the ground (k)	1.59 $Wm^{-1}K^{-1}$
Thermal diffusivity of the ground (α)	6.944×10^{-7} m^2s^{-1}
Volumetric heat capacity of the ground (ρc)	2.290×10^{6} $Jm^{-3}K^{-1}$
Volumetric heat capacity of water ($\rho_w c_w$) at 6 °C	4.200×10^{6} $Jm^{-3}K^{-1}$

Although hydraulic conditions were not reported in the project, a preliminary study [40] shows that the influence of groundwater flow can be illustrated for the Peclet number Pe > 1.74 on a single borehole. Hence, a scenario was defined with a uniform velocity of about $u_d = 4 \times 10^{-8}$ ms^{-1} (or Pe = 7.5) to represent the heat conduction-advection condition. In comparison, another scenario was defined at u_d = 0 ms^{-1} (or Pe = 0) for the conduction-dominated condition.

Finally, a customized MATLAB code was employed to calculate the MFLSD solutions for the average borehole wall temperature variation ($\overline{\Delta T}$). For the evaluation of a single integral, the

MATLAB *integral* function with a tolerance of 10^{-12} was used. All calculations were performed on an Intel Xeon-E3 3.10 GHz processor with 64 GB RAM.

2.2.5 Model verification through 3D finite element modelling

Similar to many previous studies [64, 111-113], 3D finite element (FE) modelling in COMSOL Multiphysics was used for the verification of *g*-function from the MFLSD solution. Borehole geometries and thermal properties were the same as those tested in the real case scenario. A 3 × 2 borehole field was selected for verification. A symmetrical boundary condition was applied to reduce the domain size by half. Each borehole in the field was represented by a cylinder aligned with the *z*-axis, and its surrounding ground was built as a water-saturated porous medium with constant thermal properties. In contrast to the line source in the analytical model, constant continuous heat flux was applied directly to the borehole wall in the 3D-FE COMSOL model. This difference would result in a great discrepancy between the MFLSD and the 3D-FE COMSOL solutions in the short-term. However, the discrepancy is acceptable since the *g*-functions are used for long-term prediction, and some other methods are used for short-term prediction [114-116]. For this reason, the reported simulation results for the verification started from 20 hours rather than time zero.

In the 3D-FEM COMSOL model, the initial and boundary conditions were set in such a way that they met the assumptions made for the MFLSD solution. A uniform groundwater flow was assigned throughout the entire domain along the *x*-axis. A uniform initial temperature of 6 °C was assigned to the entire domain to represent undisturbed ground temperature (T_0). A fixed temperature of 6 °C was also assigned to the top boundary to represent constant ground surface temperature.

A preliminary analysis has been done to ensure the simulation results are independent from the model domain. More detailed information is provided in Guo et al. [40]. After the preliminary analysis, a model was constructed with a horizontal domain of (x = 800 m) × (y = 200 m) and a thickness of (z = 280 m). At the selected domain size, temperature changes at the external boundaries were less than 0.003 °C at the end of the simulations. Although the temperature should be kept in undisturbed conditions at the far boundary in principle, a 0.003 °C temperature change was selected to ensure a reasonable domain size and to preserve calculation accuracy [94].

To have a more accurate temperature variation at the borehole wall, finer elements (0.018 m) were meshed at areas that are close to the borehole, and coarser elements (20 m) were meshed at regions that are relatively far away (see Figure 2-3). Tye-Gingras and Gosselin [36] suggested that a mesh-independent solution can be obtained when the number of meshes is doubled, yielding a relevant difference of less than 1% for the results under every time-step. Therefore, a comparison of average borehole wall temperatures was carried out with an increasing number of elements on the borehole wall boundary. In our case, when the number of elements of the domain was doubled from about five million to eleven million, the maximum difference in the average borehole wall temperature was about 0.04% in the considered time domain. This difference is acceptable since it is far less than 1%. Finally, the mesh geometry with about eleven million (11,000,000) elements was selected, which can ensure a reasonable number of elements and preserve calculation accuracy.

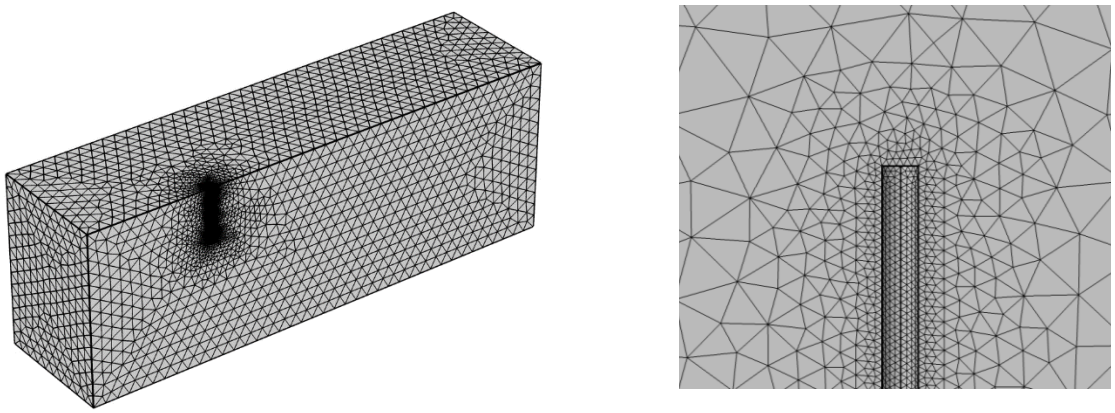

(a) (b)

Figure 2-3. Mesh used in numerical simulations using free tetrahedral elements: (a) the mesh of the borehole field and (b) the mesh around the top end of a single borehole. Finer elements (0.018 m) were meshed at areas that were close to the borehole, and coarser elements (20 m) were meshed at regions that were relatively far away.

To calculate the discrepancy between the MFLSD solution and the 3D-FE COMSOL solution, the mean absolute error (MAE) and root mean squared deviation (RMSD) were computed over the given time period from 20 hours to 100 years. MAE and RMSD are two of the most well-known and commonly accepted estimators that tell how much spread there is for the solutions in the vertical direction [85, 117]. In our case, the MAE represents the average magnitude of the differences between the temperature predicted from the MFLSD solution and the temperature observed from the 3D-FE COMSOL solution,

$$MAE = \frac{\sum_{i=1}^{n} \left| \overline{\Theta_A}(Fo_i) - \overline{\Theta_C}(Fo_i) \right|}{n}, \tag{2-19}$$

and RMSD represents the standard deviation of that difference,

$$RMSD = \sqrt{\frac{\sum_{i=1}^{n}\left(\overline{\Theta_A}(Fo_i)-\overline{\Theta_C}(Fo_i)\right)^2}{n}}. \quad (2\text{-}20)$$

2.2.6 Criterion

Acceptable values for MAE and RMSD are chosen for each specific case [118]. In this study, 0.02 was set as the threshold limit on the MAE and RMSD with respect to $\overline{\Theta_N}$ that meets the criterion of Molina-Giraldo et al. [35] and the criterion of Tye-Gingras and Gosselin [36].

An acceptable limit on oversizing or undersizing depends on the situation, using a simplified method to predict the temperature variations in the borehole field (i.e., *g*-function). In this study, a one percent (1%) difference was chosen that meets the criterion of Molina-Giraldo et al. [35] to decide whether the effect of buried depth is negligible. With the *g*-function for d = 0 as the reference, the effect of buried depth is not negligible when the discrepancy is over 1% between the reference and the MFLSD solution for other various buried depths (i.e., $\left|\overline{\Theta_N}(d)/\overline{\Theta_N}(d=0)-1\right| > 1\%$). At that time, *g*-functions from the MFLSD solution must be used to address the effect of buried depth in a borehole field with groundwater flow.

2.3. Results and discussion

2.3.1 Verification

A comparison was conducted between the analytical *g*-functions from the MFLSD solution and the results from the 3D-FE COMSOL model. As shown in Figure 2-4, the temperature variation ($\overline{\Delta T}$) in a 3 × 2 borehole field was plotted against the Fourier number (*Fo*) for three borehole spacings (*B* = 6 m, *B* = 7.6 m, and *B* = 8 m) and two Peclet numbers (*Pe* = 0 and *Pe* = 7.5). In Figure 2-4, it was shown that the temperature variation obtained from the MFLSD solution was in good agreement with the numerical solution generated with COMSOL Multiphysics over a 100-year (or *Fo* = 0.5) continuous operation. It can be seen from Table 2-3, for the given results of this section, that the maximum values of MAE and RMSD were about 0.012 and 0.015, respectively, which are lower than the thresholds of the acceptable MAE (0.02) and RMSD (0.02). Therefore, the *g*-functions from the MFLSD solution for borehole fields were considered to be numerically verified.

In addition, a comparison with the solution by Tye-Gingras and Gosselin [26] was also carried out. The *g*-functions from the MFLSD solution are identical to the solution by Tye-Gingras and Gosselin [26] for *D* = 0 m. However, the solution by Tye-Gingras and Gosselin [26] underestimates the temperature variations when buried depth is considered. For instance, the results from the solution by Tye-Gingras and Gosselin [26] were smaller than the results from the 3D-FE COMSOL model by about 7.0% and 4.2% for *Pe* = 0 and *Pe* = 7.5, respectively, at 100 years for *D* = 8 m and *B* = 7.6 m. The underestimation is caused by the thermal resistance of the ground layer between the ground surface and BHEs. The thermal resistance diminishes the changes in temperature [34]. Accounting for the effect of buried depth, the *g*-function from the MFLSD

solution gives a better prediction of the temperature variation of a borehole field with groundwater flow in the long term.

Table 2-3. MAE and MRSD between the *g*-functions predicted from the MFLSD solution and results observed from the 3D-FE COMSOL model.

Discrepancy	*Pe* = 0			*Pe* = 7.5		
	B = 6 m	7.6 m	8 m	6 m	7.6 m	8 m
RMSD	0.015	0.013	0.014	0.008	0.007	0.007
MAE	0.012	0.010	0.011	0.007	0.006	0.006

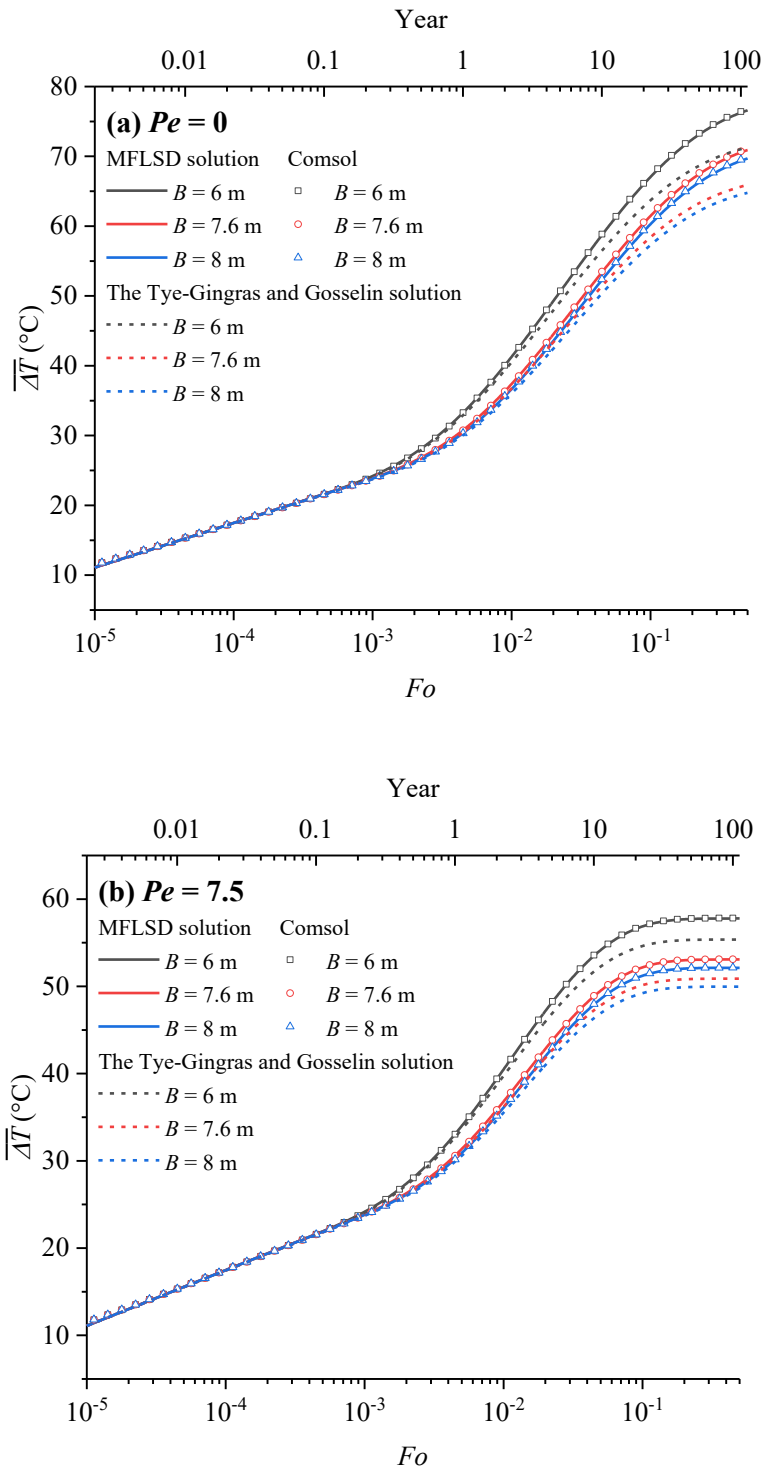

Figure 2-4. Borehole wall temperatures in a borehole field with 3 × 2 boreholes against the Fourier number for the given parameters (a) $Pe = 0$ and $D = 8$ m and (b) $Pe = 7.5$ and $D = 8$ m.

The *g*-function from the MFLSD solution (in case M1) was also verified with the solution in case M2. The non-dimensional temperature response ($\overline{\Theta_N}$) was plotted in Figure 2-5 for three different borehole arrays (i.e., 3 × 2, 4 × 4, 10 × 10 borehole fields). In general, the $\overline{\Theta_N}$ tended to reach a higher value for a large borehole field. This is because the thermal interaction becomes stronger in a large borehole field. As shown in Figure 2-5(a), the MFLSD solution in case M1 is in good agreement with the result in case M2 for a 3 × 2 borehole field in a pure heat conduction scenario. The difference is only about 0.36% between the two solutions for Fo = 0.5. Therefore, the *g*-function from the MFLSD solution (in case M1) was considered to be verified. However, the difference became noticeable in a larger borehole field. Due to the greater thermal interaction in the larger borehole field, inner boreholes have higher borehole wall temperatures. In case M2, in a pure heat conduction scenario that was constrained by the borehole wall temperature, less heat was transferred by the inner boreholes, and therefore the borehole wall temperature response became smaller [38]. In contrast, when groundwater existed in case M2, more heat was transferred by the upper-stream boreholes, and therefore the borehole wall temperature response increased.

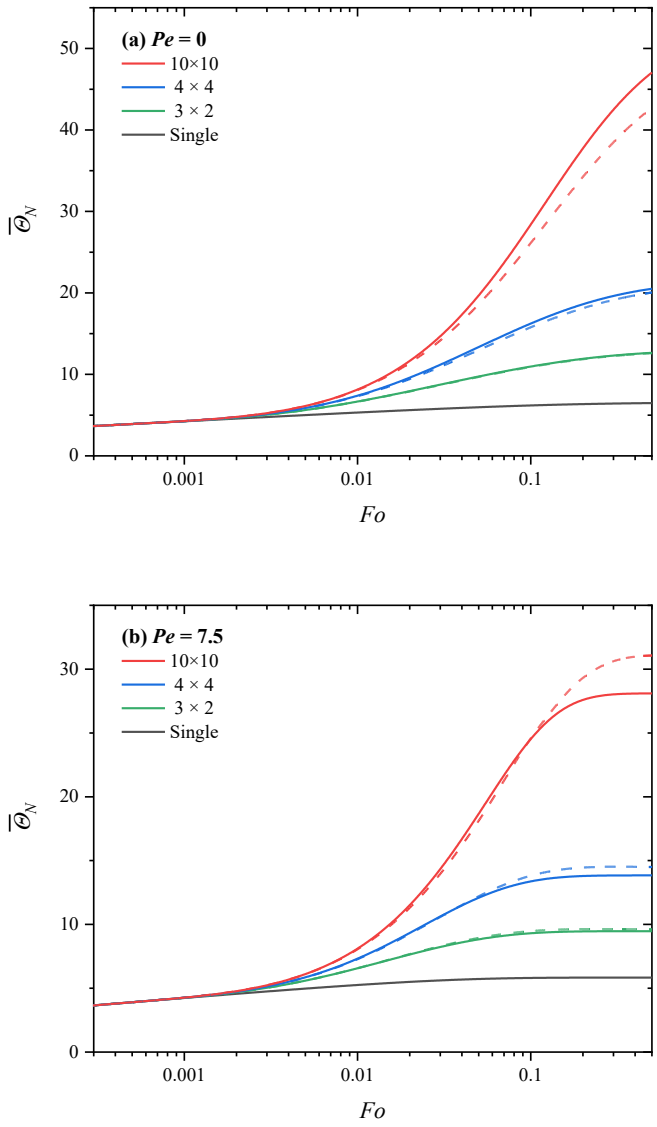

Figure 2-5. Non-dimensional temperature response from the MFLSD solution in case M1 (solid lines) and in case M2 (dashed lines) for three different borehole arrays (B = 7.6 m and D = 8 m).

The computational time was also compared between the MFLSD solution and the 3D-FE model. The comparison indicated that using numerical models (i.e., the 3D-FE model) to determine temperature variation at the borehole wall is a time-consuming and computationally intensive task. For example, the COMSOL results (shown in Figure 2-4) were obtained from numerical

simulations that calculated the temperature variation for 96 timesteps. For a scenario with Pe = 7.5, D = 8 m, and B = 7.6 m, the numerical simulation took 27,669 s (equivalent to 7 hours, 41 minutes, and 9 seconds) of computing time. The other simulations had a similar computational time of about 8 hours. Contrary to the numerical simulations, the analytical simulation (i.e., the MFLSD solution) cost 0.62 s in the calculation of the 96 timesteps, and it only took 3,813 s (equivalent to 1 hour, 3 minutes, and 33 seconds) in an hourly simulation that contained 876,000 timesteps. When the number of boreholes was extended to 100 (i.e., in a 10 × 10 borehole field), the analytical simulation spent 9.71 s in the calculation of the 96 timesteps. Therefore, it can be seen that analytical g-functions are favoured over numerical models for sizing, optimizing, and simulating the BHE system due to the superior saving of computational time.

2.3.2 Borehole field

Coupled with the superposition scheme, the MFLSD solution was extended from a single borehole to a borehole field. In order for the effects of buried depth and groundwater flow in borehole fields to be investigated, a parametric study was carried out based on the identified non-dimensional variables.

2.3.2.1 The effect of thermal interaction in a borehole field

Figure 2-6 demonstrates the non-dimensional temperature response $\overline{\Theta_{3\times2}}(Fo)$obtained with the MFLSD solution for Pe = 0, R_b= 0.001, d = 0.02. Based on ASHRAE's Handbook [95], we selected the values of borehole spacing (B) varying from 5 m to 8 m in this section. According to the typical length of a vertical borehole (50 m to 150 m), the ratio $b = B/H$ varying from 0.03 to 0.2 was considered. Two other values (0.06 and 0.1) were chosen within this range for the

sensitivity study. In addition, a theoretical lower bound solution corresponding to $b = \infty$ was also tested to set the lower limit of the solutions, which is identical to the MFLSD solution for a single borehole. For every d value, the $\overline{\Theta_{3\times2}}(Fo)$ rises as Fo increases and eventually reaches a steady state. As shown in Table 2-4, as the ratio $b =$ reduces from 0.2 to 0.03, the steady-state value increases from 9.62 to 17.64. This is because the thermal interaction between distant boreholes becomes weaker [119]. For the same reason, the influence of the thermal interactions appears early with a shorter borehole spacing. For example, all the $\overline{\Theta_{3\times2}}(Fo)$ with different borehole spacing overlap at the beginning. Then, the $\overline{\Theta_{3\times2}}(Fo)$ for b = 0.03 increases more dramatically than the others at $Fo > 10^{-4}$. On the contrary, the $\overline{\Theta_{3\times2}}(Fo)$ for b = 0.2 has a similar sharp increase until $Fo > 4.5 \times 10^{-3}$. In general, the effect of the thermal interactions appears faster and is stronger when the B/H ratio is smaller.

Table 2-4. Non-dimensional temperature response for Pe = 0, R_b= 0.001, d = 0.02, considering various d ranging from 0 to infinity.

Fo	Non-dimensional temperature response				
	b = 0.03	0.06	0.1	0.2	∞
0.00003	2.10	2.10	2.10	2.10	2.10
0.0001	2.78	2.73	2.73	2.73	2.73
0.001	5.76	4.22	3.88	3.85	3.85
0.01	11.21	8.23	6.48	5.17	4.89
10	17.64	14.43	12.23	9.62	5.98

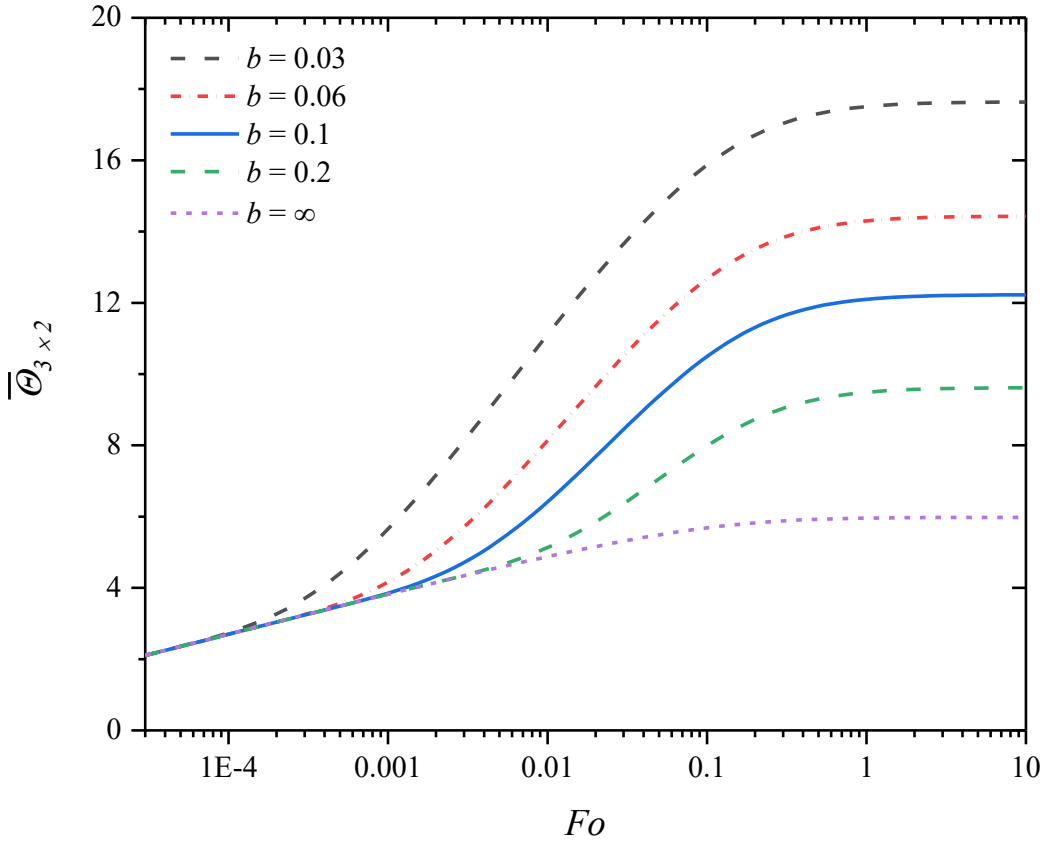

Figure 2-6. Non-dimensional temperature response from the MFLSD solution for Pe = 0, R_b= 0.001, and d = 0.02, considering various b ranging from 0 to infinity.

2.3.2.2 The effect of buried depth (d) in a borehole field without groundwater flow

To assess the influence of buried depth in a borehole field, we carried out a comparison between the MFLSD solution ($\overline{\Theta_{MFLSD}}$) of a single borehole and the solution of borehole fields. The effect of buried depth for a single borehole was evaluated in Guo. et al. [40]. Figure 2-7 demonstrates the non-dimensional temperature response $\overline{\Theta_{3\times2}}(Fo)$ obtained with b = 0.1. As shown, the $\overline{\Theta_{3\times2}}(Fo)$ rises as Fo increases and eventually reaches a steady state. As the ratio $d = D/H$ is enlarged from 0 to 0.2, the steady-state limit increases by 12.22% from 11.97 to 13.43. This

percentage difference in a 3 × 2 borehole field is much larger than the percentage difference (5.00%) obtained from $\overline{\Theta_{MFLSD}}$ for a single borehole [40].

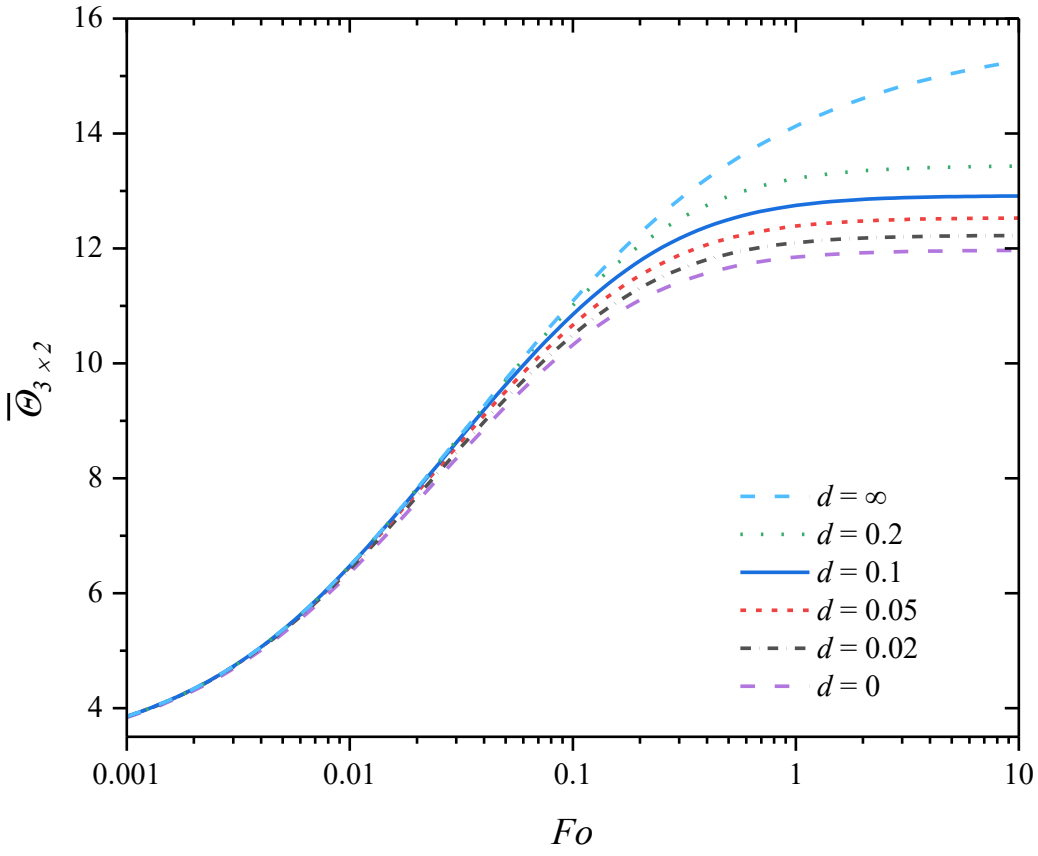

Figure 2-7. Non-dimensional temperature response from the MFLSD solution for Pe = 0, R_b = 0.001, and b = 0.1, considering various d ranging from 0 to 0.2.

Figure 2-8 demonstrates the non-dimensional temperature response for three different rectangle borehole arrays. The limits of the solutions for each borehole array were laid out by a lower bound solution corresponding to d = 0 and a theoretical upper bound solution corresponding to d = ∞. As shown, the interval between upper and lower limits increases as the size of the borehole field increases and as time goes on. For Fo = 10, the percentage difference between the upper limit and the lower limit increases from 10.22% for a single borehole to 41.47% for a 4 × 4 borehole field,

and finally up to 83.06% for a 10 × 10 borehole field. The temperature response for arbitrary d differs more significantly from that for the borehole starting from the ground surface (i.e., $d = 0$) in larger borehole fields. This is because the increasing number of boreholes exacerbates the effect of buried depth. Therefore, it is concluded that the buried depth is a significant parameter for large borehole fields that cannot be neglected in the design of BHE systems.

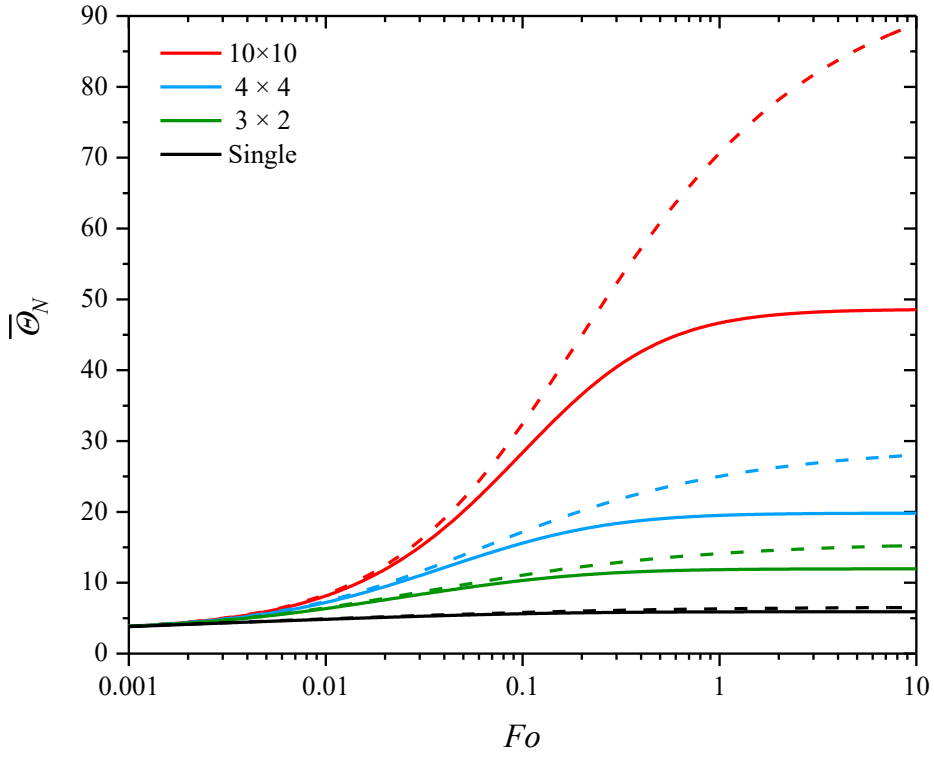

Figure 2-8. Non-dimensional temperature response from the MFLSD solution for different rectangle borehole arrays ($Pe = 0$, $R_b = 0.001$, and $b = 0.1$). The solid lines represent the lower bounds, and the dashed lines represent the upper bounds.

2.3.2.3 The effect of buried depth (d) in a borehole field with groundwater flow

A previous study [40] shows that the effect of buried depth for a single borehole heavily depends on the groundwater velocity. The increase in the groundwater flow velocity reduces the effect of

buried depth. The same influence can also be observed in borehole fields. As shown in Figure 2-9(a), in a 3 × 2 borehole field, the ratio of $\overline{\Theta_N}(d = 0.2)/\overline{\Theta_N}(d = 0)$ is about 12% for Pe = 0.1, and it falls to about 0.001% for Pe = 1000. Moreover, the ratio of $\overline{\Theta_N}(d = \infty)/\overline{\Theta_N}(d = 0)$ laid out the limit of the effect of buried depth for each borehole array in different groundwater flow scenarios. Due to the thermal interaction between the boreholes, the limit expanded as the number of boreholes increased. For example, to reduce the percentage difference between $\overline{\Theta_N}(d = \infty)$ and $\overline{\Theta_N}(d = 0)$ to less than 1%, the Pe was required to be greater than about 22 for a single borehole, 43 for a 3 × 2 borehole field, 75 for a 4 × 4 borehole field, and 197 for a 10 × 10 borehole field. In other words, although the effect of buried depth could be neglected for Pe > 22 for a single borehole, it could not simply be neglected in a large borehole field. Therefore, the analytical g-function from the MFLSD solution must be used in the BHE design to consider the combined effects of buried depth and groundwater flow.

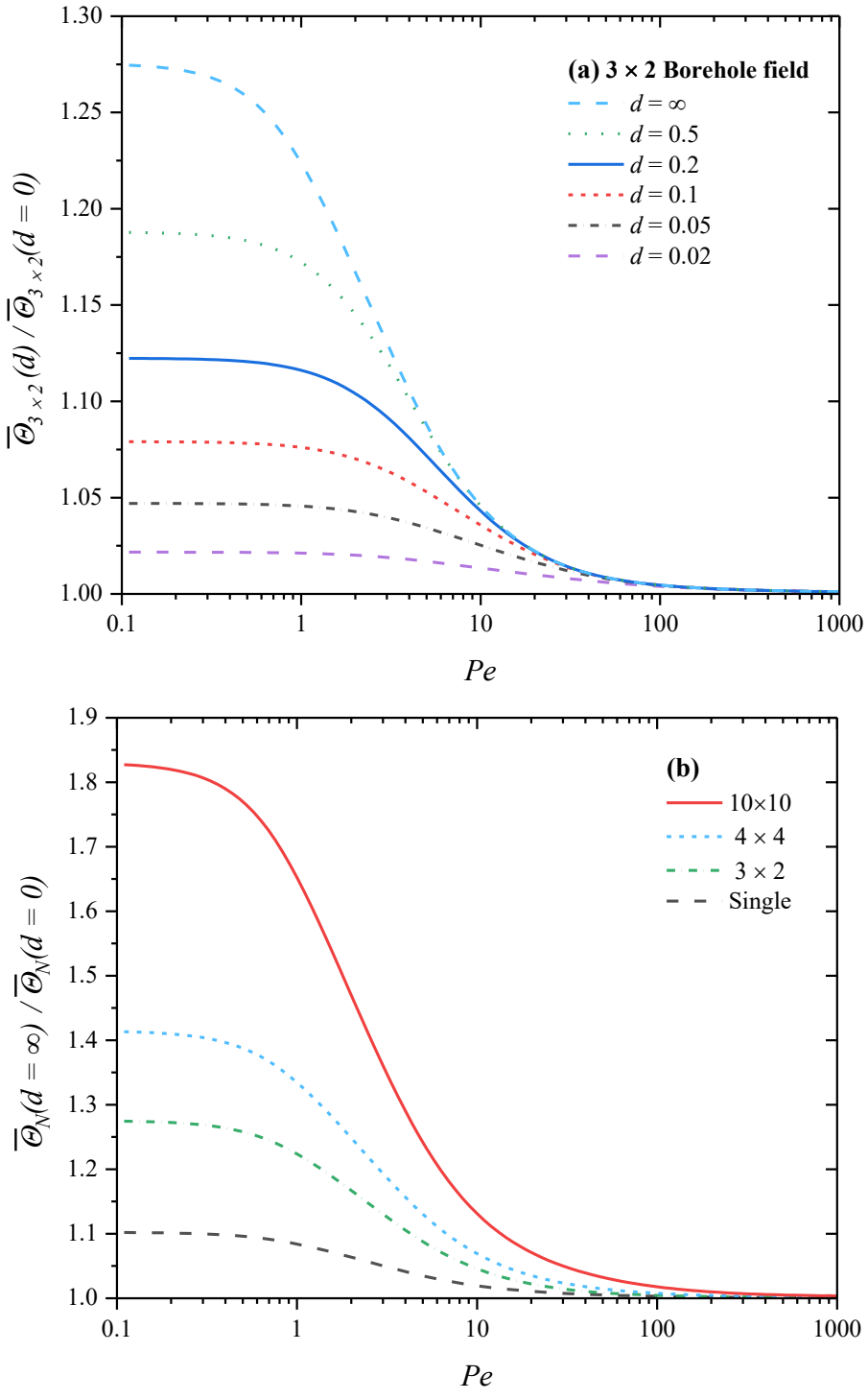

Figure 2-9. (a) The percentage difference of the temperature response for various buried depths over the temperature response for $d = 0$, considering various Peclet numbers ranging from 0.1 to 1000 in a 3 × 2 borehole field; (b) Limits of the percentage difference for different rectangle borehole arrays ($R_b = 0.001$ and $b = 0.1$).

2.4. Influence of buried depth at fixed borehole lengths

Although the aforementioned non-dimensional variables have obvious advantages, parameters with physical meanings are of great concern in engineering design, including borehole length, buried depth, and operation time. The non-dimensional borehole wall temperature response was calculated for a common borehole length ranging from 50 m to 150 m, $u_d = 4 \times 10^{-8}$ ms^{-1}, and B = 7.6 m with two buried depths of D = 2 m and 8 m. Other borehole geometries and thermal properties were the same as in the real GeoExchange system project. The simulation was run for 30 years (a typical lifetime of GSHP systems [92]).

As shown in Figure 2-10, it is demonstrated that the impact of buried depth gets larger as the borehole length reduces. For example, referring to the solution for the borehole starting from the ground surface (i.e., D = 0 m), the $\overline{\Theta_{3\times2}}$ rises by 1.81% for a 150 m borehole buried 8 m below the surface, and it rises by 6.14% if the borehole is only 50 m in length (see Table 2-5). Meanwhile, the rise in temperature response $\overline{\Theta_N}$ is much larger for a borehole field than for a single borehole. For example, when the buried depth varies from 0 m to 2 m and H = 70 m, the temperature response increases by 1.01% for a single borehole, by 1.83% for a 3 × 2 borehole field, by 2.37% for a 4 × 4 borehole field, and by 3.23% for a 10 × 10 borehole field. For this reason, the buried depth becomes a significant parameter for non-residential applications that comprise borehole fields of the order of 10-100 boreholes. Neglecting the buried depth, the temperature response of a borehole field would be under-predicted, resulting in an over-prediction of the rate of heat exploitation due to the borehole wall temperature constraints. Therefore, the g-function from the MFLSD solution should be used in the BHE design to provide a better prediction of the temperature variation of a borehole field with groundwater flow.

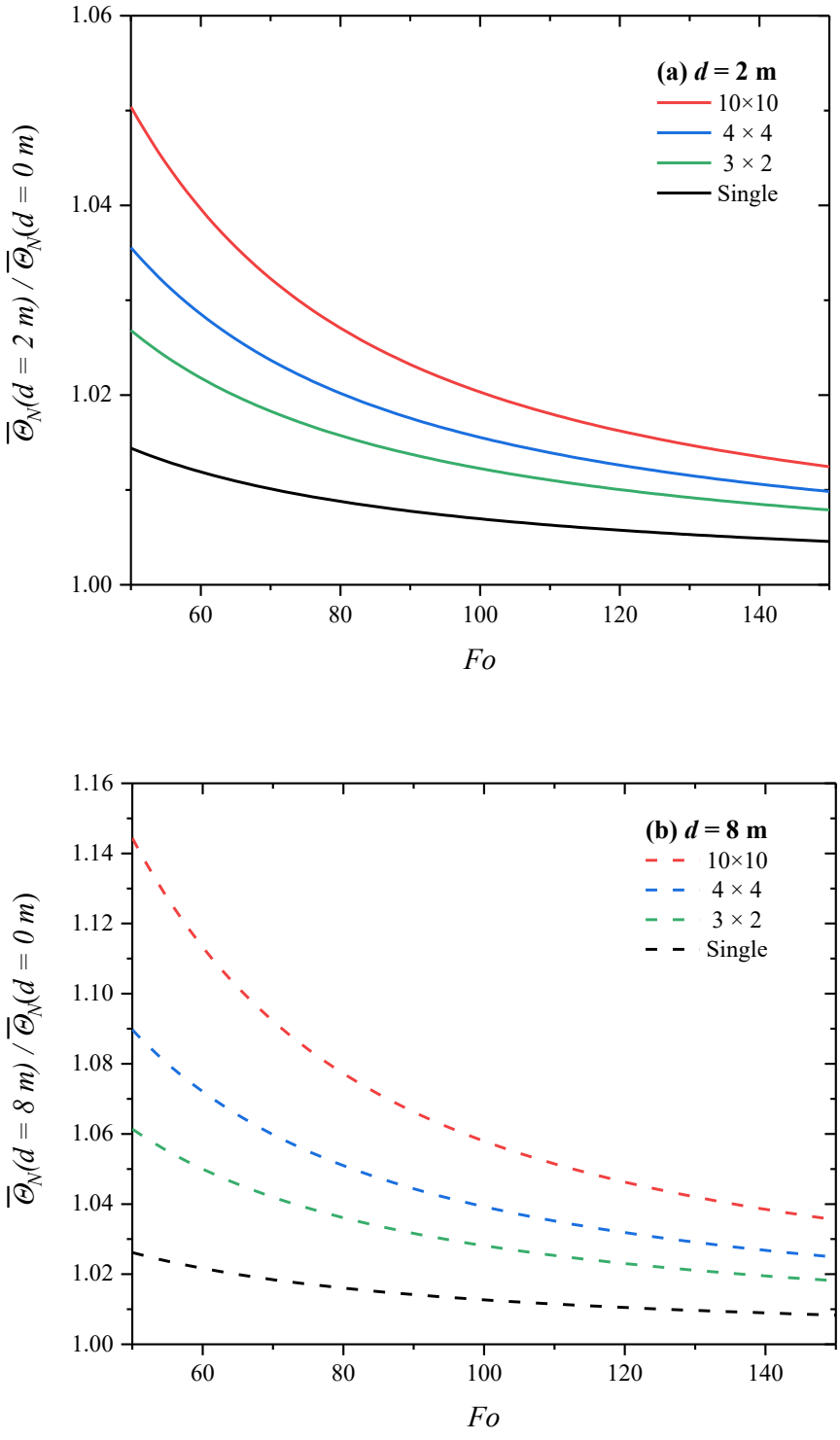

Figure 2-10. Effect of buried depth against various borehole lengths for different rectangle borehole arrays.

Table 2-5. Non-dimensional temperature response for different buried depths at 30 years (*Pe* = 7.5).

Field	Buried depth (*D*)	Non-dimensional temperature response				% Difference			
		H = 50 m	70 m	100 m	150 m	50 m	70 m	100 m	150 m
Single	**0 m**	5.57	5.72	5.83	5.92	**Ref**			
	2 m	5.65	5.77	5.87	5.94	1.44%	1.01%	0.70%	0.46%
	8 m	5.72	5.82	5.90	5.97	2.62%	1.84%	1.27%	0.83%
3 × 2	**0 m**	8.46	9.02	9.46	9.80	**Ref**			
	2 m	8.69	9.19	9.58	9.88	2.68%	1.83%	1.23%	0.79%
	8 m	8.98	9.40	9.73	9.98	6.14%	4.20%	2.81%	1.81%
4 × 4	**0 m**	11.68	12.86	13.80	14.54	**Ref**			
	2 m	12.09	13.17	14.02	14.69	3.56%	2.37%	1.55%	0.98%
	8 m	12.73	13.63	14.34	14.90	8.97%	5.98%	3.92%	2.48%
10 × 10	**0 m**	20.38	24.05	27.08	29.49	**Ref**			
	2 m	21.41	24.83	27.63	29.86	5.04%	3.23%	2.03%	1.25%
	8 m	23.33	26.27	28.65	30.54	14.44%	9.22%	5.80%	3.55%

2.5. Conclusion

The following conclusions were drawn from the study:

(1) The moving finite line source solution while considering buried depth (MFLSD) was coupled with a spatial superposition scheme to compute the *g*-functions for borehole fields. The *g*-functions from the MFLSD solution were verified numerically with a three-dimensional (3D) finite-element (FE) model. Compared with the numerical 3D-FE model, the analytical MFLSD solution is more efficient in light of computational time. For the given parameters in this study, the numerical simulation took 27,669 s in the calculation of the 96 points in time, and the MFLSD solution cost only 0.62 s for the same calculation.

(2) The effect of buried depth is amplified in a borehole field due to the thermal interaction between boreholes. For the given parameters in this study, the steady-state limit rises by about 5.00% as the non-dimensional buried depth (d) is enlarged from 0 to 0.2 for a single borehole and the steady-state limit increases by 12.22% from 11.97 to 13.43 for a 3 × 2 borehole field with the same change in the d value. Therefore, the effect of buried depth becomes more significant in a borehole field.

(3) The buried depth is a significant parameter in the design of the non-residential borehole heat exchanger system. For the given parameters in this study (including Peclet number Pe = 7.5), for a single borehole with a borehole length of 70 m, the average non-dimensional temperature response rises by about 1.01% as the buried depth increases from 0 m to 2 m; in a 3 × 2 borehole field, the non-dimensional temperature response rises by about 1.83% with the same change in buried depth. The effect of buried depth becomes more apparent in a non-residential application, which comprises a borehole field of the order of 10-100

boreholes than that of a single borehole or a small 3 × 2 borehole field. Therefore, analytical *g*-functions from the MFLSD solution should be considered in BHE designs for large-scale applications.

Chapter 3. Effects of varying heat transfer rates for borehole heat exchangers in layered subsurface with groundwater flow

This chapter has been submitted for peer review as **Guo, Y.**, Zhao, J., & Liu, W. V. Effects of varying heat transfer rates for U-shaped borehole heat exchangers in layered subsurface with groundwater flow. *Applied Thermal Engineering*. Unpublished © Elsevier. (under review)

Nomenclature

A	cross-sectional area of the circulating fluid	[m^2]
c	specific heat capacity	[$Jkg^{-1}K^{-1}$]
D	depth	[m]
d	shank spacing	[m]
d_h	hydraulic equivalent diameter	[m]
$erf(X)$	error function	
f_D	Darcy friction factor	
H	borehole length	[m]
h	vertical distance	[m]
I_0	modified zero-order Bessel function of the first kind	
k	thermal conductivity	[$Wm^{-1}K^{-1}$]
M	Mass flow rate	[kgs^{-1}]
Q	heat load	[W]
q_l	heat transfer rate per unit length	[Wm^{-1}]
Δq	incremental heat load	
$R_1^{\Delta}, R_2^{\Delta}, R_{12}^{\Delta}$	delta-circuit thermal resistances	[mKW^{-1}]
r	radial distance	[m]
T	temperature	[°C]
ΔT	temperature variation	[°C]
t	time	[s]
U	effective thermal transfer velocity	[ms^{-1}]
u_d	Darcy velocity	[ms^{-1}]
V	circulating fluid flow rate	[m^3s^{-1}]
v	fluid velocity	[ms^{-1}]
x, y, z, z'	coordinates	[m]

Greek symbols

α	thermal diffusivity	[m^2s^{-1}]
β	dimensionless thermal conductance	

ρ	density	[kgm^{-3}]

Subscripts

b	borehole	*out*	fluid outlet
down	downward-flowing fluid	*p*	pipe
eff	effective properties	*par*	parallel to bedding planes
f	circulating fluid	*per*	perpendicular to bedding planes
g	grout	*up*	upward-flowing fluid
in	fluid inlet	*w*	groundwater
o	pipe outer wall	*x, y, z*	coordinates

Abbreviations

BHE	Borehole heat exchanger
CQ	Constant heat transfer rate
FE	Finite element
GSHP	Ground source heat pump
MAPE	Mean Absolute Percentage Error
MFLS	Moving finite line source
MVQ	Multilayered ground with varying heat transfer rate

3.1. Introduction

The global coalition of countries committed to achieving net-zero carbon emissions by 2050 or earlier has propelled the transition towards sustainable energy sources, becoming an ongoing endeavour for various industries [120]. Among technologies that are considered renewables, the ground source heat pump (GSHP) system has emerged as a standout option, primarily owing to its minimal carbon dioxide emissions and remarkable energy efficiency [84]. In comparison to traditional heating systems, the GSHP system has demonstrated the potential to cut energy usage by over 30% [121] and decrease carbon dioxide emissions by about 20% [122].

GSHP systems commonly employ vertical borehole heat exchangers (BHEs), which consist of an arrangement of pipes placed within vertical boreholes. The main configurations of these pipes currently include U-shaped, double U-shaped, spiral-shaped, and coaxial [10]. Among these, the U-shaped pipe configuration is favoured for its simplicity in installation and cost-effectiveness [11]. Within the pipes, a fluid mixture consisting of water and antifreeze circulates to facilitate the transportation of heat between the heat pump and the ground [13, 14]. Borehole depths commonly range from 50 m to 150 m [15], traversing different types of geologic layers through which groundwater may flow.

Extensive studies [42-47] have shown that groundwater flow considerably changes the thermal performance of a BHE. In an in-situ experiment conducted by Wang et al. [47], the impacts of groundwater flow on BHE performance were investigated, revealing an average enhancement of 9.8% in heat injection and 12.9% in heat extraction. Similarly, Angelotti et al. [42] created a three-dimensional model to assess the energy performance of a BHE under different groundwater

velocities. Their simulations demonstrated that the heat extraction rate increased by 22%, 76%, and 105%, respectively, as the groundwater velocity increased from 0 m/s to 10^{-6} m/s, 5×10^{-6} m/s, and 10^{-7} m/s. In summary, groundwater flow plays a significant role in enhancing heat exchange between the BHE and its surrounding ground, benefiting the long-term performance of the entire GSHP system.

Over the last two decades, abundant analytical and semi-analytical models [35, 36, 48-50, 53, 64, 123] have been proposed to address the impact of groundwater flow on BHEs. Based on the moving sources theory [31], Diao et al. [49] and Sutton et al. [48] presented the moving infinite line source model that approximates the BHE as an infinite line source in an infinite homogenous medium with horizontal groundwater advection. Subsequently, Tye-Gingras and Gosselin [36] and Molina-Giraldo et al. [35] proposed the moving finite line source (MFLS) model to consider the finite length of the BHE. To better reproduce the heat transfer near the surface, Rivera et al. [50] and Zhou et al. [53] incorporated a convective boundary at the ground surface. More recently, Hu [123] and Erol and François [64] extended the MFLS model to encompass the BHE in multilayered ground conditions. However, these previous solutions [35, 36, 48-50, 53, 64, 123] typically assumed that the rate of heat transfer per unit borehole length remains constant. This assumption contradicts the reality that heat transfer from the BHE to the ground exhibits non-uniform variations in both time and depth [17, 124]. Additionally, this variation becomes significantly more pronounced in layered ground conditions, particularly in layers where groundwater flow is present. As an example, in an investigation carried out by Luo et al. [70] involving a BHE situated in the ground with five distinct layers, their findings revealed that the efficacy of heat transfer in the layers with groundwater flow was at least 25.9% greater than that in the layers without

groundwater flow. It is important to note, neglecting this heat transfer rate variation may result in significant temperature overestimations. As emphasized by Li et al. [71], their double-layered sandbox experiment and simulation (comprising sand and clay) resulted in temperature overpredictions of up to 76.6% in the clay layer due to the assumption of a constant heat transfer rate. Such temperature overpredictions can result in the use of oversized BHEs, leading to substantial increases in expenses associated with drilling and materials [17].

Until recently, there have been limited solutions [66, 72, 125] available in the literature for addressing the complex issue of heat transfer rate variation in BHEs within multilayered ground conditions. For instance, in our previous study [72], we introduced a so-called MVQ solution to address this issue. In this acronym, "MVQ" stands for "Multilayered ground with Varying heat transfer rate," with "Q" representing the heat transfer rate. Nevertheless, these existing solutions [66, 72, 125] were primarily focused on cases of pure heat conduction and did not account for the impact of groundwater flow. This represents a significant gap in understanding the actual effect of groundwater flow in multilayered ground conditions, which is essential for predicting accurate ground temperatures and designing effective GSHP systems. Therefore, the primary objective of this study is to bridge the existing research gap by adapting and modifying the MVQ solution to accommodate scenarios where groundwater flow is present in the subsurface layers. Despite the alterations made, the resulting solution continues to be referred to as the MVQ solution. This solution provides a means to approximate the long-term behaviour of BHEs while incorporating the effects of groundwater flow. It also offers valuable insights for designing BHE systems in practical applications with complex geological conditions.

3.2. MVQ model

3.2.1 Problem description

The illustration in Figure 3-1 outlines the installation of a single BHE within a multilayered ground, which includes aquifers. While Figure 3-1 depicts a ground configuration with four layers, it is important to note that the model is flexible to accommodate any number of layers, matching the geological condition of the site. In this present study, a few assumptions have been made to simplify the heat transfer model due to the complexity of heat exchange between the BHE and ground:

a. Groundwater flow: In the context of groundwater flow, the assumption proposed in prior studies [35, 36, 49] was adopted, which presumed the water flows uniformly in the x-direction, parallel to the ground surface, with a consistent Darcy velocity u_d.

b. Local thermal equilibrium: The concept of local thermal equilibrium was adopted, wherein the groundwater temperature aligns with the ground temperature at any given location. This assumption is widely used in the context of heat transfer within porous media [101]. It holds true at a macroscopic scale since the groundwater movement occurs at a slow pace, which results in negligible temperature variations between the water and solid components over both time and space [102].

c. Initial and boundary conditions: In prior studies of BHEs [10, 86], it is a common practice to assume that both initial and boundary conditions are homogenous. This simplification was also adopted in this study, which allows us to concentrate our investigation on

analyzing temperature changes resulting from the varying heat generation rate of the BHE. It is essential to note that the initial and boundary conditions can become non-homogeneous due to factors like thermal gradients and temperature fluctuations at the ground surface. Such non-homogeneous conditions can be accounted for using the superposition principle, as demonstrated in the study of Bandos et al. [26].

d. Temperature-independent physical and thermal properties: Thermal properties were assumed to remain constant regardless of temperature. This is because the temperature range relevant to shallow BHE problems is relatively narrow, and variations in physical and thermal properties within this range can be considered negligible [23].

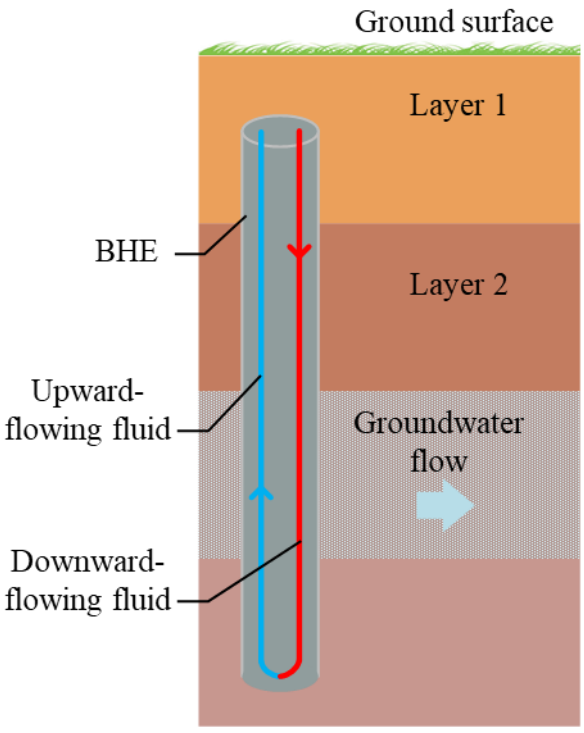

Figure 3-1. Illustration of a BHE situated within a multilayered ground, considering the presence of groundwater flow.

In the conventional analysis of shallow BHEs, due to the inherent complexity of the heat transfer process, the problem is typically separated into two distinct regions: the interior region within the borehole and the exterior region outside the borehole [10, 28, 86]. These two regions are interconnected at the interface of the borehole wall.

In the thermal analysis of the exterior region, the line [27, 28] or cylindrical [126] heat source models are widely employed to predict temperature changes at the borehole wall. These models necessitate a prescribed heat generation rate for heat sources. For the thermal analysis of the interior region, models [127, 128] are used to calculate the outlet fluid temperature. These models rely on a given temperature at the borehole wall as a boundary condition. Building upon the approach established in our previous study [72], the current study considered a two-way coupling scheme that allows for the simultaneous analysis of both the exterior and interior regions, thereby addressing the varying heat transfer rate in the BHE.

3.2.2 Heat transfer outside the borehole

In the exterior region outside the borehole, the governing three-dimensional (3-D) heat equation is expressed within a Cartesian coordinate system (x, y, z) as follows [31]:

$$\rho c \frac{\partial T}{\partial t} = k_x \frac{\partial^2 T}{\partial x^2} + k_y \frac{\partial^2 T}{\partial y^2} + k_z \frac{\partial^2 T}{\partial z^2} - u_d (\rho c)_w \frac{\partial T}{\partial x} + q \tag{3-1}$$

where T [K] represents the temperature, ρc [$Jm^{-3}K^{-1}$] represents the volumetric heat capacity of the bulk porous media, $(\rho c)_w$ [$Jm^{-3}K^{-1}$] represents the volumetric heat capacity of the groundwater, k [$Wm^{-1}K^{-1}$] represents the thermal conductivity, and q [Wm^{-3}] is the volumetric heat source.

In an infinite medium, the solution to this partial differential equation at any arbitrary point (x, y, z) and any given later time (t) due to an instantaneous point source at coordinate (0, 0, z') releasing heat at a time (τ) can be obtained using the Green's function method [129]:

$$\Delta T = \frac{q(0,0,z',\tau)}{8(\rho c)_{eff}\sqrt{\alpha_x\alpha_y\alpha_z}\left(\pi(t-\tau)\right)^{\frac{3}{2}}} \exp\left(-\frac{\left(x-U(t-\tau)\right)^2}{4\alpha_x(t-\tau)} - \frac{y^2}{4\alpha_y(t-\tau)} - \frac{(z-z')^2}{4\alpha_z(t-\tau)}\right) \qquad (3\text{-}2)$$

where ΔT [K] is the temperature change, $U = \frac{u_d(\rho c)_w}{\rho c}$ [ms^{-1}] is the effective thermal transfer velocity, and $\alpha = \frac{k}{\rho c}$ [m^2s^{-1}] is the thermal diffusivity.

In this study, when dealing with a horizontally layered medium, the composite medium method introduced by Abdelaziz et al. [58] was employed. This approach produces acceptable approximations that describe the composite section between the observation point (x, y, z) and the heat point source (0, 0, z') as an equivalent homogeneous medium, and it has been widely accepted and has been utilized in numerous other studies [62-65]. Within this framework, the effective properties of the composite section are computed by considering the properties and relative

fractions of each individual layer. Specifically, the effective volumetric heat capacity of the composite section can be obtained by the sum of the heat capacities of different constituent layers [130],

$$(\rho c)_{eff} = \frac{\sum_{i=1}^{N} h_j (\rho c)_j}{\sum_{i=1}^{N} h_j} \tag{3-3}$$

where $(\rho c)_{eff}$ [$Jm^{-3}K^{-1}$] is the effective volumetric heat capacity of the composite section, N is the number of ground layers in between, and h [m] is the vertical distance within a ground layer.

Due to the layering configuration, the ground is considered a transversely isotropic material. In this context, two effective thermal conductivity components, k_{par} and k_{per}, are considered, which represent the effective thermal conductivity component parallel to and perpendicular to layering planes, respectively. With respect to the heat flow direction, ground layers are connected in parallel in the horizontal directions. Specifically, in both the x and y-directions, the effective thermal conductivity is determined using the parallel model [131, 132], which calculates it as the weighted arithmetic mean value,

$$k_{par} = \frac{\sum_{i=1}^{N} h_i k_{x,i}}{\sum_{i=1}^{N} h_i} \tag{3-4}$$

The effective thermal diffusivity by definition can be estimated as

$$\alpha_{par} = \frac{k_{par}}{(\rho c)_{eff}} \tag{3-5}$$

In the z-direction, the effective thermal diffusivity is estimated using an expression proposed by Schimmel et al. [133], which has the form

$$\frac{(\sum_{i=1}^{N} h_i)^2}{\alpha_{per}} = \sum_{i=1}^{N} \frac{{h_i}^2}{\alpha_{z,i}} + 2 \sum_{i=1}^{N-1} \sum_{j=i+1}^{N} h_i h_j \frac{k_{z,j}}{k_{z,i}\alpha_{z,j}} \tag{3-6}$$

It is worth noting that different values of α_{per} are obtained from Equation (3-6) when the arrangement of layers is interchanged. Based on the effective thermal diffusivity obtained from Equation (3-6), the effective thermal conductivity in the z-direction is evaluated as

$$k_{per} = \alpha_{per}(\rho c)_{eff} \tag{3-7}$$

The ground is typically treated as a semi-infinite medium with a single plane surface that is the ground surface. In accordance with prior studies [28, 29, 134], the ground surface is assumed to be maintained at a fixed temperature. To achieve this boundary condition, the method of images [31] is utilized in the solution. This method involves introducing image heat sinks positioned above the actual ground surface. Through the symmetrical distribution of these point heat sources and sinks, a stable and fixed temperature is established at the ground surface. Applying the method of images yields

$$\Delta T = \frac{q(0,0,z',\tau)}{8k_{par}\sqrt{\alpha_{per}}\left(\pi(t-\tau)\right)^{\frac{3}{2}}} \exp\left(-\frac{\left(x-U(t-\tau)\right)^2+y^2}{4\alpha_{par}(t-\tau)}\right) \left[\exp\left(-\frac{(z-z')^2}{4\alpha_{per}(t-\tau)}\right)-\exp\left(-\frac{(z+z')^2}{4\alpha_{per}(t-\tau)}\right)\right] \tag{3-8}$$

It is important to highlight that the original expression provided by Abdelaziz et al. [58] did not satisfy the ground surface boundary condition. However, this issue has been resolved in Equation (3-8).

In accordance with Kelvin's theory [30] of the heat source, one can perform integration across both spatial and temporal variables from the solution for an instantaneous point source to obtain the solution for a continuous line heat source [135]. If the heat source releases its energy spontaneously from time zero, the average temperature response due to the line heat source

segment, which initiates at depth D_i and extends for a finite length h_i along the vertical z-axis, can be expressed as

$$\Delta T = \frac{q_{l_i}}{8(\pi)^{\frac{3}{2}}} \int_0^t \int_{D_i}^{D_i+h_i} \frac{1}{k_{par}\sqrt{\alpha_{per}}(t-\tau)^{\frac{3}{2}}} \exp\left(-\frac{\left(x-U(t-\tau)\right)^2+y^2}{4\alpha_{par}(t-\tau)}\right) \left[\exp\left(-\frac{(z-z')^2}{4\alpha_{per}(t-\tau)}\right) - \exp\left(-\frac{(z+z')^2}{4\alpha_{per}(t-\tau)}\right)\right] dz'd\tau \quad (3\text{-}9)$$

where the subscript i denotes the line heat source segment and q_{l_i} [$\mathrm{Wm^{-1}}$] represents the heat generation rate per unit length of line heat source segment i (with $i = 1,2,\cdots N$).

Determining the average temperature over the borehole wall is crucial, as it serves as a boundary condition for heat transfer within the interior region. However, calculating this average temperature typically involves a surface integration over the borehole wall, which can significantly increase computational demands, especially when the effective thermal properties are functions of integral variables. To overcome this challenge, we evaluated the effective thermal properties of the composite section using the midpoints of both the line heat source segments and the borehole wall segments. Consequently, the average temperature change at borehole wall segment j attributed to line heat source segment i can be formulated as

$$\frac{\overline{\Delta T}_{ij}}{q_{l_i}/2\pi k_{par}} = \frac{1}{2h_j} I_0\left(\frac{r_b U}{2\alpha_{par}}\right) \int_{\frac{1}{\sqrt{4\alpha_{per}t}}}^{\infty} \frac{1}{s^2} \exp\left(-\frac{U^2}{16\alpha_{par}\alpha_{per}s^2} - \frac{\alpha_{per}}{\alpha_{par}} {r_b}^2 s^2\right) \Big[-\text{ierf}\big(s(D_j + h_j - D_i - h_i)\big) + \text{ierf}\big(s(D_j - D_i - h_i)\big) + \text{ierf}\big(s(D_j + h_j - D_i)\big) - \text{ierf}\big(s(D_j - D_i)\big) - \text{ierf}\big(s(D_j + h_j + D_i + h_i)\big) + \text{ierf}\big(s(D_j + D_i + h_i)\big) + \text{ierf}\big(s(D_j + h_j + D_i)\big) - \text{ierf}\big(s(D_j + D_i)\big)\Big] ds \tag{3-10}$$

where

$$\text{ierf}(X) = \int_0^X \text{erf}(Y)\, dY = X\text{erf}(X) - \frac{1}{\sqrt{\pi}}\left(1 - e^{-X^2}\right) \tag{3-11}$$

$s = \frac{1}{\sqrt{4\alpha_{per}(t-\tau)}}$, r_b [m] is the radius of the borehole, $\text{erf}(X) = \frac{2}{\sqrt{\pi}}\int_0^X e^{-t^2}\, dt$ is the error function, $I_0(X) = \frac{1}{\pi}\int_0^\pi e^{X\cos(\varphi)} d\varphi$ is a modified Bessel function of the first kind, and the subscript j denotes the borehole wall segment that starts from depth D_j with finite length h_j with $j = 1,2,\cdots,N$. It is important to note that the non-dimensional term $\frac{\overline{\Delta T}_{ij}}{q_{l_i}/2\pi k_{par}} = \Theta_{ij}$ is also known as the thermal response factor. This factor characterizes the temperature change attributed to a unit heat pulse.

In real BHE applications, ground loads vary with time. Predicting the temperature evolution at the borehole wall due to time-varying heat sources can be achieved using the well-known Duhamel's theorem [32],

$$\overline{\Delta T}_{ij}(t) = \frac{1}{2\pi k_{par}} \frac{\partial}{\partial \tau} \int_0^t q_{l_i}(t) \Theta_{ij}(t-\tau)\, d\tau \tag{3-12}$$

Due to the software used in building energy simulations, it is common to present heat loads as discrete stepwise values [105]. When dealing with stepwise heat loads, the use of Fast Fourier Transform (FFT) algorithms is a more efficient approach for the temporal superposition [107]. The equation that describes this approach is:

$$\frac{\partial}{\partial \tau} \int_0^t q_{l_i}(t) \theta_{ij}(t-\tau)\, d\tau = \sum_{p=1}^{M} \Delta q_{l_i}(t_p) \theta_{ij}(t_M - t_{p-1}) = \Im^{-1}\left[\Im(\hat{\theta}_{ij}) \Im\left(\widehat{\Delta q_{l_i}}\right)\right] \tag{3-13}$$

where subscript $p = 1, 2, \cdots, M$ denotes the discrete time step, t_p [s] represents the discrete time, $\Delta q_l(t_p) = q_l(t_p) - q_l(t_{p-1})$ corresponds to the incremental heat load between two heat pulses, $\Im$ and $\Im^{-1}$ respectively represent the FFT and the inverse-FFT, and $\hat{\theta}_{ij}$ and $\widehat{\Delta q_{l_i}}$ are two sequences in discrete time.

Finally, the average temperature $\overline{T}_{b_j}$ at borehole wall segment *j* was evaluated by aggregating the contributions of these time-varying line heat source segments,

$$\overline{T}_{b_j} = \frac{1}{2\pi}\sum_{i=1}^{N}\frac{1}{k_{par}}\Im^{-1}\left[\Im(\hat{\theta}_{ij})\Im\left(\widehat{\Delta q}_{l_i}\right)\right] \tag{3-14}$$

3.2.3 Heat transfer within the borehole

In the interior region within the borehole, heat transfer is represented using a thermal resistance circuit in a stationary condition, as detailed in reference [128]. This is illustrated as a delta-circuit in Figure 3-2, which connects one borehole wall node and two fluid temperature nodes [136]. This delta-circuit thermal resistance model was developed on the assumption that thermal equilibrium is immediately established between the inlet and outlet pipes at any given time. For long-term predictions, the analytical solution under this assumption has demonstrated notable accuracy and reliability, thereby offering a viable approach [137].

In the delta-circuit thermal resistance model, the conductive heat transfer in the fluid can be neglected due to the relatively small temperature gradient along the flow direction (only a few degrees Celsius difference from the inlet to the outlet) [128]. Then, at steady-state, the convective heat transfer through fluid circulation and the associated heat losses to the surroundings are determined through energy conservation equations,

$$Mc_f\frac{\partial T_{down}}{\partial z} = \frac{T_b - T_{down}}{R_1^{\Delta}} + \frac{T_{up} - T_{down}}{R_{12}^{\Delta}} \tag{3-15}$$

$$-Mc_f \frac{\partial T_{up}}{\partial z} = \frac{T_b - T_{up}}{R_2^{\Delta}} + \frac{T_{down} - T_{up}}{R_{12}^{\Delta}} \tag{3-16}$$

where T_{down} [K] is the temperature for the downward-flowing fluid, T_{up} [K] is the temperature for the upward-flowing fluid, R_1^{Δ}, R_2^{Δ} and R_{12}^{Δ} [mKW^{-1}] represent the delta-circuit thermal resistances between the borehole wall node and the circulating fluid nodes, M [m^{3}s^{-1}] is the mass flow rate, c_f [JK^{-1}kg^{-1}] represents the specific heat capacity of the circulating fluid, of the circulating.

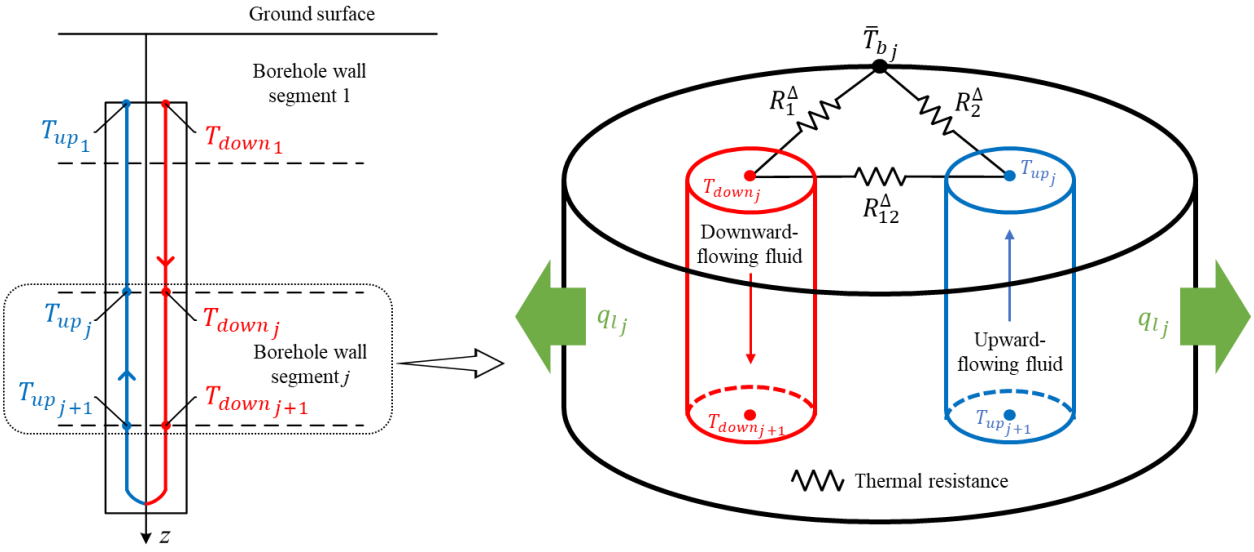

Figure 3-2. Illustration of the thermal resistance circuit within a borehole segment.

Consistent with the heat transfer analysis outside the borehole, the interior region is also divided into segments. We derive the solution to the thermal resistance model described in Equations (3-15) and (3-16) for each segment through the utilization of Laplace transforms. It is noteworthy

that, although a distinct mathematical function in this study, the methodology shares similarities with that outlined by Eskilson [23] and Hellström [128], Therefore, only the final results were present,

$$T_{down_{j+1}}(t) = \underbrace{\exp(\beta)\left[\cosh(\gamma) - \frac{\beta-\beta_2-\beta_{12}}{\gamma}\sinh(\gamma)\right]}_{f_1(h_j)} T_{down_j}(t) + \underbrace{\frac{\beta_{12}}{\gamma}\exp(\beta)\sinh(\gamma)}_{f_2(h_j)} T_{up_j}(t) + \underbrace{\left\{1-\exp(\beta)\left[\cosh(\gamma)+\frac{\beta-\beta_2}{\gamma}\sinh(\gamma)\right]\right\}}_{f_4(h_j)}\overline{T}_{b_j} \tag{3-17}$$

$$T_{up_{j+1}}(t) = -f_2(L_i)T_{down_j}(t) + \underbrace{\exp(\beta)\left[\cosh(\gamma)+\frac{\beta+\beta_1+\beta_{12}}{\gamma}\sinh(\gamma)\right]}_{f_3(h_j)} T_{up_j}(t) + \underbrace{\left\{1-\exp(\beta)\left[\cosh(\gamma)+\frac{\beta+\beta_1}{\gamma}\sinh(\gamma)\right]\right\}}_{f_5(h_j)}\overline{T}_{b_j} \tag{3-18}$$

where $\beta_1 = \frac{h_j}{V(\rho c)_f R_1^4}$, $\beta_2 = \frac{h_j}{V(\rho c)_f R_2^4}$, and $\beta_{12} = \frac{h_j}{V(\rho c)_f R_{12}^4}$ are the dimensionless thermal conductance, $\beta = \frac{\beta_2-\beta_1}{2}$, $\gamma = \sqrt{\frac{(\beta_1+\beta_2)^2}{4} + \beta_{12}(\beta_1+\beta_2)^2}$, and $\cosh(X)$ and $\sinh(X)$ are the hyperbolic functions.

Various types of boundary conditions can be applied to control heat transfer in the circulating fluid, including prescribed temperatures at either the inlet or the outlet. In this study, a prescribed heat load (Q) is considered in alignment with the line heat source solution,

$$Q(t) = Mc_f\left(T_{down_1} - T_{up_1}\right) \tag{3-19}$$

Equations (3-17) to (3-19) form a system of linear equations, as demonstrated in the example of a four-segment scenario.

$$\begin{bmatrix} -f_4(h_1)\overline{T}_{b_1} \\ -f_4(h_2)\overline{T}_{b_2} \\ -f_4(h_3)\overline{T}_{b_3} \\ [f_5(h_4) - f_4(h_4)]\overline{T}_{b_4} \\ f_5(h_1)\overline{T}_{b_1} \\ f_5(h_2)\overline{T}_{b_2} \\ f_5(h_1)\overline{T}_{b_3} \\ Q \end{bmatrix} = \begin{bmatrix} f_1(h_1) & -1 & 0 & 0 & f_2(h_1) & 0 & 0 & 0 \\ 0 & f_1(h_2) & -1 & 0 & 0 & f_2(h_2) & 0 & 0 \\ 0 & 0 & f_1(h_3) & 0 & 0 & 0 & f_2(h_3) & 0 \\ 0 & 0 & 0 & f_1(h_4) + f_2(h_4) & 0 & 0 & 0 & f_2(h_4) - f_3(h_4) \\ f_2(h_1) & 0 & 0 & 0 & 1 & -f_3(h_1) & 0 & 0 \\ 0 & f_2(h_2) & 0 & 0 & 0 & 1 & -f_3(h_2) & 0 \\ 0 & 0 & f_2(h_3) & 0 & 0 & 0 & 1 & -f_3(h_3) \\ Mc_f & 0 & 0 & 0 & -Mc_f & 0 & 0 & 0 \end{bmatrix} \begin{bmatrix} T_{down_1} \\ T_{down_2} \\ T_{down_3} \\ T_{down_4} \\ T_{up_1} \\ T_{up_2} \\ T_{up_3} \\ T_{up_4} \end{bmatrix} \tag{3-20}$$

The fluid temperatures are determined by solving these linear equations. The rate of heat generation in each segment is determined through the energy conservation equation formulated for the circulating fluid,

$$q_{l_j}(t) = \frac{Mc_f}{h_j}\left[T_{down_j}(t) - T_{down_{j+1}}(t) + T_{up_{j+1}}(t) - T_{up_j}(t)\right] \quad (3\text{-}21)$$

3.2.4 Two-way coupling

The current study employed a two-way coupling approach that combines the line heat source solution with a thermal resistance model [128] simultaneously. This coupling approach led to the development of the MVQ solution, which is specifically designed to account for the varying heat transfer rate over time and depth. The schematic diagram outlining this approach is illustrated in Figure 3-3. In this coupling approach, the thermal resistance model calculates the varying heat generation rate for the exterior region, while the line heat source model sets the temperature boundary conditions for the interior region. These models for the internal and external regions are then iterated to refine the temperature and heat transfer rate predictions. Through several iterative steps, this process yields a close approximation of the heat transfer rate and temperature distribution within each segment at any given time.

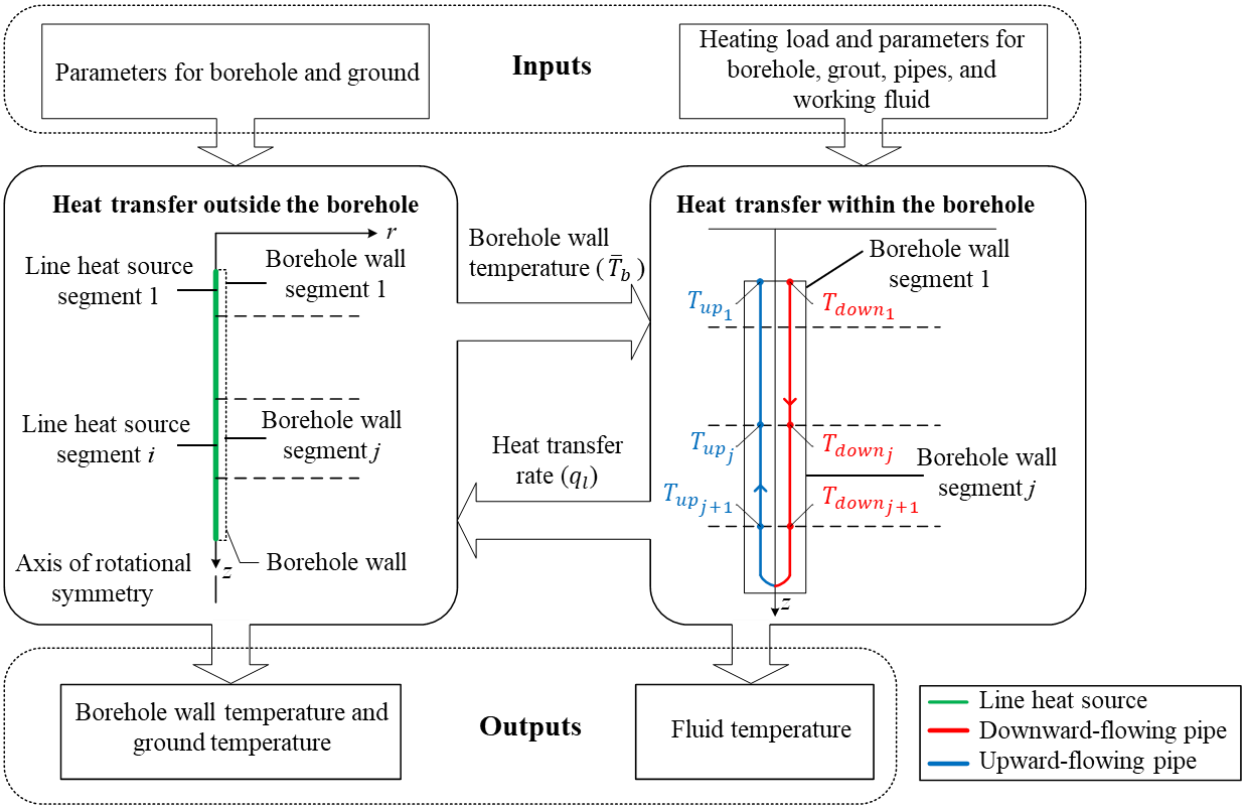

Figure 3-3. Schematic diagram of the MVQ solution.

3.3. Numerical model and scenarios

Before discussing the computational results obtained using the MVQ solution, it is necessary to ensure its accuracy and reliability. To achieve this, as seen in numerous prior studies [64, 111-113], a common approach involves the comparison with a 3-D numerical model constructed in a finite element (FE) software package. The FE modelling can be validated through a comparison with field-scale experimental data available in the literature. While a few laboratory-scale experiments [12, 13, 138, 139] have been reported, the sandbox test conducted by Beier et al. [13]

was particularly chosen for comparison due to its well-controlled laboratory conditions and the availability of more comprehensive measurements compared to other studies.

3.3.1 Scenario for validation

The constructed numerical model was first compared with a reference dataset reported by Beier et al. [13]. The experimental setup featured a single U-shaped BHE positioned at the centre of a large sandbox, as illustrated in Figure 3-4. This setup was designed for investigating the heat transfer characteristics of a single BHE within homogeneous ground.

The dataset included sand temperature measurements at various radial positions within the sandbox. Per the study by Beier et al. [13], the thermal conductivity of the sand used in the sandbox was independently measured using a transient thermal probe inserted at four different locations. These measurements resulted in an average thermal conductivity value of 2.82 $Wm^{-1}K^{-1}$. Table 3-1 lists the thermal properties of the materials involved, including the ground, grout, and circulating fluid, along with the geometric parameters of the BHE. More in-depth information regarding this reference dataset can be found in the original paper by Beier et al. [13].

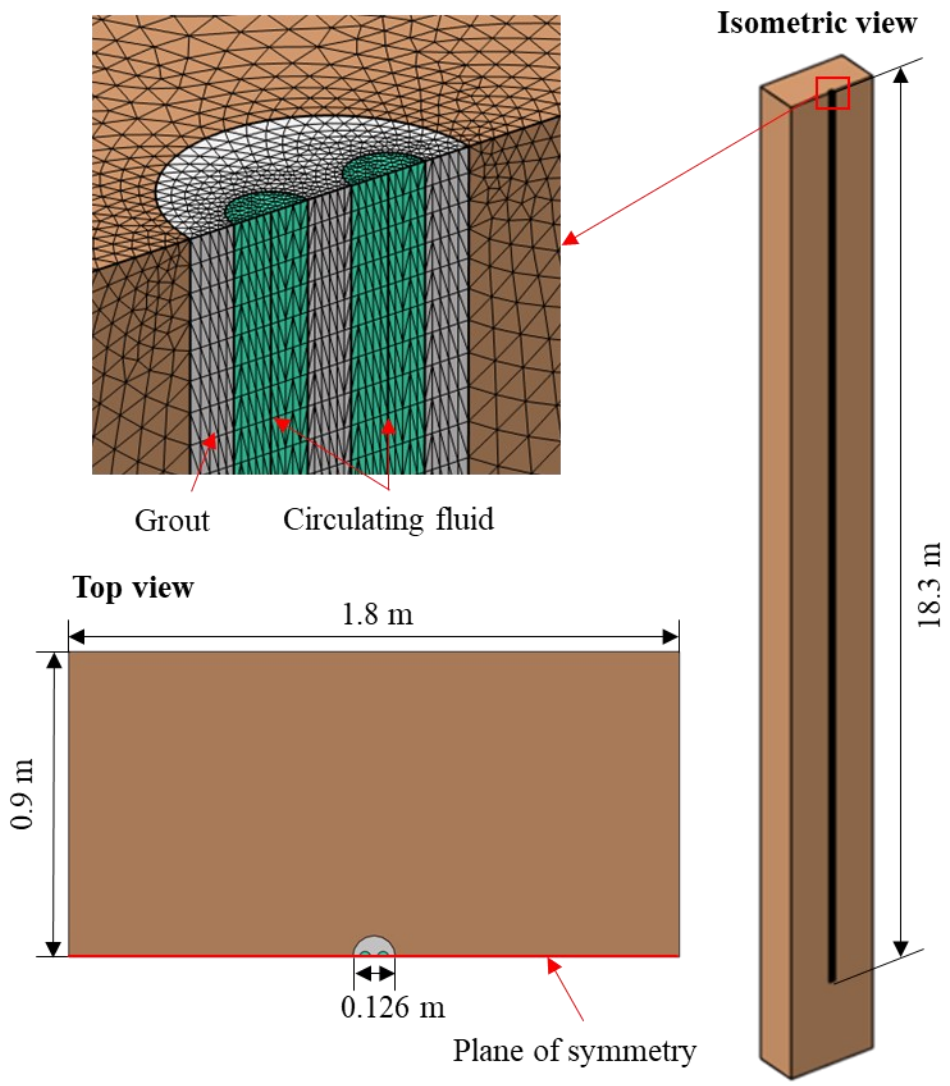

Figure 3-4. Schematic diagram of the sandbox test.

Table 3-1. Parameters for the sandbox test [13, 140]

Parameter	**Symbol**	**Value**
Ground thermal conductivity	k_s	2.82 $Wm^{-1}K^{-1}$
Estimated ground volumetric heat capacity	$(\rho c)_s$	3.2×10^6 $Jm^{-3}K^{-1}$
Grout thermal conductivity	k_g	0.73 $Wm^{-1}K^{-1}$
Estimated grout volumetric heat capacity	$(\rho c)_g$	3.8×10^6 $Jm^{-3}K^{-1}$
Pipe thermal conductivity	k_p	0.39 $Wm^{-1}K^{-1}$
Fluid thermal conductivity	k_f	0.60 $Wm^{-1}K^{-1}$
Fluid volumetric heat capacity	$(\rho c)_f$	4.181×10^6 $Jm^{-3}K^{-1}$
Average flow rate of circulating fluid	V	0.197 Ls^{-1}
Length of the borehole	H	18.3 m
Borehole radius	r_b	63.0 mm
Pipe outer radius	r_o	16.7 mm
Pipe wall thickness		3.035 mm
Shank spacing	d	53.0 mm
Heat load	Q	1056 W

3.3.2 Numerical model

Based on the previously introduced scenario, 3-D FE models were constructed in COMSOL Multiphysics to simulate the heat exchange between the circulating fluid and the surrounding ground. Due to the symmetrical geometry of the U-shaped BHE, the computational domain size can be reduced by implementing a symmetric boundary condition to the symmetric plane within this 3-D FE model. This comprehensive 3-D FE model incorporated the heat conduction equation to account for heat transfer within both the ground and the grout material inside the borehole. Additionally, it solved the heat convection and diffusion equation for the circulating fluid within the pipes. The velocity field of the flow was determined by solving the Navier–Stokes equations using a *k*-epsilon turbulence model [141]. In the simulation, the pipes were intentionally neglected to reduce the computational complexity associated with meshing extremely thin pipe walls, which were approximately 3.0 mm thick. This simplification was considered because, as per the study by Beier [140], the thermal resistance of the pipe becomes negligible and has virtually no impact on the results after a few hours of operation (specifically less than 10 hours). To establish the initial condition, a uniform temperature was set throughout all components, including the ground, grout, and circulating fluid. The exact initial temperature depended on the undisturbed ground temperature relevant to the specific scenario being considered.

To determine the appropriate mesh size, a mesh convergence study was performed. A higher concentration of elements was allocated near the borehole region where higher temperature gradients were expected. The mesh was refined to ensure that simulation results were not affected by changes in mesh size. In this study, convergence was achieved when the difference in borehole

wall temperatures obtained from two successive simulations was less than 0.01 °C. Considering computational efficiency and accuracy, a mesh with 2,514,171 elements was employed, as shown in Figure 3-4.

3.3.3 Validation of the numerical model

A comparison was conducted between the results obtained from COMSOL modelling and the temperature measurements recorded during the sandbox experiments conducted by Beier et al. [13]. Figure 3-5 plots the temperature change from the initial temperature at various radial positions, spanning a timeframe from 0 to 3,106 minutes. The plot demonstrates a strong agreement between the sandbox measurements and the results from the COMSOL modelling. Specifically, the maximum temperature difference at the borehole wall during the entire simulation period occurred at the end of the simulation, and it was only 0.20 °C. This difference corresponds to approximately 3.05% of the temperature change at the borehole wall. It is worth noting that a prior study conducted by Li and Lai [142] also compared the same dataset [13] with their analytical solution. In their study [142], they considered a relative error of up to 10% as acceptable between the experimental data and their predictions. They found a relative difference of approximately 6% that emerged at the borehole wall after about 52 hours. It is essential to acknowledge that a primary contributor to the observed discrepancy between the simulation results and the sandbox measurements is the estimated thermal conductivity of the sand, which comes with an uncertainty of 5% [13]. Despite these factors, the current level of discrepancy, with a maximum percentage difference of 3.05% at the borehole wall, remains well within the acceptable threshold. This

affirmed the validity and accuracy of the COMSOL model constructed in the current study in simulating the behaviour of BHEs.

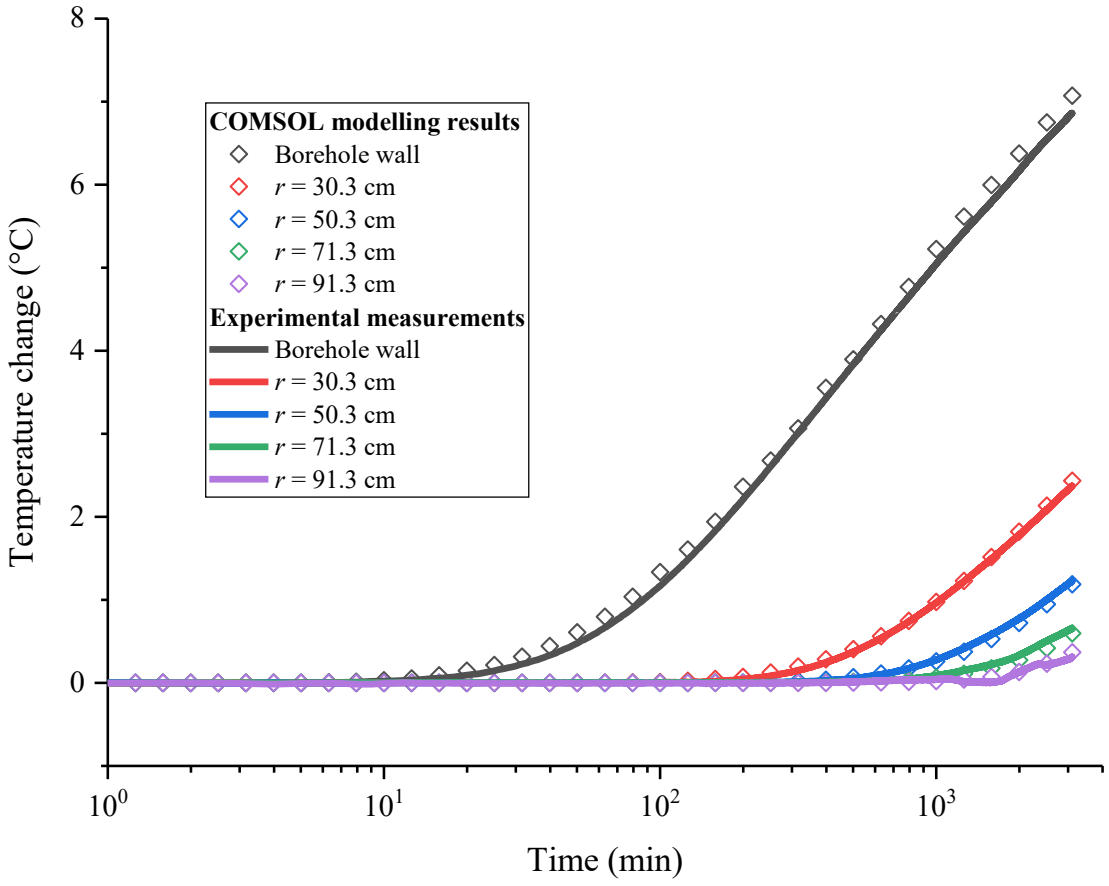

Figure 3-5. Comparison of temperatures in different radial positions between results from the COMSOL modelling and experimental measurements [13].

3.3.4 Scenario for ongoing analysis

The heat transfer of a BHE embedded in a multilayered ground is analyzed using the modified MVQ solution and the constructed 3-D FE model. The parameter inputs were taken from a previous study by Hu [123]. In the study, the complex geological area consisted of three bedded

layers, each possessing distinct thermal and hydraulic characteristics, as depicted in Figure 3-6. The middle was an aquifer layer with various groundwater flow velocities equal to 10^{-8} ms^{-1}, 10^{-7} ms^{-1}, and 10^{-6} ms^{-1}, encompassing a broad velocity range that represented a diverse set of hydrogeological conditions [49]. Table 3-2 shows the values of thermal and hydraulic properties for each ground layer. Table 3-3 shows the parameters for the borehole geometry.

Within the 3-D FE model, the treatment of the pipes and circulating fluid differed from the sandbox scenario. In the multilayered ground simulation, the pipes and circulating fluid were simplified to one-dimensional (1-D) modelling using a non-isothermal pipe flow module [143]. This 1-D simplification was chosen to avoid the computational burden associated with meshing extremely thin pipes, as the heat capacity of the components within the borehole primarily influences the thermal behaviour of the BHE for the initial few hours but becomes less significant after a few days [10, 36]. Therefore, the 1-D simplification is suitable for long-term thermal analysis of BHEs. The physics interfaces in the pipe flow module define the conservation of energy of the circulating fluid inside pipes [143],

$$A(\rho c)_f \frac{\partial T}{\partial t} = Ak_f \frac{\partial^2 T}{\partial z^2} + f_D \frac{A\rho_f}{2d_h}|v|^3 - Mc_f \frac{\partial T}{\partial z} + q_{l_p} \tag{3-22}$$

where A [m^2] is cross-sectional area of the circulating fluid, v [ms^{-1}] is the fluid velocity averaged at the cross-section, f_D is Darcy friction factor; d_h [m] is hydraulic equivalent diameter, and q_{l_p} [Wm^{-1}] is the heat transfer rate per unit length through the pipe wall. The velocity and temperature

in Equation (3-22) are modelled as cross-section averaged quantities, exhibiting variation solely along the length of the pipes. It aligns with the treatment employed in the thermal resistance model described in Equations (3-15) and (3-16).

In the multilayered ground simulation, a domain independence test was conducted. The primary objective of this test is to keep the temperature at the external boundary undisturbed. As suggested by Priarone and Fossa [94], a tolerance of 0.005 °C was chosen to ensure the calculation accuracy while maintaining a reasonable domain size. Finally, the model domain, measuring 1,800 m in the direction of groundwater flow and 300 m perpendicular to the flow direction, was considered sufficiently large to prevent external boundary conditions from affecting the results. Finally, the mesh convergence study was undertaken, resulting in a mesh consisting of 4,022,935 elements for the multilayered ground scenario.

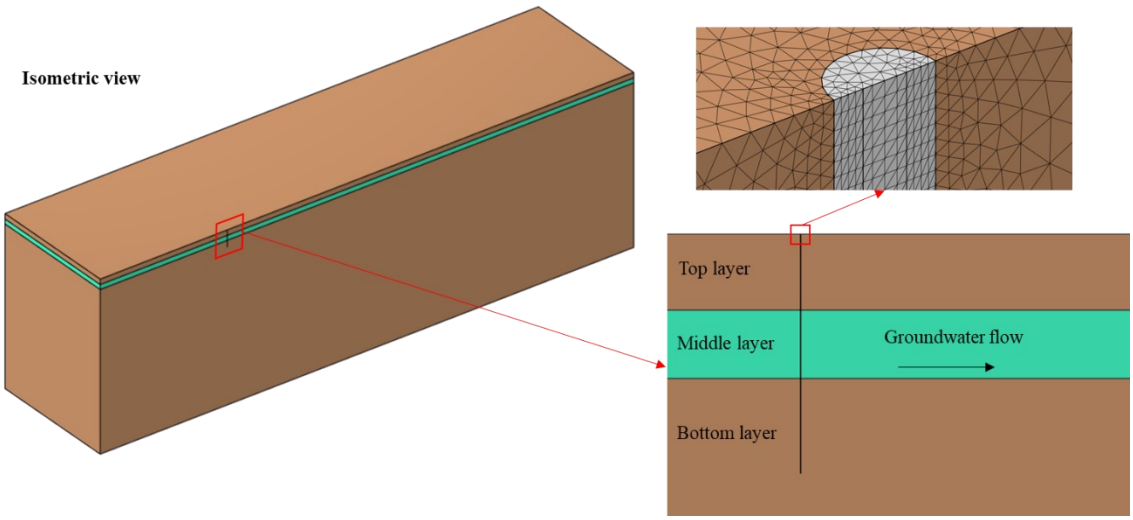

Figure 3-6. Schematic diagram of three bedded layers with an aquifer. Mesh refined near the borehole.

Table 3-2. Thermal and hydraulic properties of three ground layers. The parameters are presented for each ground layer [123].

Parameter	**Top layer**	**Middle layer**	**Bottom layer**
Depth (m)	0 – 20	20 – 38	38 - 63
Thermal conductivity ($Wm^{-1}K^{-1}$)	2.12	1.20	1.61
Specific heat capacity ($Jkg^{-1}K^{-1}$)	910	2225	1400
Density (kgm^{-1})	1880	1680	1980

Table 3-3. Parameter inputs for simulations, based on the work by Hu [123]

Parameter	**Symbol**	**Value**
Grout thermal conductivity	k_g	1.5 $Wm^{-1}K^{-1}$
Estimated grout volumetric heat capacity	$(\rho c)_g$	3.2×10^6 $Jm^{-3}K^{-1}$
Pipe thermal conductivity	k_p	0.45 $Wm^{-1}K^{-1}$
Fluid thermal conductivity	k_f	0.599 $Wm^{-1}K^{-1}$
Fluid volumetric heat capacity	$(\rho c)_f$	4.2×10^6 $Jm^{-3}K^{-1}$
Average mass rate of circulating fluid	M	0.2 kgs^{-1}
Length of the borehole	H	63 m

Parameter	Symbol	Value
Borehole radius	r_b	0.07 m
Pipe outer radius	r_o	0.016 m
Pipe wall thickness		0.003 m
Shank spacing	d	0.06 m
Ground load	Q	3150 W

3.4. Results and discussion

3.4.1 Verification

Figure 3-7 depicts the average temperature at the borehole wall over time, considering four different groundwater velocities within the middle layer: 0 ms^{-1}, 10^{-8} ms^{-1}, 10^{-7} ms^{-1}, and 10^{-6} ms^{-1}. The MVQ solution and the simulation results obtained from COMSOL modelling exhibited a strong alignment throughout the entire simulation duration. To quantify this alignment, these outcomes were compared using Mean Absolute Percentage Error (MAPE) values, as listed in Table 3-4. The MAPE is a widely recognized and commonly used metric for assessing prediction accuracy, offering an intuitive measure of relative error [144]. The MAPE is defined as

$$\text{MAPE} = \frac{100\%}{N}\sum_{i=1}^{N}\left|\frac{\overline{\Delta T}_{MVQ}(t_i) - \overline{\Delta T}_{COMSOL}(t_i)}{\overline{\Delta T}_{COMSOL}(t_i)}\right| \quad (3\text{-}23)$$

where N denotes the number of sampling times; $\overline{\Delta T}_{MVQ}$ represents the average temperature change obtained from the MVQ solution at time t_i, and $\overline{\Delta T}_{COMSOL}$ represents the average temperature change obtained from the COMSOL modelling at time t_i. For the specific parameters discussed in this study, the MAPE values were approximately 0.62%, 0.61%, 0.64%, and 0.99% for groundwater velocities of 0 ms^{-1}, 10^{-8} ms^{-1}, 10^{-7} ms^{-1}, and 10^{-6} ms^{-1}, respectively. Given the small MAPE values observed, the MVQ solution can be confidently considered as numerically verified.

To elucidate the impact of varying heat transfer rates involving groundwater flow in multilayered ground conditions, a comparative study was made against two well-established constant heat transfer rate (CQ) solutions found in the literature: the solutions proposed by Erol and François [64] and Hu [123]. In contrast to the MVQ solution, CQ solutions overestimated temperature changes in most scenarios, particularly in the middle and bottom layers. For example, as demonstrated in Figure 3-7 (a), when using the solutions proposed by Erol and François [64] and Hu [123], the temperature of the middle layer was overestimated by 32.72% and 30.49%, respectively. In the same scenario, accounting for varying heat transfer rates, the MVQ solution exhibited only a 2.14% deviation from the numerical results. This contrast highlights the superior predictive accuracy of the MVQ solution, which can be approximately 15 times more accurate compared to the results obtained from CQ solutions.

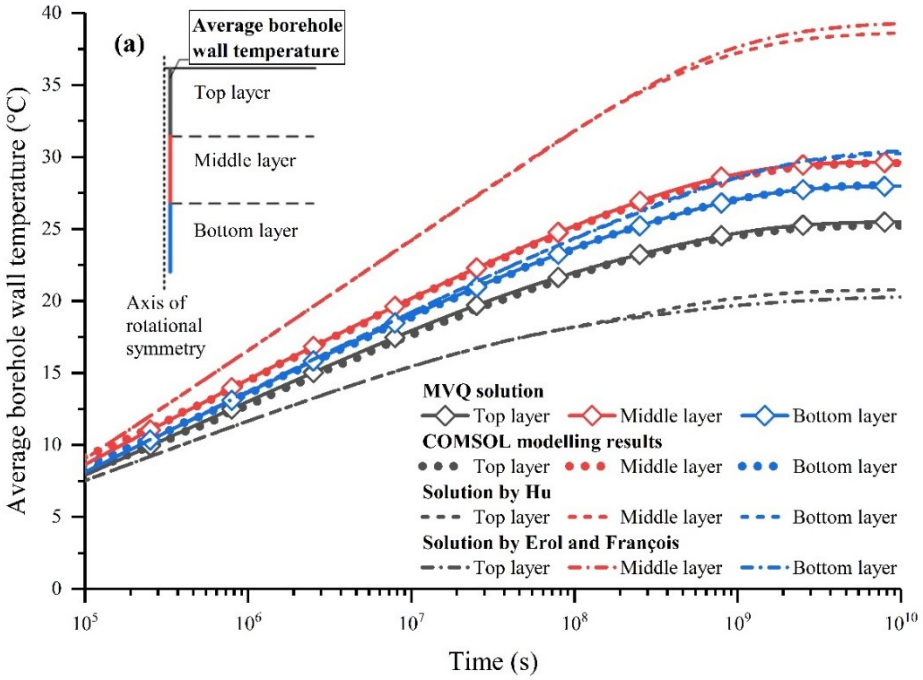
(a)
Average borehole wall temperature
Top layer
Middle layer
Bottom layer
Axis of rotational symmetry
Average borehole wall temperature (°C)
Time (s)
MVQ solution
Top layer
Middle layer
Bottom layer
COMSOL modelling results
Top layer
Middle layer
Bottom layer
Solution by Hu
Top layer
Middle layer
Bottom layer
Solution by Erol and François
Top layer
Middle layer
Bottom layer

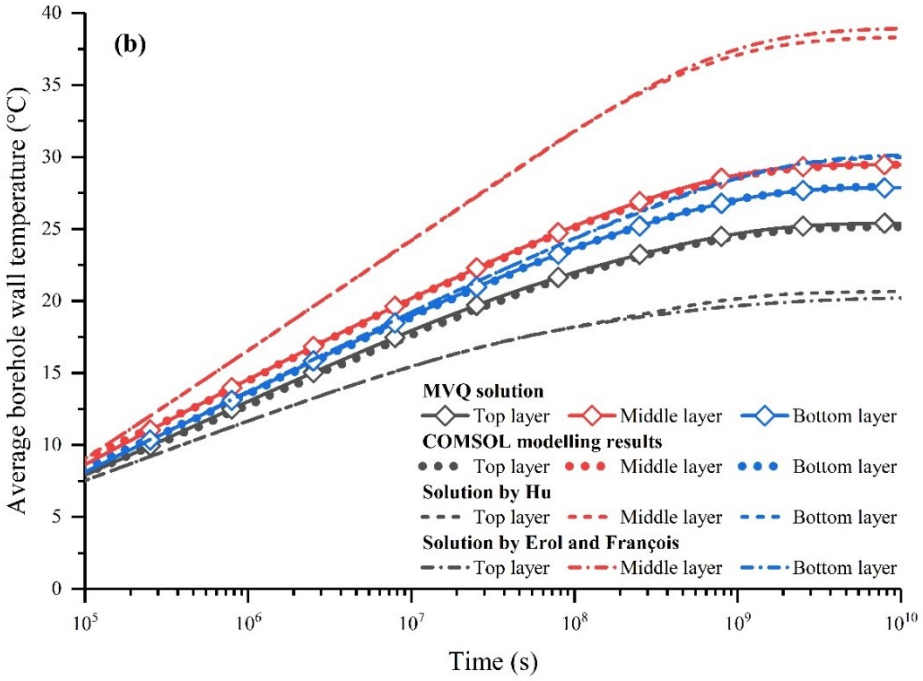
(b)
Average borehole wall temperature (°C)
Time (s)
MVQ solution
Top layer
Middle layer
Bottom layer
COMSOL modelling results
Top layer
Middle layer
Bottom layer
Solution by Hu
Top layer
Middle layer
Bottom layer
Solution by Erol and François
Top layer
Middle layer
Bottom layer

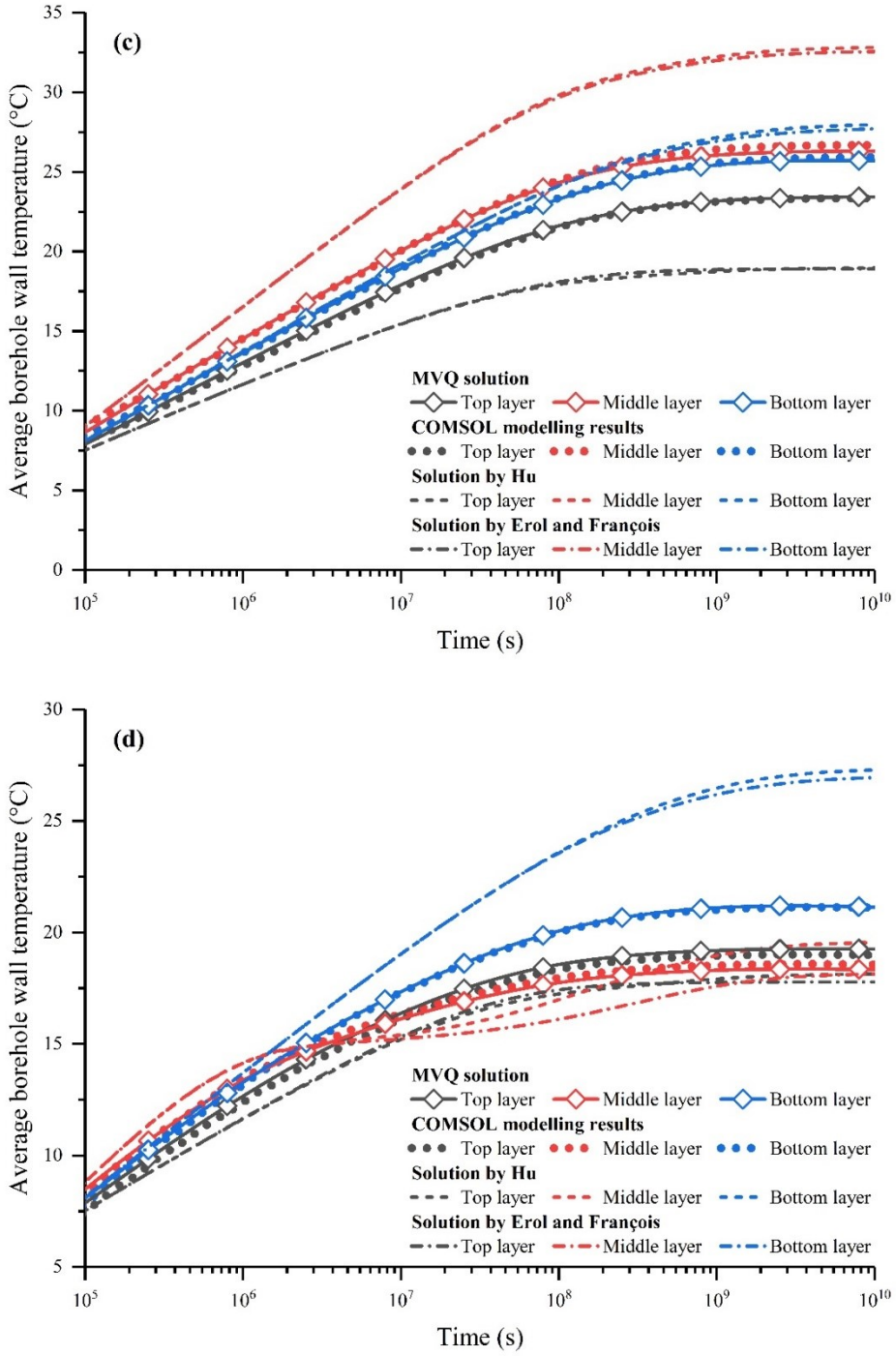

Figure 3-7. The average borehole wall temperature for each layer under four groundwater velocities: 0 ms^{-1}, 10^{-8} ms^{-1}, 10^{-7} ms^{-1}, and 10^{-6} ms^{-1}.

Table 3-4. The MAPE values between temperatures simulated by the COMSOL modelling and those evaluated by (semi-)analytical solutions.

Groundwater flow velocity (u_d)	**0 ms^{-1}**	**10^{-8} ms^{-1}**	**10^{-7} ms^{-1}**	**10^{-6} ms^{-1}**
MVQ solution	0.62%	0.61%	0.64%	0.99%
Solution by Erol and François [64]	15.06%	14.95%	12.95%	9.54%
Solution by Hu [123]	14.61%	14.53%	13.37%	9.13%

3.4.2 Borehole wall temperature

Figure 3-8 demonstrates the temperature profile along the borehole wall in a multilayered condition, in which the middle layer is subjected to four different groundwater velocities (i.e., 0 ms^{-1}, 10^{-8} ms^{-1}, 10^{-7} ms^{-1}, and 10^{-6} ms^{-1}). All the solutions discussed here clearly illustrate the temperature variations across the different layers. Under scenarios where heat conduction dominates, specifically When u_d = 0 ms^{-1}, 10^{-8} ms^{-1}, and 10^{-7} ms^{-1}, the middle layer exhibited the highest temperature among the three ground layers. It can primarily be attributed to the low thermal conductivity of the middle layer, which was set at 1.20 $Wm^{-1}K^{-1}$. However, the introduction of groundwater flow within the middle layer facilitated the dissipation of heat away from the borehole. As the velocity of the groundwater flow increased, the temperature within the middle layer decreased.

In contrast to the CQ solutions, the temperature variations between ground layers were notably smaller in the solutions incorporating a non-uniform heat transfer rate, such as the COMSOL

modelling and the MVQ solution. This phenomenon aligns with Newton's law of cooling [145], where the heat transfer rate depends on the temperature difference between the circulating fluid and the surrounding ground. Accordingly, the circulating fluid tends to discharge more heat into layers with lower temperatures while releasing less heat into layers with higher temperatures. This phenomenon ultimately results in reduced temperature disparities between ground layers when a non-uniform heat transfer rate is accounted for. Capturing this phenomenon, the MVQ solution provides better temperature prediction for BHE in multilayered ground conditions with groundwater flow.

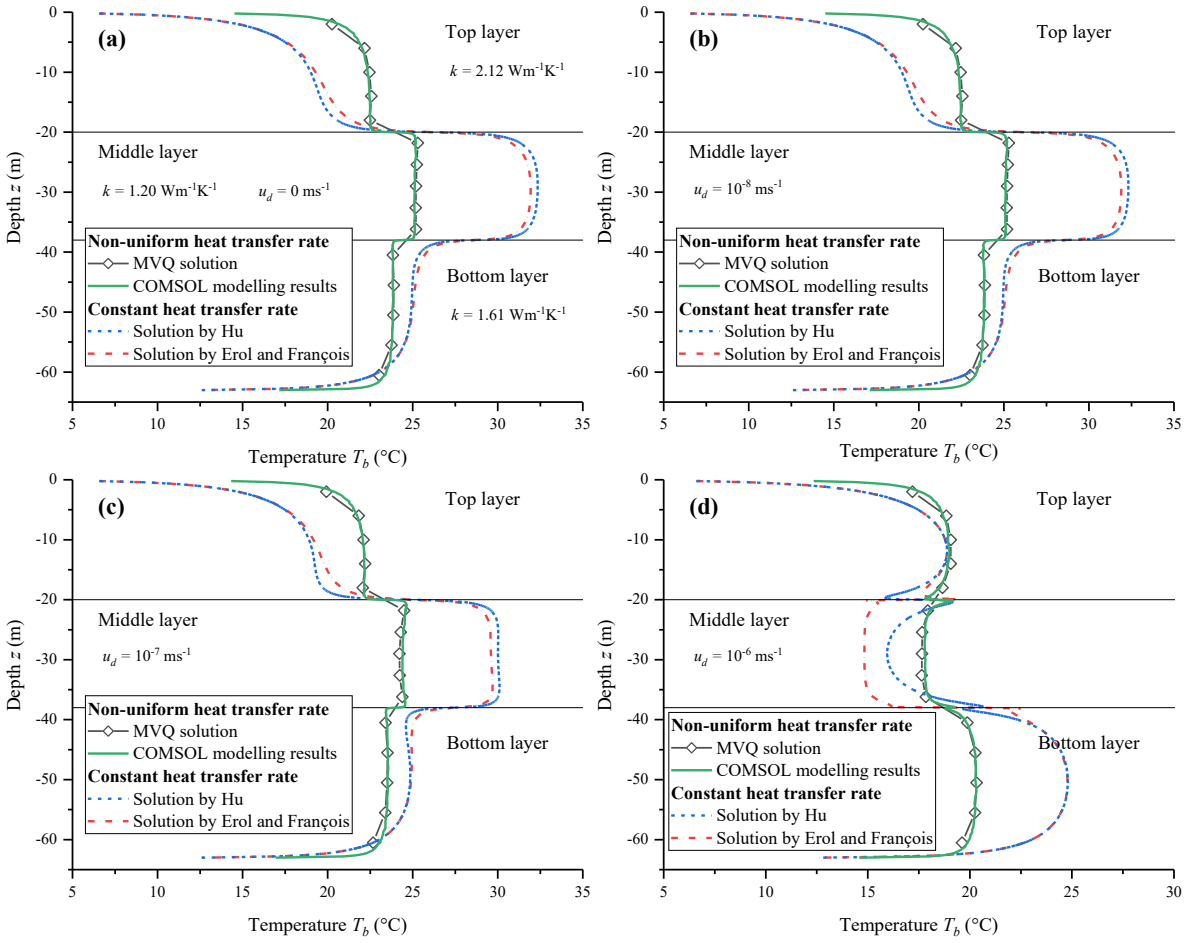

Figure 3-8. Temperature profiles along the borehole wall at 10^8s (about 3 years). The middle layer was under four different groundwater flow velocities: (a) 0 ms^{-1}, (b) 10^{-8} ms^{-1}, (c) 10^{-7} ms^{-1}, and (d) 10^{-6} ms^{-1}.

3.4.3 Profile of heat transfer rate

Figure 3-9 illustrates profiles of the heat transfer rate under the condition of pure heat conduction (i.e., $u_d = 0$ ms^{-1}). In the absence of groundwater flow, both the MVQ solution and the results from COMSOL modelling show that the heat transfer rate in the top layer was faster, exceeding the

average rate of 50 Wm^{-1}. This contrasted with the uniform distribution assumed in the CQ solutions. The reason for this discrepancy is the variation in thermal conductivity among the layers. Specifically, the top layer was assigned wait a higher thermal conductivity value of 2.12 $Wm^{-1}K^{-1}$, whereas the middle and bottom layers had relatively lower thermal conductivity values of 1.20 $Wm^{-1}K^{-1}$ and 1.61 $Wm^{-1}K^{-1}$, respectively. Thus, the top layer allowed for a more rapid dissipation of heat energy due to its higher thermal conductivity.

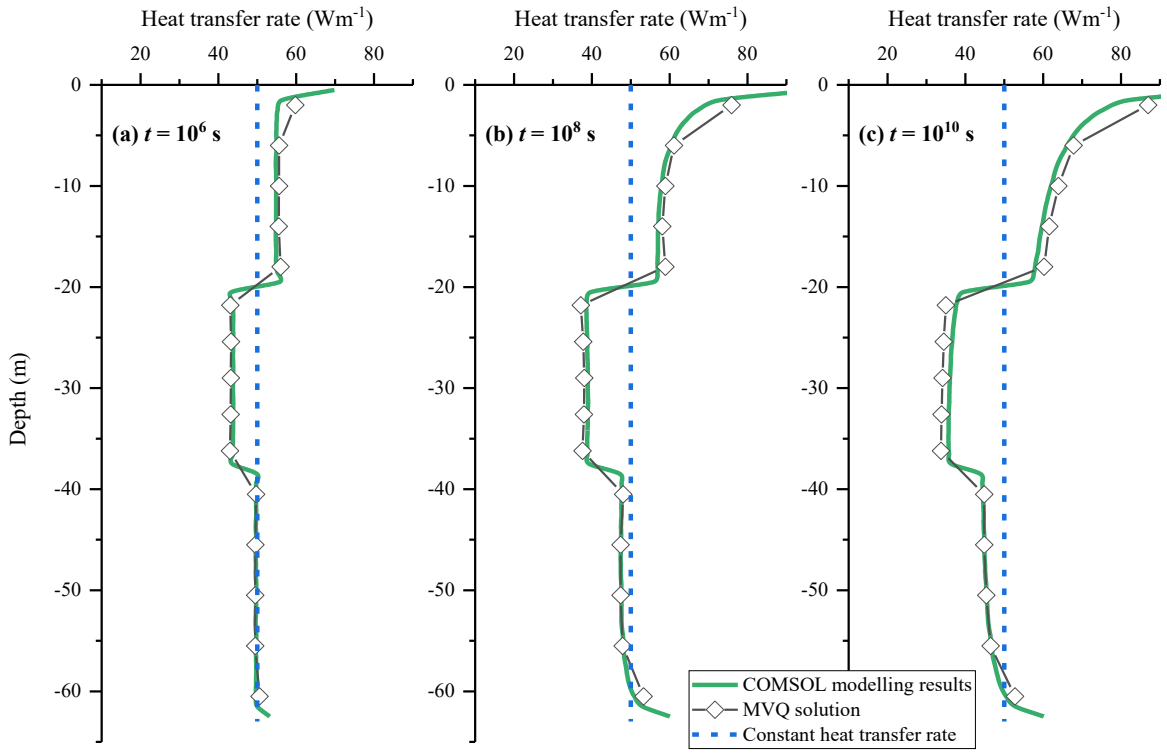

Figure 3-9. The heat transfer rate profiles in the pure heat conduction condition (i.e., no groundwater flow, u_d = 0 ms^{-1}) at different time intervals: (a) 10^6 s, (b) 10^8 s, and (c) 10^{10} s.

When the groundwater flow was involved, it played an important role in enhancing heat transfer in the middle layer. As depicted in Figure 3-10, the average heat transfer rate of the middle layer experienced a significant increase, going from 38.96 Wm^{-1} to 40.41 Wm^{-1} and 55.23 Wm^{-1} after the simulation of the 10^8 seconds, corresponding to varying groundwater flow velocities of 10^{-8} ms^{-1} to 10^{-7} ms^{-1} and 10^{-6} ms^{-1}, respectively. Notably, under a groundwater flow velocity of 10^{-6} ms^{-1}, the rate exceeded the average rate by about 15.33% and it was about 32.41% higher than that observed in the bottom layer. These findings are consistent with the study conducted by Luo et al. [70] involving a scenario with five bedded layers. Their findings revealed that the efficacy of heat transfer in the layers with groundwater flow was at least 25.9% greater than that in the layers without groundwater flow. In general, the heat transfer rate is enhanced within layers where the groundwater flow is present. By addressing this phenomenon, the MVQ solution provides valuable insights into evaluating the actual effect of groundwater flow in multilayered ground conditions.

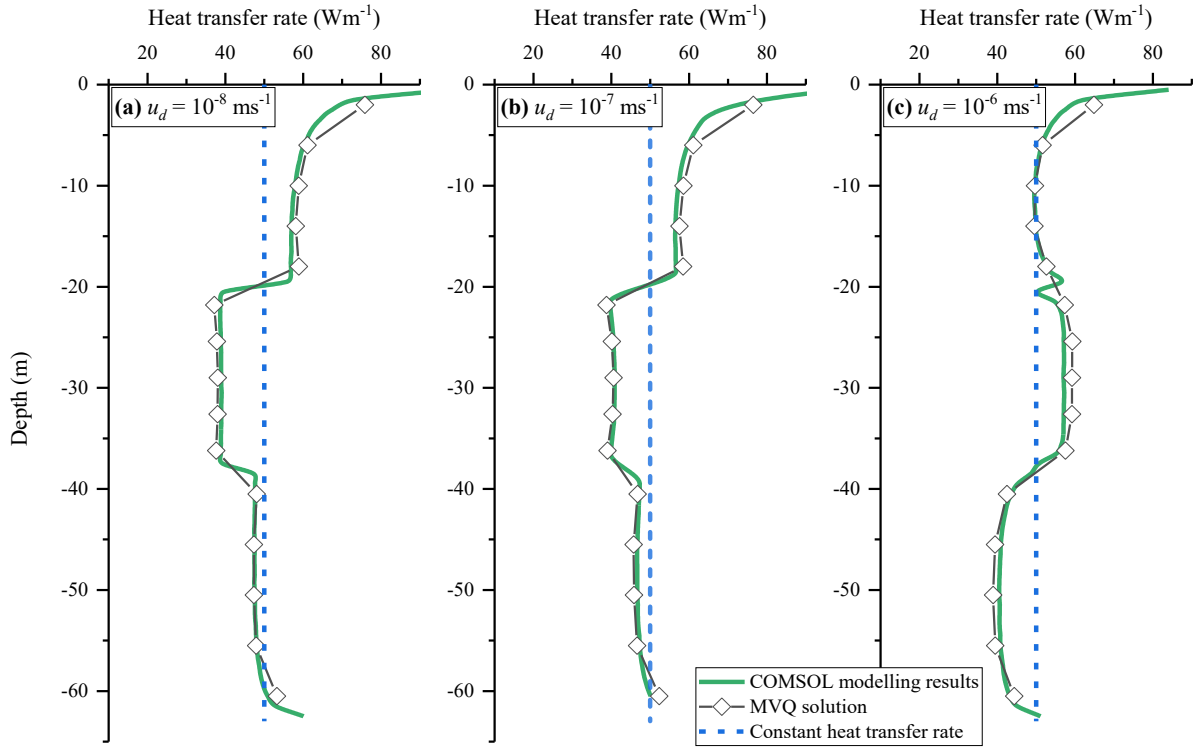

Figure 3-10. The heat transfer rate profiles along the borehole at different groundwater flow velocities: (a) 10^{-8} ms^{-1}, (b) 10^{-7} ms^{-1}, and (c) 10^{-6} ms^{-1}.

3.4.4 Upstream and downstream temperature

Figure 3-11 presents isothermal contours near a BHE in the *xz*-plane under different groundwater flow velocities, based on the COMSOL modelling over a period of 10^{10} seconds. When there was no groundwater flow, the isothermal contours exhibited axial symmetry around the BHE. However, in the presence of groundwater flow, heat was transported from the BHE downstream due to the flow, resulting in elongated contours in the direction of the flow. The affected region expanded as the flow velocity increased.

In larger applications such as commercial buildings, the ground heat exchanger system may necessitate a borehole field containing tens to hundreds of boreholes [128, 146]. These boreholes are usually spaced 6 to 8 meters apart within the field [147]. However, due to the shared utilization of the same underground reservoir, adjacent boreholes can significantly influence the heat transfer efficiency of each other after a few months [68, 87, 93]. For example, inner boreholes, surrounded by adjacent boreholes on all sides, tend to exchange less heat compared to their outer counterparts. Furthermore, in the presence of groundwater, downstream boreholes are affected by the heat dissipated from upstream boreholes conveyed by the flow. Consequently, as discussed in our previous study [148], more heat is transferred by the upstream boreholes than by the downstream ones. In this context, it is essential not only to account for the variation in heat transfer rate along the boreholes but also to consider the variation of heat load between boreholes. Currently, the MVQ solution focuses on a single borehole. Therefore, there is a need to extend the MVQ solution to encompass borehole fields, taking into account the intricate interactions that occur within such BHE systems.

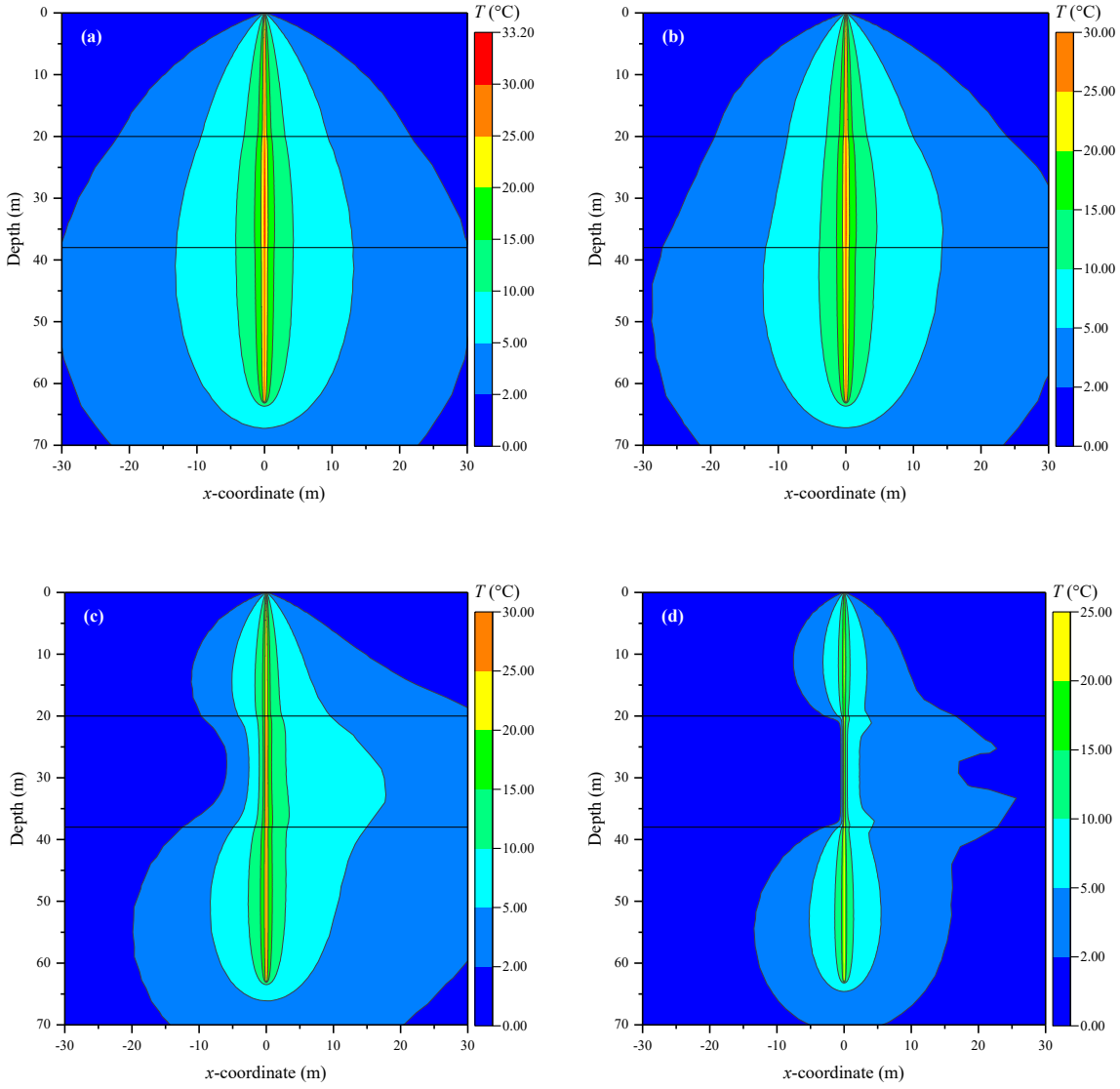

Figure 3-11. The isothermal contours of the ground in an *xz*-plane view under different groundwater flow velocities after 10^{10} seconds of operation: (a) 0 ms^{-1}, (b) 10^{-8} ms^{-1}, (c) 10^{-7} ms^{-1}, and (d) 10^{-6} ms^{-1}.

3.5. Conclusion

This study introduces a novel solution, termed the "MVQ solution" (multilayered ground with varying heat transfer rate), for analyzing borehole heat exchangers (BHEs) placed in multilayered ground with groundwater flow. The MVQ solution allows a simultaneous analysis of heat transfer both outside and with the borehole. It addresses the variation in heat transfer rate over time and depth, eliminating the common assumption of a constant heat transfer rate in conventional analytical methods. This novel solution holds the potential to facilitate the design of BHE systems, making them more thermally efficient in practical engineering applications. The key findings of this study are as follows:

(1) The MVQ solution was verified against a three-dimensional (3-D) numerical model established in a commercial finite element software package, specifically COMSOL Multiphysics. Over an extended period spanning up to 10^{10} seconds, the maximum percentage difference between the COMSOL modelling results and the MVQ solution was 2.14%, and the mean absolute percent error remained below 1% in all investigated scenarios. This small discrepancy signifies the reliability and potential of the MVQ solution for the practical BHE design.

(2) This study demonstrated that the heat transfer in the layer with groundwater flow intensifies as the flow velocity increases. For the given parameters, the presence of groundwater flow elevated the average heat transfer rate in the middle layer from 38.96 Wm^{-1} to 40.41 Wm^{-1} and 55.23 Wm^{-1}, as the flow velocity increased from 10^{-8} ms^{-1} to 10^{-7} ms^{-1} and 10^{-6} ms^{-1}, respectively. This thermal enhancement resulting from groundwater flow is typically

neglected in conventional solutions that assume a constant heat transfer rate. By addressing this phenomenon, it becomes possible to assess the actual effects of groundwater flow in multilayered ground conditions.

(3) The consideration of varying heat transfer rates in the MVQ solution redistributes heat within the multilayered ground, effectively preventing the overestimation of ground temperature. In the scenario investigated, neglecting the varying heat transfer rate could result in a temperature overprediction of up to 32.72%. Therefore, the MVQ solution is a critical tool for more accurate assessments of BHE performance in real-world conditions. It offers valuable insights for practical geothermal system design. Consequently, the MVQ solution is a critical tool for achieving more accurate assessments of BHE performance in real-world conditions. Its application will provide valuable insights for practical geothermal system design.

Appendix 3-A. Calculation of delta-circuit thermal resistances

Hellström [128] describes the delta-circuit thermal resistances using the total internal thermal resistance (R_a) between the two pipes and the borehole thermal resistance (R_b) between the pipes and the borehole wall. For a single U-tube case, if the two pipes are symmetrically placed, the three delta-circuit thermal resistances between circulating fluid nodes and the borehole wall node are given by

$$R_1^{\Delta} = R_2^{\Delta} = 2R_b \tag{A-1}$$

$$R_{12}^{\Delta} = \frac{2R_a R_1^{\Delta}}{2R_1^{\Delta} - R_a} \tag{A-2}$$

The borehole thermal resistance and the total internal resistance can be estimated using the multipole method proposed by Bennet et al. [149]. The multipole solution is in the form of a mathematical series, i.e. multipole expansion [33]. The accuracy of the approximation is increased by increasing the order of the multipole expansion used for the calculation [17]. For a single U-tube case with two symmetrically placed pipes, Hellström [128] derived the following first-order multipole formulae:

$$R_b = \frac{1}{2}\left[\frac{1}{4\pi k_g}\left(\ln\left(\frac{r_b}{r_o}\right) + \ln\left(\frac{r_b}{2d}\right) + \sigma \ln\left(\frac{r_b^4}{r_b^4 - d^4}\right) - \eta_b\right) + R_f + R_p\right] \quad \text{(A-3)}$$

$$R_a = \frac{1}{\pi k_g}\left[\ln\left(\frac{2d}{r_o}\right) + \sigma \ln\left(\frac{r_b^2 + d^2}{r_b^2 - d^2}\right) - \eta_a\right] + 2\left(R_f + R_p\right) \quad \text{(A-4)}$$

where $\sigma = \frac{k_g - k_{si}}{k_g + k_{si}}$, k_g [$\mathrm{Wm^{-1}K^{-1}}$] is the thermal conductivity of the grouting material, r_o [m] is the pipe's outer radius, d [m] is the shank spacing that is defined as half the centre-to-centre distance between the two legs of the U-tube, η_b and η_a are the corrections based on the multipole expansion, and R_f and R_p [$\mathrm{mKW^{-1}}$] are the thermal resistances of the circulating fluid and the pipe, respectively. The first order corrections are defined by

$$\eta_b = \frac{\left[\frac{r_o}{2x}\left(1 - \frac{4\sigma r_b^4}{r_b^4 - d^4}\right)\right]^2}{\frac{1 + 2\pi k_g R_{fp}}{1 - 2\pi k_g R_{fp}} + \left(\frac{r_o}{2d}\right)^2\left[1 + \frac{16\sigma r_b^4}{(r_b^4 - d^4)^2}\right]} \quad \text{(A-5)}$$

$$\eta_a = \frac{\left[\frac{r_o}{2d}\left(r_b^4 - d^4 + 4\sigma d^2 r_b^2\right)\right]^2}{\frac{1 + 2\pi k_g\left(R_f + R_p\right)}{1 - 2\pi k_g\left(R_f + R_p\right)}(r_b^4 - d^4)^2 - \left[\frac{r_o}{2d}(r_b^4 - d^4)\right]^2 + 2\sigma\left(\frac{r_o}{r_b}\right)^2(r_b^4 + d^4)} \quad \text{(A-6)}$$

The pipe and fluid thermal resistances can be found as

$$R_{fp} = R_f + R_p = \frac{1}{\pi N u k_f} + \frac{\ln\left(\frac{r_o}{r_i}\right)}{2\pi k_p} \tag{A-7}$$

where k_f and k_p [$Wm^{-1}K^{-1}$] are the thermal conductivity of the circulating fluid and pipe, respectively, r_i [m] is the pipe's inner radius, and Nu is the Nusselt number. The Nusselt number is evaluated by the Gnielinski correlation [150] for transitional and turbulent flow,

$$Nu = \frac{\left(\frac{f_D}{8}\right)(Re - 1000)Pr}{1 + 12.7\left(\frac{f_D}{8}\right)^{\frac{1}{2}}\left(Pr^{\frac{2}{3}} - 1\right)} \tag{A-8}$$

where $Re = \frac{\rho_f}{\mu} \cdot \frac{2V}{\pi r_i}$ is the Reynolds number, $Pr = \frac{c_f \mu}{k_f}$ is the Prandtl number, μ [$kgm^{-1}s^{-1}$] is the dynamic viscosity of the circulating fluid, and f_D is the Darcy friction factor that can be evaluated by the Sonnad and Goudar approximation [151],

$$\frac{1}{\sqrt{f}} = 0.8686 \ln\left(\frac{0.4587Re}{\ln(0.4587Re - 0.28)^{\frac{\ln(0.4587Re)}{\ln(0.4587Re)+0.98}}}\right) \quad \text{(A-9)}$$

Chapter 4. A new semi-analytical solution addressing varying heat transfer rates for U-shaped vertical borehole heat exchangers in multilayered ground

This chapter has been accepted as Guo, Y., Huang, G., & Liu, W. V. A new semi-analytical solution addressing varying heat transfer rates for U-shaped vertical borehole heat exchangers in multilayered ground. *Energy*, *274*, 127373.

Nomenclature

c	specific heat capacity	[$Jkg^{-1}K^{-1}$]
d	shank spacing	[m]
D	depth	[m]
Fo	Fourier number	
G	Green's function	
H	borehole length	[m]
k	thermal conductivity	[$Wm^{-1}K^{-1}$]
L	dimensionless thickness	
q_l	heat transfer rate	[Wm^{-1}]
q_v	vertical heat flux	[Wm^{-2}]
q'	incremental heat flux	

Greek symbols

α	thermal diffusivity	[m^2s^{-1}]
Θ	dimensionless temperature	

Subscripts

Q	heat load	[W]
r_b	borehole radius	[m]
R_1^{Δ} , R_2^{Δ} , R_{12}^{Δ}	delta-circuit thermal resistance	[mKW^{-1}]
t	time	[s]
T	temperature	[°C]
T_0	undisturbed ground temperature	[°C]
ΔT	temperature variation	[°C]
V	circulating fluid flow rate	[m^3s^{-1}]
r, r', z, z'	coordinates	[m]

ρ	density	[kgm^{-3}]

down	downward-flowing fluid	*up*	upward-flowing fluid
g	grout	*w*	water
i	= 1, 2, … *n* Layer number	*r, z*	directions

Superscripts

$\bar{}$	$= \frac{1}{h}\int_0^h \cdots \, dz'$ integral mean

4.1. Introduction

With a growing coalition of countries pledging the goal of net-zero carbon emissions by 2050 or earlier, many industries are transitioning towards cleaner energy sources and deploying decarbonization solutions [120]. Among various solutions, shallow geothermal energy has been receiving increasing interest due to its high energy efficiency and low greenhouse gas emissions [152]. By exploiting shallow geothermal energy, ground source heat pump (GSHP) systems efficiently provide space heating and cooling as well as domestic hot water in buildings [6]. Compared with conventional heating and air-conditioning systems, GSHP systems can reduce energy consumption in heating by 30-70% and in cooling by 20-50% [121].

A core component of the GSHP system is the exterior heat exchanger that is in contact with the ground. When installed vertically, a heat exchanger construction usually comprises a single (or double) U-tube made of high-density polyethylene pipes placed in a vertical borehole, also known as the borehole heat exchanger (BHE) [14]. In the tube, a working fluid (usually a water and antifreeze mixture) is circulated to extract heat from the ground or dissipate heat to the ground [10]. BHEs are typically installed to a depth ranging from 50 m to 150 m [15]. At such depths, engineering applications have commonly found the surrounding ground to be stratified with multilayers [54-56]. For example, a drilling project [56] was conducted to investigate the geological information in the Edmonton area (Alberta, Canada) for GSHP applications. In the project, boreholes encountered a variety of sediments and rocks with thermal conductivities ranging from 0.62–3.22 $Wm^{-1}K^{-1}$ [56].

In the current literature, there are a few numerical and experimental studies that have been conducted to investigate the heat transfer of BHE in multilayered ground. For instance, Perego et

al. [57] studied a GSHP system in Italy that was installed in highly heterogeneous alluvials. The study showed that by ignoring stratifications the simulation underestimated the ground temperature change by as much as 25%. Deng and Fedler [69] measured and simulated the heat transfer rates in a triple-layer soil system comprised of coarse sand, clay, and fine sand. During 24 hours of operation, they found that the coarse sand and the fine sand dissipated over 62% and 27% more heat than the clay, respectively [69]. Another study by Luo et al. [70] examined the thermal performance of a BHE in the ground with five bedded layers, including an upper unsaturated layer, three middle layers containing groundwater flow, and a lower aquiclude. The results showed that the heat transfer efficacy in the lower layer was about 25.9% lower than that in the aquifers [70].

In addition to numerical and experimental studies, the literature contains a few available analytical solutions for BHE that consider the effects of multilayered ground. A multilayer line source solution has been developed by Abdelaziz et al. [58] based on Green's function method. This study [58] addressed the effect of the multilayered ground by utilizing the principle of superposition. That is, in horizontally layered ground, a BHE is divided into several line heat source segments by the boundary of each ground layer, and then the temperature variation at any arbitrary point in the ground is estimated by summing up the contributions of all BHE segments. Also, Zhou et al. [60] developed cylindrical and ring-coil heat source solutions for the double-layered ground using Green's function method, and Pan et al. [59] developed a cylindrical source solution for the multilayered ground using the integral-transformation method. These solutions [58-60] require a prescribed heat transfer rate as the boundary condition, such as a constant heat transfer rate along the borehole length [58]. However, this boundary condition (constant heat transfer rate) contradicts the reality of varying heat distribution in engineering applications [17]. In fact, the heat transfer rate is non-uniformly distribute along the borehole depth, and the distribution is changing during

the operation. For example, Monzó et al. [89] examined the heat transfer rate along the BHE depth in a homogeneous condition undertook a constant heating load. The numerical results demonstrated that the normalized heat transfer rate varied by about 0.92 between the top (about 1.8) and middle (about 0.88) areas of a 100 m BHE after 1 year operation, while the variation increased to about 1.92 after 25 years operation. The non-uniform distribution of the heat transfer rate has a significant impact on the thermal performance of BHEs, especially in layered ground. This effect has been investigated by Li et al. [71] based on a double-layered (sand and clay) sandbox experiment and simulation. The results revealed that the varying heat transfer rate provides a more accurate prediction of the ground temperature, while the constant heat transfer rate overpredicted the clay temperature by up to 76.6%. The ground temperature represents a crucial criterion in the design over the lifespan of a BHE system [86]. In real projects, the design goal of a BHE system is to maximize the system's thermal performance while controlling the ground temperature change. Deviating from this goal and overpredicting the ground temperature change can result in an underestimation of the geothermal potential and an oversizing of the BHE system. The oversized design can considerably increase financial costs due to the additional drilling and materials for longer BHEs, as well as the additional energy consumption for operating the system [17].

The downside of the constant heat transfer rate assumption is evident; however, the varying heat transfer rates have rarely been studied for U-shaped BHEs in multilayered ground. To this end, the objective of this study is to fill this research gap and develop a new semi-analytical solution addressing the effects of varying heat transfer rates for vertical borehole heat exchangers in multilayered ground. This new solution is named the "MVQ solution"—Multilayered ground with Varying heat transfer rates (Q). It is semi-analytical because it involves non-analytical vertical

discretization along the borehole length. The MVQ solution aims to improve the design expressions for vertical BHEs. It can enable rapid calculations and predict the long-term behaviour of BHE systems, and it can provide significant references for the design of BHE systems in shallow geothermal applications.

4.2. MVQ Solution

4.2.1 Description of the problem

As illustrated in Figure 4-1, a BHE is installed in the multilayered ground. The ground is commonly regarded as a semi-infinite body bounded by the ground surface. Conventional methods [86] analyzed the heat transfer problem in two separate regions: one outside the borehole, and one within the borehole. Consequently, a boundary condition (e.g., constant heat transfer rate) is prescribed along the borehole length at the borehole wall. To address the effect of heat transfer rate variation, the two regions need to be analyzed simultaneously. Enlightened by Cimmino [68], this study proposes a new method that integrates Green's function method [31] for the exterior region with a thermal resistance model [128] for the interior region.

To develop the MVQ solution for BHEs, following assumptions are made to simplify the problem. These assumptions are consistent with the study by Eskilson [23]:

a. For the exterior region, the borehole is approximated as a line heat source with its radial dimension neglected. This approximation is made because a typical BHE is 50 ~ 200 m in depth and 0.1 ~ 0.15 m in diameter, having a large aspect ratio.

b. The ground has a uniform initial temperature, T_0.

c. At the ground surface, a fixed temperature (i.e., T_0) was assumed as a boundary condition. This assumption is based on the fact that the temperature variation at the ground surface vanishes a few metres below ground, and its influence is negligible on the thermal performance of BHEs [23].

d. The thermal properties can be represented by constant values.

e. For the interior region, the borehole wall temperature is taken to be equal to the average temperature over the borehole wall surface as an approximate boundary condition. This simplification were widely accepted in the analytical analysis [23, 128, 153] and design [95] of shallow BHEs.

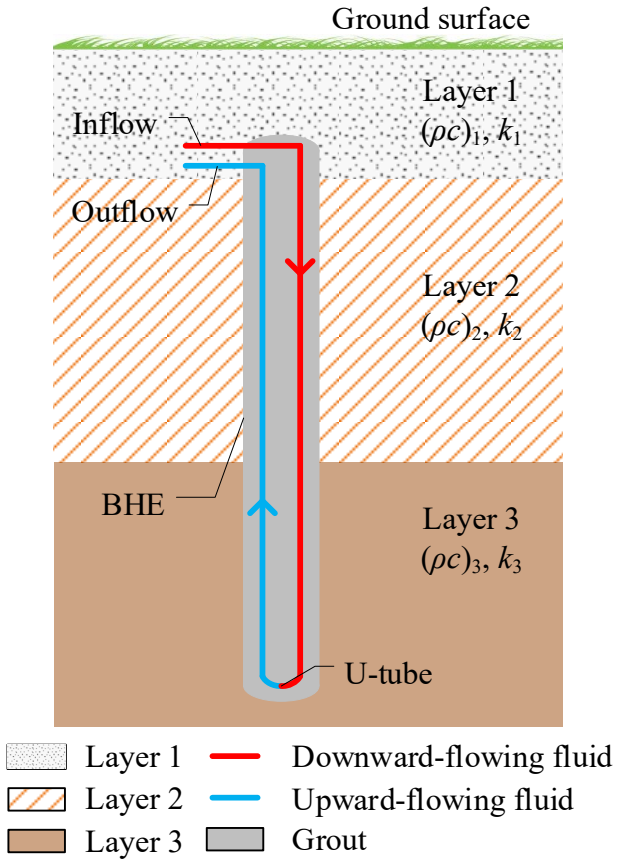

Figure 4-1. Schematic of a BHE embedded in the multilayered ground.

For each layer, the governing heat equation for the cylindrical coordinate system (r, z) can be expressed as follows [31]:

$$\rho c \frac{\partial T}{\partial t} = k \left[\frac{1}{r} \frac{\partial}{\partial r} \left(r \frac{\partial T}{\partial r} \right) + \frac{\partial^2 T}{\partial z^2} \right] \tag{4-1}$$

where T [°C] is the temperature, k [$Wm^{-1}K^{-1}$] is the ground thermal conductivity, and ρc [$Jm^{-3}K^{-1}$] is the volumetric heat capacity of the ground layer.

4.2.2 Heat transfer outside the borehole

To analyze the heat transfer outside the BHE systems, many analytical solutions [28, 29, 35, 134] have been developed based on Kelvin's theory [30] of heat source. That is, taking the solution for an instantaneous point source as the fundamental solution, the solution for a continuous heat source can be obtained by integration of the fundamental solution with respect to the time and the space variable [31]. The fundamental solution is given by Green's function method [31]. However, it is difficult to define a Green's function for the ground with more than three layers due to the complexity of the function [154]. Inspired by Cole [155], we assigned a simple Green's function for a homogenous body within each layer, and the heat transfer between adjacent layers were approximated using unknown time-varying vertical heat fluxes (q_v) at the interfaces.

As illustrated in Figure 4-2, an unknown time-varying vertical heat flux leaves the lower layer and enters the upper layer at each interface, severing as nonhomogeneous boundary conditions of the

second kind, i.e., prescribed surface heat flux on the boundary. Then, the problem in each layer becomes a nonhomogeneous transient heat conduction problem involving nonhomogeneous boundary conditions and internal heat generation. By using the principle of superposition [129], the temperature change in a layer at any time (t) and at any arbitrary point (r, z) is calculated by superimposing the contributions of the vertical heat fluxes with the contribution of the internal heat generation (T_E):

$$\Delta T_i(r,z,t) = T_{E_i}(r,z,t) + T_{U_i}(r,z,t) + T_{V_i}(r,z,t), \qquad i = 1,2,\cdots n \tag{4-2}$$

where ΔT [°C] is the temperature change from the initial temperature (T_0) for layers i = 1, 2, … n, T_U [°C] represents the contribution of the vertical heat flux at the upper boundary surface and T_V [°C] represents the contribution of the vertical heat flux at the lower boundary surface. It is noted that the solution (ΔT_1) for the topmost ground layer does not contain the T_U term and the solution (ΔT_n) for the bottommost ground layer does not contain the T_V term.

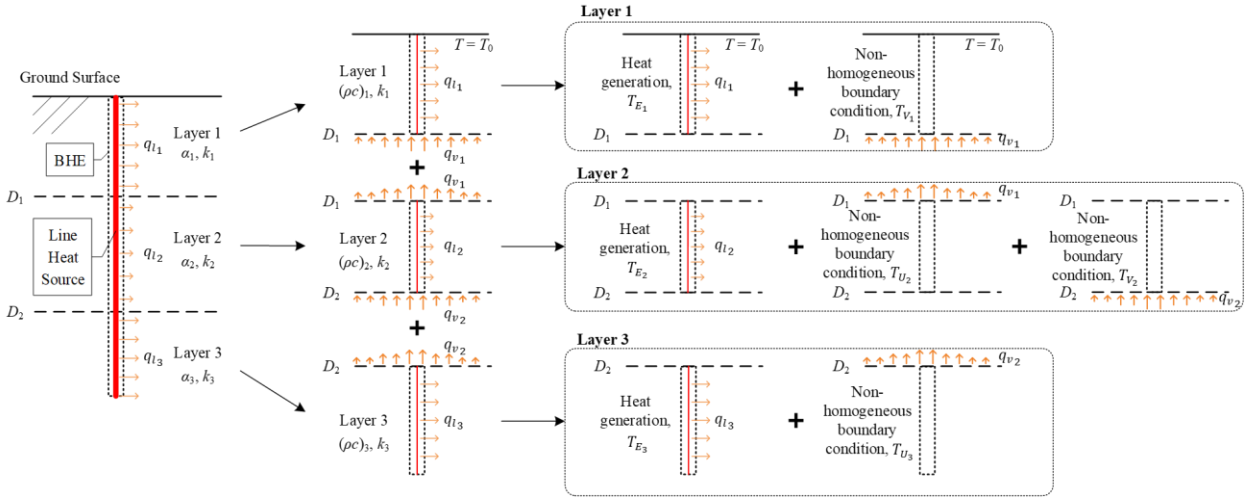

Figure 4-2. Schematic of a BHE embedded in the multilayered ground with unknown vertical heat fluxes at the interfaces between adjacent layers. Though the triple-layer ground was illustrated, the ground can be extended to other numbers of layers, depending on geological conditions. *D* denotes depths. q_l is the heat transfer rate per unit length.

The expressions of temperature, T_E, T_U, and T_V, can be found by the method of Green's functions [135],

$$T_{E_i}(r,z,t) = \frac{\alpha_i}{k_i}\int_{\tau=0}^{t} q_{l_i}(\tau)\int_{0}^{H_i} G_i\left(r,z,t\,\middle|\,0,z',\tau\right)dz'\,d\tau \tag{4-3}$$

$$T_{U_i}(r,z,t) = -\frac{\alpha_i}{k_i}\int_{\tau=0}^{t}\int_{0}^{r_\infty} q_{v_{i-1}}(r',\tau)G_i\left(r,z,t\,\middle|\,r',0,\tau\right)2\pi r'dr'\,d\tau \tag{4-4}$$

$$T_{v_i}(r,z,t) = \frac{\alpha_i}{k_i}\int_{\tau=0}^{t}\int_{0}^{r_\infty} q_{v_i}(r',\tau)G_i\left(r,z,t\,\middle|\,r',H_i,\tau\right)2\pi r'dr'\,d\tau \tag{4-5}$$

where H_i [m] is the borehole length in each layer, q_l [Wm^{-1}] is the heat transfer rate per unit length between the BHE and its surrounding ground, q_v [Wm^{-2}] is the unknown vertical heat flux at the interfaces, and $G_i(r, z, t \mid r', z', \tau)$ denotes the transient Green's function representing the response at a given observation location (r, z) to an impulsive heat source released at time τ [s], located at (r', z'). To present the contents of this work with clarity, the numbering system of Green's functions described by Cole et al. [135] is adopted. For instance, the bottommost ground layer is considered a semi-infinite body heated by a heat flux at the top surface (second-kind boundary condition) and unbounded on the other side. The Green's function for this layer is denoted as G_{Z20}. In another example, the topmost ground layer is considered a flat plate heated by a heat flux at the bottom surface with a fixed temperature at the top surface (first-kind boundary condition). The Green's function for this layer is denoted as G_{Z12}. In the same way, the intermediate layer is a flat plate with heat fluxes on both sides, and the Green's function is denoted as G_{Z22}. The Green's functions G_{Z20}, G_{Z12}, and G_{Z22} can be found in Appendix 4-B.

To approximate an arbitrary $q_v(r')$ curve, a simple way introduced by Monte et al. [156] is to divide the curve into multiple intervals and to apply a uniform heat flux within each of these intervals. This results in a stepwise profile as shown Figure 4-3. Applying the stepwise distribution of heat flux approximation, the spatial integral in Equations (4-4) and (4-5) can be approximated as a summation of the heat flux components,

$$\int_0^{r_\infty} q_{v\,i-1}(r', \tau) G_i(r, z, t \mid r', 0, \tau)\, 2\pi r' dr' = \sum_{p=1}^{P} q_{v\,i-1,p}(\tau) \int_{r_p}^{r_{p+1}} G_i(r, z, t \mid r', 0, \tau)\, 2\pi r' dr' \qquad (4\text{-}6)$$

$$\int_0^{r_\infty} q_{v_i}(r',\tau)G_i(r,z,t\,|\,r',H_i,\tau)\,2\pi r'dr' = \sum_{p=1}^{P} q_{v_{i,p}}(\tau)\int_{r_p}^{r_{p+1}} G_i(r,z,t\,|\,r',H_i,\tau)\,2\pi r'dr' \qquad (4\text{-}7)$$

where r_p [m] is the radial distance to divide the $q_v(r')$ curve (with $p = 1, 2, \cdots P$), and $r_1 = 0$ is the centreline. The integral of G_{Z20} over r' is given in Appendix 4-B. The integral of G_{Z12} and G_{Z22} can be found in the same method.

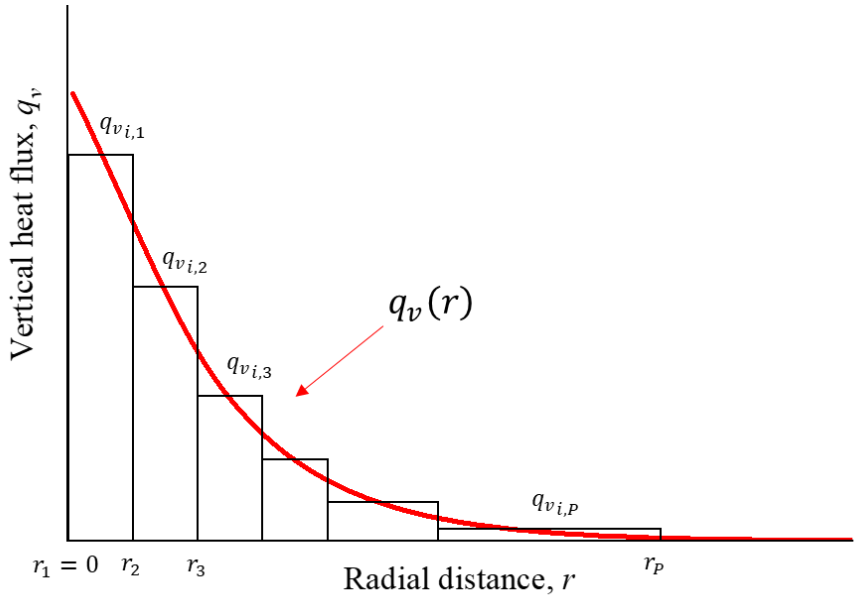

Figure 4-3. A schematic of approximating an unknown heat flux $q(r)$ at the boundary surface using a stepwise distribution.

Letting $U_{i,p}(r,z,t) = \frac{\alpha_i}{k_i}\int_{r_p}^{r_{p+1}} G_i(r,z,t\,|\,r',0,\tau)\,2\pi r'dr'$ and $V_{i,p}(r,z,t) = \frac{\alpha_i}{k_i}\int_{r_p}^{r_{p+1}} G_i(r,z,t\,|\,r',H,\tau)\,2\pi r'dr'$, then Equations (4-4) and (4-5) can be rewritten as

$$T_{U_i}(r,z,t) = -\int_{\tau=0}^{t} \overline{U_l}(r,z,t)\overline{q_{v_{i-1}}}(\tau)d\tau \tag{4-8}$$

$$T_{v_i}(r,z,t) = \int_{\tau=0}^{t} \overline{V_l}(r,z,t)\overline{q_{v_i}}(\tau)d\tau \tag{4-9}$$

where $\overline{U_l} = [U_{i,1} \quad U_{i,2} \quad \cdots \quad U_{i,P}]$, $\overline{V_l} = [V_{i,1} \quad V_{i,2} \quad \cdots \quad V_{i,P}]$, and $\overline{q_{v_l}} = \begin{bmatrix} q_{v_{i,1}} \\ q_{v_{i,2}} \\ \vdots \\ q_{v_{i,P}} \end{bmatrix}$.

In BHE applications, the heat loads are typically presented as stepwise values on an hourly basis due to time-varying demands [105]. With a stepwise heat transfer rate, an efficient theoretical approach is used to decompose the hourly heat transfer rates into a series of heat transfer rate increments and superimpose the response of each heat transfer rate increment [106],

$$T_E(r,z,t_m) = \sum_{j=1}^{m} q'_l(t_j)E(r,z,t_m - t_j), \qquad j = 1,2,\cdots m \tag{4-10}$$

where t_j is the discrete time that the heat transfer rate varies at (with $j = 1,2,\cdots m$), $q'_l(t_j) = q_l(t_j) - q_l(t_{j-1})$ is the incremental heat transfer rate between two consecutive time steps, and $E_i(r,z,t) = \frac{\alpha_i}{k_i}\int_0^{H_i} G_i(r,z,t \mid 0,z',\tau)\,dz'$.

The linear convolution sum of the two discrete sequences (i.e., q'_l and E), can be solved efficiently using the fast Fourier transform (FFT) algorithms via the circular convolution theorem [107]. Specifically, the linear convolution sum of the two discrete sequences can be found by taking an FFT of each sequence, multiplying them pointwise in the frequency domain, and then performing an inverse FFT [108],

$$T_E(r,z,t_m) = \Im^{-1}\left[\Im(q'_l)\Im\left(E(r,z)\right)\right] \tag{4-11}$$

where, in the discrete case, $\Im$ denotes the FFT, and $\Im^{-1}$ denotes the inverse-FFT.

Similarly, the linear convolution sum in Equations (4-8) and (4-9) can be rewritten as

$$T_{U_i}(r,z,t_m) = -\Im^{-1}\left[\Im\left(\overline{U}_l(r,z)\right)\Im\left(\overline{q'_{v-1}}\right)\right] \tag{4-12}$$

$$T_{v_i}(r,z,t_m) = \Im^{-1}\left[\Im\left(\overline{V}_l(r,z)\right)\Im\left(\overline{q'_v}\right)\right] \tag{4-13}$$

where $q'_v(t_j) = q_v(t_j) - q_v(t_{j-1})$ is the incremental heat flux between two consecutive time steps.

Now, Equations (4-11)-(4-13) can be substituted into the Equation (4-2) for the temperature. At each interface, and the ground temperature is continuous,

$$\Delta T_{i+1}(r, D_i, t) = \Delta T_i(r, D_i, t) \tag{4-14}$$

Regarding Equation (4-14), a system of linear equations is formed at each time step,

$$\begin{bmatrix} \Im[T_{E_2}(D_1) - T_{E_1}(D_1)] \\ \Im[T_{E_3}(D_2) - T_{E_2}(D_2)] \end{bmatrix} = \begin{bmatrix} \Im[\overline{V_1}(H_1) + \overline{U_2}(0)] & -\Im[\overline{V_2}(0)] \\ -\Im[\overline{U_2}(H_2)] & \Im[\overline{V_2}(H_2) + \overline{U_3}(0)] \end{bmatrix} \begin{bmatrix} \Im\left(\overline{q'_{v_1}}\right) \\ \Im\left(\overline{q'_{v_2}}\right) \end{bmatrix} \tag{4-15}$$

The solution of the system of linear equations gives the vertical heat flux at each interface. By substituting the solution back into Equations (4-2), (4-12), and (4-13), the temperature change in each ground layer can be determined. In the design [95], the borehole wall temperature is taken to be equal to the average temperature over the borehole wall surface as an approximate boundary condition. The average temperature can be obtained by spatial integration over the length of the borehole in each ground layer,

$$\overline{T_{b_i}} = \frac{\int_0^{H_i} \Delta T_i(r_b, z) dz}{H_i} \tag{4-16}$$

4.2.3 Heat transfer within the borehole

As illuminated by Cimmino [68], the heat transfer inside the borehole is incorporated by which the heat transfer rate varying along the borehole depth is considered. The heat transfer within a

borehole is often analyzed as a steady-state thermal resistance between the circulating fluid and the borehole wall. Within the borehole region, a delta-circuit is formed by connecting the two fluid temperature nodes and one borehole wall node (as shown in Figure 4-4), where the two fluid nodes address the different temperatures within the two pipes.

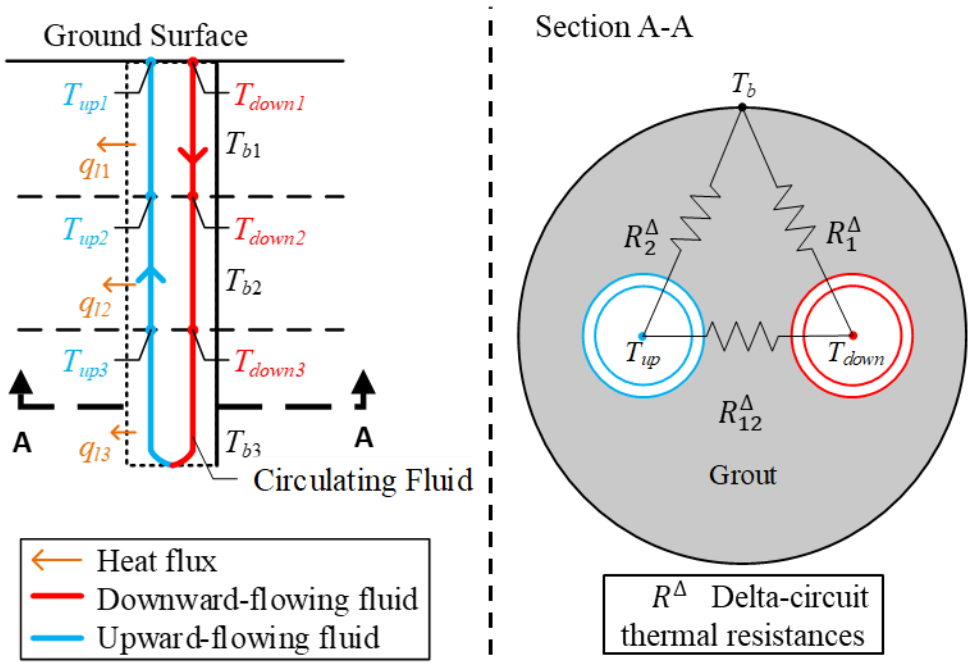

Figure 4-4. The schematic figure for the delta-circuit thermal resistance model with a single U-tube.

Taking account of the fluid temperature variation along the borehole depth, energy balance equations can be written for both the upward-flowing fluid (T_{up}) and the downward-flowing fluid (T_{down}),

$$V(\rho c)_f \frac{\partial T_{down}}{\partial z} = \frac{T_b - T_{down}}{R_1^\Delta} + \frac{T_{up} - T_{down}}{R_{12}^\Delta} \tag{4-17}$$

$$-V(\rho c)_f \frac{\partial T_{up}}{\partial z} = \frac{T_b - T_{up}}{R_2^{\Delta}} + \frac{T_{down} - T_{up}}{R_{12}^{\Delta}} \tag{4-18}$$

where R_1^{Δ}, R_2^{Δ} and R_{12}^{Δ} [mKW^{-1}] are three delta-circuit thermal resistances between the circulating fluid nodes, the borehole wall node, $(\rho c)_f$ [Jm^{-3}K^{-1}], is the volumetric heat capacity of the circulating fluid, and V [m^{3}s^{-1}] is the average flow rate of the circulating fluid.

A general solution to Equations (4-17) and (4-18) is derived using Laplace transforms and is given by Eskilson [23] and Hellström [128]. Assuming a uniform wall temperature in each ground layer, the quasi-three-dimensional solution for the downward-flowing fluid (T_{down}) is

$$T_{down_i}(L_i, t) = T_{down_i}(0, t) \cdot f_1(L_i) + T_{up_i}(0, t) \cdot f_2(L_i) + \overline{T_{b_i}} \cdot f_4(L_i) \tag{4-19}$$

and for the upward-flowing fluid (T_{up}) is

$$T_{up_i}(L_i, t) = -T_{down_i}(0, t) \cdot f_2(L_i) + T_{up_i}(0, t) \cdot f_3(L_i) + \overline{T_{b_i}} \cdot f_5(L_i) \tag{4-20}$$

where

$$f_1(L_i) = \exp(\beta L_i) \cdot \left[\cosh(\gamma L_i) - \frac{\beta - \beta_2 - \beta_{12}}{\gamma}\sinh(\gamma L_i)\right] \quad (4\text{-}21)$$

$$f_2(L_i) = \frac{\beta_{12}}{\gamma} \cdot \exp(\beta L_i) \cdot \sinh(\gamma L_i) \quad (4\text{-}22)$$

$$f_3(L_i) = \exp(\beta L_i)\left[\cosh(\gamma L_i) + \frac{\beta + \beta_1 + \beta_{12}}{\gamma}\sinh(\gamma L_i)\right] \quad (4\text{-}23)$$

$$f_4(L_i) = 1 - \exp(\beta L_i)\left[\cosh(\gamma L_i) + \frac{\beta - \beta_2}{\gamma}\sinh(\gamma L_i)\right] \quad (4\text{-}24)$$

$$f_5(L_i) = 1 - \exp(\beta L_i)\left[\cosh(\gamma L_i) + \frac{\beta + \beta_1}{\gamma}\sinh(\gamma L_i)\right] \quad (4\text{-}25)$$

$L_i = \frac{z - D_{i-1}}{H_i}$ is the dimensionless length from the top of each layer, $\beta_1 = \frac{H_i}{V(\rho c)_f R_1^{\Delta}}$, $\beta_2 = \frac{H_i}{V(\rho c)_f R_2^{\Delta}}$, and $\beta_{12} = \frac{H_i}{V(\rho c)_f R_{12}^{\Delta}}$ are the dimensionless thermal conductance, $\beta = \frac{\beta_2 - \beta_1}{2}$, $\gamma = \sqrt{\frac{(\beta_1+\beta_2)^2}{4} + \beta_{12}(\beta_1 + \beta_2)^2}$, and *sinh*(*X*) and *cosh*(*X*) are hyperbolic functions. The calculations of delta-circuit thermal resistances are presented in Appendix 3-A.

At each interface, a relationship is given by the continuity of the fluid temperature,

$$T_{down_i}(H_i, t) = T_{down_{i+1}}(0, t) \quad (4\text{-}26)$$

$$T_{up_i}(H_i, t) = T_{up_{i+1}}(0, t) \quad (4\text{-}27)$$

In addition, a temperature difference is imposed between the pipe inlet and outlet accounting for heat load (Q) according to

$$Q(t) = V(\rho c)_f \left(T_{down_1} - T_{up_1}\right) \tag{4-28}$$

Equations (4-19)- (4-28) form a system of linear equations,

$$\begin{bmatrix} -f_4(H_1)\overline{T_{b_1}} \\ -f_4(H_2)\overline{T_{b_2}} \\ [f_5(H_3) - f_4(H_3)]\overline{T_{b_3}} \\ f_5(H_1)\overline{T_{b_1}} \\ f_5(H_2)\overline{T_{b_2}} \\ Q \end{bmatrix} = \begin{bmatrix} f_1(H_1) & -1 & 0 & f_2(H_1) & 0 & 0 \\ 0 & f_1(H_2) & -1 & 0 & f_2(H_2) & 0 \\ 0 & 0 & f_1(H_3) + f_2(H_3) & 0 & 0 & f_2(H_3) - f_3(H_3) \\ f_2(H_1) & 0 & 0 & 1 & -f_3(H_1) & 0 \\ 0 & f_2(H_2) & 0 & 0 & 1 & -f_3(H_2) \\ V(\rho c)_f & 0 & 0 & -V(\rho c)_f & 0 & 0 \end{bmatrix} \begin{bmatrix} T_{down_1} \\ T_{down_2} \\ T_{down_3} \\ T_{up_1} \\ T_{up_2} \\ T_{up_3} \end{bmatrix} \tag{4-29}$$

The solution of the system of linear equations gives the fluid temperatures. The heat transfer rate per unit length in each ground layer is given by an energy balance on the circulating fluid,

$$q_{l_i}(t) = \frac{V(\rho c)_f}{H_i}\left[T_{down_{i-1}}(t) - T_{down_i}(t) + T_{up_i}(t) - T_{up_{i-1}}(t)\right] \quad (4\text{-}30)$$

4.2.4 Calculation process

The flowchart of the calculation process is shown in Figure 4-5. To address the effect of the heat transfer rate variation, the heat transfer inside and outside the borehole is analyzed simultaneously. At each time step, the calculation process starts with an initial guess of the temperature at the borehole wall. The guess value can be the temperature obtained from the previous time step. Then, iterating the two matrixes (i.e., Equations (4-15) and (4-29)), the output from one matrix is used as the input to the other matrix. The error of the solution is estimated while solving matrixes. The tolerance was set to be 10^{-6} °C to preserve calculation accuracy. When the error estimate is less than the tolerance, the temperature change and heat transfer rate in each layer are returned.

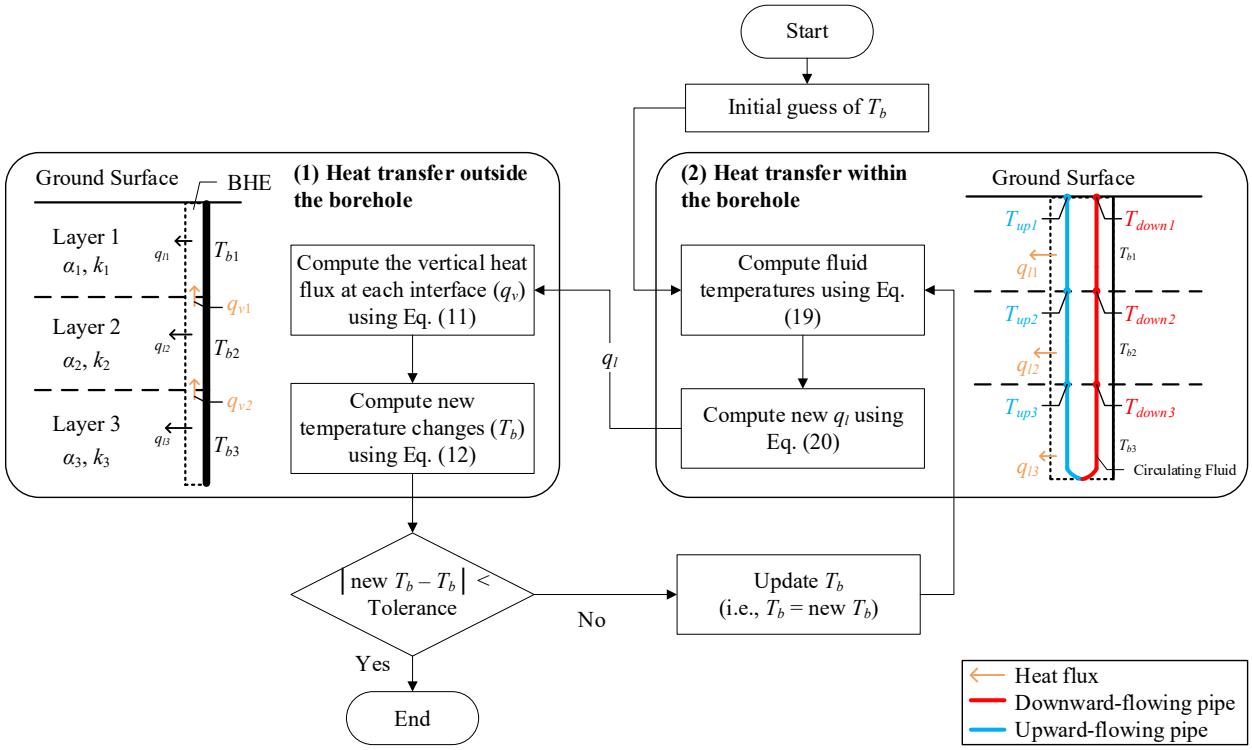

Figure 4-5. The flowchart of the calculation process.

The results are converted to dimensionless forms to show the generality of application to a broad class of situations rather than to just one set of dimensional parameters. The dimensionless form has been widely used in other studies [10, 23, 28] since it reduces the number of variables and facilitates the analysis. In the current study, two dimensionless variables are additionally introduced: the Fourier number and the thermal response factor. Taking the length of the borehole (H) as the characteristic length, the Fourier number is given by $Fo = \alpha_1 t/H^2$. The thermal response factor (Θ) gives the dimensionless temperature change responding to a unit heat transfer rate (Q/H = 1 Wm^{-1}), and it is expressed as [23, 95]

$$\Theta = 2\pi k_1 \frac{T - T_0}{Q/H} \tag{4-31}$$

where T_0 [°C] is the undisturbed ground temperature.

4.3. Numerical verification

Before discussing the MVQ solution's computational results, numerical verification is necessary to determine whether it provides satisfactory predictions for BHE problems. In the ongoing analysis, all semi-analytical results were computed with MATLAB scripts in which the MVQ solutions were implemented, and the MATLAB *vpaintegral* function was used for evaluating integrals. In a manner similar to many previous studies [64, 111-113], detailed 3-D finite-element (FE) modelling in COMSOL Multiphysics was used for numerical verification.

The verification of the MVQ solution was done under simplified scenarios, i.e., the double-layered ground scenarios, which were similar to previous studies [59, 60]. The layer interface divided the borehole into two equal parts. The upper layer extended from the ground surface to the middle of the borehole, and the lower layer extended from there to infinity. Different thermal conductivity values were assigned to each layer to examine their effect on the varying heat transfer rate in a pure conductive condition. Typical thermal conductivity values of geologic materials usually fall in the range of 1.00 – 4.00 $Wm^{-1}K^{-1}$ [157]. Therefore, values within this range were assigned to the upper and lower layers, respectively. To simplify the discussion, the values for density and specific heat capacity were set the same for each layer. The borehole was designed based on a

BHE project in Edmonton, Canada [97]. Its geometric parameters and thermal properties are listed in Table 4-1.

Table 4-1. Parameter inputs for simulations

Parameter	**Symbol**	**Value**
Grout thermal conductivity	k_g	1.47 $Wm^{-1}K^{-1}$
Grout volumetric heat capacity	$(\rho c)_g$	3.21×10^6 $Jm^{-3}K^{-1}$
Pipe thermal conductivity	k_p	0.38 $Wm^{-1}K^{-1}$
Fluid thermal conductivity	k_f	0.60 $Wm^{-1}K^{-1}$
Fluid volumetric heat capacity	$(\rho c)_f$	4.11×10^6 $Jm^{-3}K^{-1}$
Fluid viscosity	μ	0.00255 $kgm^{-1}s^{-1}$
Average flow rate of working fluid	V	0.00271 m^3s^{-1}
Length of the borehole	H	70 m
Borehole radius	r_b	45.95 mm
Pipe outer radius	r_o	13.35 mm
Pipe wall thickness		2.45 mm
Shank spacing	d	48.00 mm

In the 3-D FE model, a symmetrical boundary condition was applied to reduce the domain size by half. The fluid flow and heat transfer in the pipes were expressed in one dimension with a non-isothermal pipe flow model developed by Lurie [143].

A preliminary analysis was completed to ensure that the simulation results are independent of the model domain and the mesh geometry. The model domain was determined to be large enough such that the far-field temperature at the external boundary would change by less than 0.005 °C within the simulated time. In principle, the temperature at the far boundary is supposed to be kept in an undisturbed condition; the selected 0.005 °C tolerance assures a reasonable domain size and preserves calculation accuracy [94]. To have a more accurate evaluation of temperature around the borehole wall, finer elements (0.01 m) meshed at areas that were close to the borehole, and coarser elements (50 m) meshed at regions that were relatively far away, as shown in Figure 4-6.

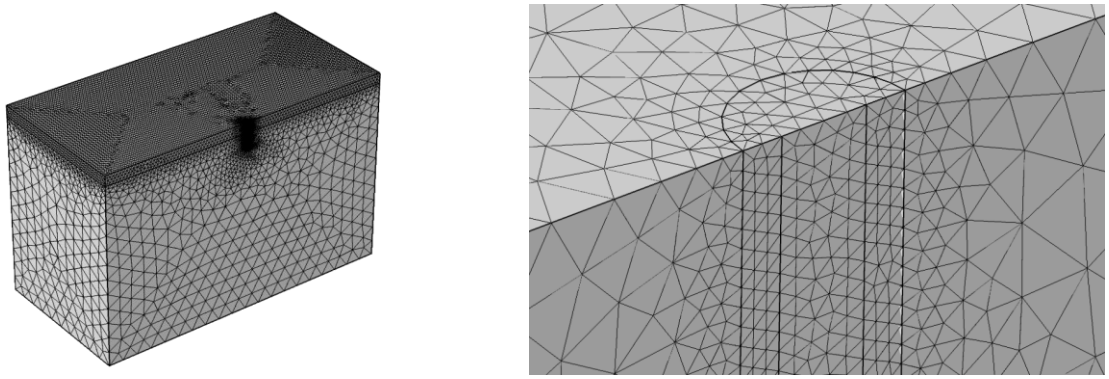

(a) (b)

Figure 4-6. Mesh is used in numerical simulations using free tetrahedral elements: (a) the mesh of the ground and (b) the mesh around the top end of the BHE. Finer elements (0.01 m) meshed at areas that were close to the borehole, and coarser elements (50 m) meshed at regions that were relatively far away.

The initial and boundary conditions were set in such a way that they met the assumptions made for the MVQ solution. A uniform initial ground temperature of 0 °C was assigned to the entire domain to represent an undisturbed ground temperature (T_0). A fixed temperature was also assigned to the top boundary to represent a constant ground surface temperature, which is equal to the undisturbed ground temperature. Because the model domain is large enough, applying either fixed temperature boundary conditions or insulation boundary conditions on the external boundaries gives the same result.

To calculate the discrepancy between the MVQ solution and the numerical results, mean absolute percent error (MAPE) was computed over the given time period. MAPE is a well-known and commonly accepted measure of the accuracy of a prediction and works intuitively in terms of relative error [144]. MAPE is given as

$$MAPE = \frac{100\%}{N}\sum_{i=1}^{N}\left|\frac{\Theta_A(Fo_i) - \Theta_C(Fo_i)}{\Theta_C(Fo_i)}\right| \tag{4-32}$$

where N denotes the sampling times, Θ_A is the MVQ solution, and Θ_C is the COMSOL modelling.

4.4. Method of comparison study and parametric analysis

The MVQ solution was compared with the results of numerical simulations for verification purposes. Meanwhile, a comparison with the constant heat transfer rate solutions was conducted to specify the effect of varying heat transfer rates in the multilayered ground. It is worth noting

that a few multilayer solutions are available in the literature [58-61]. These available solutions were developed using different methods and simplified the BHE in different geometries (see Table 4-2). The solution by Hu [61] and the solution by Abdelaziz et al. [58] were selected in the comparison study, since they adopted the same heat source configuration as this work (line heat source). It is worth noting that the solution by Abdelaziz et al. [58] introduced a simple formula for heat transfer rate in each layer, and the solution were adopted by many other studies [62-65].

Table 4-2. Currently available multilayer solutions

Multilayer solutions	**Heat source configuration**	**Methods**
Solution by Hu [61]	Line	Green's function method
Solution by Abdelaziz et al. [58]	Line	Green's function method
Solution by Zhou et al. [60]	Cylindrical, ring-coil	Separation of variables method, Green's function method
Solution by Pan et al. [59]	Cylindrical	Laplace transform, Hankel transform, Numerical inverse transforms

A feature of the MVQ solution is its ability to deal with the multilayered ground. To demonstrate this feature, the MVQ solution is further examined under different stratification conditions, as listed in Table 4-3. In these scenarios, the double-layered ground is defined by the thermal conductivity ratio (k_1/k_2), the volumetric heat capacity ratio ($(\rho c)_1/(\rho c)_2$), and the dimensionless lower layer thickness (H_2/H). In Scenario 1, the thermal conductivity ratio ranges from 1 to 1/4,

since typical thermal conductivity values of geologic materials usually fall in the range of 1.00-4.00 $Wm^{-1}K^{-1}$ [157]; in Scenario 2, the volumetric heat capacity ratio varies from 1/2 to 2; and in Scenario 3, the thickness of the lower layer changes from 0.1 to 0.9 of the borehole length. To highlight the feature of the multilayered ground, the thermal conductivity ratio is taken as 1/4 in Scenario 3.

Table 4-3. Ground parameters of the three test scenarios

Ground scenarios	k_1/k_2	$(\rho c)_1/(\rho c)_2$	H_2/H
Scenario 1	1, 2/3, 1/2, and 1/4	1	1/2
Scenario 2	1	1/2, 1, 2	1/2
Scenario 3	1/4	1	0.1-0.9

4.5. Results and discussion

4.5.1 Verification

A comparison was conducted between the MVQ solution and the numerical results. All dimensional numerical results were converted into dimensionless forms to show the generality of application to a broad class of situations rather than to just one set of dimensional parameters. As shown in Figure 4-7, the dimensionless temperature change at the borehole wall was plotted against the Fourier number for three thermal conductivity ratios (1/4, 1/2, and 1). Over the simulation period, the MVQ solution presented a good agreement with numerical results. The results were compared in terms of MAPE values. Table 4-4 shows that, for the given parameters of this section, the MAPE yields values of about 2.49%, 1.90%, and 1.60% for three thermal conductivity ratios of 1/4, 1/2, and 1, respectively. The acceptable value for MAPE was decided

for each specific case [118]. Regarding the homogeneous condition ($k_1/k_2 = 1$), Zhang et al. [158] have proposed a model with a varying heat transfer rate profile, which presents the MAPE value of 1.68%. The same study also considers 6% as the allowable threshold limit on the relative error, while the maximum relative error of the model [158] is 3.85%. In the current study, the maximum relative error for the MVQ solution was found to be 4.42% in the homogeneous condition. Since the maximum relative error is lower than the suggested allowable threshold, the MVQ solution is considered to be verified.

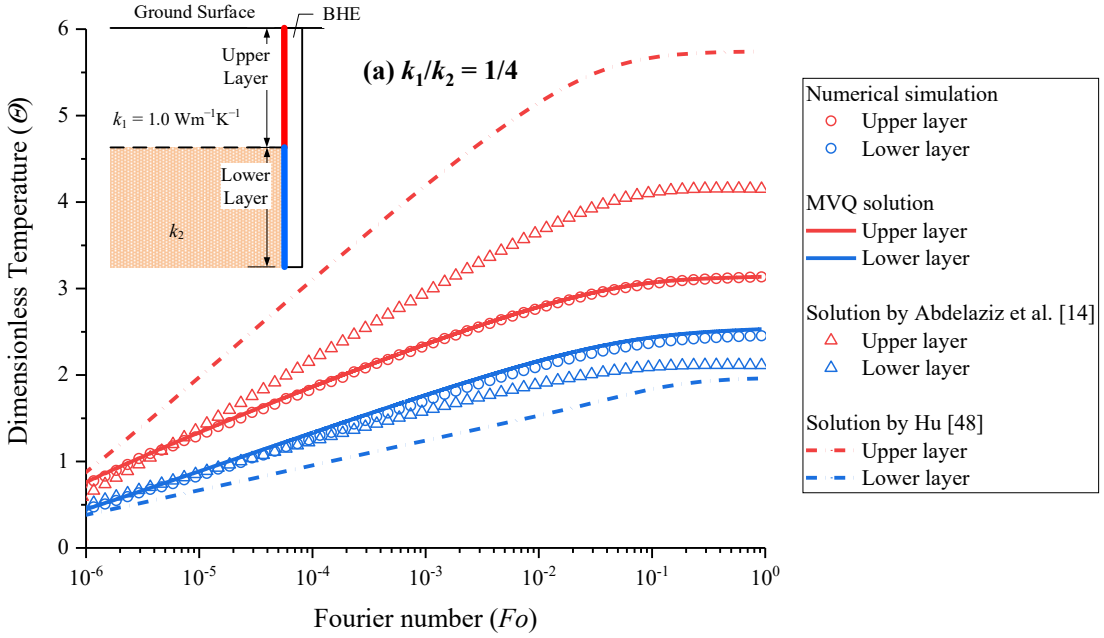

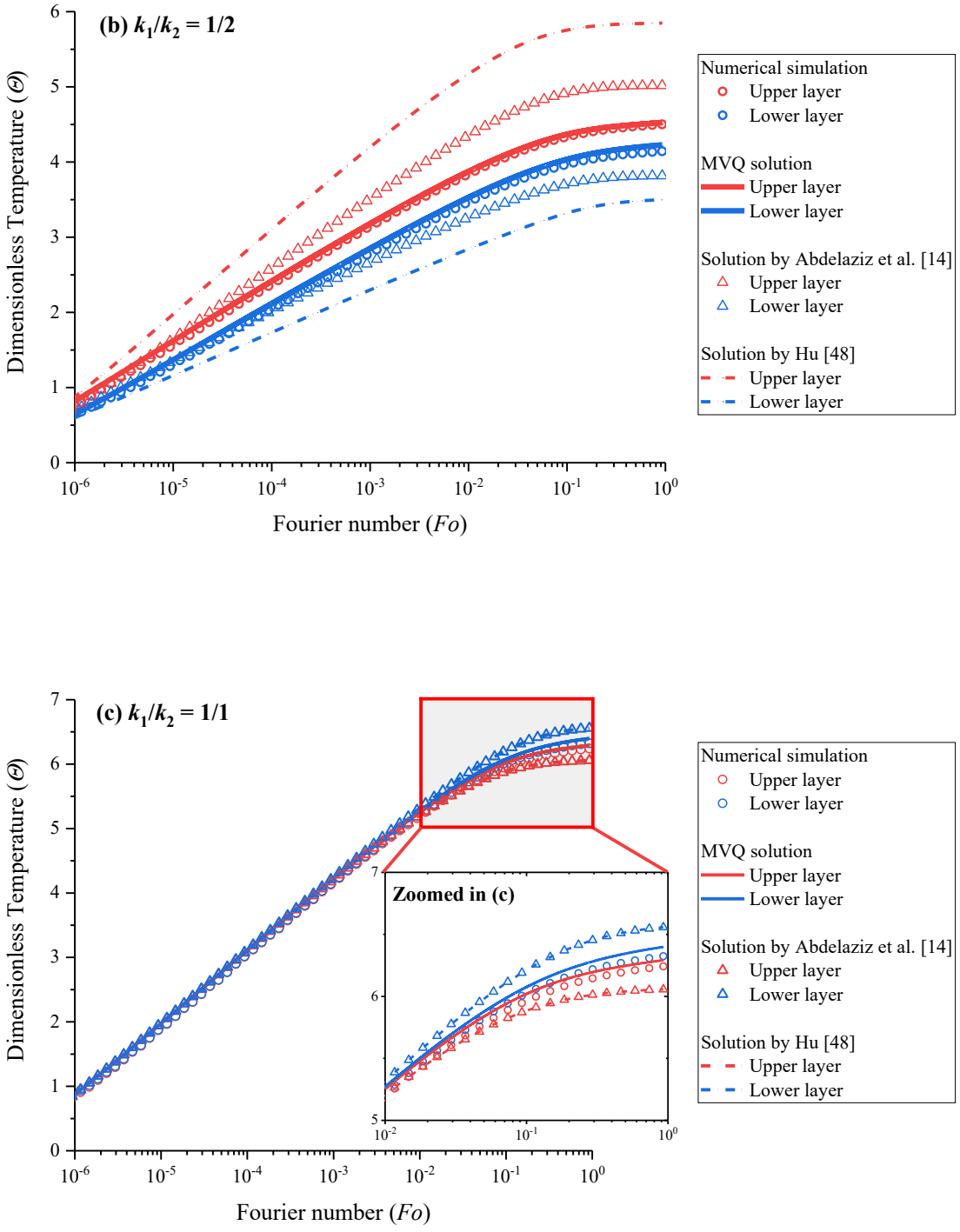

Figure 4-7. The dimensionless temperature change at the borehole wall averaged over the upper layer (red) and lower layer (blue) for three thermal conductivity ratios.

Table 4-4. MAPE between the temperature changes predicted from (semi-)analytical solutions and that simulated from the numerical model.

Thermal conductivity ratio (k_1/k_2)	**1/4**	**1/2**	**1/1**
MVQ solution	2.49%	1.90%	1.60%
Solution by Hu [61]	50.82%	24.05%	2.10%
Solution by Abdelaziz et al. [58]	16.88%	7.93%	2.10%

4.5.2 Comparison with constant heat transfer rate solutions

A comparison with constant heat transfer rate solutions was also conducted to specify the effect of varying heat transfer rates in the multilayered ground. The two multilayer line source solutions [58, 61] was selected for the comparison. Figure 4-7 shows a large discrepancy between the MVQ solution and the constant heat transfer rate solutions. For the thermal conductivity ratio of 1/2, the constant heat transfer rate solutions overestimate the temperature change in the upper layer, and the overestimation gets larger with time. In the end, the dimensionless temperature change in the upper layer was 4.52 when computed by the MVQ solution, and it was 4.50 when given by the numerical simulation. This value is overestimated by 11.45% and 29.93% using the solution by Abdelaziz et al. [58] and the solution by Hu [61], respectively. The overestimation of temperature, caused by constant heat transfer rate solutions, can be more clearly seen in the temperature profiles across the entire depth of the borehole. As shown in Figure 4-8, when Fo = 1, the maximum overprediction of the solution by Hu [61] is about 38.82% which occurred at about z = 25 m. The overestimation could be further increased if the thermal conductivity varies to a larger extent between layers. For the thermal conductivity ratio of 1/4, the overestimation can reach 97.55%

with the solution by Hu [61]. The same phenomenon has been observed by Li et al. [71] in a double-layered (sand and clay) sandbox experiment and simulations. In that study [71], the temperature of the clay was overpredicted by up to 76.6%. As shown in the maximum overestimation occurs near the middle of the top layer. In general, the constant heat transfer rate assumption could significantly reduce the accuracy of the temperature prediction in the multilayered ground, causing improper BHE design.

In comparison with the constant heat transfer rate solutions, the MVQ solution exhibited a better agreement with the numerical results. For example, the constant heat transfer rate solution differed by 50.82% from the numerical results for the thermal conductivity ratio of 1/4, while the MVQ solution differed by 2.49% from the numerical results in the same case (see Table 4-4). Overall, the results show that the MVQ solution has superior accuracy compared to the constant heat transfer rate solutions.

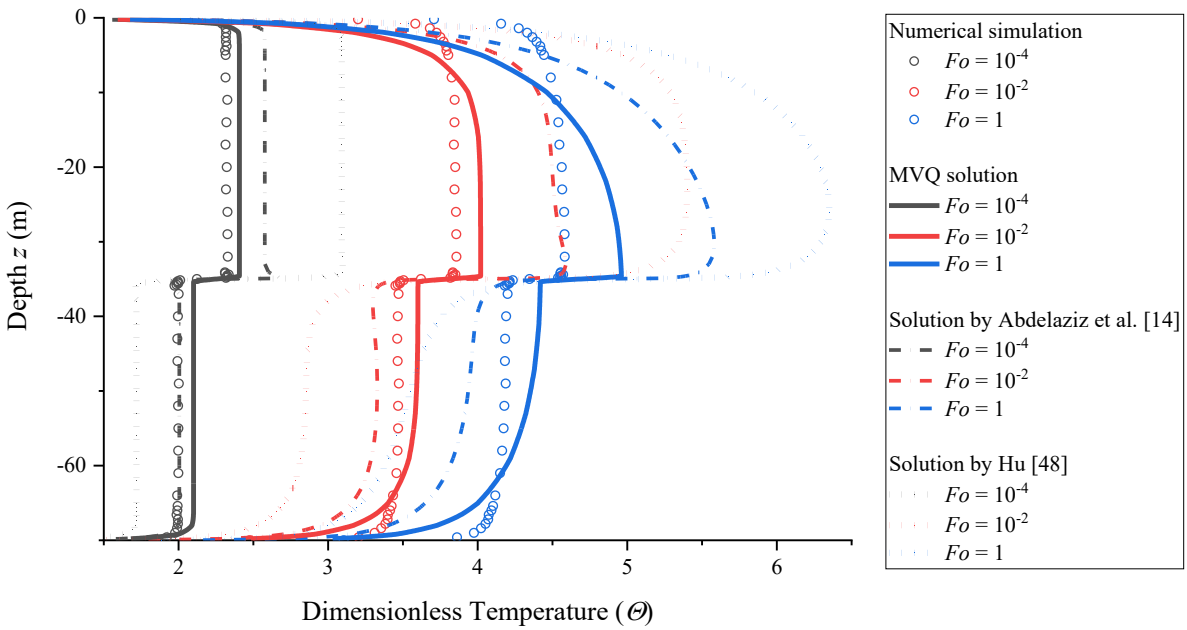

Figure 4-8. The temperature profiles at the borehole wall for conductivity ratio of 1/2 at different times.

4.5.3 Heat transfer rate profiles

Figure 4-9 describes the heat transfer rate profiles along the borehole at different times. Referring to the definition of the thermal response factor [23], a unit heat transfer rate (Q/H = 1 Wm^{-1}) was initially assigned to the borehole. Compared with the linear distribution predicted by the constant heat transfer rate solutions, the heat transfer rate was faster (> 1 Wm^{-1}) in the lower layer for both the MVQ solution and the numerical results. This can be explained using the following relationship [10, 31]: $q_l = \frac{\Delta T}{R_b}$, where ΔT [°C] is the temperature difference between the circulating fluid and the borehole wall, and R_b [mKW^{-1}] denotes the steady-state borehole thermal resistance per unit length. As indicated in the relationship, the heat transfer rate is directly proportional to the temperature difference between the circulating fluid and the borehole wall. In Scenario 1, a higher

thermal conductivity is assigned to the lower layer, thus the heat energy can be dissipated to distant places in the lower layer more rapidly, leading to smaller temperature change over time (blue lines) near the borehole wall as shown in Figure 4-7 (a) and (b). For this reason, the temperature difference between the circulating fluid and the borehole wall is much greater in the lower layer than in the upper layer (see Figure 4-10). Therefore, more heat (> 1 Wm^{-1}) is transferred through the lower layer than through the upper layer. By capturing the varying heat transfer rate, the MVQ solution exhibits its capability of analyzing the BHE problem in the multilayered ground. In the BHE design and simulation, constant heat transfer rate solutions evenly distribute heat along the borehole, yielding an overprediction of the temperature in the ground layers with relatively higher thermal conductivity values. By contrast, the MVQ solution can redistribute heat to the ground layers with relatively higher thermal conductivity values. Thus, it prevents temperature overprediction, avoids the underestimation of the geothermal potential, and provides more thermally efficient designs.

In Figure 4-9, numerical results exhibit an increase in the heat transfer rate near the ends of the borehole. For example, the heat transfer rate rises to 1.29 Wm^{-1} at 0.5 m below the ground surface at Fo = 1, which is much greater than the average value (0.77 Wm^{-1}) in the upper layer. A similar distribution is also found in simulations for a double-layered (sand and clay) sandbox [71] and the homogenous ground [96]. In the double-layered sandbox simulation [71], the heat flux transferred through the borehole wall exceeded 1250 Wm^{-2} near the top end, and dropped to about around 600 Wm^{-2} at the middle of the top layer. Li et al. [71] pointed out that the more heat transferred near the top end is caused by the fixed temperature boundary condition at the ground surface. While the borehole wall temperature increases over time, the ground surface temperature maintains its initial value (0 °C). Hence, the temperature difference is enlarged between the borehole wall and

the ground surface, leading to a higher heat transfer rate near the surface. However, because more complex ground surface conditions in engineering applications may be encountered—such as air convection, evaporation, and surface radiation [76]—the boundary condition at the ground surface should be further studied for the MVQ solution in our future work.

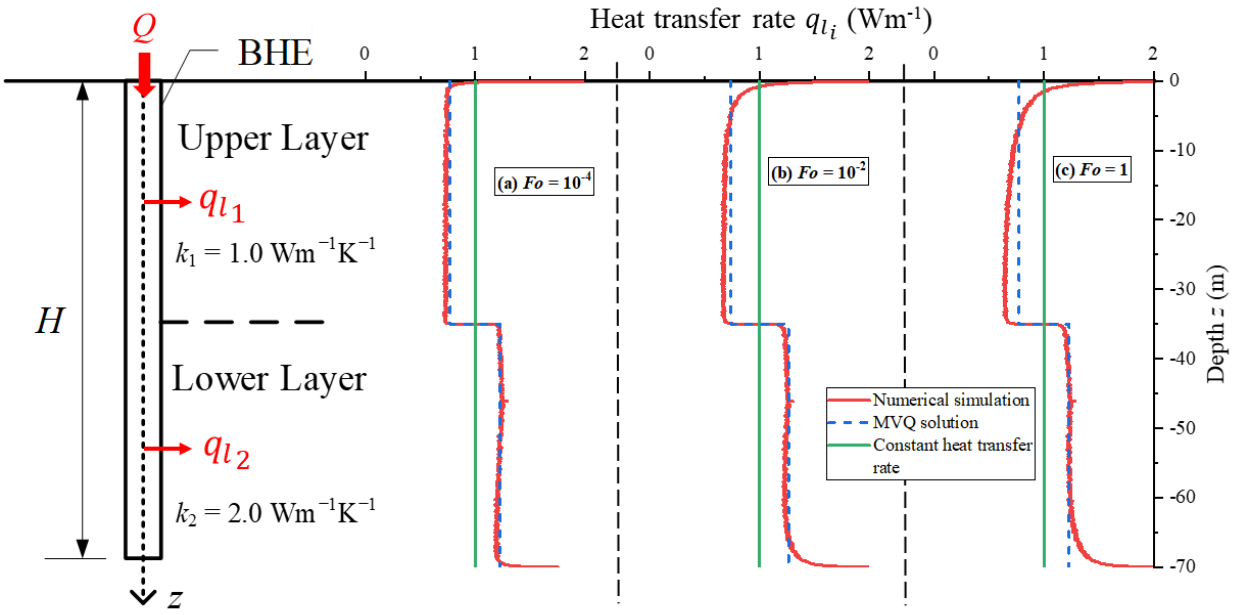

Figure 4-9. The dimensionless heat transfer rate profiles along the borehole at different times.

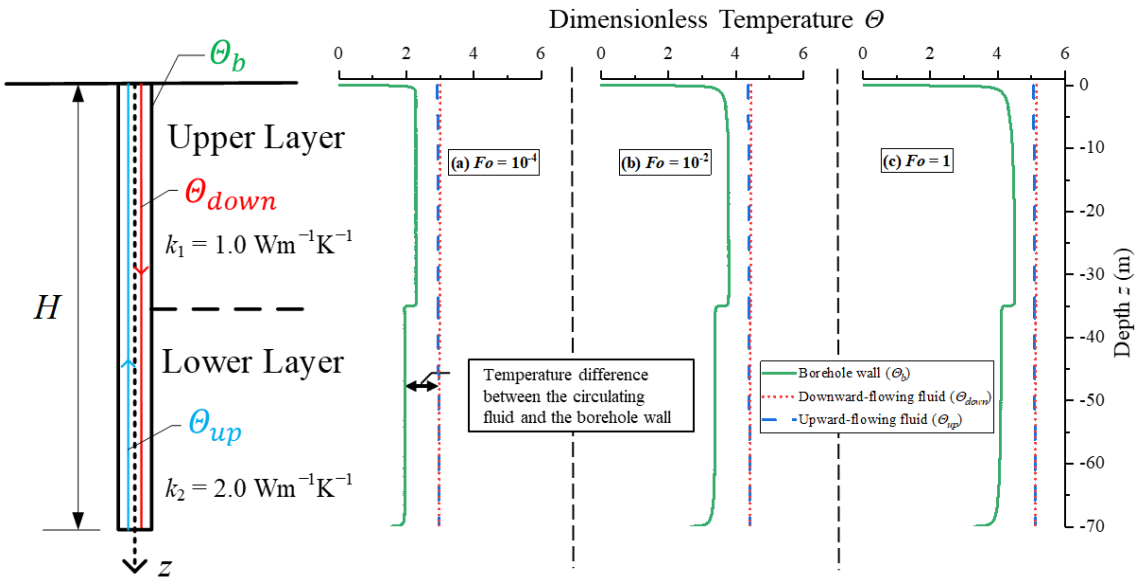

Figure 4-10. The dimensionless temperature profiles for both borehole wall and circulating fluid at different times.

4.5.4 Computational time

Computational time is another important aspect used to compare (semi-)analytical and numerical models. In this work, computational time represents the total amount of time required to execute MATLAB scripts or numerical simulations. All calculations were performed on an Intel Xeon-E3 3.10 GHz processor with 64 GB RAM.

To obtain the data for Figure 4-7, the computational time for each method is listed in Table 4-5. Compared with the solution by Abdelaziz et al. [58], the simulation of the MVQ solution took 1,394 s (23.23 minutes) of computing time, which is almost triple the time of computing. This is due to the fact that the MVQ is time-dependent, and therefore, smaller time intervals were selected to approximate the time-varying heat transfer rate. Although the MVQ solution took more time, it offered more accurate temperature predictions. For example, the MAPE values for the MVQ solution and the solution by Abdelaziz et al. [58] are 2.49% and 53.41%, respectively, when the

thermal conductivity ratio is 1/4. In addition, compared with numerical simulations, the MVQ solution is more computationally efficient from the viewpoint of time usage. The numerical simulation consumed 54,410 s, whereas the MVQ solution used 1,394 s, which is a thirty-nine-fold reduction in computational time. The computational time determines the productivity of a given method since models are executed repeatedly for sizing, optimizing, and simulating the BHE system. In engineering applications, rapid computation is a major reason that analytical solutions are generally favoured over numerical models [43]. Several well-known design tools for BHEs have been developed based on analytical solutions, including GchpCalc [159], Ground Loop Design [25] and GeoStar [160]. Meanwhile, analytical solutions are widely used in optimizing BHE fields and energy extraction [93, 161, 162]. The superior computational time and acceptable accuracy gives the MVQ solution great potential for BHE design.

Table 4-5. Comparison of the computational time for the analytical and numerical solutions.

Solutions	**Computational time (s)**
MVQ solution	1,394
Solution by Abdelaziz et al. [58]	564
Numerical simulations	54,410

4.6. Heat transfer in double-layered ground

4.6.1 Impact of thermal conductivity ratio and volumetric heat capacity ratio

In engineering applications, the multilayered ground exhibits the inhomogeneity of thermal properties (including thermal conductivity and volumetric heat capacity). However, in the

literature, the impact of inhomogeneity on the heat transfer rate profile has been examined only under a single set of ground parameters [71]. The relationship between thermal properties and the non-linear heat transfer rate has not been investigated. To reveal the relationship, the MVQ solution was examined under different stratification scenarios defined by the thermal conductivity ratio (k_1/k_2) and the volumetric heat capacity ratio ($(\rho c)_1/(\rho c)_2$).

In Scenario 1, the thermal conductivity ratio ranges from 1 to 1/4, since typical thermal conductivity values of geologic materials usually fall in the range of 1.00 – 4.00 $Wm^{-1}K^{-1}$ [157]. For these thermal conductivity ratios, the dimensionless heat transfer rate at the borehole wall is plotted against the Fourier number (see Figure 4-11). The dimensionless heat transfer rate is defined as q_{l_1}/q_{l_2}. Excluding the homogenous condition ($k_1/k_2 = 1$), the ratio of heat transfer rates is less than 1 over the simulation period in all other three cases, which means that more heat is transferred through the lower layer than through the upper layer. As previously discussed, this is due to the higher thermal conductivity of the lower layer. At the end of the simulation, the ratio of heat transfer rates dropped from 0.81 to 0.63 and 0.36, respectively, as the thermal conductivity ratio varied from 2/3 to 1/2 and 1/4. One can conclude that the heat transfer rate variation between ground layers was intensified as the thermal conductivities between ground layers varied to a greater extent.

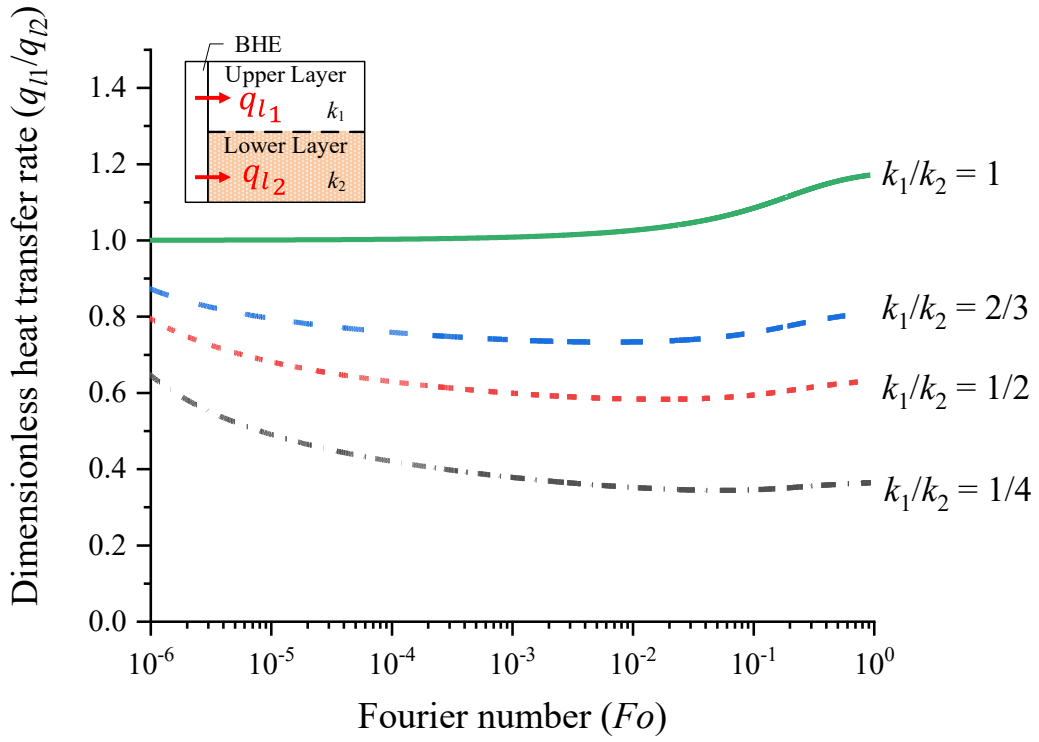

Figure 4-11. The dimensionless heat transfer rate at the borehole wall in the double-layered ground for the thermal conductivity ratios of 1, 2/3, 1/2, and 1/4.

Figure 4-12 shows the dimensionless heat transfer rate at the borehole wall against the Fourier number for various volumetric heat capacity ratios in Scenario 2. For the volumetric heat capacity ratios of 1/2 and 2, the volumetric thermal capacities of the upper and lower layers are opposite, while the thermal conductivities of the two layers are the same. In the long-term ($Fo > 10^{-2}$), the ratio of heat transfer rates is greater than 1 and increases with time in all three cases. In other words, more heat is transferred through the upper layer than through the lower layer. As previously discussed, this is caused by the fixed temperature boundary condition at the ground surface. For the MVQ solution, the long-term ground surface boundary condition should be further improved in our future work. For $Fo < 10^{-2}$, the layer absorbs more heat near the borehole with a higher value

of the volumetric heat capacity, but the difference in the heat transfer rate between the two layers slowly diminishes as *Fo* increases. Taking $(\rho c)_1/(\rho c)_2 = 2$ for example, the ratio of heat transfer rates is around 1.09 at $Fo = 10^{-4}$, which means that the upper layer absorbs more heat than the lower layer by about 9%. After that, the percentage difference reduces to 6.84% at $Fo = 10^{-2}$. This phenomenon can be explained by the volumetric heat capacity. The volumetric heat capacity of a material is associated with the amount of heat desired to cause an increase in the material's temperature. With a larger value of the volumetric heat capacity, the upper layer requires more heat to raise its temperature, leading to a smaller temperature change over time near the borehole wall. This coincides with the results reported by Luo et al. [65]. Luo et al. [65] simulated a coaxial borehole heat exchanger in a double-layered scenario, using the same thermal conductivity ratio and volumetric heat capacity ratio as Scenario 2. For $(\rho c)_1/(\rho c)_2 = 2$, the simulated dimensionless borehole wall temperature was about 0.37 near the middle of the upper layer while it was about 0.43 near the middle of the lower layer [65]. Consequently, more heat was transferred through the upper layer due to the greater temperature difference between the circulating fluid and borehole wall in that layer. Afterwards, as the area near the borehole gradually reached a quasi-steady state, the impact of the volumetric heat capacity diminished.

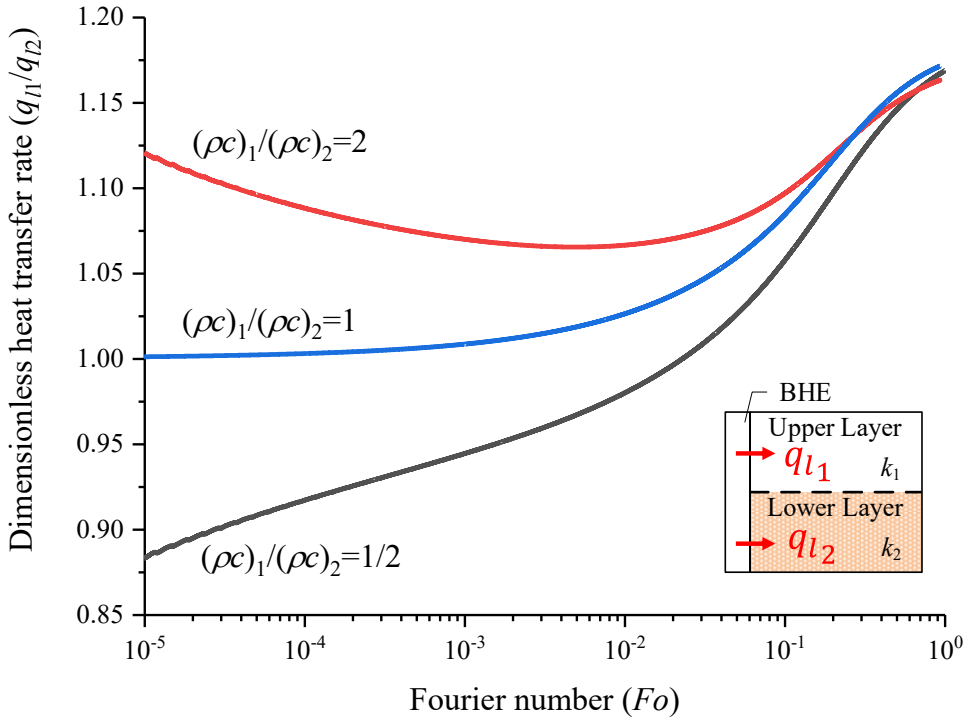

Figure 4-12. The dimensionless heat transfer rate at the borehole wall in the double-layered ground for the volumetric heat capacity ratios of 1/2, 1, and 2.

As the above parametric studies depicted, the inhomogeneity of both thermal conductivity and volumetric heat capacity has a vital effect on the variation of the heat transfer rate. The ground layers with higher values of thermal conductivity and volumetric heat capacity express the slowness of transferring heat near the borehole wall. In engineering applications, boreholes may encounter a variety of sediments and rocks with various thermal properties [56]. By employing the MVQ solution, the heat transfer rate in each layer can be accurately addressed under different ground scenarios, which helps keep drilling and operating costs at a minimum.

4.6.2 Effect of thickness

Besides the thermal properties, the thickness fraction of each layer (H_i/H) is another important parameter for the analysis of the heat distribution in the double-layered ground. The thickness of each ground layer may differ greatly from the layers above or below it. For example, an installation in Nuremberg (Germany) [70] showed that the borehole penetrated five major geological layers, and their thickness varied from 4 m to 30 m. To illustrate the effect of thickness, this study investigated the heat load in each layer under different thickness ratios between the lower layer and the borehole length.

In Figure 4-13, the dimensionless heat load of the lower layer (Q_2) is plotted against the thickness fraction of the lower layer (H_2/H) for Fo = 1. To highlight the inhomogeneity of the multilayered ground, the thermal conductivity ratio is kept at 1/4. If employing a constant heat flow rate per unit length, the heat load of each layer should be proportional to its thickness. However, this relationship becomes non-linear when the varying heat flow rate is considered. For example, 30% of the BHE in the lower layer provides more than half of the total heat load (57.04%), and this value rises to 73.28% when half of the BHE length is installed in the lower layer. This tendency has not been discussed in previous studies [58-60, 71], since the assumption is often made that the two layers have the same thickness. In general, the influence of the thickness fraction of each layer is significant to the BHE system's thermal performance, especially when the thermal properties of the ground layers have obvious differences. Thus, is it important for the designer to have a good understanding of the composition, thickness, and thermal properties of the geological materials for the BHE installation. In relation to the geotechnical information, the MVQ can accurately distribute heat to each ground layer, leading to thermally efficient designs.

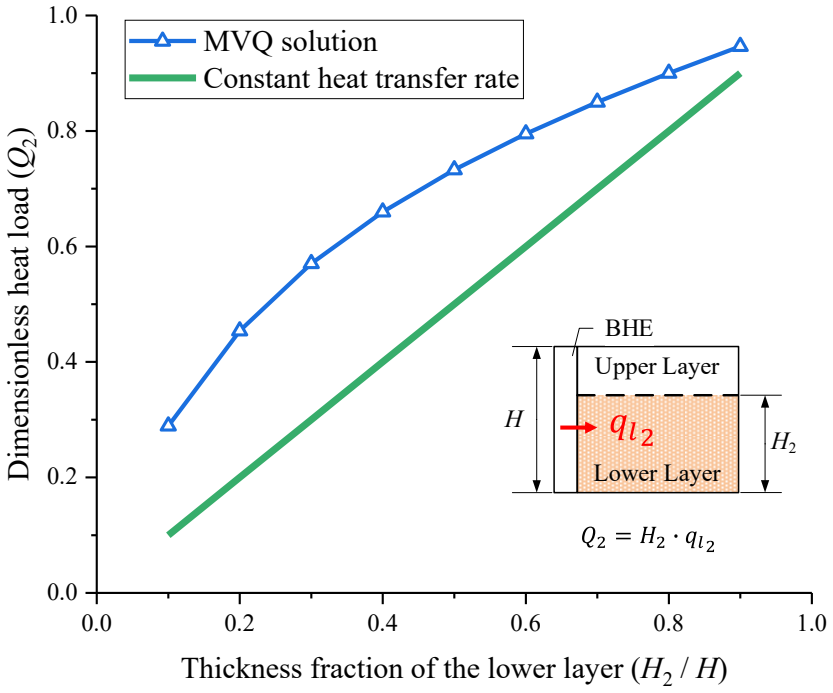

Figure 4-13. The heat load in the lower layer of a double-layered ground for the thermal conductivity ratio of 1/4 and Fo = 1.

4.7. Conclusion

An innovative solution was proposed in this study for vertical BHEs in multilayered ground. The new solution was named the "MVQ solution"—Multilayered ground with Varying heat transfer rates (Q). The main novelty of the MVQ solution is that it has the capacity to analyze the heat transfer both outside and inside the borehole simultaneously. Therefore, the MVQ solution can address varying heat transfer rates along the borehole length in multilayered ground. The MVQ solution also features superior computational time and accuracy, which can improve the design expressions for vertical BHEs and ultimately provide more thermally efficient designs of BHE systems in geothermal applications. The following conclusions were drawn from the study:

(1) The MVQ solution was compared with a 3-D FE model constructed with COMSOL Multiphysics for verification purposes. The mean absolute percent error between the MVQ solution and the numerical results was less than 2.50%, which is acceptable in engineering applications. The MVQ solution was thus verified numerically. Moreover, the MVQ solution provides a significant reduction of computational time; compared with numerical simulations, the MVQ solution can cut computational time by a factor of 39 times. Because of its superior computational time and accuracy, the MVQ solution has great potential in the design of vertical BHEs.

(2) The MVQ solution addresses the heat flux variation along the borehole length in multilayered ground. Conventional solutions prescribe a constant heat transfer rate along the borehole length, and thus overestimate the temperature of the ground layer with a relatively lower thermal conductivity value. For the given parameters in the double-layered scenario, the constant heat transfer rate assumption results in an overprediction of up to 97.55%. By addressing the heat transfer rate variation, the MVQ solution can accurately predict the ground temperature change, leading to a refined design of the BHE system.

(3) The heat flow rate in the multilayered ground is impacted by both the thermal conductivity ratio (k_1/k_2) and volumetric heat capacity ratio ($(\rho c)_1/(\rho c)_2$). The inhomogeneity of the volumetric heat capacity ratio has an impact on the heat transfer rate variation between layers in an early period (i.e., Fo smaller than 10^{-2}), and its impact gradually diminishes. In contrast, the inhomogeneity of thermal conductivity strengthens the heat transfer rate variation with time in most cases. The heat transfer rate variation also intensifies under larger thermal conductivity ratios (i.e., 1/4). For the given parameters in this study, the

lower layer extracted the heat about three times as quickly as the upper layer when the thermal conductivity ratio was 1/4.

(4) The MVQ solution redistributes the heat along the borehole length in the multilayered ground. This significantly affects the thermal performance of BHEs in each layer. For the given parameters in this study, 57.04% of the thermal energy was shown to be provided by 30% of the BHE length installed in more conductive ground layers. Thus, the MVQ solution is indispensable for thermal performance predictions of BHEs in the multilayered ground. The MVQ solution is an effective and accurate design tool for vertical BHEs.

Appendix 4-B. Green's functions used in the study

In this study, a set of exact Green's functions was used to solve the heat conduction problem. Transient Green's functions $G(r, z, t \mid r', z', \tau)$ give the fundamental solution of the partial differential equation (Equation (4-1)) at a given observation location (r, z) to an impulsive heat source released at time τ, located at (r', z'). Green's functions can be found in many different textbooks [31, 129, 135].

The bottommost layer, considered as a semi-infinite body heated by a heat flux at $z = 0$ with a heat source at (r', z'), can be described by [135]

$$G_{Z20}(r, z, t \mid r', z', \tau) = \frac{1}{8(\pi\alpha(t-\tau))^{\frac{3}{2}}} I_0\left(\frac{rr'}{2\alpha(t-\tau)}\right) \cdot \left[exp\left(-\frac{r^2 + r'^2 + (z-z')^2}{4\alpha(t-\tau)}\right) + exp\left(-\frac{r^2 + r'^2 + (z+z')^2}{4\alpha(t-\tau)}\right)\right] \quad \text{(B-1)}$$

where $I_0(X)$ is a modified zero-order Bessel function of the first kind.

When the source is located at the centreline of the body at $r' = 0$, the solution is reduced to

$$G_{Z20}(r, z, t \mid r', z', \tau) = \frac{1}{8(\pi\alpha(t-\tau))^{\frac{3}{2}}}\left[exp\left(-\frac{r^2 + (z-z')^2}{4\alpha(t-\tau)}\right) + exp\left(-\frac{r^2 + (z+z')^2}{4\alpha(t-\tau)}\right)\right] \quad \text{(B-2)}$$

The integral over z' from 0 to H is

$$\int_{z'=0}^{H} G_{Z20}(r,z,t\,|\,0,z',\tau)dz' = \frac{1}{8\pi\alpha(t-\tau)} exp\left(-\frac{r^2}{4\alpha(t-\tau)}\right)\left[\text{erf}\left(\frac{H-z}{\sqrt{4\alpha(t-\tau)}}\right) + \text{erf}\left(\frac{H+z}{\sqrt{4\alpha(t-\tau)}}\right)\right] \tag{B-3}$$

At the interface $z = 0$, the body subjected a heat flux $r_j < r' < r_{j+1}$. However, the form of Equation (B-1) is difficult for subsequent integration over r'. An alternative form of G_{Z20} is [135]

$$\begin{aligned} G_{Z20}(r,z,t\,|\,r',z',\tau) = {} & \frac{1}{4\pi^{\frac{3}{2}}(\alpha(t-\tau))^{\frac{1}{2}}}\left[exp\left(-\frac{(z-z')^2}{4\alpha(t-\tau)}\right) + exp\left(-\frac{(z+z')^2}{4\alpha(t-\tau)}\right)\right] \\ & \cdot \int_{\beta=0}^{\infty} exp(-\alpha(t-\tau)\beta^2)\beta J_0(\beta r)J_0(\beta r')d\beta \end{aligned} \tag{B-4}$$

using the integral [129]

$$\int_{\beta=0}^{\infty} exp(-\alpha(t-\tau)\beta^2)\beta J_0(\beta r)J_0(\beta r')d\beta = \frac{1}{2\alpha(t-\tau)} exp\left(-\frac{r^2+r'^2}{4\alpha(t-\tau)}\right) I_0\left(\frac{rr'}{2\alpha(t-\tau)}\right), \tag{B-5}$$

where $J_0(X)$ is a zero-order Bessel function of the first kind.

The form of Equation (B-4) can be integrated separately over r', since the integral on r' acts only on the term $J_0(\beta r')$,

$$\int_{r\prime=r_p}^{r_{p+1}} J_0(\beta r')2\pi r' dr' = \frac{2\pi\left[r_{p+1}J_1\left(r_{p+1}\beta\right) - r_p J_1\left(r_p\beta\right)\right]}{\beta} \tag{B-6}$$

where $J_1(X)$ is a first-order Bessel function of the first kind.

The topmost layer, subjected to a heat flux at $z = H$ with a fixed temperature at the $z = 0$ and a heat source at (0, z'), can be described by [135]

$$\begin{aligned} G_{Z12}(r,z,t\,|\,0,z',\tau) = {} & \frac{1}{8\left(\pi\alpha(t-\tau)\right)^{\frac{3}{2}}} \\ & \cdot \sum_{n=-\infty}^{\infty} (-1)^n \left[exp\left(-\frac{r^2+(2nH+z-z')^2}{4\alpha(t-\tau)}\right) - exp\left(-\frac{r^2+(2nH+z+z')^2}{4\alpha(t-\tau)}\right)\right] \end{aligned} \tag{B-7}$$

The integral over z' from 0 to H is

$$\begin{aligned} & \int_{z\prime=0}^{H} G_{Z12}(r,z,t\,|\,0,z',\tau)dz' \\ & = \frac{1}{8\pi\alpha(t-\tau)} exp\left(-\frac{r^2}{4\alpha(t-\tau)}\right) \\ & \cdot \sum_{n=-\infty}^{\infty} (-1)^n \left[2\mathrm{erf}\left(\frac{2nH+z}{\sqrt{4\alpha(t-\tau)}}\right) - \mathrm{erf}\left(\frac{(2n-1)H+z}{\sqrt{4\alpha(t-\tau)}}\right) - \mathrm{erf}\left(\frac{(2n+1)H+z}{\sqrt{4\alpha(t-\tau)}}\right)\right] \end{aligned} \tag{B-8}$$

The intermediate layers, heated by heat fluxes at $z = 0$ and H with a heat source at (0, z'), can be described by [135]

$$G_{Z22}(r,z,t\,|\,r',z',\tau)=\frac{1}{8\left(\pi\alpha(t-\tau)\right)^{\frac{3}{2}}}\sum_{n=-\infty}^{\infty}\left[exp\left(-\frac{r^2+(2nH+z-z')^2}{4\alpha(t-\tau)}\right)-exp\left(-\frac{r^2+(2nH+z+z')^2}{4\alpha(t-\tau)}\right)\right] \quad \text{(B-9)}$$

The integral over z' from 0 to H is

$$\int_{z'=0}^{H}G_{Z22}(r,z,t\,|\,0,z',\tau)dz'=\frac{1}{8\pi\alpha(t-\tau)}exp\left(-\frac{r^2}{4\alpha(t-\tau)}\right)\sum_{n=-\infty}^{\infty}\left[\text{erf}\left(\frac{(2n+1)H+z}{\sqrt{4\alpha(t-\tau)}}\right)-\text{erf}\left(\frac{(2n-1)H+z}{\sqrt{4\alpha(t-\tau)}}\right)\right] \quad \text{(B-10)}$$

The alternative forms of G_{Z12} and G_{Z22} are found by substituting Equation (B-5) into Equations (B-7) and (B-9), respectively.

Chapter 5. A new semi-analytical solution for U-shaped vertical borehole heat exchangers in multilayered ground with third-type boundary condition

This chapter has been submitted for peer review as **Guo, Y.**, Zhao, J., & Liu, W. V. A new semi-analytical solution for U-shaped vertical borehole heat exchangers in multilayered ground with third-type boundary condition. *International Journal of Thermal Sciences*. Unpublished © Elsevier. (under review)

Nomenclature

A	albedo	
c	specific heat capacity	[$Jkg^{-1}K^{-1}$]
d	shank spacing	[m]
D	depth	[m]
Fo	Fourier number	
g	rate of energy generation	[Wm^{-3}]
G	Green's function	
h	overall heat transfer coefficient	[$Wm^{-2}K^{-1}$]
H	borehole length	[m]
H_1, H_2	two ends of borehole	[m]
k	thermal conductivity	[$Wm^{-1}K^{-1}$]
L	ground layer thickness	[m]
q_l	heat transfer rate	[Wm^{-1}]
q_v	vertical heat flux	[Wm^{-2}]
Δq	incremental heat flux	
Q	heat load	[W]
r, r'	radial coordinate	[m]
R_1^{Δ}, R_2^{Δ}, R_{12}^{Δ}	delta-circuit thermal resistance	[mKW^{-1}]
S	incident solar radiation	[Wm^{-2}]
t	time	[s]
T	temperature	[°C]
T_0	undisturbed ground temperature	[°C]
ΔT	temperature variation	[°C]
V	circulating fluid flow rate	[m^3s^{-1}]
z, z'	axial coordinate	[m]
α	thermal diffusivity	[m^2s^{-1}]
β_1, β_2, β_{12}	dimensionless thermal conductance	
$\varepsilon \Delta R$	net long-wave radiation	[Wm^{-2}]
Θ	dimensionless temperature	
λE	latent heat flux	[Wm^{-2}]
ρ	density	[kgm^{-3}]

ψ influence function

Subscripts

amb ambient air

b borehole

down downward-flowing fluid

E contribution of heat generation

g grout

i = 1, 2, … *I* - 1 ground layer

I bottommost layer

j = 1, 2, … *J* line source segment

m, n = 1, 2, … *N* surface element

p = 1, 2, … *P* time step

up upward-flowing fluid

U contribution of upper surface boundary

V contribution of lower surface boundary

w water

r, z directions

5.1. Introduction

To avert the worst impacts of climate change, an expanding alliance of countries pledged a goal of achieving net-zero emissions by 2050 [120]. A significant aspect in attaining this goal is addressing the contribution of heat consumption to global CO_2 emissions, which accounts for more than 40% (13.1 Gt) of energy-related CO_2 emissions in 2020 [163]. A measure to reduce the carbon footprint associated with heating is the global transition from fossil-based systems to renewable heat technologies (such as bioenergy, solar thermal, and heat pumps) [164]. Among these viable options, heat pumps have been recognized as the "central technology" by International Energy Agency (IEA) for fuel-shifting and heat decarbonization [165].

Heat pumps harness the heat from surroundings sources such as air and ground, and then amplify the heat to provide heating. These systems can also be reversed for cooling purposes. In comparison with the air source systems, ground source systems offer significant benefits, including over 30% reduction in energy consumption [121] and a decrease in carbon footprint by 20%-22% [122]. In ground source heat pump (GSHP) systems, the vertical borehole heat exchanger (BHE) is commonly employed to collect heat from the ground and convey it to the heat pump. Drilled boreholes typically reach depths between 15 m and 120 m, passing through various geologic layers with different thermal properties [54-56]. For instance, as outlined in a geoscience information report for investigating GSHP application at the Hastings Lake Community Hall site in Alberta, Canada, thermal conductivities of sediments and rocks were tested within a range of 0.62 to 3.22 $Wm^{-1}K^{-1}$ [56].

As for the thermal behavior of a BHE in the multilayered ground, several analytical and semi-analytical solutions [58-61, 72] have been proposed over the last decade. Abdelaziz et al. [58]

approached the problem by employing the principle of superposition. In this approach, a BHE was partitioned into distinct line heat source segments, corresponding to boundaries of underlying ground layers. By aggregating the contributions of these segments, the temperature change at an observation point within the ground was evaluated. For analysis simplification, the region between each line heat source segment and the observation point was treated as a homogeneous body with effective thermal and physical properties. It is worth noting that this assumption of homogeneity has also been adopted by many other studies [62-65] to account for the multilayered ground conditions. Unlike assuming homogeneity, Pan et al. [59] used the integral-transformation method and proposed a cylindrical source solution describing the thermal behaviour of the BHE within multiple ground layers. Additionally, Zhou et al. [60] used Green's function method and derived solutions for two ground layers, and the same research group currently extended the capabilities of these solutions to accommodate more layers [66]. In our previous study [72], we presented a semi-analytical model to analyze the BHE in multilayered ground. The model takes into consideration the non-uniform heat transfer rate along the length of the borehole, incorporating a two-way coupling of the heat transfer occurring inside and outside the borehole. These solutions [58-61, 72] were derived by solving the transient heat conduction problem with a boundary condition at the ground surface.

In the modelling of BHEs, the proper treatment of the ground surface boundary is essential for assessing the thermal performance of the system. Most analytical solutions [27-29, 35, 58-61, 68, 72] implemented a homogenous boundary condition of the first-type (or Dirichlet) at the ground surface, where the ground surface temperature remains unchanged at its initial temperature. This homogenous boundary condition is mathematically simple but unrealistic in practice since the ground surface temperature varies over time. The seasonal and daily temperature oscillations at

the ground surface (i.e., the non-homogenous boundary condition) can be accounted for by utilizing the superposition principle, as shown in the study by Bandos et al. [26]. The significance of time-independent ground surface temperature has been highlighted by Bidarmaghz et al. [73]. Specifically, the results indicated that the length could be reduced by approximately 11% and 6% for borehole lengths of 30 m and 50 m due to the temperature fluctuations at the ground surface. However, it might be difficult to implement this time-dependent temperature as the boundary condition in practice, as ground surface temperature measurements are often limited in availability. For example, despite having over 350 weather stations across Alberta, Canada, providing comprehensive meteorological data, less than 10% of them actively monitor ground surface temperatures [166]. As an alternative to relying on ground surface temperature, a third-type (or Robin) boundary condition, which considers the energy balance at the ground surface, has gained more attention in GSHP modelling in recent years [74-78]. The surface energy balance involves balancing net radiation, the fluxes of sensible and latent heat, and the heat flux from or to the subsurface [79, 80]. This approach requires meteorological data, including ambient air temperature, wind speed, and incoming solar radiation. Such meteorological data is typically more accessible and better-monitored than ground surface temperature measurements. It is noteworthy that Oosterkamp et al. [167] conducted a comprehensive investigation into eight different ground surface boundary conditions and their impact on predicting the thermal regime in the ground. The findings revealed that employing the measured ground surface temperature and the surface energy balance equation as the ground surface boundary condition leads to highly accurate predictions of the soil temperature.

Until recently, while a few analytical solutions [50-53, 82] for BHEs have incorporated the third-type boundary condition at the ground surface, these have been limited to homogeneous ground

conditions. Meanwhile, analytical solutions [58-61, 72] for a BHE in multilayered ground have typically been constrained to a homogeneous Dirichlet boundary condition at the ground surface. Remarkably, there has been no prior (semi-)analytical solution for BHEs considering the ground surface condition in a multilayered ground, creating a significant research gap in predicting ground temperatures and designing GSHP systems. This study fills this research gap by extending the previously proposed MVQ solution that is described in our previous study [72]. Here, the MVQ is an acronym for multilayered ground with varying heat transfer rates. Through this study, we aim to enhance the understanding of the ground surface conditions in BHE simulations and provide improved approximations of their long-term behaviour. The findings of this study will serve as valuable references for researchers and practitioners involved in the design and implementation of BHE systems.

5.2. Model development

5.2.1 Problem description

The heat transfer problem of a BHE installed in the multilayered ground is illustrated in Figure 5-1. The thermal analysis of this problem can be approached by decomposing the problem into two distinct regions: the interior region within the borehole and the exterior region outside the borehole [10, 28, 86]. These two regions are then recoupled at the interface of the borehole wall. For simplification, several assumptions have been made, which are aligned with the study conducted by Eskilson [23]:

a. Within the borehole, the average surface temperature is used for the borehole wall. This approximation relaxes the stringent requirement of temperature continuity and heat flux continuity at the interface between the borehole and the surrounding ground. It has gained

wide acceptance in both analytical analysis [23, 128, 153] and design [95] of shallow BHEs.

b. Outside the borehole, the borehole is simplified as a line heat source. This simplification is employed due to the large aspect ratio of typical BHEs, which depths ranging from 15 to 120 m and diameters ranging from 0.1 to 0.15 m.

c. The ground has a uniform initial temperature, T_0, which aligns with existing analytical solutions [10, 27, 28]. Although the non-uniform initial temperature caused by the thermal gradient can be considered using the superposition principle, as shown in the study by Bandos et al. [26], for the sake of simplicity, the current study assumes a uniform initial temperature.

d. The thermal properties are independent of temperature. This assumption was made because the range of temperature concerned in the shallow BHE problem is relatively small, and the variation in thermal properties within this temperature range can be negligible [23].

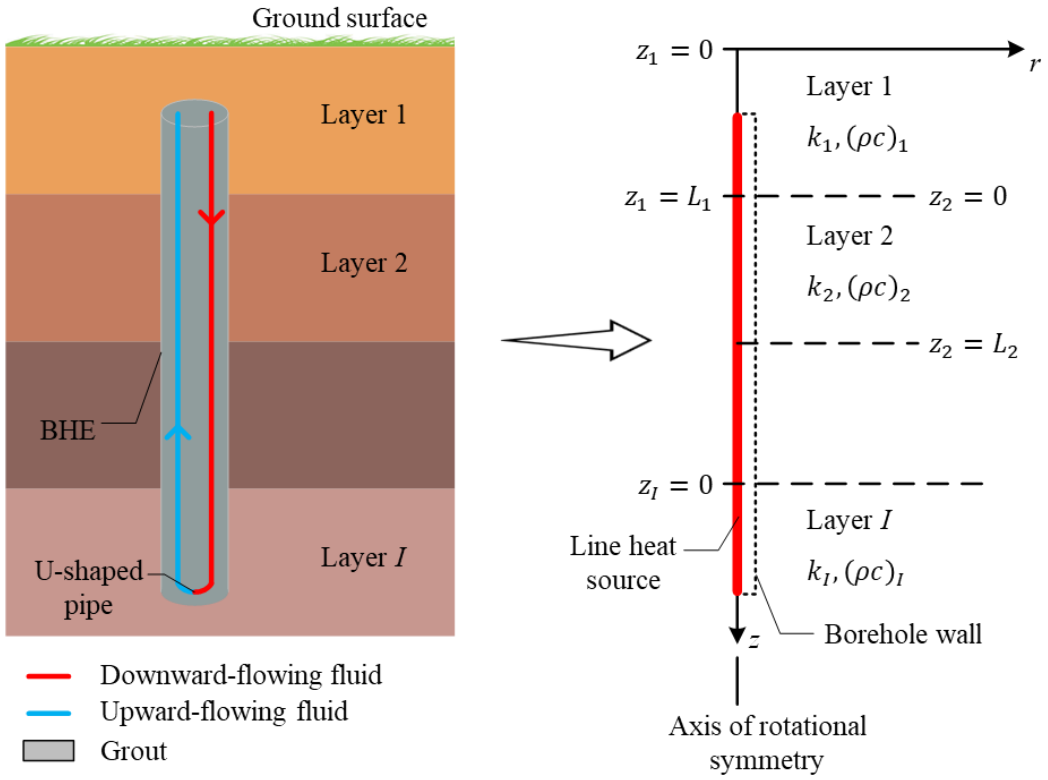

Figure 5-1. Schematic of a U-shaped BHE drilled into the ground passing through multiple ground layers.

In the exterior region, the governing equation of heat conduction in the cylindrical coordinate system (r, z) can be represented by the following governing equation [31]

$$\rho c \frac{\partial T}{\partial t} = \frac{1}{r}\frac{\partial}{\partial r}\left(kr\frac{\partial T}{\partial r}\right) + \frac{\partial}{\partial z}\left(k\frac{\partial T}{\partial z}\right) + g(r,z,t) \tag{5-1}$$

where ρc [$Jm^{-3}K^{-1}$] is the volumetric heat capacity, k [$Wm^{-1}K^{-1}$] is the ground thermal conductivity, T [°C] is the temperature, and $g(r,z,t)$ [Wm^{-3}] is the rate of energy generation per unit volume.

The ground, bounded by the ground surface on one side, is typically considered a semi-infinite body that extends indefinitely on the other side. At the ground surface, the heat flux can be described with a general energy balance equation [168],

$$-k\frac{\partial T}{\partial z}\Big|_{z=0} = h(T_{amb} - T|_{z=0}) + [(1-A)S - LR - \lambda E] \tag{5-2}$$

where T_{amb} [°C] is the ambient air temperature at a reference height, h [$Wm^{-2}K^{-1}$] is the overall heat transfer coefficient from the ground surface to the reference height, A is the albedo, S [Wm^{-2}] is the magnitude of solar radiation, LR [Wm^{-2}] is the net long-wave radiation, and λE [Wm^{-2}] is the latent heat flux due to evaporation. The detailed formulations of LR and λE are available in the literature, as presented in studies conducted by Badache et al. [80] and Aguareles et al. [169].

In terms of heat conduction, other boundary conditions for the differential equation (Equation (5-1)) are given by

$$T(z \to \infty) = T_0 \tag{5-3}$$

$$\frac{\partial T}{\partial r}\Big|_{r=0} = 0 \tag{5-4}$$

$$T(r \to \infty) = T_0 \tag{5-5}$$

In addition to the exterior boundary conditions (Equations (5-2)-(5-5)), the boundary conditions for the interface between the two layers are also considered. According to the principle of energy conservation, the heat flux leaving one layer through the interface is equal to the heat flux entering the other layer.

$$-k_{i+1}\left.\frac{\partial T_{i+1}}{\partial z_{i+1}}\right|_{z_{i+1}=0} = -k_i\left.\frac{\partial T_i}{\partial z_i}\right|_{z_i=L_i} \tag{5-6}$$

where subscript i denotes the ground layer with $i = 1, 2, \cdots, I-1$, and I denotes the bottommost layer. The temperature difference between adjacent layers is directly proportional to the heat flux passing through a contact resistance at each interface. To simplify the analysis, we considered a simplified scenario where adjacent layers are in perfect thermal contact. In the simplified scenario, the interface boundary condition can be described by the continuity of temperature,

$$T_{i+1}(r, 0, t) = T_i(r, L_i, t) \tag{5-7}$$

5.2.2 Heat transfer outside the borehole

5.2.2.1 Homogenous ground

By considering the ground as a homogenous body, numerous analytical solutions [28, 29, 35, 134] have been developed using Green's function method [31]. The transient Green's functions

$G(r, z, t|r', z', \tau)$ solve the governing equation (Equation (5-1)) at any time t and observation location (r, z) within the domain, due to an impulsive point heat source located at (r', z') and released at time τ. Numerous textbooks [31, 129, 135] offer references to Green's functions. The temperature change due to an instantaneous point source at (0, z') is given by Green's function [135],

$$\Delta T = T - T_0 = \frac{Q_p}{\rho c} G_{R00}(r, t|0, \tau) G_{Z30}(z, t|z', \tau) \tag{5-8}$$

$$G_{R00}\left(r, t \,\middle|\, r', \tau\right) = \frac{1}{4\pi\alpha(t-\tau)} \exp\left[-\frac{r^2 + r'^2}{4\alpha(t-\tau)}\right] I_0\left[\frac{rr'}{2\alpha(t-\tau)}\right] \tag{5-9}$$

$$\begin{aligned} G_{Z30}(z, t|z', \tau) = {} & \frac{1}{2\sqrt{\pi\alpha(t-\tau)}} \left\{ \exp\left[-\frac{(z-z')^2}{4\alpha(t-\tau)}\right] + \exp\left[-\frac{(z+z')^2}{4\alpha(t-\tau)}\right] \right\} \\ & - \frac{h}{k} \exp\left[\alpha(t-\tau)\frac{h^2}{k^2} + \frac{h}{k}(z+z')\right] \operatorname{erfc}\left[\frac{z+z'}{\sqrt{4\alpha(t-\tau)}} + \frac{h}{k}\sqrt{4\alpha(t-\tau)}\right] \end{aligned} \tag{5-10}$$

where Q_p [W] is the point heat source, ΔT [°C] denotes the temperature change, $I_0(X)$ is a modified zero-order Bessel function of the first kind, and $\operatorname{erfc}(X)$ is the complementary error function in mathematics. To clearly convey the information contained in this work, a numbering system outlined by Cole et al. [135] for Green's functions is employed herein. For example, G_{R00} denotes Green's function for the radial heat flow in the infinite body, and G_{Z30} describes Green's function for the axial heat flow in the semi-infinite body with a third-type boundary condition.

By integrating the instantaneous point source solution (Equation (5-8)) over space and time, the solution for a continuous line heat source ($D_j < z' < D_{j+1}$) is obtained [31],

$$T_E(r,z,t) = \frac{q_l}{\rho c}\int_{\tau=0}^{t}\int_{z'=D_1}^{D_2} G_{R00}(r,t|0,\tau)G_{Z30}(z,t|z',\tau)dz'd\tau \tag{5-11}$$

where D_1 and D_2 [m] are two ends of the line heat source with $D_1 < z' < D_2$, $q_l = \frac{Q}{D_2 - D_1}$ [Wm^{-1}] is the heat transfer rate per unit length, Q [W] is the heat load on the line heat source, and T_E [°C] is the temperature response due to the line heat source.

For BHE applications, a dimensionless parameter known as the thermal response factor is widely used in some software design tools for sizing the design length [86]. Thermal response factors describe the temperature change, averaged over the borehole wall surface, due to a unit heat flow rate.

$$\Theta_E = \frac{\bar{T}_E}{q_l/2\pi k} \tag{5-12}$$

$$\bar{T}_E(r_b,t) = \frac{1}{H_2 - H_1}\int_{z=H_1}^{H_2} T_E(r_b,z,t)dz \tag{5-13}$$

where H_1 and H_2 [m] are two ends of the borehole with $H_1 < z < H_2$, and r_b [m] is the radius of the borehole.

Interchanging the order of integration, followed by using the substitution $s = \frac{1}{\sqrt{4\alpha(t-\tau)}}$, the temporal integral of G_{Z30} from $\tau = 0$ to t is

$$\int_{\tau=0}^{t} G_{R00}(r_b, t|0, \tau) G_{Z30}(z, t|z', \tau) d\tau = \frac{1}{4\pi\alpha} \int_{1/\sqrt{4\alpha t}}^{\infty} \exp(-{r_b}^2 s^2) g_1(z, z', s)\, ds \tag{5-14}$$

$$g_1(z, z', s) = \frac{2}{\sqrt{\pi}} \exp[-(z - z')^2 s^2] + \frac{2}{\sqrt{\pi}} \exp[-(z + z')^2 s^2] - \frac{2h}{sk} \exp\left[\frac{h^2}{4s^2k^2} + \frac{h}{k}(z + z')\right] \operatorname{erfc}\left[(z + z')s + \frac{h}{2sk}\right] \tag{5-15}$$

The double integral on space variables z and z' acts only on the function $f_1(z, z', s)$, and the double integral is given by

$$\int_{z=H_1}^{H_2} \int_{z'=D_j}^{D_{j+1}} g_1(z, z', s) dz' dz = \frac{g_2(s)}{s^2} - \frac{2k}{sh} g_3(s) \tag{5-16}$$

$$g_2(s) = -\operatorname{ierf}[s(H_1 - D_1)] + \operatorname{ierf}[s(H_1 - D_2)] + \operatorname{ierf}[s(H_2 - D_1)] - \operatorname{ierf}[s(H_2 - D_2)] - \operatorname{ierf}[s(H_1 + D_1)] + \operatorname{ierf}[s(H_1 + D_2)] + \operatorname{ierf}[s(H_2 + D_1)] - \operatorname{ierf}[s(H_2 + D_2)] \tag{5-17}$$

$$
\begin{aligned}
g_3(s) = \operatorname{erf}\left[s\left(H_1 + D_j\right)\right] &+ \exp\left[\frac{h^2}{4s^2k^2} + \frac{h}{k}(H_1 + D_1)\right]\operatorname{erfc}\left[(H_1 + D_1)s + \frac{h}{2sk}\right] - \operatorname{erf}[s(H_1 + D_2)] \\
&- \exp\left[\frac{h^2}{4s^2k^2} + \frac{h}{k}(H_1 + D_2)\right]\operatorname{erfc}\left[(H_1 + D_2)s + \frac{h}{2sk}\right] - \operatorname{erf}[s(H_2 + D_1)] \\
&- \exp\left[\frac{h^2}{4s^2k^2} + \frac{h}{k}(H_2 + D_1)\right]\operatorname{erfc}\left[(H_2 + D_1)s + \frac{h}{2sk}\right] + \operatorname{erf}[s(H_2 + D_2)] \\
&+ \exp\left[\frac{h^2}{4s^2k^2} + \frac{h}{k}(H_2 + D_2)\right]\operatorname{erfc}\left[(H_2 + D_2)s + \frac{h}{2sk}\right]
\end{aligned}
\tag{5-18}
$$

where $\operatorname{erf}(X)$ is the error function, and $\operatorname{ierf}(X) = \int_0^X \operatorname{erf}(x)\,dx = X\operatorname{erf}(X) + \frac{1}{\sqrt{\pi}}\left(e^{-X^2} - 1\right)$.

Finally, the thermal response factor can be written as

$$
\begin{aligned}
\Theta_E\left(\frac{r_b}{H}, \frac{\alpha t}{{r_b}^2}, \frac{h}{k}\right) &= \frac{\bar{T}_E}{q_l/2\pi k} \\
&= \frac{1}{2(H_2 - H_1)} \int_{1/\sqrt{4\alpha t}}^{\infty} \exp(-{r_b}^2 s^2)\left[\frac{g_2(s)}{s^2} - \frac{2k}{sh} g_3(s)\right] ds
\end{aligned}
\tag{5-19}
$$

5.2.2.2 Multilayered ground

For the ground with more than three layers, Green's function is difficult to define due to the complexity of the function [154]. Herein, we utilized the unsteady surface element method [170], a robust technique used to solve transient heat transfer problems associated with layered bodies. The unsteady surface element method is a boundary discretization method that divides the interface into *N* surface elements (which are not necessarily equal), as illustrated in Figure 5-2. At the interface of two contacting layers, the boundary conditions described in Equations (5-6) and (5-7)

necessitate the matching of vertical heat flux and temperature for all points along the interface at all times. However, the unsteady surface element method [170] considers a less stringent requirement that the surface-average temperatures match simultaneously between the coupled surface elements,

$$\overline{\Delta T}_{i+1,n}(0,t) = \overline{\Delta T}_{i,n}(L_i,t), \quad \text{for } i = 1,2,\cdots \quad \text{and } n = 1,2,\cdots,N \tag{5-20}$$

where the subscript *i* denotes the ground layer, $\overline{\Delta T}_{i,n}(t)$ represents the surface-average temperature of surface element n (with $n = 1,2,\cdots N$), r_n [m] is the outer dimension of the surface element, r_{N-1} [m] denotes the distance where the temperature remains unaffected by the line heat source, and the outermost surface element *N* is boundless as extending from r_{N-1} to infinity. For higher precision in temperature values, smaller surface elements can be selected. In the current study, the error of the proposed solution was smaller than 0.61% with four surface elements.

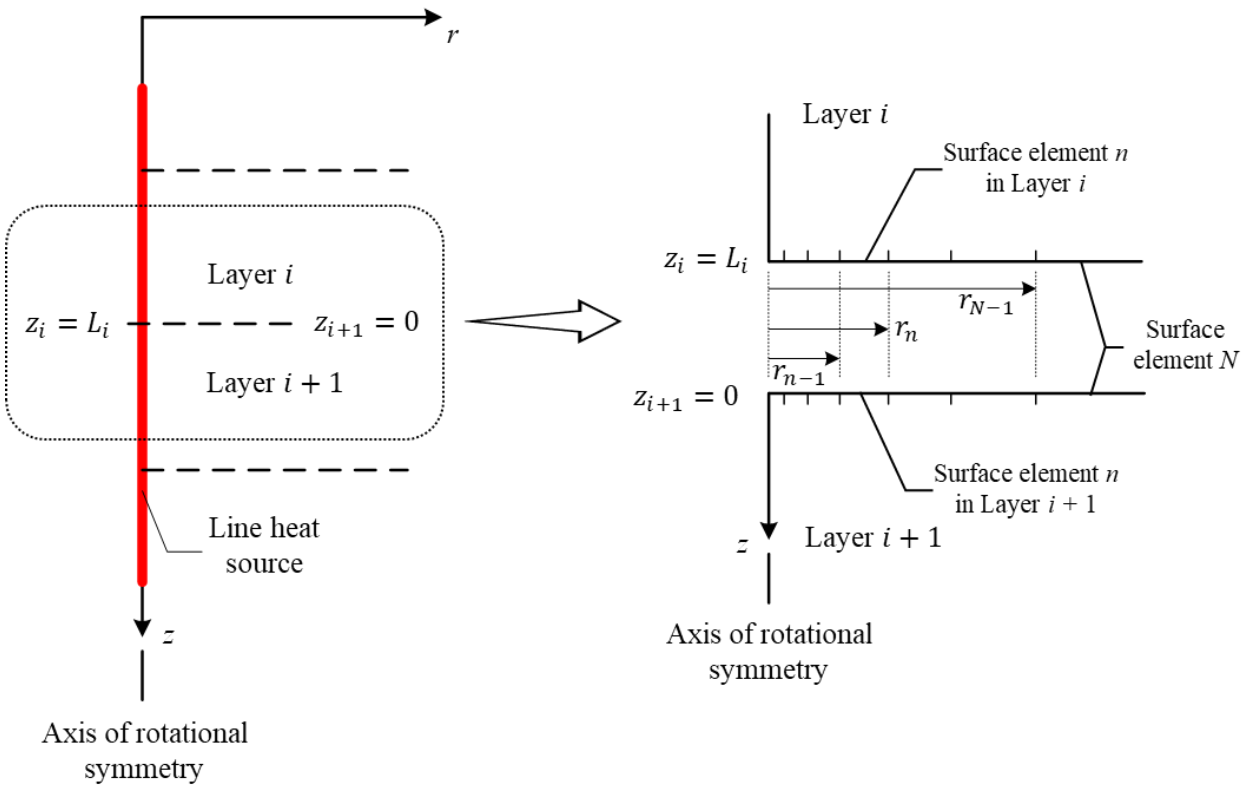

Figure 5-2. A schematic of the surface element method for the interface of two contacting layers.

At the interface of two contacting layers, a vertical heat flux (q_v) transfers heat from the lower layer to the upper layer (i.e., conservation of energy). The vertical heat flux varies with time and varies across the boundary surface. In each homogenous layer, the vertical heat flux is seen as a prescribed heat flux at the boundary surface, which is known as a second-type boundary condition. The temperature change in each layer is calculated by applying the principle of superposition [52], where the contributions of the line heat source and the vertical heat fluxes are superimposed (as illustrated in Figure 5-3),

$$\Delta T_i(r,z,t) = T_{E_i}(r,z,t) - T_{U_i}(r,z,t) + T_{V_i}(r,z,t), \quad \text{for } i = 1,2,\cdots,I \tag{5-21}$$

where T_U and T_V [°C] are the temperature responses due to the vertical heat flux at the boundary surfaces, subscripts U and V respectively denote the upper and the lower surfaces, and T_E [°C] is the temperature response due to the line heat source. Since the bottommost ground layer does not have a lower surface, the T_V term would not be included in its temperature solution. By using Green's functions method [135], the expressions of temperature, T_E, T_U, and T_V, can be found,

$$T_{E_i}(r,z,t) = \frac{\alpha_i}{k_i}\int_{\tau=0}^{t}\int_{z'=0}^{L_i} q_{l_i}(z',\tau)G_{R00}(r,t|0,\tau)G_i(z,t|z',\tau)\,dz'\,d\tau \tag{5-22}$$

$$T_{U_i}(r,z,t) = \frac{\alpha_i}{k_i}\int_{\tau=0}^{t}\int_{r'=0}^{\infty} q_{v_{i-1}}(r',\tau)G_{R00}(r,t|r',\tau)G_i(z,t|0,\tau)\,2\pi r' dr'\,d\tau \tag{5-23}$$

$$T_{V_i}(r,z,t) = \frac{\alpha_i}{k_i}\int_{\tau=0}^{t}\int_{r'=0}^{\infty} q_{v_i}(r',\tau)G_{R00}(r,t|r',\tau)G_i(z,t|L_i,\tau)\,2\pi r' dr'\,d\tau \tag{5-24}$$

where L_i [m] is the thickness of each ground layer, and q_v [Wm^{-2}] is the unknown vertical heat flux at the interfaces. Following the numbering system [135], the number 2 is assigned to the boundaries with prescribed heat flux (or second-type boundary conditions). Accordingly, the topmost, intermediated, and bottommost ground layers are referred to as G_{Z32}, G_{Z22}, G_{Z20}, respectively. The corresponding Green's functions for these layers are provided in the Appendix 5-C.

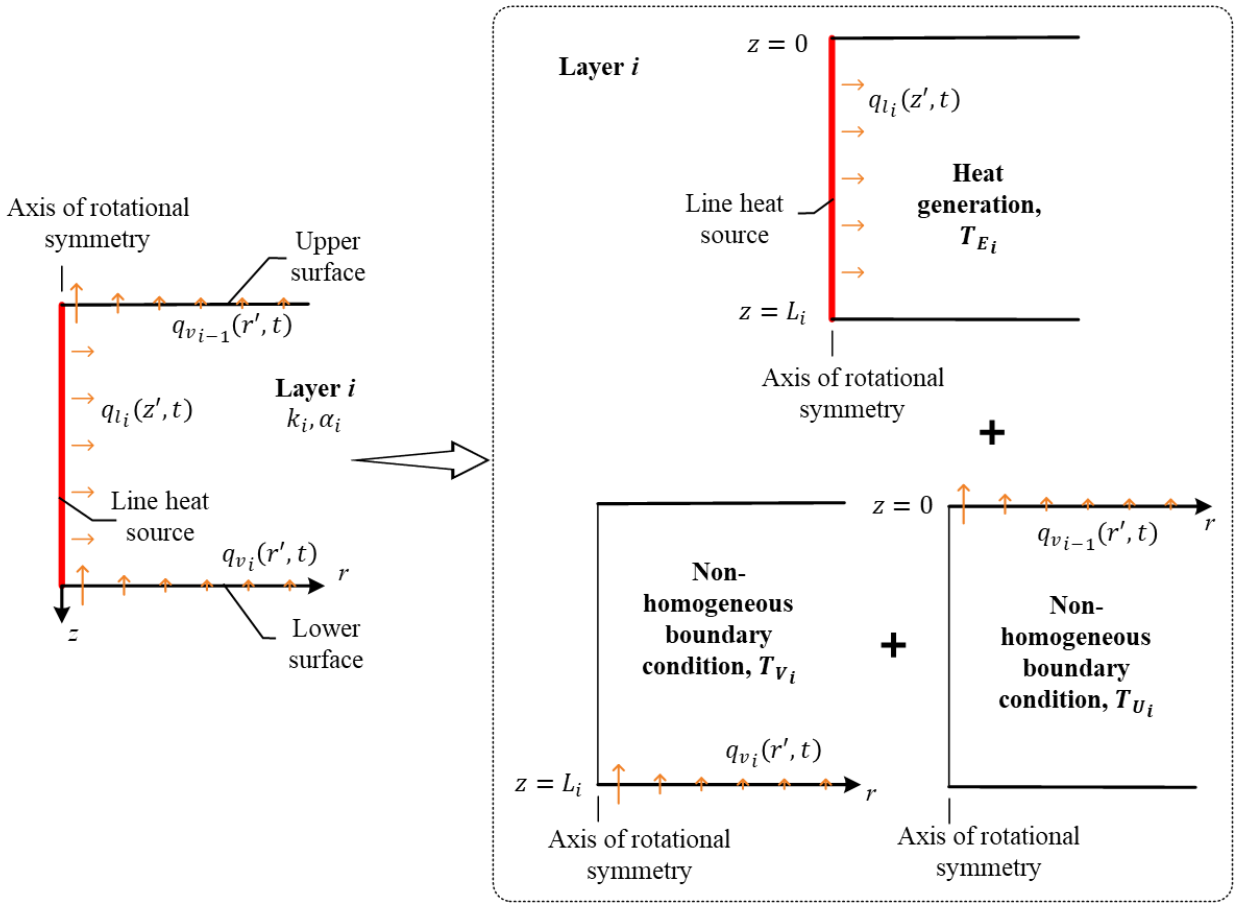

Figure 5-3. A schematic of the superposition scheme for heat generation and non-homogenous boundary conditions.

The unknown vertical heat flux with spatial variation can be approximated by applying a uniform heat flux within each surface element, resulting in a stepwise profile as illustrated in Figure 5-4. Then, the spatial integral in Equations (5-23) and (5-24) can be approximated by summing up the individual heat flux components,

$$\frac{\alpha_i}{k_i}\int_{r'=0}^{\infty} q_{v_{i-1}}(r',\tau)G_{R00}(r,t|r',\tau)G_i(z,t|0,\tau)\,2\pi r'dr'$$

$$= \sum_{m=n=1}^{N} q_{v_{i-1,m}}(\tau)\underbrace{\frac{\alpha_i}{k_i}G_i(z,t|0,\tau)\int_{r'=0}^{r_n} G_{R00}(r,t|r',\tau)2\pi r'dr'}_{\psi_{U_{i,m}}(r,z,t-\tau)} \tag{5-25}$$

$$\frac{\alpha_i}{k_i}\int_{r'=0}^{\infty} q_{v_i}(r',\tau)G_{R00}(r,t|r',\tau)G_i(z,t|L_i,\tau)\,2\pi r'dr'$$

$$= \sum_{m=n=1}^{N} q_{v_{i,m}}(\tau)\underbrace{\frac{\alpha_i}{k_i}G_i(z,t|L_i,\tau)\int_{r'=0}^{r_n} G_{R00}(r,t|r',\tau)\,2\pi r'dr'}_{\psi_{V_{i,m}}(r,z,t-\tau)} \tag{5-26}$$

where $\psi_{U_{i,m}}$ and $\psi_{V_{i,m}}$ are influence functions that represent the temperature response at location (r, z) due to a unit step heat flux over the surface element m (with $m = 1,2,\cdots,N$).

Similarly, the line heat source in each layer is divided into J segments, and a uniform heat transfer rate is applied within each segment. The number of segments in each layer is not necessarily equal. The spatial integral in Equation (5-22) is then replaced with a summation of the line heat source segments,

$$\frac{\alpha_i}{k_i}\int_{z'=0}^{L_i} q_{l_i}(z',\tau)G_{R00}(r,t|0,\tau)G_i(z,t|z',\tau)\,dz'$$

$$= \sum_{j=1}^{J} q_{l_{i,j}}(\tau)\underbrace{\frac{\alpha_i}{k_i}G_{R00}(r,t|0,\tau)\int_{z'=D_{j-1}}^{D_j} G_i(z,t|z',\tau)\,dz'}_{\psi_{E_{i,j}}(r,z,t-\tau)} \tag{5-27}$$

where subscript $j = 1,2 \cdots J$ denotes the line heat source segment, and ψ_{E_j} is temperature response at location (r, z) due to a unit line heat source segment ($D_{j-1} < z' < D_j$).

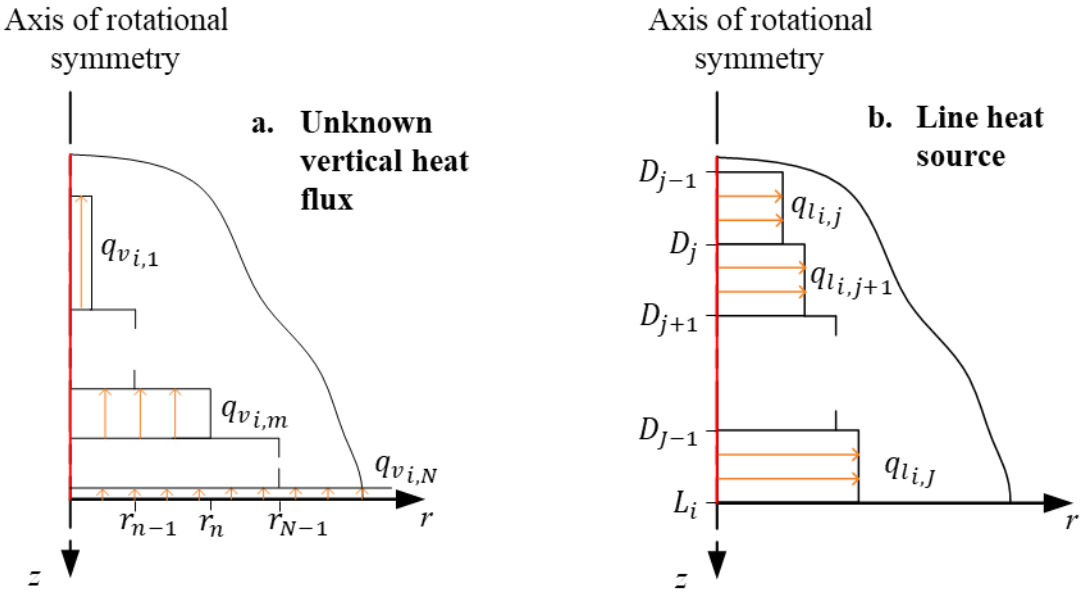

Figure 5-4. A schematic of discretizing the surface heat flux and the line heat source. (a) The unknown heat flux at boundary surfaces is approximated using a stepwise distribution; (b) the line heat source is approximated using a stepwise distribution.

For each interface (z = 0 or L_i), by taking the surface average over the surface element n, one can get the influence functions that represent the surface-average temperature response of the element n for a unit step heat flux over the surface element m,

$$\bar{\psi}_{U\,mn}(z, t-\tau) = \frac{1}{\pi(r_n^2 - r_{n-1}^2)} \int_{r=r_{n-1}}^{r_n} \psi_{U\,m}(r, z, t-\tau)\, dr, \quad \text{for } m = 1,2,\cdots,N \qquad (5\text{-}28)$$

$$\bar{\psi}_{V\,mn}(z,t-\tau)=\frac{1}{\pi(r_n^2-r_{n-1}^2)}\int_{r=r_{n-1}}^{r_n}\psi_{V\,m}(r,z,t-\tau)\,dr,\quad \text{for } m=1,2,\cdots,N \tag{5-29}$$

for a unit line heat source segment *j,*

$$\bar{\psi}_{E\,jn}(z,t-\tau)=\frac{1}{\pi(r_n^2-r_{n-1}^2)}\int_{r=r_{n-1}}^{r_n}\psi_{E\,j}(r,z,t-\tau)\,dr,\quad \text{for } j=1,2,\cdots,J \tag{5-30}$$

Notice that influence functions $\bar{\psi}$ involve double integrals. These integrations can be performed analytically and are given in the Appendix 5-C.

In BHE applications, it is common to present heat loads (Q) as stepwise values due to varying demands over time [105]. The stepwise approximation over time can also be applied to vertical heat fluxes. With stepwise values of q (including both q_l and q_v) over time, the temperature response at the end of P^{th} time step is computed as a temporal superposition of the response for each of the preceding time steps. An alternative, more efficient approach involves converting stepwise values of q into a series of increments Δq. Subsequently, the linear convolution sum of Δq and ψ is efficiently solved by the fast Fourier transform (FFT) algorithms [107]. Using this approach [107], the temporal integrals in Equations (5-22)-(5-24) are performed

$$\int_{\tau=0}^{t}q(\tau)\psi(t-\tau)d\tau=\sum_{p=1}^{P}\Delta q(t_p)\psi(t_P-t_p)=\Im^{-1}[\Im(\psi)\Im(\Delta q)] \tag{5-31}$$

where subscript $p = 1, 2, \cdots P$ denotes the time step, t_p [s] is the discrete time, $\Delta q(t_p) = q(t_p) - q(t_{p-1})$, $\Im$ represents the FFT, and $\Im^{-1}$ represents the inverse-FFT.

Finally, the surface-average temperature $\Delta T_{i,n}$ can be written for the surface element n (with $n = 1,2, \cdots, N$) at $z = 0$ or L_i in layer i,

$$\overline{\Delta T}_{i,n}(z, t_p) = \sum_{j=1}^{J} \Im^{-1}\left[\Im\left(\bar{\psi}_{E\,i,jn}(z)\right)\Im\left(\Delta q_{l_{i,j}}\right)\right] - \sum_{m=1}^{N} \Im^{-1}\left[\Im\left(\bar{\psi}_{U\,i,mn}(z)\right)\Im\left(\Delta q_{v_{i-1,m}}\right)\right] + \sum_{m=1}^{N} \Im^{-1}\left[\Im\left(\bar{\psi}_{V\,i,mn}(z)\right)\Im\left(\Delta q_{v_{i,m}}\right)\right] \tag{5-32}$$

Equation (5-32) can be expressed in matrices,

$$\overline{\overline{\Delta T}}_i(z, t_p) = \Im^{-1}\left[\bar{\bar{\psi}}_{E\,i}(z)\overline{\overline{\Delta q}}_{l_i}\right] - \Im^{-1}\left[\bar{\bar{\psi}}_{U\,i}(z)\overline{\overline{\Delta q}}_{v_{i-1}}\right] + \Im^{-1}\left[\bar{\bar{\psi}}_{V\,i}(z)\overline{\overline{\Delta q}}_{v_i}\right] \tag{5-33}$$

where

$$\overline{\overline{\Delta T}}_i = \begin{bmatrix} \overline{\Delta T}_{i,1} \\ \overline{\Delta T}_{i,2} \\ \vdots \\ \overline{\Delta T}_{i,N} \end{bmatrix} \tag{5-34}$$

$$\bar{\bar{\psi}}_{E_i} = \begin{bmatrix} \Im\left(\bar{\psi}_{E_{i,11}}\right) & \Im\left(\bar{\psi}_{E_{i,21}}\right) & \cdots & \Im\left(\bar{\psi}_{E_{i,J1}}\right) \\ \Im\left(\bar{\psi}_{E_{i,12}}\right) & \Im\left(\bar{\psi}_{E_{i,22}}\right) & \cdots & \Im\left(\bar{\psi}_{E_{i,J2}}\right) \\ \vdots & \vdots & \ddots & \vdots \\ \Im\left(\bar{\psi}_{E_{i,1N}}\right) & \Im\left(\bar{\psi}_{E_{i,2N}}\right) & \cdots & \Im\left(\bar{\psi}_{E_{i,JN}}\right) \end{bmatrix}, \quad \overline{\overline{\Delta q}}_{l_i} = \begin{bmatrix} \Im\left(\Delta q_{l_{i,1}}\right) \\ \Im\left(\Delta q_{l_{i,2}}\right) \\ \vdots \\ \Im\left(\Delta q_{l_{i,J}}\right) \end{bmatrix} \tag{5-35}$$

$$\bar{\bar{\psi}}_{U_i} = \begin{bmatrix} \Im\left(\bar{\psi}_{U_{i,11}}\right) & \Im\left(\bar{\psi}_{U_{i,21}}\right) & \cdots & \Im\left(\bar{\psi}_{U_{i,N1}}\right) \\ \Im\left(\bar{\psi}_{U_{i,12}}\right) & \Im\left(\bar{\psi}_{U_{i,22}}\right) & \cdots & \Im\left(\bar{\psi}_{U_{i,N2}}\right) \\ \vdots & \vdots & \ddots & \vdots \\ \Im\left(\bar{\psi}_{U_{i,1N}}\right) & \Im\left(\bar{\psi}_{U_{i,2N}}\right) & \cdots & \Im\left(\bar{\psi}_{U_{i,NN}}\right) \end{bmatrix}, \quad \overline{\overline{\Delta q}}_{v_i} = \begin{bmatrix} \Im\left(\Delta q_{v_{i,1}}\right) \\ \Im\left(\Delta q_{v_{i,2}}\right) \\ \vdots \\ \Im\left(\Delta q_{v_{i,N}}\right) \end{bmatrix},$$

$$\text{and } \bar{\bar{\psi}}_{V_i} = \begin{bmatrix} \Im\left(\bar{\psi}_{V_{i,11}}\right) & \Im\left(\bar{\psi}_{V_{i,21}}\right) & \cdots & \Im\left(\bar{\psi}_{V_{i,N1}}\right) \\ \Im\left(\bar{\psi}_{V_{i,12}}\right) & \Im\left(\bar{\psi}_{V_{i,22}}\right) & \cdots & \Im\left(\bar{\psi}_{V_{i,N2}}\right) \\ \vdots & \vdots & \ddots & \vdots \\ \Im\left(\bar{\psi}_{V_{i,1N}}\right) & \Im\left(\bar{\psi}_{V_{i,2N}}\right) & \cdots & \Im\left(\bar{\psi}_{V_{i,NN}}\right) \end{bmatrix} \tag{5-36}$$

By introducing Equation (5-33) into the interface boundary condition Equation (5-20), a set of linear equations is formed at each time step. It can be expressed in matrices,

$$\begin{bmatrix} \bar{\bar{\psi}}_{E_2}(0)\overline{\overline{\Delta q}}_{l_2} - \bar{\bar{\psi}}_{E_1}(L_1)\overline{\overline{\Delta q}}_{l_1} \\ \bar{\bar{\psi}}_{E_3}(0)\overline{\overline{\Delta q}}_{l_3} - \bar{\bar{\psi}}_{E_2}(L_2)\overline{\overline{\Delta q}}_{l_2} \\ \vdots \\ \bar{\bar{\psi}}_{E_I}(0)\overline{\overline{\Delta q}}_{l_I} - \bar{\bar{\psi}}_{E_{I-1}}(L_{I-1})\overline{\overline{\Delta q}}_{l_{I-1}} \end{bmatrix}$$

$$= \begin{bmatrix} \bar{\bar{\psi}}_{U_2}(0) + \bar{\bar{\psi}}_{V_1}(L_1) & -\bar{\bar{\psi}}_{U_1}(L_1) & 0 & \cdots & 0 \\ -\bar{\bar{\psi}}_{V_2}(0) & \bar{\bar{\psi}}_{U_3}(0) + \bar{\bar{\psi}}_{V_2}(L_2) & -\bar{\bar{\psi}}_{U_2}(L_2) & \ddots & \vdots \\ 0 & -\bar{\bar{\psi}}_{V_3}(0) & \ddots & \ddots & 0 \\ \vdots & \ddots & \ddots & \ddots & -\bar{\bar{\psi}}_{U_{I-1}}(L_{I-1}) \\ 0 & \cdots & 0 & -\bar{\bar{\psi}}_{V_I}(0) & \bar{\bar{\psi}}_{U_I}(0) + \bar{\bar{\psi}}_{V_{I-1}}(L_{I-1}) \end{bmatrix} \begin{bmatrix} \overline{\overline{\Delta q}}_{v_1} \\ \overline{\overline{\Delta q}}_{v_2} \\ \vdots \\ \overline{\overline{\Delta q}}_{v_{I-1}} \end{bmatrix} \tag{5-37}$$

By solving the above linear equations, the vertical heat flux over each surface element at each interface is provided. From the solutions of vertical heat fluxes, the temperature change ΔT_i at location (r, z) in for $i = 1, 2, \cdots, I$ can be determined,

$$\Delta T_i(r,z,t) = \sum_{j=1}^{J} \Im^{-1}\left[\Im\left(\psi_{E_{i,j}}(r,z)\right)\Im\left(\Delta q_{l_{i,j}}\right)\right] - \sum_{m=1}^{N} \Im^{-1}\left[\Im\left(\psi_{U_{i,m}}(r,z)\right)\Im\left(\Delta q_{v_{i-1,m}}\right)\right] + \sum_{m=1}^{N} \Im^{-1}\left[\Im\left(\psi_{V_{i,m}}(r,z)\right)\Im\left(\Delta q_{v_{i,m}}\right)\right] \tag{5-38}$$

5.2.3 Heat transfer inside the borehole

Inside a borehole, a heat exchanger is installed to facilitate the circulation of a heat-carrying fluid. One commonly used configuration for the heat exchanger is a U-shaped pipe, which has gained significant popularity due to its ease of installation and cost-effectiveness [11]. To analyze the heat transfer within the borehole region, a delta-circuit thermal resistance model [23, 128] is employed, considering the interaction between the borehole wall and the circulating fluid. As shown in Figure 5-5, a delta circuit is established by connecting one node representing the temperature at the borehole wall and two nodes representing fluid temperatures. These two fluid nodes represent distinct temperatures within the respective pipes. According to the principle of energy conservation, the temperatures of the downward-flowing (T_{down}) and upward-flowing (T_{up}) fluids are formulated,

$$-V(\rho c)_f \frac{\partial T_{up}}{\partial z} = \frac{T_b - T_{up}}{R_2^{\Delta}} + \frac{T_{down} - T_{up}}{R_{12}^{\Delta}} \tag{5-39}$$

$$V(\rho c)_f \frac{\partial T_{down}}{\partial z} = \frac{T_b - T_{down}}{R_1^{\Delta}} + \frac{T_{up} - T_{down}}{R_{12}^{\Delta}} \tag{5-40}$$

where V [m^3s^{-1}] is the volumetric flow rate of the fluid, $(\rho c)_f$ [$Jm^{-3}K^{-1}$] is the volumetric heat capacity of the fluid, and R_1^{Δ}, R_2^{Δ} and R_{12}^{Δ} [mKW^{-1}] are three thermal resistances between the nodes.

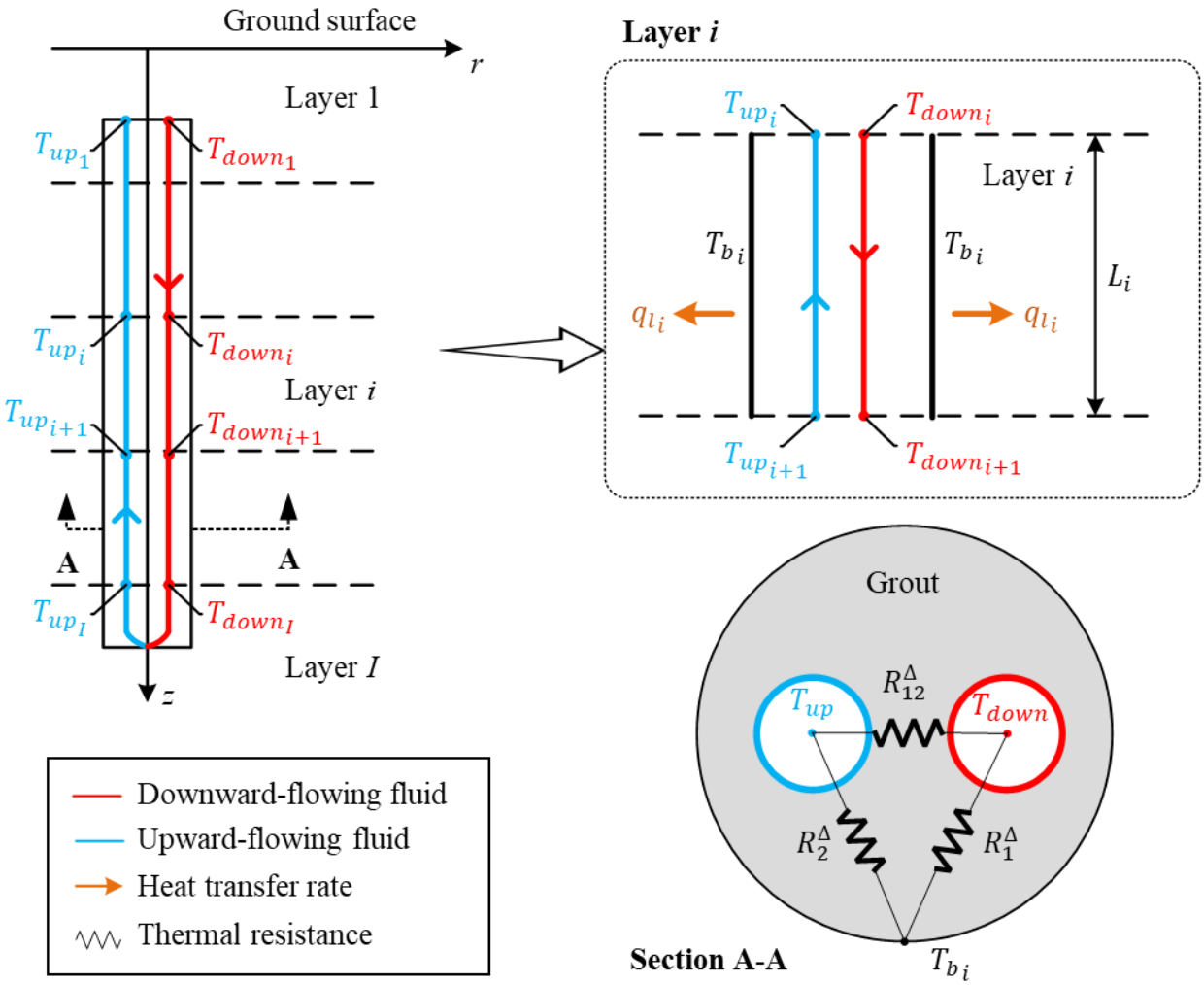

Figure 5-5. A schematic of the heat transfer inside the borehole with a single U-shaped pipe. A delta-circuit thermal resistance model is established by connecting temperature nodes with corresponding thermal resistances.

Eskilson [23] and Hellström [128] have derived a general solution for the fluid temperatures through Laplace transforms. This solution is given by the following expressions:

$$T_{down_{i+1}}(t) = \underbrace{\exp(\beta)\left[\cosh(\gamma) - \frac{\beta - \beta_2 - \beta_{12}}{\gamma}\sinh(\gamma)\right]}_{f_1(L_i)} T_{down_i}(t) + \underbrace{\frac{\beta_{12}}{\gamma}\exp(\beta)\sinh(\gamma)}_{f_2(L_i)} T_{up_i}(t) + \underbrace{\left\{1 - \exp(\beta)\left[\cosh(\gamma) + \frac{\beta - \beta_2}{\gamma}\sinh(\gamma)\right]\right\}}_{f_4(L_i)} \overline{T_{b_i}} \tag{5-41}$$

$$T_{up_{i+1}}(t) = -f_2(L_i) T_{down_i}(t) + \underbrace{\exp(\beta)\left[\cosh(\gamma) + \frac{\beta + \beta_1 + \beta_{12}}{\gamma}\sinh(\gamma)\right]}_{f_3(L_i)} T_{up_i}(t) + \underbrace{\left\{1 - \exp(\beta)\left[\cosh(\gamma) + \frac{\beta + \beta_1}{\gamma}\sinh(\gamma)\right]\right\}}_{f_5(L_i)} \overline{T_{b_i}} \tag{5-42}$$

where $\beta_1 = \frac{L_i}{V(\rho c)_f R_1^A}$, $\beta_2 = \frac{L_i}{V(\rho c)_f R_2^A}$, and $\beta_{12} = \frac{L_i}{V(\rho c)_f R_{12}^A}$ are the dimensionless thermal conductance, $\beta = \frac{\beta_2 - \beta_1}{2}$, $\gamma = \sqrt{\frac{(\beta_1 + \beta_2)^2}{4} + \beta_{12}(\beta_1 + \beta_2)^2}$, and *sinh*(*X*) and *cosh*(*X*) are hyperbolic functions. Furthermore, heat loads yield a difference between the inlet and outlet temperatures,

$$Q(t) = V(\rho c)_f \left(T_{down_1}(t) - T_{up_1}(t)\right) \tag{5-43}$$

A set of linear equations was established with Equations(5-41)–(5-43),

$$\begin{bmatrix} -f_4(L_1)\overline{T_{b_1}} \\ f_5(L_1)\overline{T_{b_1}} \\ -f_4(L_2)\overline{T_{b_2}} \\ f_5(L_2)\overline{T_{b_2}} \\ \vdots \\ [f_5(L_I) - f_4(L_I)]\overline{T_{b_I}} \\ Q \end{bmatrix}$$

$$= \begin{bmatrix} f_1(L_1) & f_2(L_1) & -1 & 0 & \cdots & 0 & 0 \\ f_2(L_1) & -f_3(L_1) & 0 & 1 & \ddots & 0 & 0 \\ 0 & 0 & f_1(L_2) & f_2(L_2) & \ddots & 0 & 0 \\ 0 & 0 & f_2(L_2) & -f_3(L_2) & \ddots & 0 & 0 \\ \vdots & \ddots & \ddots & \ddots & \ddots & \ddots & \vdots \\ 0 & 0 & 0 & 0 & \ddots & f_1(L_I) + f_2(L_I) & f_2(L_I) - f_3(L_I) \\ V(\rho c)_f & -V(\rho c)_f & 0 & 0 & \cdots & 0 & 0 \end{bmatrix} \begin{bmatrix} T_{down_1} \\ T_{up_1} \\ T_{down_2} \\ T_{up_2} \\ \vdots \\ T_{down_I} \\ T_{up_I} \end{bmatrix} \tag{5-44}$$

The fluid temperatures can be determined by solving the above linear equations. The heat transfer rate of each line heat source segment is calculated by performing an energy balance on the circulating fluid,

$$q_{l_i}(t) = \frac{V(\rho c)_f}{L_i}\left[T_{down_i}(t) - T_{down_{i+1}}(t) + T_{up_{i+1}}(t) - T_{up_i}(t)\right] \tag{5-45}$$

5.2.4 Two-way coupling scheme

The two-way coupling scheme takes into account the simultaneous heat transfer processes occurring inside and outside the borehole (Figure 5-6). By employing this scheme, the solution specifically accounts for the variation in heat transfer rates over time and depth. It was referred to

as the MVQ solution [72], where MVQ is an acronym for multilayered ground with varying heat transfer rates.

The scheme initiates a guess for borehole wall temperatures, which can be the temperatures calculated from the preceding time step. The undisturbed ground temperature would be the initial guess for the first time step. The models for the internal and external regions are then iterated, with the output from one model serving as the input for the other model, as depicted in Figure 5-6. In the current study, the temperature responses and heat transfer rates were determined and returned within a maximum of 22 iterations. To improve convergence, it is suggested to explore the use of a root-finding method in future studies.

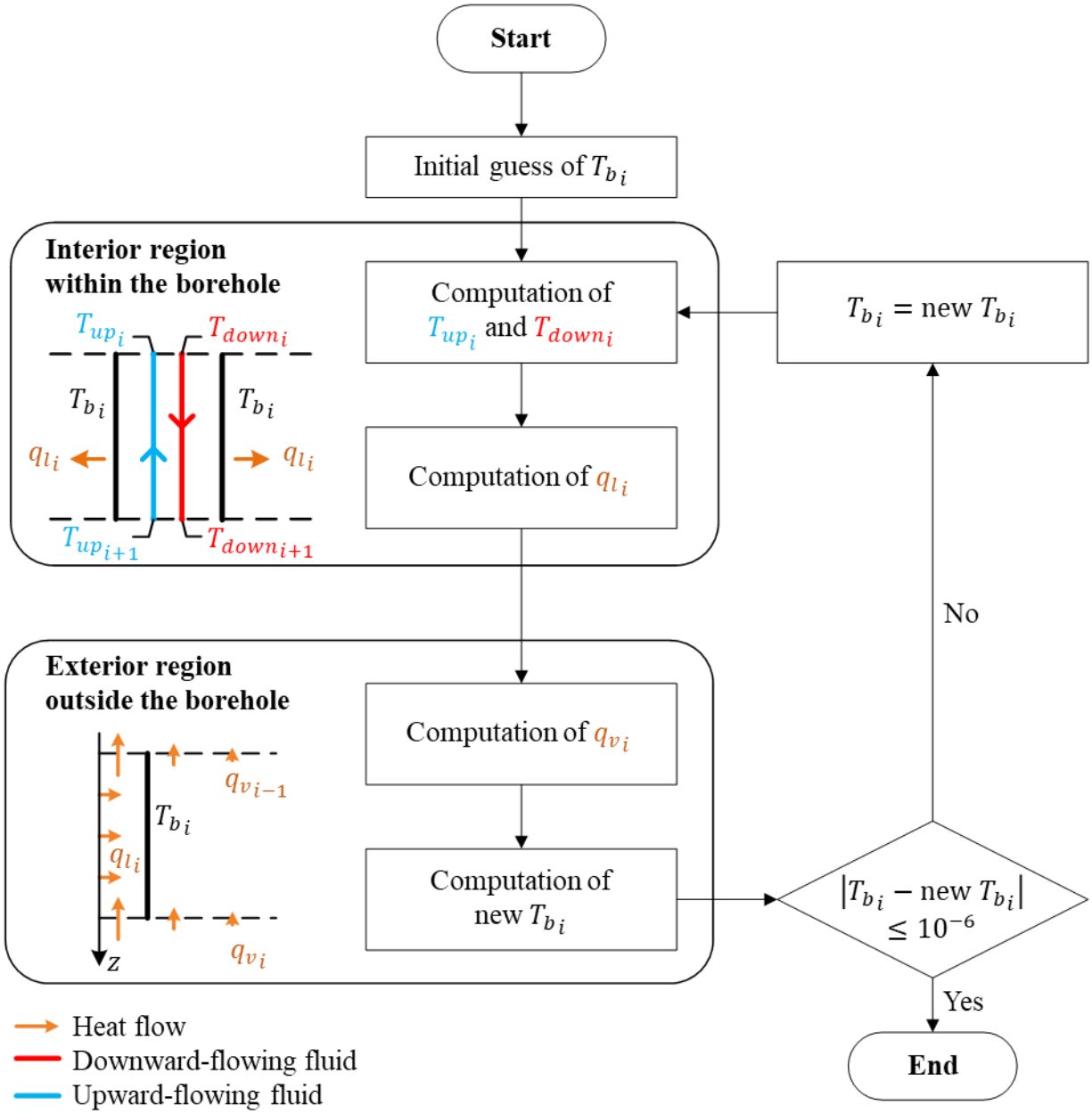

Figure 5-6. The flowchart of the two-way coupling scheme.

5.3. Verification and scenarios

5.3.1 Model verification

Prior to delving into the results of the MVQ solution, it is necessary to ensure the correctness of the temperature expressions, computational algorithm, and computer code. The MVQ solution can be verified by comparing its results to those obtained from an exact solution, i.e., the line heat source solution (Equation(5-19)). This verification was performed in a scenario where the thermal properties within the two layers were assumed to be identical, as the exact solution is only valid in a homogeneous ground. In the ongoing analysis, both solutions were implemented and evaluated in MATLAB. In line with many previous studies [64, 111-113], a double-layered ground scenario was employed. In this scenario, the borehole was evenly divided into two parts by the interface of two horizontally stratified ground layers.

In addition to the exact solution, a detailed finite-element (FE) model was constructed in COMSOL Multiphysics for verification purposes. The COMSOL model was initially verified in a homogeneous ground scenario, and then a comparison was made between the results obtained from the COMSOL model and those obtained from the MVQ solution in a scenario where the thermal properties differed between the two layers. To mitigate computational requirements, a two-dimensional axisymmetric model was employed in the finite element analysis. A higher concentration of elements was allocated near the borehole region where higher temperature gradients were anticipated. In accordance with the assumption for analytical solutions, a uniform initial condition was set across the entire domain. Additionally, a preliminary investigation was performed to make sure that simulation outcomes remained independent of the mesh resolution and domain size. As a result, it was determined that the model domain, measuring 500 m in width

and 500 m in thickness, was sufficiently large to prevent external boundary conditions from influencing the results. The mesh resolution was refined by progressively increasing the number of elements in the region near the borehole and throughout the entire domain until the mesh produced a mesh-independent solution.

5.3.2 Scenarios

The MVQ solution was demonstrated in five scenarios, as listed in Table 5-1. In Scenarios 1-3, the verification of the MVQ solution was carried out by comparing its results to those obtained from the exact solution and the COMSOL model. In these scenarios, the borehole configuration was disregarded and simplified as a line, and a uniform heat flow rate was assumed along the entire length of the line throughout the analysis. This simplification aligns with the analytical solutions for BHEs in the homogeneous ground with either the first-type [27-29, 35, 68] or third-type [50-53, 82] boundary conditions. By considering a uniform heat transfer rate, the analysis maintains consistency with these established analytical solutions. However, this simplification overlooks the heat transfer that occurs through the circulation of the heat-carrying fluid inside the borehole. The circulation of the fluid within the borehole results in a non-uniform distribution of the heat transfer rate along the length of the borehole, and this distribution dynamically changes during system operation [72]. To take account of the effects of circulating fluid, the heat transfer inside the borehole is incorporated in Scenarios 4 and 5.

Table 5-1. Ground parameters used in five test scenarios

Ground scenarios	k_1/k_2	r_b/H	h/k [m^{-1}]
Scenario 1	1	0.00042, 0.0015, and 0.005	0.5
Scenario 2	1, 1/2, and 1/4	0.00042	0.5
Scenario 3	1	0.00042-0.005	0-∞
Scenarios 4 & 5	1/2	0.00066	0.5

Scenarios 1-3 were specifically designed to explore and analyze the solutions based on four key parameters. These parameters are crucial in defining the characteristics of the solutions. They include Fourier number $Fo = \frac{\alpha t}{{r_b}^2}$ representing the dimensionless time, borehole geometry r_b/H, thermal conductivity ratio k_1/k_2 defining the double-layered ground, and the h / k ratio [m^{-1}]. It is important to note that the volumetric heat capacity values were kept consistent across all layers for simplicity.

Scenario 1 involved calculating the dimensionless mean temperature response at the borehole wall as a function of Fourier number for different borehole geometries in homogenous conditions. The ratio of r_b/H ranged from around 0.00042 to 0.005, corresponding to typical borehole diameters of 0.1 m to 0.15 m and lengths of 15 m to 120 m.

Scenario 2 aimed to examine the accuracy of the MVQ solution in the multilayered ground. The range of thermal conductivity ratios investigated spanned from 1 to 1/4. This range covers the typical thermal conductivity values observed in geological materials, which typically fall within the range from 1.00 to 4.00 $Wm^{-1}K^{-1}$ [157].

Scenario 3 investigated the influence of the ground surface condition. The overall heat transfer coefficient h theoretically ranges between 0 and infinite, representing a perfectly insulated and a first-type boundary condition at the ground surface, respectively. The actual value of h varies under diverse ambient conditions, including factors such as wind speed, vegetation [171, 172], snow cover [173, 174], and insulation layers [175]. In alignment with established solutions [50, 51, 82], our study examined two theoretical extreme values (0 and infinite) for h and an additional value of 0.5 m^{-1} for the h / k ratio.

Scenarios 4 and 5 incorporated the heat transfer inside the borehole. The specific details and values for the input parameters related to the internal region can be found in Table 5-2. In these two scenarios, a comprehensive 3-D FE model was developed for verification. The details of the 3-D FE model have been extensively discussed in our previous study [72]. In Scenario 4, the heat-carrying fluid within the borehole is assumed to have a slightly higher temperature than the surrounding ground, and it continuously releases heat at a rate of q_l = 1 Wm^{-1}. In the same way as calculating thermal response factors, Scenario 5 evaluated the temperature change, averaged over the borehole wall surface, responding to a unit heat flux at the ground surface. In this scenario, the heat load on the BHE is set to zero.

Table 5-2. Input parameters for the internal region

Parameter	**Symbol**	**Value**
Grout thermal conductivity	k_g	1.47 $Wm^{-1}K^{-1}$
Grout volumetric heat capacity	$(\rho c)_g$	3.21×10^6 $Jm^{-3}K^{-1}$
Pipe thermal conductivity	k_p	0.38 $Wm^{-1}K^{-1}$
Fluid thermal conductivity	k_f	0.60 $Wm^{-1}K^{-1}$
Fluid volumetric heat capacity	$(\rho c)_f$	4.11×10^6 $Jm^{-3}K^{-1}$
Fluid viscosity	μ	0.00255 $kgm^{-1}s^{-1}$
Volumetric fluid flow rate	V	0.00271 m^3s^{-1}
Borehole length	H	70 m
Borehole radius	r_b	45.95 mm
Pipe outer radius	r_o	13.35 mm
Pipe wall thickness		2.45 mm
Shank spacing	d	48.00 mm

5.4. Results and discussion

5.4.1 Verification

In order to verify the MVQ solution, it was compared the exact solution and the numerical results under a homogeneous condition. In this verification process, a uniform heat flow rate was maintained at all times.

Figure 5-7 depicts the relationship between the dimensionless mean borehole wall temperature and the Fourier number for a BHE with three different r_b/H ratios. For each r_b/H ratio, the dimensionless mean temperature response demonstrates a monotonic increase as the Fo increases, eventually reaching a steady state. Over the simulation period, minor discrepancies were observed between the MVQ solution and the exact solution, particularly for longer times. For example, at $Fo = 2 \times 10^5$, the relative error was measured to be 0.20%, 0.15%, and 0.07% for BHE with r_b/H ratios of 0.00042, 0.0015, and 0.005, respectively. Given that the maximum error was observed in the short borehole scenario, the subsequent examination continued with the same borehole geometric parameters.

In Figure 5-8, the dimensionless mean temperature response at the borehole wall is presented as a function of Fourier number. As the exact solution is unavailable, the comparison is only conducted between the MVQ solution and the numerical results. Similar to the homogeneous condition, minor discrepancies were observed at longer times. At the end ($Fo = 2 \times 10^5$), the maximum relative difference was found to be 0.20%, 0.32%, and 0.61% for double-layered ground with k_1/k_2 ratios of 1, 1/2, and 1/4, respectively. It is noted that the value of $Fo = 2 \times 10^5$ corresponds to about 35.8 years for a geologic material with a thermal diffusivity of 10^{-6} m^2s^{-1} (such as clay and sandstone) when considering a borehole diameter of 0.15 m. Further testing revealed that reducing

the size of the surface elements leads to a decrease in the observed discrepancies. Nevertheless, this refinement results in a notable rise in computational time. In our current study, the solution error was found to be less than 0.61% with four surface elements. This level of accuracy is deemed satisfactory to confirm the correctness of the MVQ solution.

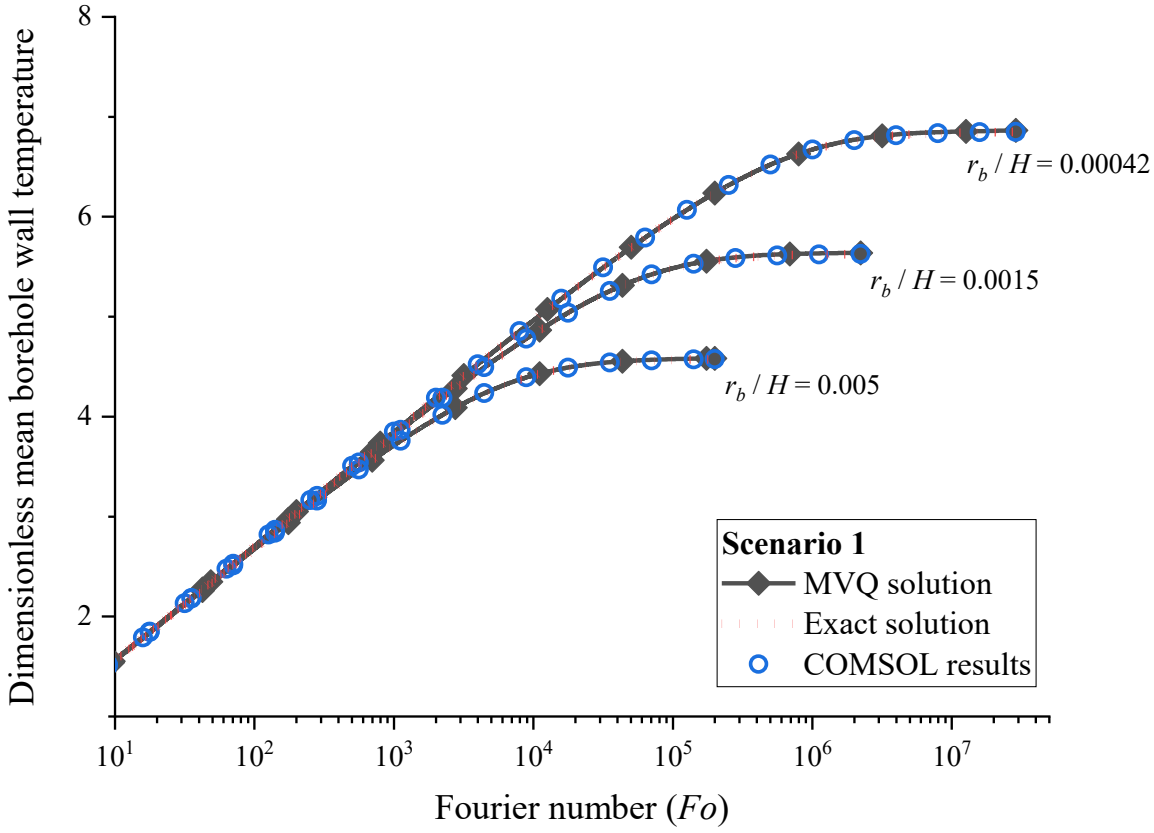

Figure 5-7. The dimensionless mean temperature response at the borehole wall as a function of Fourier number for three different borehole geometries in homogenous conditions.

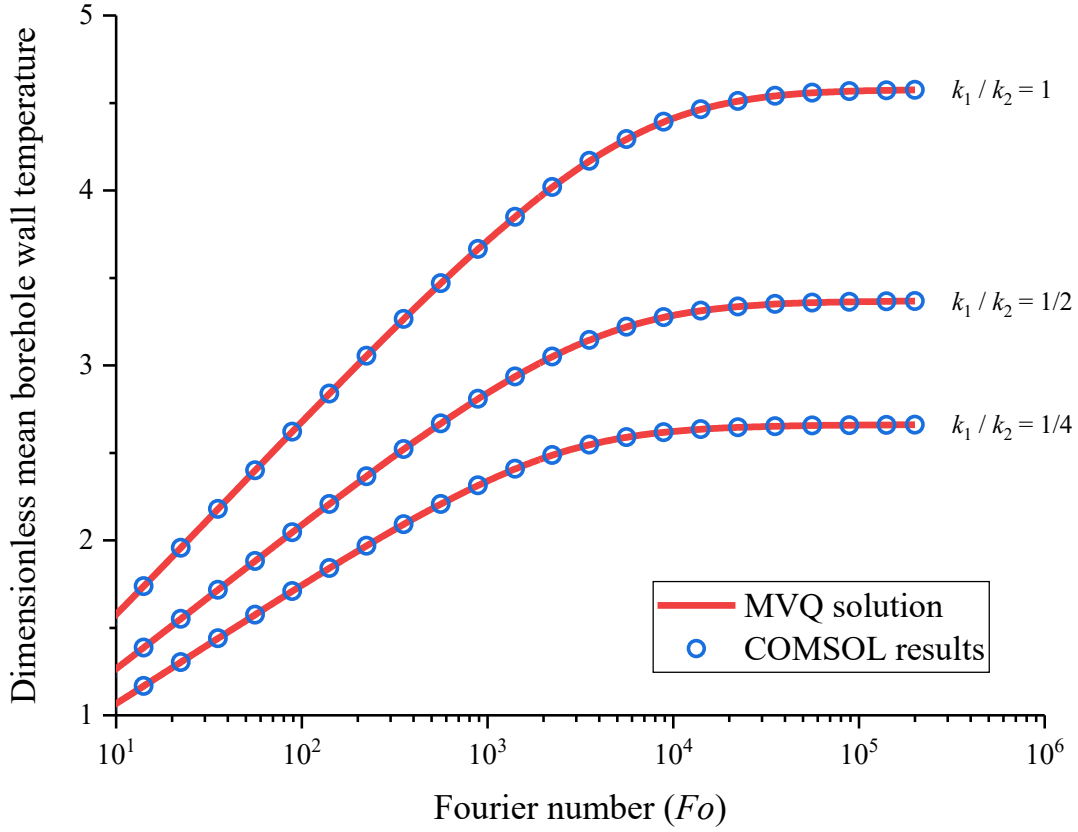

Figure 5-8. The dimensionless mean temperature response at the borehole wall as a function of Fourier number for three different thermal conductivity ratios.

5.4.2 Effects of ground surface boundary conditions

Existing analytical solutions [27-29, 35, 59, 68, 72] for BHEs often utilize the homogeneous boundary condition of the first-type at the ground surface, assuming that the ground surface temperature remains zero. The first-type boundary condition can be seen as a special case of the third-type boundary condition, where the h / k ratio approaches infinity. To evaluate the impact of ground surface boundary conditions, the finite line source (FLS) solution derived by Claesson and Javed [29] employing the homogeneous boundary condition of the first-type is considered as the

benchmark. The relative difference between the mean borehole wall temperature using first-type and third-type surface boundaries can be defined as

$$\text{Relative difference} = 100\% \times \left(\frac{\theta_E\left(\frac{h}{k}\right)}{\theta_{FLS}} - 1 \right) \tag{5-46}$$

Consistent with the FLS solution [29], only homogeneous boundary conditions were considered in these calculations. Figure 5-9 illustrates the relative differences observed at various *Fo* values, corresponding to different *h* / *k* ratios. Both the MVQ solution and the exact solution are presented in the plot, and they show a strong agreement with each other throughout the simulation period. In Figure 5-9, the relative difference exhibits an increase as the *h* / *k* ratio decreases. Specifically, the relative difference spans from 1.2% to 26.3% as the *h* / *k* ratio varies from 5 m^{-1} to 0 (perfectly insulated) for $Fo = 2 \times 10^5$. This trend is attributed to the fact that a smaller *h* / *k* ratio signifies stronger thermal insulation at the ground surface, thereby enhancing the heat accumulation below the ground surface. In contrast, the traditional finite line source (FLS) solution neglects thermal insulation, resulting in an underestimation of the temperature response in the ground. Besides, for a given borehole length, the relative differences tend to increase as the *Fo* value increases. For instance, when $Fo < 10^3$, the relative differences remain below 5%; for $Fo = 2 \times 10^5$, the relative differences range from 26.3% to 1.2% as the *h* / *k* ratio varies from 0 (perfectly insulated) to 5, indicating a significant impact of the ground surface condition on BHE performance. This increase in relative differences over time highlights the growing influence of the ground surface condition on the BHE system, as heat requires time to diffuse through the subsurface.

It is crucial to acknowledge that many real-world scenarios may involve small values of h, primarily due to the thermal insulation effect of the ground cover. For instance, BHE systems find widespread use in thermal energy storage applications, as highlighted in studies [175-178]; In these applications, the ground is covered by a layer of insulation to prevent heat losses to the environment. Commonly used insulating materials with thermal conductivities between 0.03 and 0.05 $Wm^{-1}K^{-1}$ [179] can reduce the value of h to less than 0.25 $Wm^{-2}K^{-1}$, when there is a 0.2 m insulation layer [178]. Another scenario is the presence of seasonal snow cover in cold climates, which acts as an insulator of the ground and dampens surface temperature variations. For long-term thermal analysis considering the effects of snow cover on ground temperatures, the snow cover can be represented as a simple constant thermal resistance based on its thickness and thermal conductivity [180]. Assuming a thermal conductivity of snow cover as 0.26 $Wm^{-1}K^{-1}$ and a maximum depth of about 0.8 m as given in [181], the resulting overall heat transfer coefficient can be as small as 0.325 $Wm^{-2}K^{-1}$ associated with the thermal resistance of the snow layer. In general, it is crucial to incorporate the thermal insulation effects at the ground surface in BHE analyses, with a careful consideration of the value of h, particularly for short BHE systems in the long term.

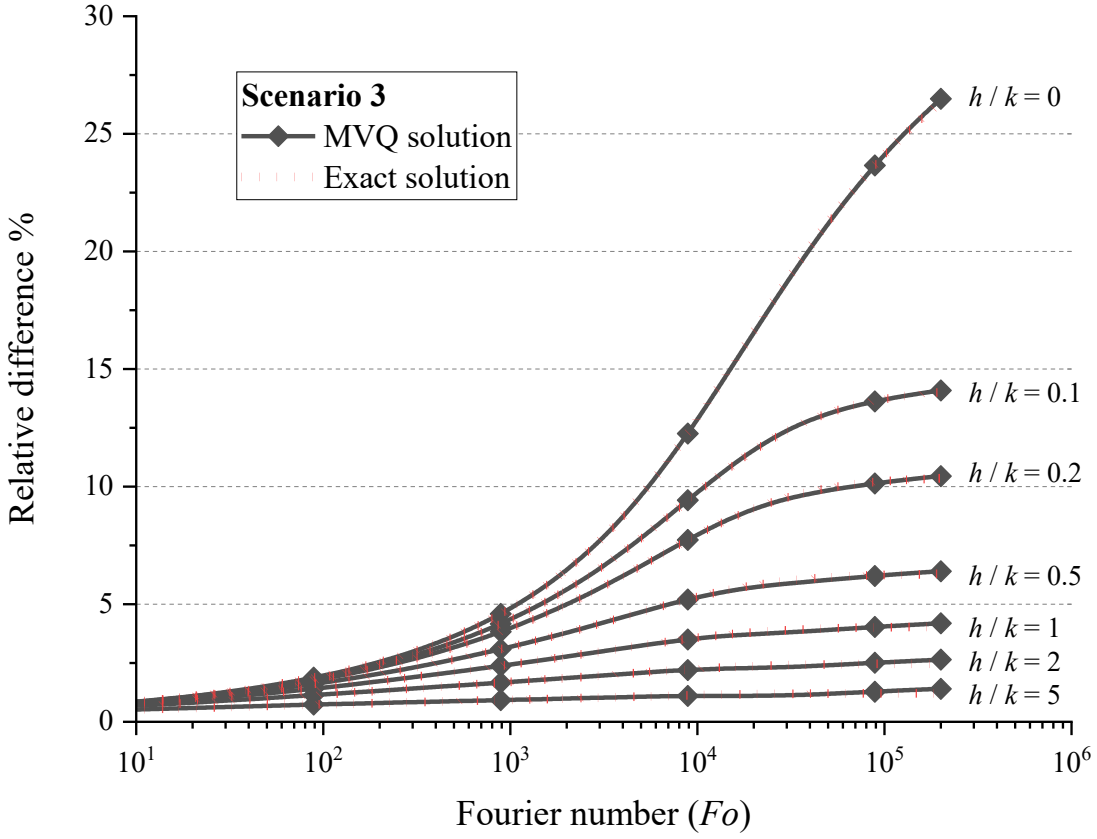

Figure 5-9. Relative differences between solutions with first-type and third-type surface boundary conditions at various *Fo* values correspond to different *h* / *k* ratios.

5.4.3 Synergistic effects of the heat-carrying fluid circulation

In the previous analysis, the results were presented based on the assumption of a uniform heat transfer rate along the borehole length, neglecting the influence of the heat-carrying fluid circulation. When the heat-carrying fluid circulates within the borehole, it transports and redistributes heat along the length of the borehole [72]. Therefore, it is essential to investigate the synergistic effect of the circulating fluid and the ground surface condition in the heat transfer analysis.

Figure 5-10 illustrates the dimensionless temperature profiles along the length of the borehole for different ground surface boundary conditions at different times. Under the circumstance of two ground layers, the higher thermal conductivity facilitated a faster dissipation of heat to distant locations in the lower ground layer. Consequently, at the borehole wall, the temperature change in the lower layer is relatively smaller compared with that in the upper layer. By comparing the temperature profiles, it becomes evident that the impact of the ground surface condition can be observed throughout the entire borehole. In comparison to the case with $h/k = 0.5$, employing the first-type boundary condition underestimates the mean borehole wall temperature by 0.88%, 1.44%, and 1.87% at approximately 1 year, 10 years, and 80 years, respectively. Furthermore, in comparison to the case with the perfectly insulated ground surface ($h/k = 0$), the underestimation is even more significant. It exceeded 1.61%, 3.74%, and 8.34% at approximately 1 year, 10 years, and 80 years, respectively. In this case, the underestimation of temperature was still notable at 70 m below the ground surface, which corresponds to the bottom of the borehole. The underestimation exceeded 1.27%, 2.99%, and 6.85% at approximately 1 year, 10 years, and 80 years, respectively. This finding contradicts the observations in the literature. Established analytical solutions [50-53, 82] that employ the third-type boundary conditions have reported that the impact of the ground surface condition diminishes a few metres below the surface. For instance, in the scenario investigated by Rivera et al. [50], the depth impacted by the ground surface condition was found to be less than 7.5 m at steady-state conditions ($Fo = \infty$).

The contrasting results in our study can be attributed to the influence of heat-carrying fluid circulation. The circulation of the fluid within the borehole results in a non-uniform distribution of the heat transfer rate along the depth of the borehole, as shown in Figure 5-11. In comparison to the homogeneous boundary condition of the first-type, the third-type boundary condition results

in reduced heat transfer near the ground surface and more heat transfer at greater depths. With more heat being injected at greater depths, the surrounding temperature accordingly experiences a greater increase. By incorporating the ground surface condition with the heat-carrying fluid circulation, the MVQ solution prevents underprediction of temperatures at greater depths. Consequently, using the MVQ solution avoids overestimation of the geothermal potential, and helps prevent undersized designs.

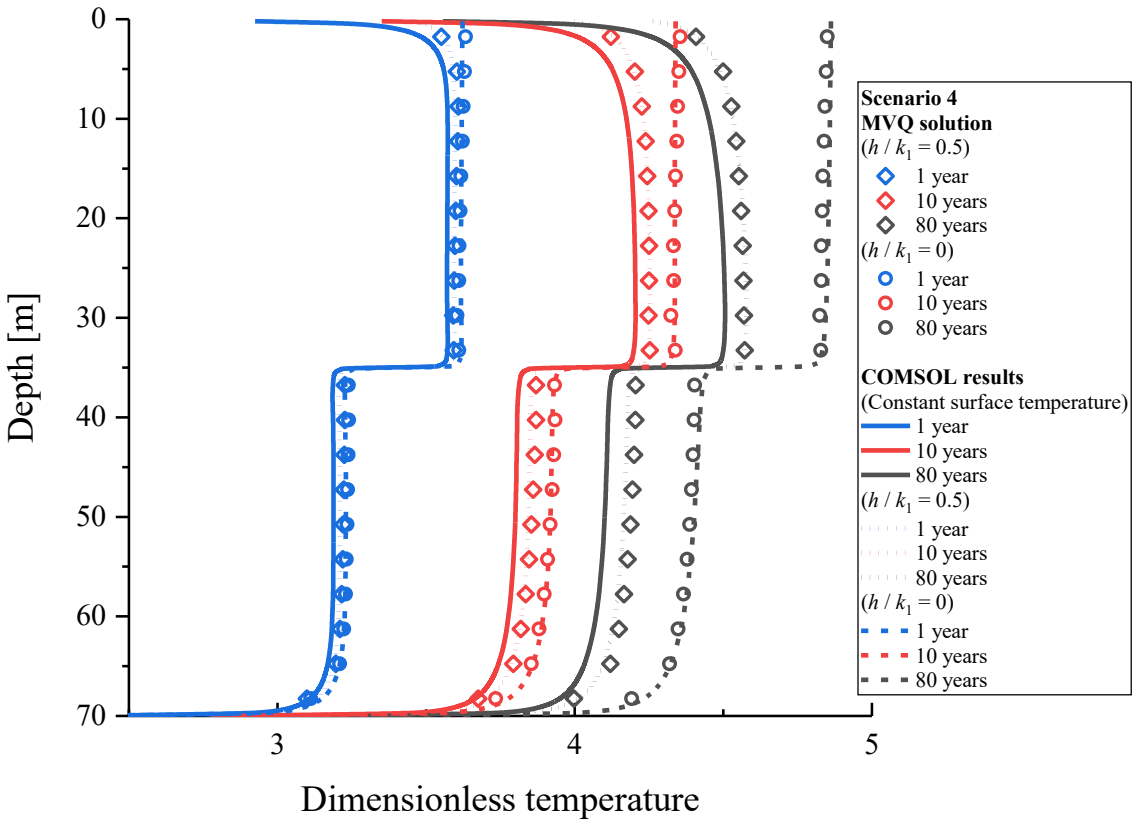

Figure 5-10. Dimensionless temperature profiles along the borehole length at three different times.

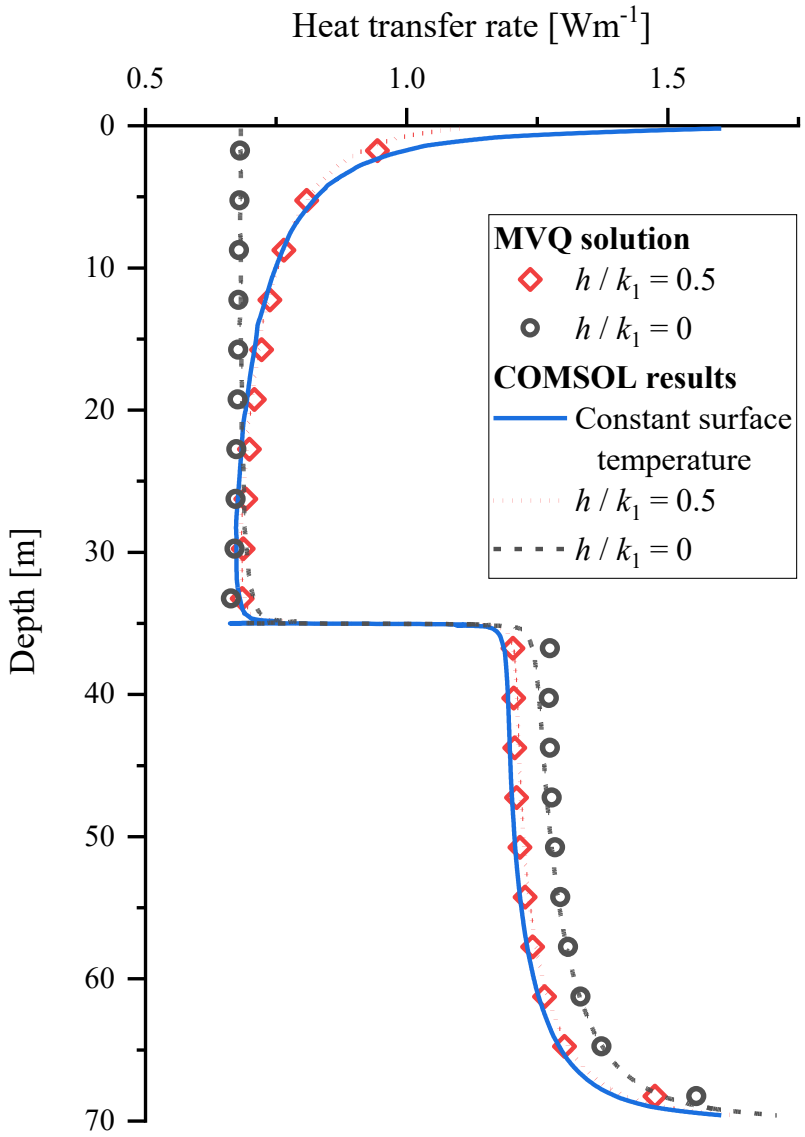

Figure 5-11. Heat transfer rate profiles at about 80 years

5.4.4 Influence of the nonhomogeneous boundary condition on the temperature

One primary characteristic of the MVQ solution is to include the contribution of the nonhomogeneous boundary condition. Figure 5-12 presents the dimensionless mean borehole wall temperature resulting from a unit heat flux at the ground surface. The temperature response

demonstrates a consistent increase as the *Fo* value increases, indicating that the nonhomogeneous ground surface condition has an impact on the long-term temperature changes in the ground. The influence of the nonhomogeneous boundary condition is crucial in practical BHE applications, particularly when there is a disparity between heating and cooling loads. In cold climates such as Edmonton (Alberta, Canada), the annual heating load is significantly higher (3.8-fold) than the annual cooling load [182]. When operating the BHE system for heating purposes, the ambient temperature is typically colder than the ground temperature, resulting in heat loss from the ground surface to the surrounding environment. Excess cooling at the ground surface can accumulate in the ground, gradually lowering the average temperature over time. In this case, neglecting the nonhomogeneous boundary condition may overestimate the thermal potential of the ground, leading to undersized designs of ground heat exchangers. Undersized designs can limit the heat transfer capacity of the system, causing insufficient heating performance and potentially requiring additional heating sources. By accounting for the nonhomogeneous boundary condition, the MVQ solution aids in preventing undersized designs of BHE systems, optimizing their performance, and maximizing energy efficiency.

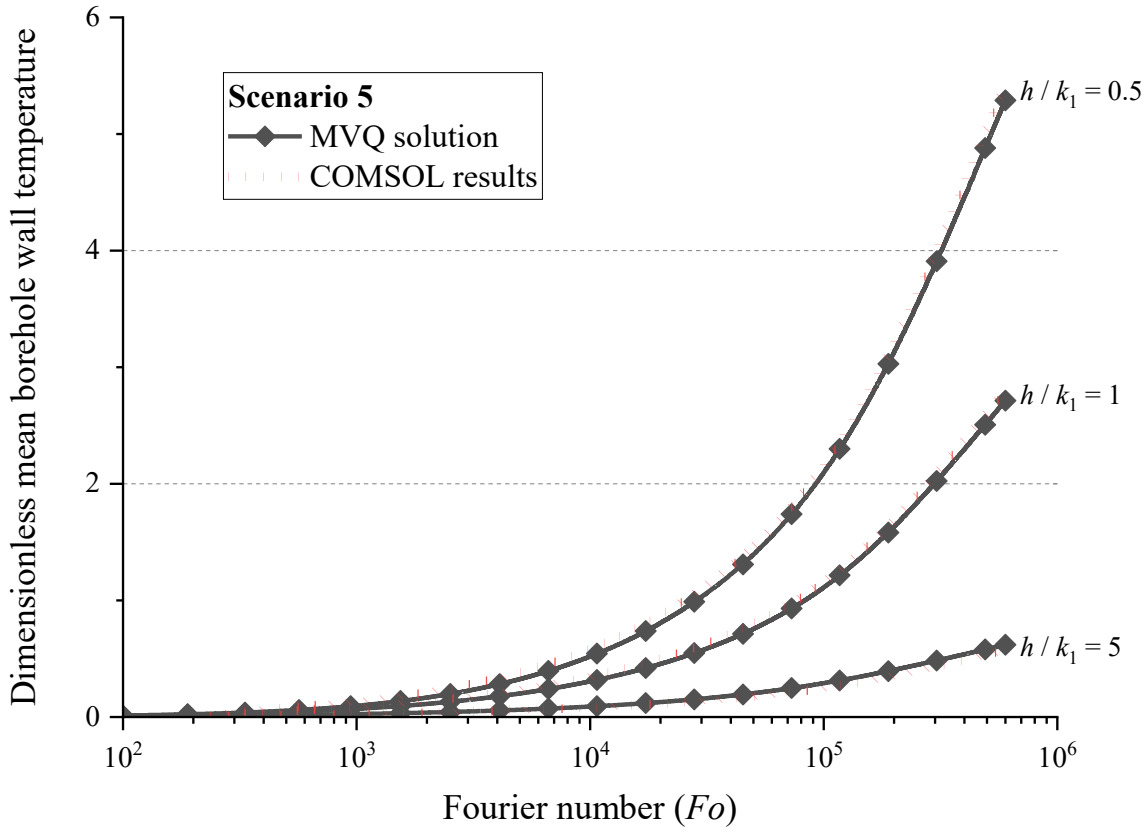

Figure 5-12. The dimensionless mean borehole wall temperature response to a unit heat flux at the ground surface as a function of Fourier number.

5.5. Conclusion

This study presents an innovative solution for borehole heat exchangers (BHEs) drilled in the layered ground, incorporating a third-type boundary condition. This solution extends the MVQ solution (Multilayered ground with Varying heat transfer rates) proposed in our previous study. The significant contribution of this study lies in accounting for the impact of the ground surface condition. Additionally, the MVQ solution exhibits remarkable accuracy, making it a valuable tool for improving the BHE design. Based on the study, the following conclusions can be drawn:

(1) The MVQ solution was verified by comparing it with an exact solution (i.e., line heat source solution) in the homogenous ground. The maximum relative error was found to be less than 0.2% between the MVQ solution and the exact solution. Additionally, the MVQ solution was compared with a two-dimensional finite element model created using COMSOL Multiphysics, and the maximum relative difference was found to be less than 0.61%. These minor discrepancies are deemed acceptable within engineering applications. The MVQ solution, given its remarkable accuracy, holds significant potential for designing BHEs.

(2) The influence of the ground surface condition was addressed in the MVQ solution. It has been observed that this influence is particularly significant in the case of short boreholes for a longer period of time. For the given parameters in this study, the relative difference from different boundary conditions may be up to 26.3% for a 15-metre BHE at $Fo = 2 \times 10^5$. By accounting for the impact of the ground surface condition, the MVQ solution enables accurate prediction of the ground temperature. Consequently, this solution can contribute to refining the design of BHE systems.

(3) It is the first time to consider the synergistic effect of the circulating fluid and the ground surface condition in analytical solutions. This synergistic effect leads to an extension of the impact of the ground surface boundary to greater depths. In comparison to the case with a perfectly insulated ground surface, employing the first-type boundary condition leads to a notable underestimation of the temperature in the ground by approximately 8.34%. Such underestimation is even apparent at a depth of 70 meters below the ground surface, with a value of 6.85%. By incorporating the heat transfer inside the borehole, the MVQ solution

prevents underprediction of temperatures at greater depths. This is crucial for accurate temperature analysis and preventing undersized designs of BHE systems.

Appendix 5-C. Green's functions and their integrals used in the study

The Green's functions G_{Z32}, G_{Z22}, and G_{z20}, used to describe the topmost, intermediated and bottommost ground layers, can be found in Appendix X of the book [135]

$$G_{Z32}(z,t\,|\,z',\tau)=\frac{2}{L_i}\sum_{m=1}^{\infty}\left\{\frac{\beta_m^2+B^2}{\beta_m^2+B^2+B}\exp\left[-\frac{\beta_m^2\alpha_i(t-\tau)}{L_i^2}\right]\cos\left[\beta_m\left(1-\frac{z}{L_i}\right)\right]\cos\left[\beta_m\left(1-\frac{z'}{L_i}\right)\right]\right\} \quad \text{(C-1)}$$

$$G_{Z22}(z,t\,|\,z',\tau)=\frac{1}{2\sqrt{\pi\alpha_i(t-\tau)}}\sum_{m=-\infty}^{\infty}\left\{\exp\left[-\frac{(2mL_i+z-z')^2}{4\alpha_i(t-\tau)}\right]+\exp\left[-\frac{(2mL_i+z+z')^2}{4\alpha_i(t-\tau)}\right]\right\} \quad \text{(C-2)}$$

$$G_{Z20}(z,t\,|\,z',\tau)=\frac{1}{2\sqrt{\pi\alpha_I(t-\tau)}}\left\{\exp\left[-\frac{(z-z')^2}{4\alpha_I(t-\tau)}\right]+\exp\left[-\frac{(z+z')^2}{4\alpha_I(t-\tau)}\right]\right\} \quad \text{(C-3)}$$

where $B=\frac{h}{k_1}L_1$ and $\beta_m\tan\beta_m=B$ is the eigencondition.

The integrals of these Green's functions over z' for a line heat source segment ($D_{j-1}<z'<D_j$) are

$$\int_{z'=D_{j-1}}^{D_j} G_{Z32}(z,t\,|\,z',\tau)dz'$$

$$= \frac{2}{\beta_m}\sum_{m=1}^{\infty}\left\{\frac{\beta_m^2+B^2}{\beta_m^2+B^2+B}\exp\left[-\frac{\beta_m^2\alpha_i(t-\tau)}{L_i^2}\right]\right. \tag{C-4}$$

$$\left.\times\cos\left[\beta_m\left(1-\frac{z}{L_i}\right)\right]\left\{\sin\left[\beta_m\left(1-\frac{D_{j-1}}{L_i}\right)\right]-\sin\left[\beta_m\left(1-\frac{D_j}{L_i}\right)\right]\right\}\right\}$$

$$\int_{z'=D_{j-1}}^{D_j} G_{Z22}(z,t\,|\,z',\tau)dz'$$

$$= \frac{1}{2}\sum_{m=-\infty}^{\infty}\left\{\mathrm{erf}\left(\frac{2mL_i+z-D_{j-1}}{\sqrt{4\alpha_i(t-\tau)}}\right)-\mathrm{erf}\left(\frac{2mL_i+z-D_j}{\sqrt{4\alpha_i(t-\tau)}}\right)\right. \tag{C-5}$$

$$\left.-\mathrm{erf}\left(\frac{2mL_i+z+D_j}{\sqrt{4\alpha_i(t-\tau)}}\right)+\mathrm{erf}\left(\frac{2mL_i+z+D_{j-1}}{\sqrt{4\alpha_i(t-\tau)}}\right)\right\}$$

$$\int_{z'=D_{j-1}}^{D_j} G_{Z20}(z,t\,|\,z',\tau)dz'$$

$$= \frac{1}{2}\left\{\mathrm{erf}\left[\frac{z-D_{j-1}}{\sqrt{4\alpha_I(t-\tau)}}\right]-\mathrm{erf}\left[\frac{z-D_j}{\sqrt{4\alpha_I(t-\tau)}}\right]+\mathrm{erf}\left[\frac{z+D_j}{\sqrt{4\alpha_I(t-\tau)}}\right]\right. \tag{C-6}$$

$$\left.-\mathrm{erf}\left[\frac{z+D_{j-1}}{\sqrt{4\alpha_I(t-\tau)}}\right]\right\}$$

The Green's function G_{R00} in Equation (5-9) is challenging to integrate over *r'*, thus its other form is considered [51]

$$\frac{1}{4\pi\alpha(t-\tau)}exp\left(-\frac{r^2+r'^2}{4\alpha(t-\tau)}\right)I_0\left(\frac{rr'}{2\alpha(t-\tau)}\right)$$

$$= \frac{1}{2\pi}\int_{\beta=0}^{\infty}\exp[-\alpha(t-\tau)\beta^2]J_0(\beta r)J_0(\beta r')\beta d\beta \tag{C-7}$$

where $J_0(X)$ is a zero-order Bessel function of the first kind. This form allows the independent computation of the integral over *r'* and the average over *r*, since they are performed on separate terms,

$$\int_{r'=r_{m-1}}^{r_m} J_0(\beta r')2\pi r' dr' = \frac{2\pi}{\beta}[r_m J_1(\beta r_m) - r_{m-1}J_1(\beta r_{m-1})] \tag{C-8}$$

$$\frac{1}{\pi(r_n^2 - r_{n-1}^2)}\int_{r=r_{n-1}}^{r_n} J_0(\beta r)2\pi r dr = \frac{2}{\beta(r_{n-1}^2 - r_n^2)}[r_n J_1(\beta r_n) - r_{n-1}J_1(\beta r_{n-1})] \tag{C-9}$$

where $J_1(X)$ is a first-order Bessel function of the first kind.

Chapter 6. Long-term performance of a vertical ground heat exchanger: a monthly simulation-based analysis

6.1. Introduction

To mitigate the severe consequences of climate change, nations worldwide have united under the banner of achieving net-zero emissions by 2050 [120]. One pivotal factor in attaining this goal is addressing the considerable contribution of heat consumption to global CO_2 emissions, which accounts for more than 40% (13.1 Gt) of energy-related CO_2 emissions in 2020 [163]. This statistic underscores the pressing need to tackle heat-related emissions, thereby underscoring the necessity for adopting high-efficiency heating and cooling systems. Among various measures to reduce the carbon footprint associated with heating, ground source heat pump systems (GSHP) have garnered increasing attention due to their potential for high energy efficiency and minimal greenhouse gas emissions [6]. By harnessing shallow geothermal energy from the Earth, GSHP systems offer a promising approach to decarbonizing the heating sector.

A typical GSHP configuration includes essential components such as distribution systems within buildings, the heat pump itself, and the ground heat exchanger [8]. As illustrated in Figure 6-1. when heating is required, a mixture of antifreeze and water circulates through the system, absorbing geothermal heat from the ground and channelling it to the heat pump. Conversely, during warmer months, excess heat is transferred back into the ground. A significant challenge in

the design phase of GSHP systems centers on the proper sizing of the ground heat exchanger to satisfy the intended heat demand over its lifespan, which can span several decades.

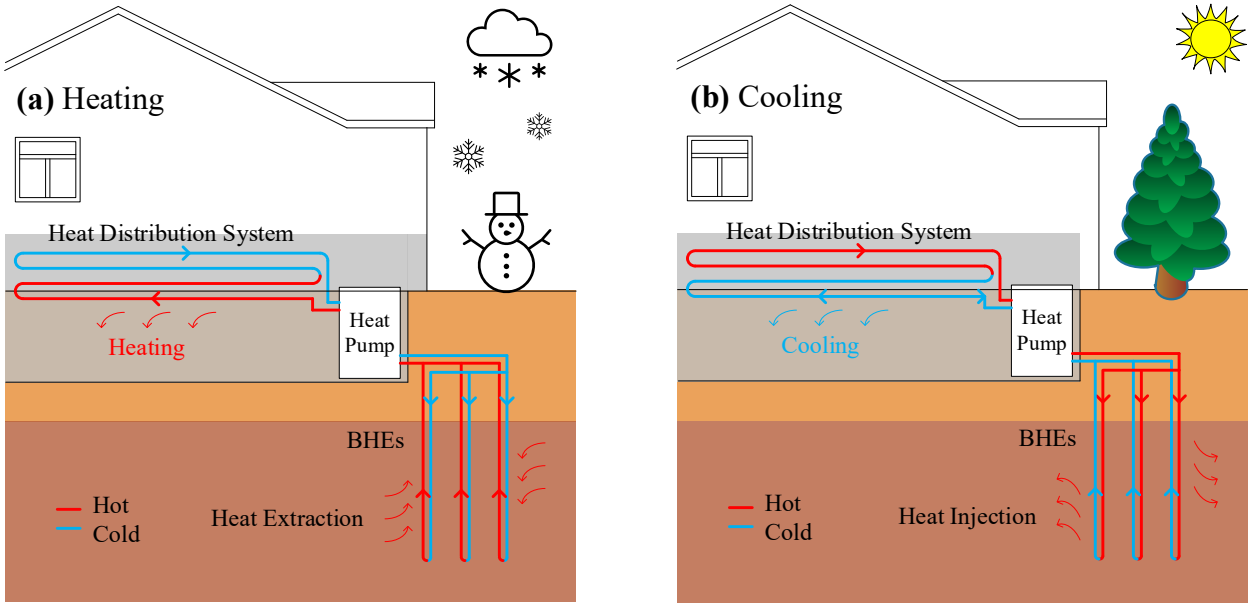

Figure 6-1. Schematics of BHEs system for space (a) heating and (b) cooling.

One of the most widely employed types of ground heat exchanger is the vertical borehole heat exchanger (BHE) [9, 85, 183]. Over the last two decades, several simulation and design tools [19-22] have been developed to facilitate the analysis of BHE systems. These tools encompasses both conductive heat transfer external to the borehole and convective heat transfer within the pipes, enabling the computation of the outlet fluid temperature. To solve the transient heat transfer problem external to a single borehole, a two-dimensional radial-axial mesh is employed, and an explicit finite difference method is utilized, as described in the study of Eskilson [23]. By superposing the solution for a single borehole across space for various geometric patterns (such as rectangular, circular, and open rectangular arrangements), the solution for borehole fields containing multiple boreholes can be evaluated [23, 49, 94]. Eskilson [23] converted the solution

of specific borehole field patterns into a set of non-dimensional thermal response factors, known as *g*-functions. These Eskilson's *g*-functions have been widely implemented in some tools such as GLHEPRO [19], Earth Energy Designer (EED) [20], eQuest [21] and EnergyPlus [22]. In contrast to the numerical approach, abundant analytical solutions [27-29, 35, 58-61, 68, 72] have been established for the transient heat transfer problem external to a single borehole. These analytical solutions offer an alternative means of calculating *g*-functions. The analytical solution [26] has also been implemented in the design tools such as Ground Loop Design (GLD) [25]. When the responses to a unit heat pulse is characterized using *g*-functions, the temperature evolution at the borehole wall due to time-varying heating and cooling loads can be predicted through the well-known Duhamel's theorem [32],

$$\Delta T(t) = \frac{1}{2\pi k_s}\frac{\partial}{\partial \tau}\int_0^t \frac{Q(t)}{H} g\left(\frac{t-\tau}{t_s}, \frac{r_b}{H}, \frac{B}{H}\right) d\tau \tag{6-1}$$

where ΔT [°C] is the temperature change at the borehole wall, k_s [$Wm^{-1}K^{-1}$] is the ground thermal conductivity, Q [W] is the time-varying heating and cooling load, H [m] is the borehole length, t and τ [s] denotes the time, and g denotes the *g*-function. A *g*-function depends on three non-dimensional parameters: (r_b/H) is the ratio of the borehole radius over the borehole length; (B/H) is the ratio of the borehole spacing over the borehole length; and (t/t_s) is the non-dimensional time where $t_s = \frac{H^2}{9\alpha}$ is the steady-state time, and α [m^2s^{-1}] is the ground thermal diffusivity. Once the borehole wall temperature is established, the fluid temperature can be approximated through a static analysis within the borehole region.

Over the past two decades, abundant (semi-)analytical solutions had been established to analyze the complex heat transfer processes for a single BHE, as alternatives to Eskilson's *g*-functions or FLS solutions. In Table 2, we present an overview of the key features and characteristics of these established solutions. In parallel with these (semi-)analytical solutions, numerical modelling is another vital tool for heat transfer analysis in the theoretical research of BHEs for studying complex and realistic scenarios, including situations involving temperature-dependent thermal properties [184, 185]. However, (semi-)analytical solutions are often favoured for engineering and practical applications due to their speed and simplicity. This preference arises because numerical simulations often demand substantial computational resources and can be time-consuming, primarily due to the large aspect ratio of the BHE and the broad time scales involved, ranging from hours to decades in lifecycle simulations.

In preceding chapters, we proposed a solution that can supplant Eskilson's *g*-functions or FLS solutions. The proposed solution is named the MVQ solution, which stands for "Multilayered ground with Varying heat transfer rates." As the name implies, a primary characteristic of the MVQ solution is to address the non-uniform distribution of heat transfer rate for a BHE within the multilayered ground. To showcase the refined method based on the MVQ solution, a long-term monthly simulation was conducted. This refined method seeks to deepen the comprehension of ground conditions in BHE simulations and to provide more accurate approximations of their long-term behaviour.

Table 6-1. Summary of heat transfer models for vertical BHE simulations.

Studies	Methods	Axial heat transfer	Layered ground profile	Ground -water flow	Nonuniformity of heat transfer rate	Robin boundary condition	Comments
Ingersoll and Plass [186], Carslaw and Jaeger [31]	Infinite line source model*	☐	☐	☐	☐	☐	It is the first presented model related to the BHE problem.
Eskilson [23], Zeng et al [27], Lamarche and Beauchamp [28]	Finite line source (FLS) model	☑	☐	☐	☐	☐	The FLS model can predict long-term responses, taking into account axial heat transfer. The integration of these solutions and the application of spatial superposition principles have been extensively used in BHE designs.
Cimmino et al. [38]	Segmented FLS	☑	☐	☐	☑	☐	To the best of the author's knowledge, this study is the first to address the non-uniformity of the heat transfer rate along the borehole length in analytical solutions. In this model, the line source is divided into multiple segments, and the ground temperature response can be evaluated by summing up the contributions from all these segments.
Abdelaziz et al. [58], Jin et al. [62]	Segmented FLS and composite section method	☑	☑	☐	☐	☐	The composite medium method, introduced by Abdelaziz et al. [58], provides reasonable approximations of ground temperature. It has been widely accepted and has been utilized in numerous other studies [62-65]. However, it is important to note that this approach is not derived directly from the governing equation, and the expression presented by Abdelaziz et al. [58] does not fulfill the ground surface boundary condition.
Luo et al. [63, 65]	Segmented FLS and composite section method	☑	☑	☐	☑	☐	The composite medium method was implemented to account for multilayered ground conditions. To the best of the author's knowledge, this solution, by accounting for variations in heat transfer rates, might significantly reduce errors in temperature

Studies	Methods	Axial heat transfer	Layered ground profile	Ground -water flow	Nonuniformity of heat transfer rate	Robin boundary condition	Comments
							predictions caused by the composite medium method.
Bnilam and Al-Khoury [125]	Spectral element method	☑	☑	☐	☑	☐	Several solutions have been proposed for a BHE within multilayered ground using various methods. From the author's perspective, the solution presented by Guo et al. [72] seems to be more easily extendable to scenarios involving more than three layers when compared to other solutions.
Pan et al. [59]	Integral-transform method	☑	☑	☐	☐	☐	
Zhang et al. [66]	Separation of variables	☑	☑	☐	☑	☐	
Guo et al. [72] (Chapter 4)	Unsteady surface element method	☑	☑	☐	☑	☐	
Diao et al. [49]	Moving infinite line source (MILS) model	☐	☐	☑	☐	☐	This model incorporated the influence of groundwater velocity on BHE responses by applying the moving source theory [31].
Molina-Giraldo et al. [35]	Moving finite line source (MFLS) model	☑	☐	☑	☐	☐	It is a combination of the FLS solution and MILS solution.
Hu [61], Erol and Francos [64]	Segmented MFLS	☑	☑	☑	☐	☐	These solutions were expanded from the MFLS solution to encompass the BHE in multilayered ground conditions. In comparison to the other two solutions, our solution effectively addresses variations in heat transfer rates over both time and depth, thus avoiding temperature overpredictions by up to 32.72%.
Guo et al. (Chapter 3)	Segmented MFLS and composite	☑	☑	☑	☑	☐	

Studies	Methods	Axial heat transfer	Layered ground profile	Ground -water flow	Nonuniformity of heat transfer rate	Robin boundary condition	Comments
	section method						
Pan et al. [82]	Integral-transform method	☑	☐	☐	☐	☑	These solutions are formulated considering a homogeneous ground with a Robin (or third-type) boundary condition. Additionally, Rivera et al. [49, 50] considered horizontal groundwater flow, while Zhou et al. [51, 52] accounted for groundwater flow in both horizontal and vertical directions.
Rivera et al. [50, 51], Zhou et al. [52, 53]	Green's function method	☑	☐	☑	☐	☑	
Guo et al. (Chapter 5)	Unsteady surface element method	☑	☑	☐	☑	☑	It is the first time to consider the synergistic effect of the circulating fluid and the ground surface condition in analytical solutions. This synergistic effect leads to an extension of the impact of the ground surface boundary to greater depths.

* Most of the listed line source models were solved using the Green's function method.

6.2. Case study

The case study focuses on simulating a single borehole heat exchanger (BHE) for a commercial building located in Edmonton, Alberta. To exemplify the refined method, this study incorporated the design specifications of the ground heat exchanger, alongside ground thermal properties and the monthly heating and cooling loads, into the MVQ solution. In parallel, a comparison was drawn by executing a simulation using the GLD software and developing a numerical model through COMSOL Multiphysics, utilizing identical input parameters for a long-term assessment.

6.2.1 Thermal properties and geometric parameters

The case study considered a simplified double-layered ground configuration, aimed at emphasizing the consequences of a non-uniform distribution of heat transfer rates in a BHE. The layer interface divided the borehole into two equal parts. The upper layer extended from the ground surface to the middle of the borehole, and the lower layer extended from there to infinity. The thermal conductivity values assigned to these layers were distinct, with 1.0 and 2.0 $Wm^{-1}K^{-1}$ for the upper and lower layers, respectively. To facilitate clarity in the discussion, the volumetric heat capacity value was kept uniform at 2.0×10^6 $Jm^{-3}K^{-1}$ for both layers. The borehole was designed based on a real world BHE project in Edmonton, Canada [97]. Its geometric parameters and thermal properties are listed in Table 6-2.

Table 6-2. Parameter inputs for simulations

Parameter	**Symbol**	**Value**
Undisturbed ground temperature	T_0	6 °C
Grout thermal conductivity	k_g	1.47 $Wm^{-1}K^{-1}$
Grout volumetric heat capacity	$(\rho c)_g$	3.21×10^6 $Jm^{-3}K^{-1}$
Pipe thermal conductivity	k_p	0.38 $Wm^{-1}K^{-1}$
Fluid thermal conductivity	k_f	0.60 $Wm^{-1}K^{-1}$
Fluid volumetric heat capacity	$(\rho c)_f$	4.11×10^6 $Jm^{-3}K^{-1}$
Fluid viscosity	μ	0.00255 $kgm^{-1}s^{-1}$
Average flow rate of working fluid	V	0.00271 m^3s^{-1}
Length of the borehole	H	70 m
Borehole radius	r_b	45.95 mm
Pipe outer radius	r_o	13.35 mm
Pipe wall thickness		2.45 mm
Shank spacing	d	48.00 mm

6.2.2 Heating and cooling loads

The building was meticulously designed to achieve net-zero energy consumption, signifying that it will generate as much energy on-site as it consumes within a year. Numerous measures were implemented to reduce the energy demands, encompassing enhancing the building envelope, installing energy-efficient mechanical systems and lighting, introducing well-insulated windows, and more. Consequently, the energy modelling revealed that the cooling demands of the building surpass its heating demands on an annual basis due to the large amounts of internal gains (coming from lightening, people, electrical equipment and appliances, solar radiations through transparent surfaces). Specifically, the annual cooling and heating loads are quantified at 140,986 and 35,013 kWh, respectively. In response to this unique energy profile, the design firm has devised a geothermal field consisting of 32 boreholes. Detailed design specifics are confidential and therefore not disclosed in this thesis.

The design firm has provided the cooling and heating load data on an hourly basis thought the year. To suit the input requirements of the design tool GLD [25], we have integrated these hourly loads into monthly data sets, as depicted in Figure 6-2. In this study, simulations were extended over a period of 30 years that is the typical lifespan of BHE systems.

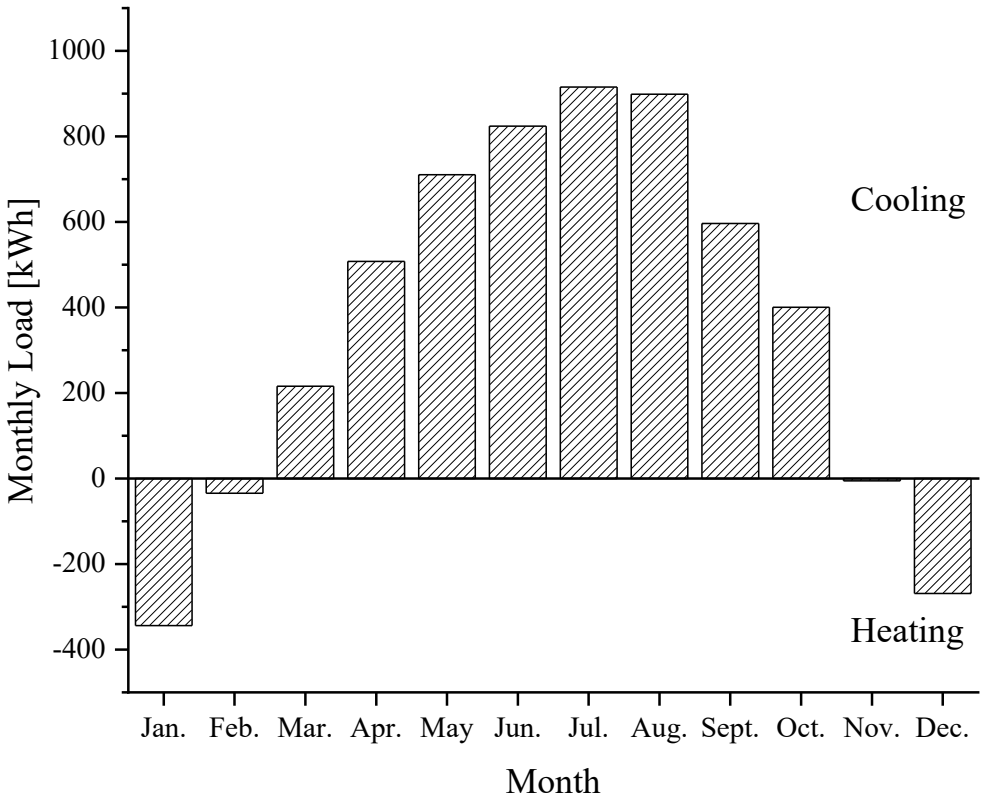

Figure 6-2. A simplified cyclic thermal load for a single borehole.

6.2.3 BHE simulation and design methods

The thermal performance of the Borehole Heat Exchanger (BHE) was assessed through three different methods, including simulation with GLD software, a numerical model built using COMSOL Multiphysics, and the refined method involving the MVQ solution.

6.2.3.1 GLD software

GLD [25] is a commercial design tool extensively employed for the design of GSHP systems. According to the International Ground Source Heat Pump Association (IGSHPA), GLD is recognized as the world's leading commercial design tool and is employed by design professionals in over 60 countries [187]. In the context of BHE design, GLD offers a dedicated Borehole Design module that serves as a comprehensive platform for inputting various design parameters. These parameters are organized into distinct panels that align with specific categories such as fluid, soil, and bore. Once parameters have been filled, the software then undertakes calculations to determine key outputs such as borehole wall temperature and fluid temperature. The calculation process is outlined in Figure 6.3 and is also employed in many other design tools [19-22], making it a commonly used approach for BHE system design. Overall, GLD's efficient framework streamlines the entire design process, making it user-friendly and intuitive for engineers in the field.

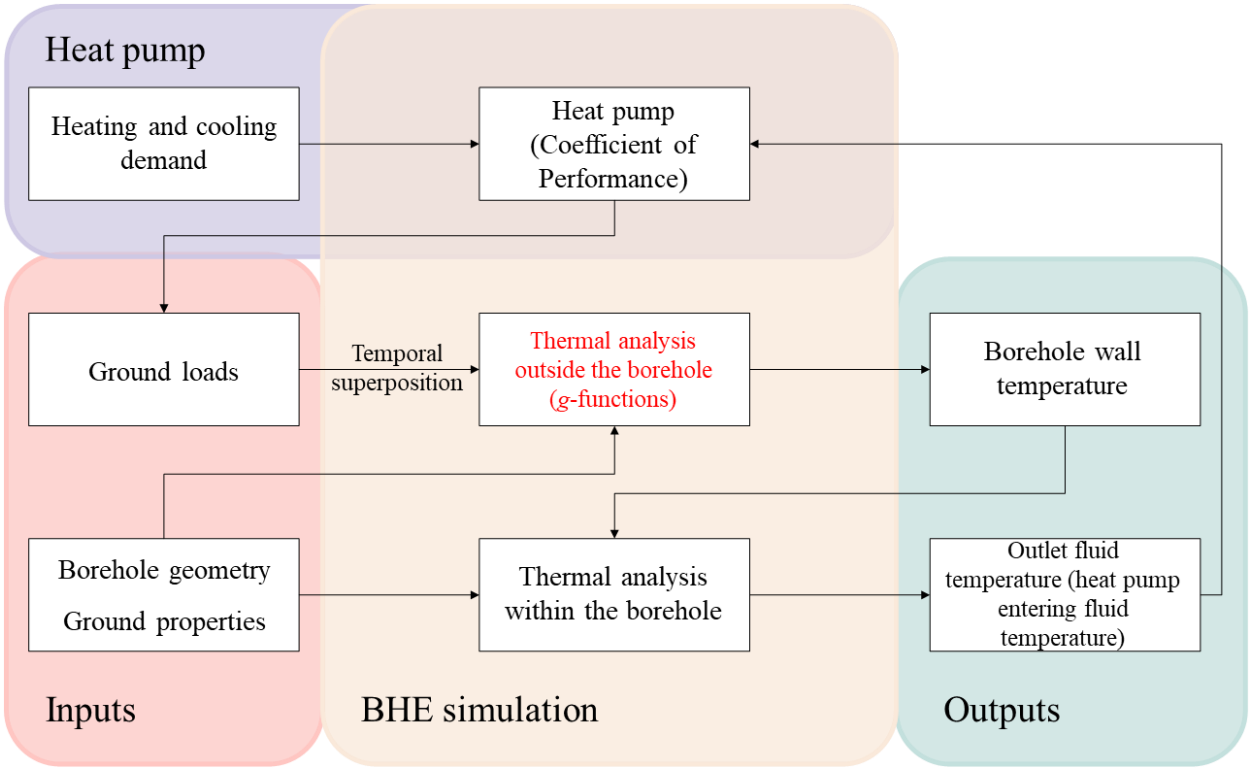

Figure 6-3.The flowchart of the BHE simulation process commonly used in BHE design tools.

Within the GLD software, the double-layered ground configuration under investigation was simplified into a homogeneous body, as boxed in Figure 6-4 (b). Consequently, the effective thermal properties were automatically derived through the computation of a weighted arithmetic mean value. It is important to acknowledge that such a simplification overlook the complexities inherent in the actual system, potentially leading to insufficient designs. The limitations of this simplification will be discussed in detail in Section 6.3.

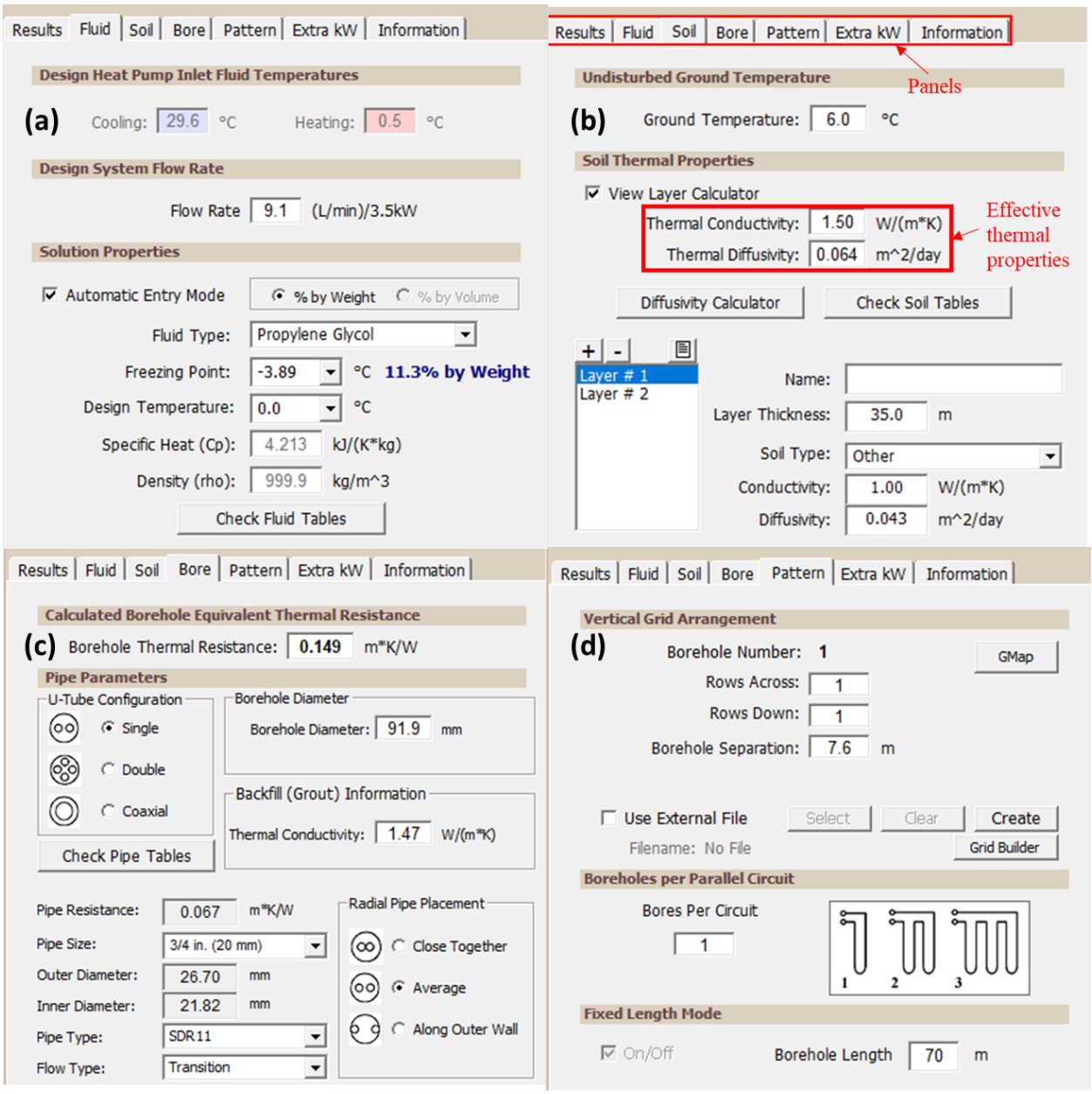

Figure 6-4. User interfaces of the GLD for inputting design parameters in categories such as (a) circulating fluid, (b) the ground, (c) borehole, and (d) borehole field arrangement.

6.2.3.2 Numerical model

The thermal behaviour of the BHE and its surrounding can also be simulated through numerical models constructed in a finite element (FE) software package. However, the numerical modelling

and simulation of transient heat transfer within the BHE prove to be significantly computationally intensive due to the extreme aspect ratio of the BHE [188]. In order to mitigate the computational burden, Al-Khoury and Bonnier [189] first introduced an approach of using one-dimensional finite element representations to model the region within the BHE. Furthermore, in an alternative strategy, Diersch et al. [188] proposed that the region within the BHE can be modelled utilizing an analytical model, i.e., the delta-circuit thermal resistance model [136]. This model was developed on the assumption that thermal equilibrium is immediately established between the inlet and outlet pipes at any given time. For long-term predictions, the analytical solution under this assumption has demonstrated notable accuracy and reliability, thereby offering a viable approach [137].

The strategy proposed by Diersch et al. [188] was implemented within the framework of this study to mitigate computational requirements. More specifically, we seamlessly integrated COMSOL Multiphysics with MATLAB using the LiveLink for MATLAB, as depicted in Figure 6-5. This feature enabled the creation of a MATLAB file version of simulations developed in COMSOL Multiphysics. With this functionality, we utilized the COMSOL Multiphysics solvers to handle transient heat transfer outside the borehole, while concurrently conducting the static heat transfer analysis within the borehole using MATLAB computing software.

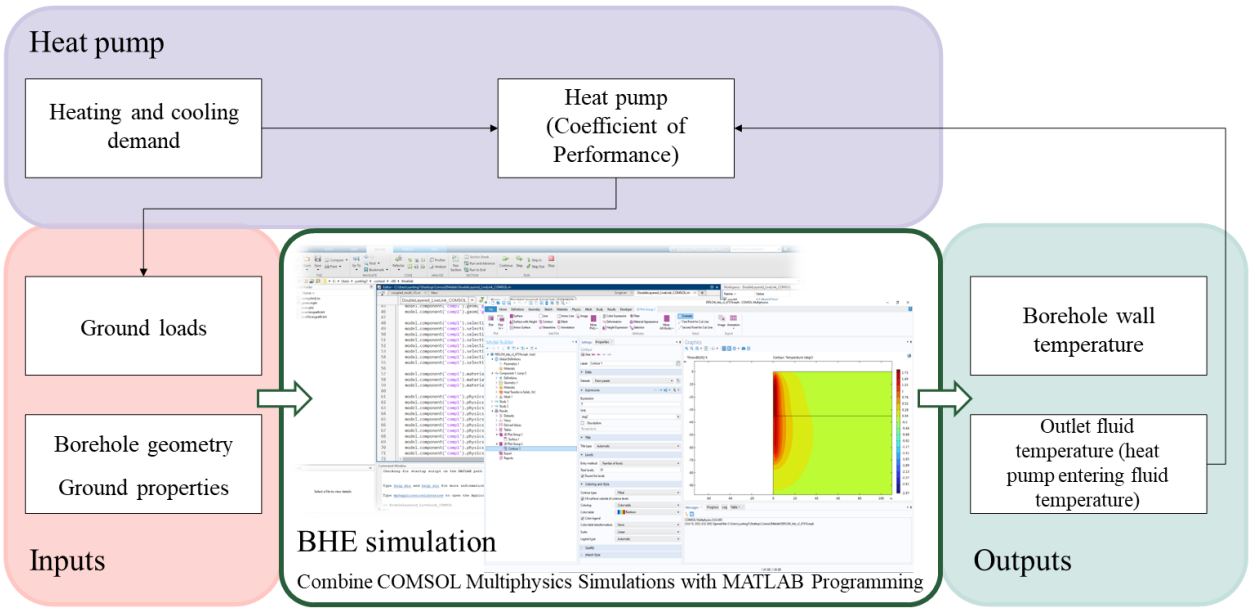

Figure 6-5. The illustration of the BHE simulation using numerical modelling. This simulation seamlessly integrates COMSOL Multiphysics with MATLAB, allowing the modelling through programming within the MATLAB environment.

Building the COMSOL model object involves several steps:

Geometry: A two-dimensional (2-D) axisymmetric model was constructed for conducting finite element analyses. In this model, the BHE systems were represented using a set of line segments that substitutes the BHE components, including the fluid, pipes, and grout. The model domain needs to be large enough to represent the ground, which is considered a semi-infinite medium. Based on a domain independence test, it was determined that a model domain measuring 500 meters in width and 500 meters in thickness is sufficiently large. This size ensures that external boundary conditions do not disrupt the temperature distributions within the ground.

Physics: The Heat Transfer in Solids Interface is used to model the BHE problem. A uniform initial ground temperature of 6 °C was assigned to the entire domain, mirroring an undisturbed ground temperature (T_0). To model the BHE, line heat sources were applied along the line segments that represent the borehole. As exemplified in Figure 6-6, the magnitude of these line heat sources were determined by evaluating the thermal resistance model [136] within the MATLAB environment. These magnitudes can be either positive or negative, corresponding to the heat injection or extraction associated with the BHE.

Mesh: A mesh was created for the 2-D axisymmetric model. To anticipate higher temperature gradients near the borehole, a denser concentration of elements was allocated in that specific region. A common characteristic of numerical models is that their results are influenced by the mesh size. In order to mitigate this dependency, a convergence test was executed. The mesh resolution was systematically refined by progressively increasing the element count in the vicinity of the borehole and across the entire domain until a mesh-independent solution was achieved. Finally, the mesh used in the simulation is shown in Figure 6-7.

Study: A Time Dependent study was added for the transient heat transfer problem.

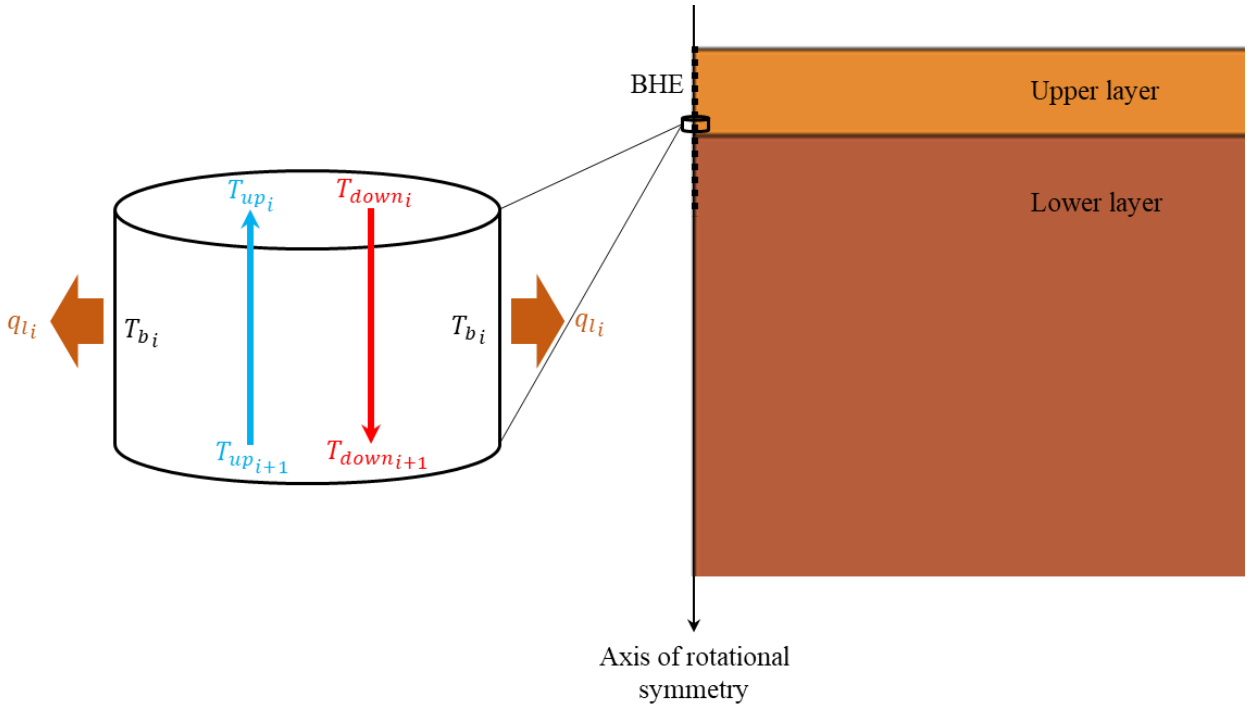

Figure 6-6. The simplification of the BHE with a series of line segments in the numerical model. These line segments are associated with a delta-circuit thermal resistance model that is tailored to simulate the heat transfer of a single U-shaped BHE.

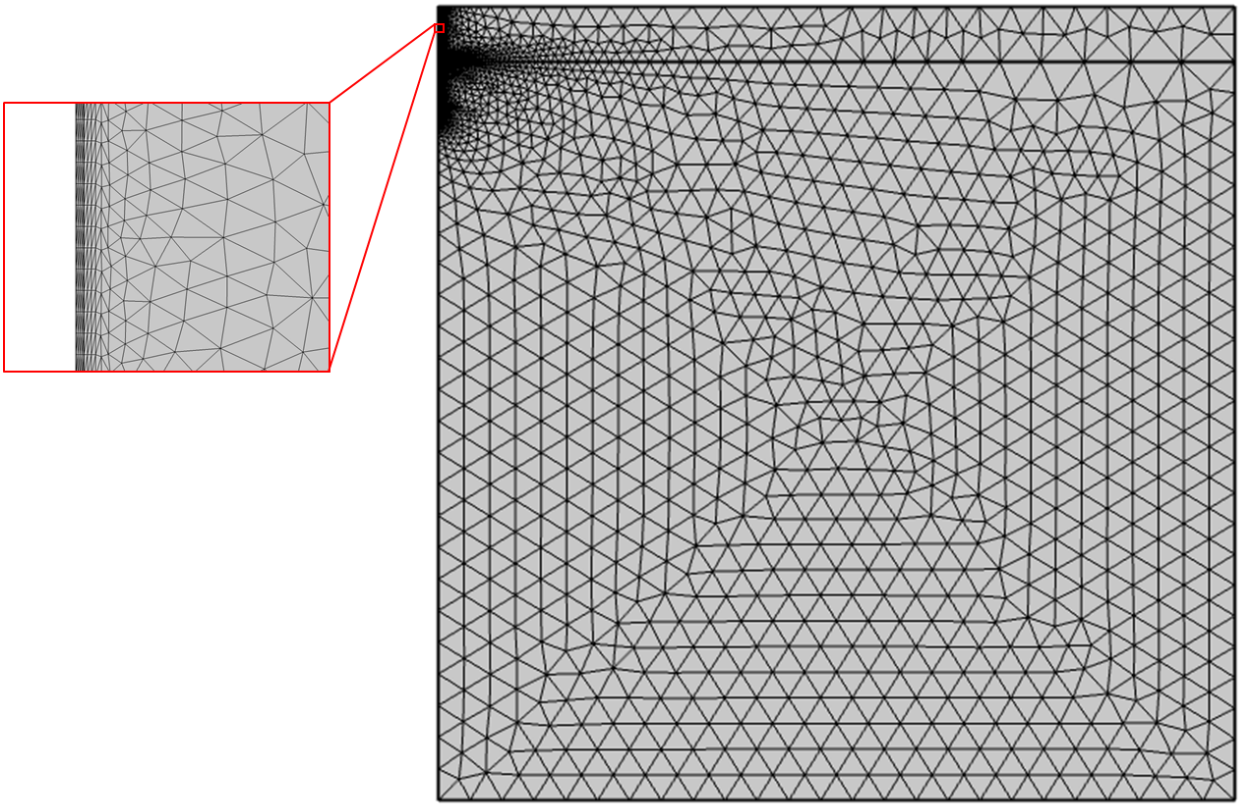

Figure 6-7. Two-dimensional triangular mesh used in numerical simulations. (Finer elements meshed at areas that were close to the borehole, and coarser elements meshed at regions that were relatively far away.)

The constructed COMSOL model object is shown in Figure 6-8. This COMSOL model object was seamlessly integrated with MATLAB through LiveLink for MATLAB. The major benefit of this integration is to command the COMSOL model using MATLAB scripts, including tasks such as updating the line heat sources. Another benefit is the ability to access results from the MATLAB workspace, allowing for tasks such as probing the borehole wall temperature. Once the COMSOL model object is constructed and the MATLAB scripts are prepared, the simulation can be executed within the MATLAB environment.

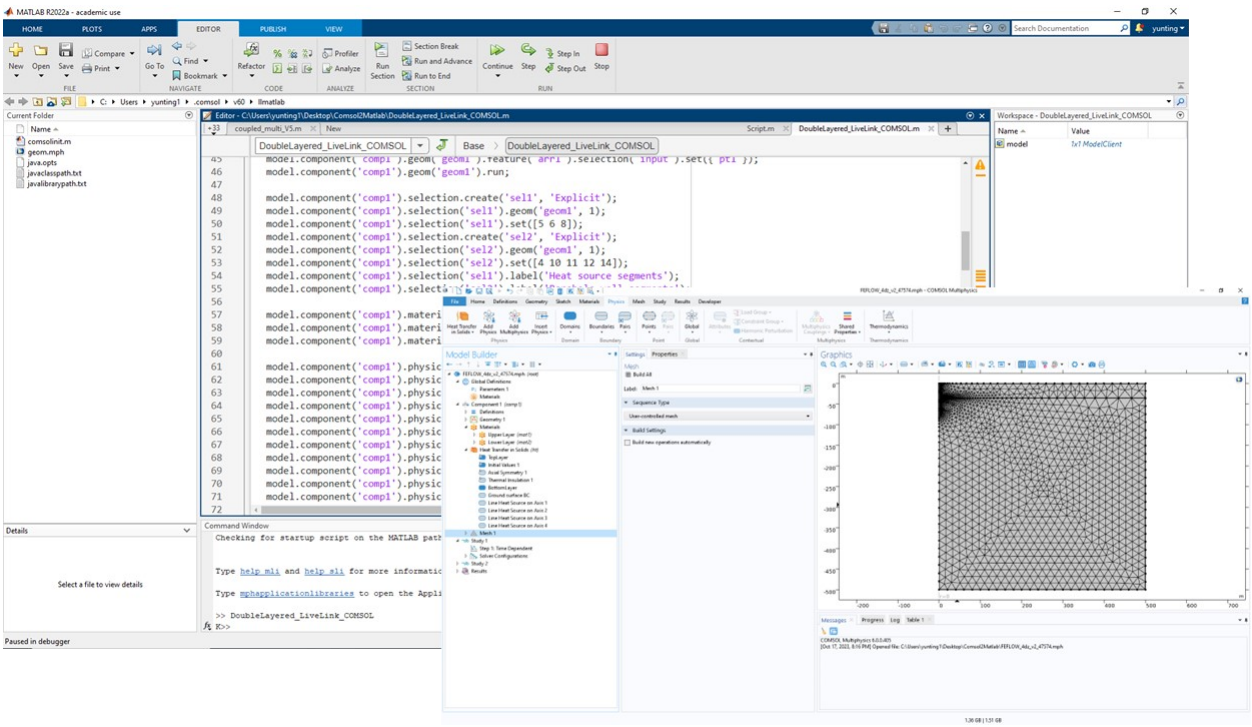

Figure 6-8. The constructed COMSOL model object and the associated MATLAB file.

6.2.3.3 Refined method based on the MVQ solution

Figure 6-9 shows a refined method for BHE simulation based on the MVQ solution that has been extensively introduced in Chapters 3-5. This refined method was implemented in MATLAB, where numerous commands and MATLAB functions were combined to create MATLAB scripts that automate the entire calculation process. By simply modifying input parameters according to

the specific case, running the script will return the borehole wall temperature and the fluid temperature. Several screenshots of the MATLAB script are presented in Figure 6-10.

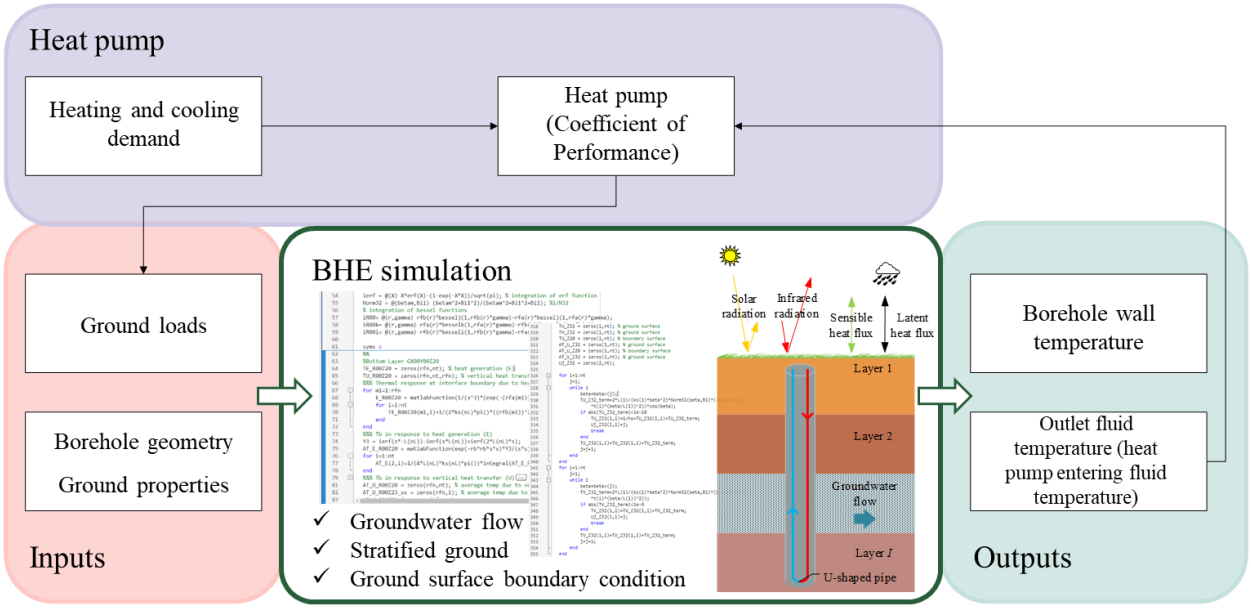

Figure 6-9. The illustration of the refined BHE simulation method based on the MVQ solution.

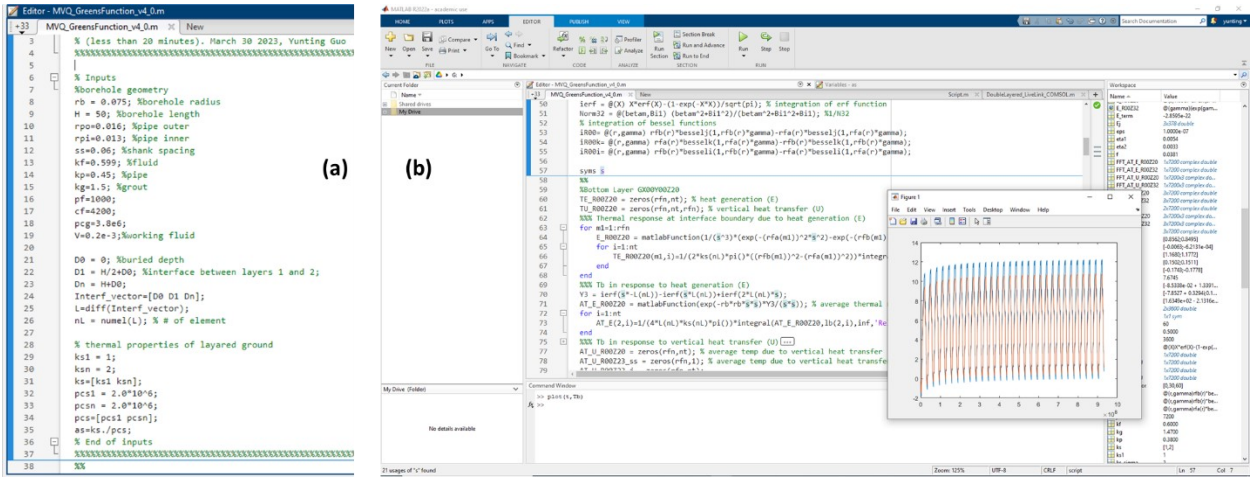

Figure 6-10. Screenshots of MATLAB scripts for the BHE simulation. This includes (a) input parameters and (b) the MVQ solution, results in the MATLAB workspace, and a plot of the borehole wall temperature.

6.2.4 Coefficient of performance and energy efficiency ratio

The efficiency of a GSHP system is typically measured by its coefficient of performance (COP) and energy efficiency ratio (EER). The COP is a ratio that indicates the amount of heat (in kW) the heat pump transfers for each unit of electrical energy (in kW) it consumes, and EER is determined by dividing the cooling capacity of the heat pump (in Btu/h) by the electrical energy input (in W) at a specific temperature. A higher COP indicates better heating efficiency, while a higher EER points to better cooling efficiency.

As introduced in studies by Tang and Nowamooz [190], Hein et al. [191], and Casasso and Sethi [192], the heat pump COP can be modeled as a linear function of the outlet temperature of the circulating fluid (T_{out}), also referred to as the inlet temperature of the heat pump. Drawing on information from Bosch [193], a linear relationship was established between the fluid outlet temperature and the COP, specifically for their water-to-air geothermal heat pump. In contrast, a parabolic relationship could potentially offer a more accurate fitting when considering the fluid outlet temperature in relation to the EER. Figure 6-11 illustrates these relationships derived through data fitting analysis.

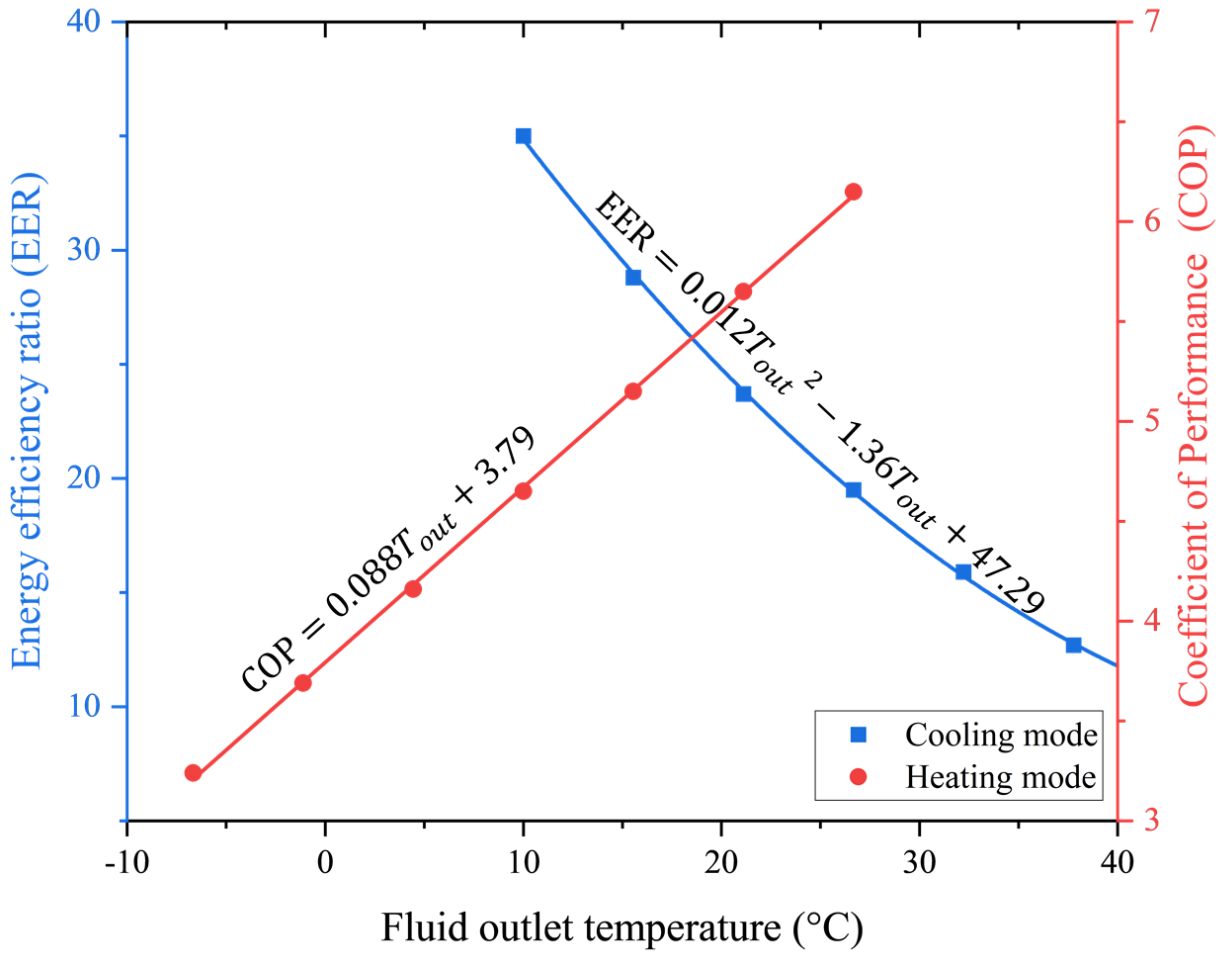

Figure 6-11. Variation of heat pump COP in heating mode and heat pump EER in cooling mode.

6.3. Results and discussion

Figure 6-12 depicts the average temperature at the borehole wall analyzed across a 30-year operational period. It is worth noting that the COMSOL simulation was limited to a 10-year span due to the substantial computational resources required by the numerical model. Despite this shorter timeframe, it shows a significant agreement between the outcomes from the refined method and the COMSOL modelling. In particular, the maximum temperature difference at the borehole wall throughout the 10-year simulation period was merely 0.15 °C. A comparison was conducted

between the results obtained from COMSOL modelling and the temperature measurements recorded during the sandbox experiments conducted by Beier et al. [13].

Over the span of the 30-year operational period, the ground exhibited gradual warming due to the accumulation of yearly net thermal storage within it. This observation is pertinent considering the cooling-dominant nature of the case under investigation. During the 1st year, the average temperature obtained from the COMSOL simulation exhibited fluctuations spanning from 3.22 °C to 14.58 °C, yielding a range of 11.36 °C. In comparison to the COMSOL simulation wherein the multilayered ground configuration is considered, the outcomes from the GLD software indicate that the simplification of stratified ground as a homogenous body leads to an overestimation of the average borehole wall temperature. The maximum overestimation, by about 1.17 °C, was found in August. By the 10th year, the average temperature at the borehole wall had risen, peaking at 15.44 °C in August. This upward trend in temperature resulted in a corresponding amplification in discrepancies between the results obtained from the COMSOL simulation and the GLD software. Notably, the maximum overestimation was measured at 1.72 °C in August, underscoring the significance of stratified ground in augmenting the performance of the BHE in the analyzed case.

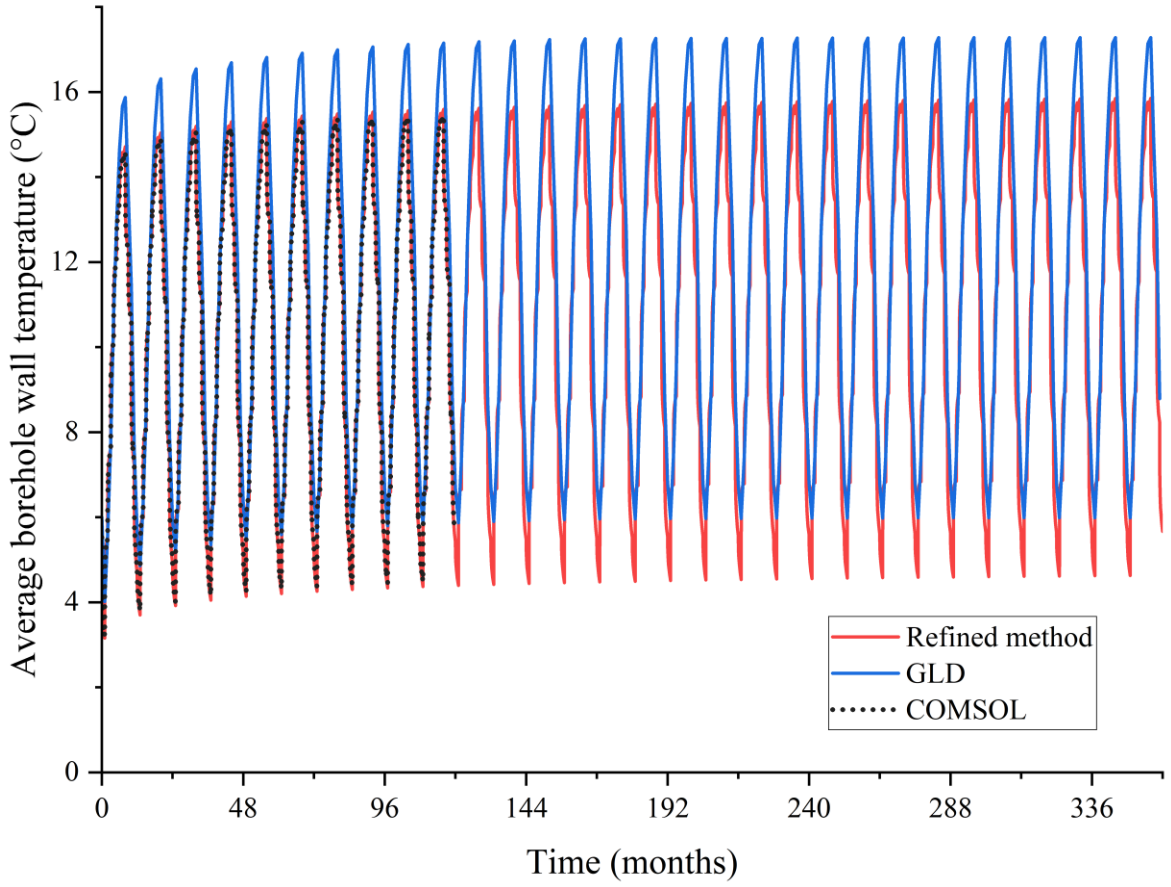

Figure 6-12. Average temperature at the borehole wall over a 30-year operational span.

To quantify this effect in terms of BHE length, a systematic simulation was undertaken wherein progressively shorter BHEs were simulated until the outcomes aligned with those from the GLD software. As illustrated in Figure 6-13, when the multilayered ground configuration was taken into account, it was determined that a BHE with a depth of 60 meters could effectively meet the same heating and cooling requirements as a 70-metre BHE analyzed with the GLD software. In other words, by incorporating the multilayered ground configuration into the engineering design of BHEs, it is possible to achieve approximately 14.3% reduction in BHE length without compromising thermal performance. This reduction in length carries substantial implications in

terms of cost savings. In a practical context, the cost of drilling and installing BHEs in Canada is estimated at around C$70 per metre [194]. Given this context, the geothermal field in this case study consisting of 32 boreholes could be saved by about C$22,400. This financial advantage underscores the practical importance of this refined method, utilizing the MVQ solution, in the engineering design of BHEs.

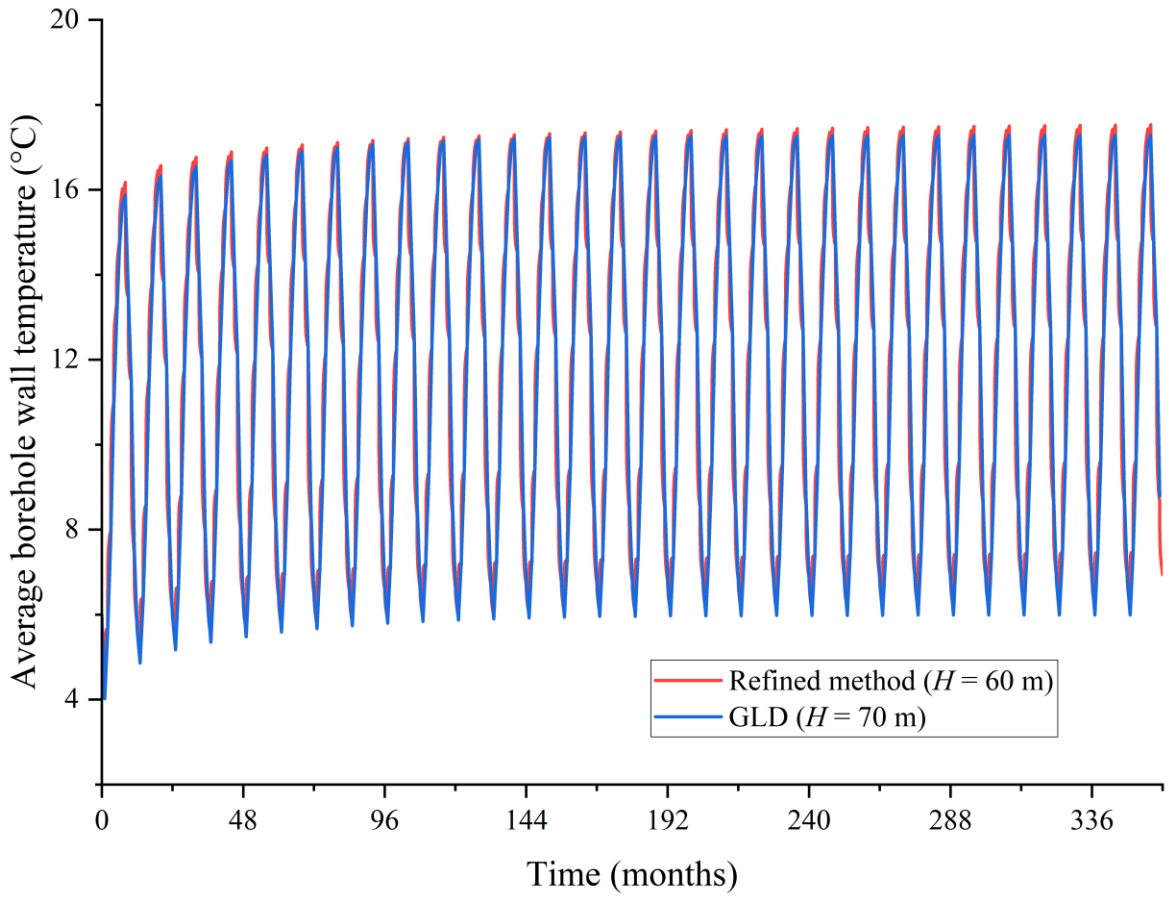

Figure 6-13. Average borehole wall temperature of a shortened BHE (60 m) obtained from the refined method.

Table 6-3 lists the COP over the heating season and seasonal energy efficiency ratio (SEER) over the cooling season of the first decade. The SEER is determined by dividing the total cooling output

provided over the cooling season (in Btu) by the total electrical energy consumption of the heat pump (in Wh). It decreases from 30.6 to 29.5 due to the ground temperature rise in a cooling-dominant case. In comparison to air conditioner (AC) units, most of which fall within a 13 to 21 SEER rating, the application of GSHP systems can lead to an energy consumption reduction of over 28% in space cooling. On the contrary, the most prominent advantage of employing a GSHP system lies in its high efficiency for heating applications. In comparison to electric furnaces, a GSHP system can potentially yield energy consumption savings of approximately 77%.

Taking the CO_2 equivalent emissions into consideration, which on average is 540 grams per kilowatt-hour of electricity consumed in Alberta, Canada [195], the operation of a GSHP system has the capacity to reduce CO_2 equivalent emissions by more than 18 tonnes annually. The savings in CO_2 equivalent emissions over the 30-year operational period was plotted in Figure 6-14. This comparison underscores the energy-efficient and environmentally-friendly attributes of GSHP technology. In the case invested in this study, the GSHP system is employed for space heating and cooling purposes. Given its notable efficiency, it is recommended to explore the integration of domestic water heating, which could further enhance the overall efficiency of the energy systems.

Table 6-3. System efficiencies and energy savings.

Year	Cooling			Heating			CO_2e-saving[c] (t)
	SEER	Input electrical energy (kWh)	Energy-saving[a]	COP	Input electrical energy (kWh)	Energy-saving[b]	
1	30.6	15699	31.5%	4.30	8134	76.8%	18.41
2	30.2	15955	30.4%	4.35	8047	77.0%	18.32
3	29.9	16069	29.9%	4.37	8011	77.1%	18.27
4	29.8	16141	29.5%	4.38	7990	77.2%	18.25
5	29.7	16194	29.3%	4.39	7975	77.2%	18.23
6	29.6	16234	29.1%	4.40	7963	77.3%	18.21
7	29.6	16266	29.0%	4.40	7954	77.3%	18.20
8	29.5	16293	28.9%	4.41	7946	77.3%	18.19
9	29.5	16316	28.8%	4.41	7940	77.3%	18.18
10	29.5	16335	28.7%	4.41	7934	77.3%	18.17

[a] Comparing with 21 SEER AC units.

[b] Comparing with electric furnaces.

[c] Referring to 540 grams of CO_2 equivalent per kilowatt hour (540 g/kWh) [195].

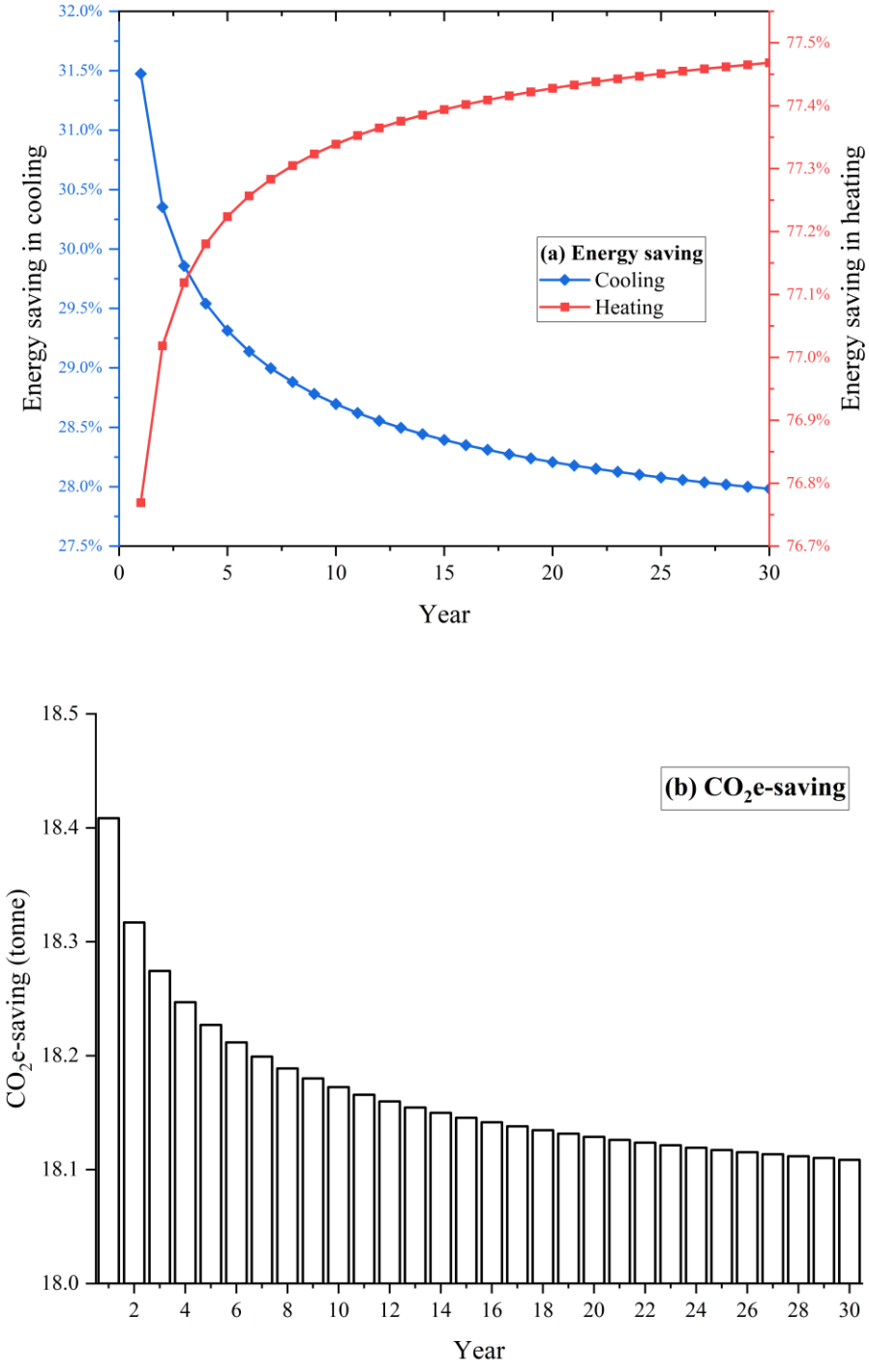

Figure 6-14.Saving of energy consumption and CO_2 equivalent emissions over the span of the 30-year operational period.

It is essential to recognize that, beyond electric-driven heat pumps, vapor-compression cycles of heat pumps can also be directly powered by a diesel engine [196] or a gas engine [197, 198]. In the case of an engine-driven heat pump, the incorporation of waste heat recovered from the engine coolant and exhaust gas makes the system highly energy-efficient [196, 199]. For instance, in a performance analysis of a diesel engine-driven heat pump [196], it was determined that the heat output relative to the fuel heat input ratio can reach up to 1.33. This high-efficiency underscores the potential of a diesel-driven heat pump as a practical solution for providing heating and cooling at off-grid mining sites, where conventional power sources may be limited.

6.4. Conclusion

This study has demonstrated a refined method for the design of borehole heat exchangers (BHEs) utilizing the MVQ (Multilayered ground with Varying heat transfer rates) solution proposed in earlier chapters. The investigation focused on assessing the thermal performance of a BHE within a commercial building over a 30-year operational span while incorporating monthly heating and cooling loads. The analysis involved the use of three methods: a conventional design tool named GLD, a numerical model created in COMSOL Multiphysics, and the refined design method employing the MVQ solution. Notably, the COMSOL simulation and the refined method considered a multilayered ground configuration. the GLD software simplified the multilayered ground configuration as a homogenous body.

The comparative study underscored that the conventional design tools adopting the homogeneous assumption might lead to underestimation of the thermal potential within the ground. This underestimation, in turn, could result in an oversized design of the BHE. The influence of the multilayered ground configuration was quantified in terms of BHE length. The refined method

revealed that incorporating the multilayered ground configuration in the design process could lead to a reduction in the depth of the BHE by approximately 14.3% for BHEs designed to be 70 metres deep under the conditions investigated in this study. By accounting for this effect, the refined design method can make the overall system more efficient and cost-effective. In comparison to the conventional space heating and cooling methods, the operation of a GSHP system can potentially reduce energy consumption in heating by around 77% and in cooling by over 28%.

Chapter 7. Conclusions and recommendations for future work

7.1. Conclusions

The main work of this thesis is the development of new solutions for borehole heat exchangers (BHEs) to analyze the complex heat transfer processes. The proposed solution is named the MVQ solution, which stands for "Multilayered ground with Varying heat transfer rates." By introducing the MVQ solution, current BHE design methods can be refined, allowing for the consideration of more complex real ground conditions, including multilayered ground structures, groundwater flow, and ground surface conditions. With the MVQ solution, this thesis thoroughly analyzes and discusses the heat transfer process of vertical BHEs under real ground conditions. The main conclusions drawn from the study are summarized as follows:

(1) The MVQ solution addresses the varying heat transfer rate for a BHE in the multilayered ground. Conventional solutions, which prescribe a uniform heat transfer rate along the borehole length, tend to overestimate the temperature of the ground layer with a relatively lower thermal conductivity value. In a double-layered scenario, the uniform heat transfer rate assumption resulted in a temperature overprediction of up to 97.55% for the given parameters. By addressing the heat transfer rate variation, the MVQ solution provides can accurate predictions of ground temperature changes, enabling a refined design of the BHE system.

(2) The MVQ solution addresses the varying heat transfer rate for a BHE with an aquifer. Conventional solutions prescribe a uniform heat transfer rate along the borehole length, thus neglecting the thermal enhancement resulting from groundwater flow. The influence of groundwater flow was examined in three bedded layers, with the middle layer being the

aquifer. For the given parameters, the results showed an enhanced average heat transfer rate for the middle layer, increasing from 34.60 Wm^{-1} to 41.00 Wm^{-1} and 60.84 Wm^{-1} as the flow velocity increased from 10^{-8} ms^{-1} to 10^{-7} ms-1 and 10-6 ms^{-1}, respectively. By addressing the varying heat transfer rate, the MVQ solution effectively considers the thermal enhancement due to groundwater flow, leading to a refined design of the BHE system.

(3) The heat transfer rate in the multilayered ground is impacted by both the thermal conductivity ratio (k_1/k_2) and volumetric heat capacity ratio ($(\rho c)_1/(\rho c)_2$). The variation in volumetric heat capacity affects the heat transfer rate between layers primarily during the early period, and its impact gradually diminishes over time. In contrast, the inhomogeneity of thermal conductivity strengthens the heat transfer rate variation as time progresses in most cases. Additionally, when there are larger thermal conductivity ratios (e.g., 1/4), the heat transfer rate variation becomes more pronounced. For the specific parameters used in this study, when the thermal conductivity ratio was 1/4, the lower layer extracted heat approximately three times as quickly as the upper layer.

(4) A novel solution has been proposed for analyzing heat transfer occurring outside the borehole in a multilayered body. This solution is based on the unsteady surface element method, which divides the layer interface into surface elements. To verify its accuracy, the solution was compared with an exact solution (line heat source solution) in a homogenous ground condition. The results of the comparison show that the maximum relative error is less than 1.6% when using only one surface element and is further reduced to 0.2% with three surface elements. In the comparison with a two-dimensional finite element (FE) model created using COMSOL Multiphysics, the maximum relative difference was found

to be less than 0.61% with three surface elements when the thermal conductivity ratio was 1/4. This indicates that the novel solution is highly accurate, even with a relatively small number of surface elements. Overall, the minor discrepancies observed in the comparisons are considered acceptable within engineering applications.

(5) The buried depth is a significant parameter in the design of the BHE systems. In the study, with given parameters (including a Peclet number of 7.5), the temperature response factor increased by about 1.01% as the buried depth of a single 70-metre borehole is increased from 0 m to 2 m. This increase raised to 1.83% and 3.23% in a 3 × 2 borehole field and a 10 × 10 borehole field, respectively. These results highlight the significance of considering buried depth in the design of BHE systems, especially for larger-scale installations involving multiple boreholes.

(6) The MVQ solution addresses the influence of the ground surface condition. This influence is particularly significant in the case of short boreholes for a longer period of time. For the given parameters in this study, the relative difference from different boundary conditions may be up to 26.3% for a 15-metre BHE after about 35.8 years.

(7) It is the first time to consider the synergistic effect of the circulating fluid and the ground surface condition in analytical solutions. This synergistic effect leads to an extension of the impact of the ground surface boundary to greater depths. In the case with a perfectly insulated ground surface, conventional solutions (employing the homogenous boundary condition of the first-type) may lead to a notable underestimation of the ground temperature by approximately 8.34%. Such underestimation is even apparent at a depth of 70 meters below the ground surface, with a value of 6.85%. By incorporating the heat transfer inside

the borehole, the MVQ solution prevents underprediction of temperatures at greater depths. This is crucial for accurate temperature analysis and preventing undersized designs of BHE systems.

(8) The refined method revealed that incorporating the multilayered ground configuration in the design process could lead to a reduction in the depth of the BHE by approximately 14.3% for BHEs designed to be 70 metres deep under the conditions investigated in this study. By accounting for this effect, the refined design method can make the overall system more efficient and cost-effective.

(9) From the viewpoint of time usage, the refined design method is more computationally efficient than numerical simulations. For the specific parameters used in this study, the refined design method consumed 1,394 s, which represents about a thirty-nine-fold reduction in computational time compared to numerical simulations. Because of its superior computational time and accuracy, the MVQ solution has great potential in the design of vertical BHEs.

7.2. Key contributions

The findings from this study are significant for the BHE applications. The key contributions of this thesis are listed as follows:

(1) This study introduces a comprehensive and accurate approach for analyzing BHEs in complex ground conditions, including multilayered ground structures, groundwater flow, and ground surface conditions. This refinement overcomes the limitations of current design methods and enables more realistic simulations of BHE performance.

(2) For the first time, the axial variation of heat transfer rate is investigated for BHE with aquifers. The presence of groundwater flow in aquifers can significantly enhance the heat transfer rate in those layers, leading to improved overall thermal performance of the BHE system. The consideration of the varying heat transfer rate is indispensable for accurately predicting the thermal performance of BHE systems in such complex geological settings.

(3) Innovatively, this study considers the synergistic effect of the circulating fluid and the ground surface condition in BHE design methods. This effect becomes important in practical BHE applications, especially when there is a disparity between heating and cooling loads. When a BHE system operates for heating purposes, the ambient temperature is typically colder than the ground temperature, leading to heat loss from the ground surface to the surrounding environment. This excess cooling at the ground surface can accumulate in the ground over time, gradually reducing the thermal potential of the ground. By accounting for this effect, the refined design method aids in preventing undersized designs and securing the long-term performance of the BHE systems.

(4) The refined BHE method offers superior computational time and accuracy, making it a promising tool for designing vertical BHEs. It enhances the understanding and capabilities of the current design methods, paving the way for more effective shallow geothermal applications.

(5) The case investigated in this study revealed that incorporating the multilayered ground configuration in the design process using the refined method could lead to a reduction in the depth of the BHE by approximately 14.3% for a 70-metre BHE. In comparison to the conventional space heating and cooling methods, the operation of a GSHP system can

potentially reduce energy consumption in heating by around 77% and in cooling by over 28%, leading a saving of CO_2 equivalent emissions by an estimated 18 tonnes annually.

7.3. Limitations and future work

(1) In order to fully utilize the refined method to consider multilayered ground structures, one needs the ground thermal properties in different layers. However, these data cannot be obtained from the conventional thermal response test [41] that is an indirect and in-situ method used to determine the integrated ground thermal property along the borehole length. A common approach to obtain thermal properties for ground layers is laboratory measurements of rock samples [54, 56]. However, variations in water content and in-situ stress can lead to significant differences in thermal conductivity between the in-situ condition and the laboratory condition, with deviations reaching as high as four times. However, due to alterations in water content and in-situ stress, the thermal conductivity measured in laboratory conditions can significantly differ from that observed in-situ, with variations as high as four times [200]. A feasible solution is to use distributed temperature sensing technologies, such as optical fiber sensor cables [54, 201] or temperature sensor cables [202], to measure temperature distribution along the length of the borehole. This allows the calculation of the thermal conductivity for each ground layer based on temperature changes.

(2) The geothermal potential for BHE systems gradually diminishes during continuous operation and imbalanced loads. In cold climates, the heat extraction from the ground commonly exceeds the heat injection into the ground due to substantial heating demands. The disparity between cooling and heating loads results in the temperature drawdown in

the ground, leading to a lower Coefficient of Performance (COP) after a few years of operation. Introducing solar energy into the ground will compensate for the temperature reduction and enhance the overall efficiency of the system, as evidenced by studies [203-205]. The current model for GSHPs can be extended to include solar heat. The hybrid systems will further enhance overall system efficiency, leading to substantial energy savings.

(3) In Chapters 4 and 5, a novel solution was proposed for analyzing heat transfer occurring outside the borehole in a multilayered body. However, this solution is not applicable to BHEs with aquifers. To analyze the effect of aquifer, the composite medium method introduced by Abdelaziz et al. [58] was employed in Chapter 3 of the current study. It is important to note that this method [58] is not derived from the governing equation, which can lead to an error of up to 15% when the thermal properties vary significantly. As far as the authors' knowledge goes, there are only two approaches used in the established solutions to account for the multilayered ground condition with aquifers. One approach is the composite medium method, which has been widely adopted by many other studies [62-65]. The alternative approach is to neglect the vertical heat transfer between layers [206], which may raise errors in the long-term. In comparison to these two approaches, the unsteady surface element method [170] used in the novel solution have possesses unique strengths in dealing with layered bodies. Therefore, the proposed solution needs to be further extended and improved to address the effect of aquifers.

(4) In the thermal analysis within the borehole region, thermal resistance models [23, 127, 128, 189, 207] are commonly employed, where the circulating fluid is represented as a lumped point. The lumped system assumes a uniform flow of the circulating fluid, which

contradicts the fact that the flow in the pipe is turbulent most of the time. In the literature to date, the influence of the uniform flow assumption has not been investigated. In future research, it is essential to systematically examine the difference in the borehole wall temperature caused by the uniform flow and turbulent flow. If a significant difference is observed, the effect of turbulent flow should be addressed in subsequent studies.

(5) The refined design method for the shallow BHEs can generally be adapted for medium deep (MD) BHEs with the depth ranging from 200m to 3000 m. In the literature, thermal analysis of MD-BHEs is primarily conducted through numerical simulations [184, 208-212]. These simulations typically involve solving the conductive and convective heat transfer, similar to the analysis for shallow BHEs. In the MD-BHE system, the temperature distribution typically varies between 20 °C and 90 °C. This relatively large temperature range in the reservoir significantly affects the physical and thermal properties of the circulating fluid and the ground, such as density, thermal conductivity, and volumetric heat capacity. It is vital to consider the non-linearity in the heat transfer problems when properties are temperature dependent. Addressing the nonlinear heat transfer is necessary to extend the validity of the BHE design method to deeper geothermal applications.

Bibliography

1. ICMM, *ICMM climate change statement*. 2021.
2. Hall, A., J.A. Scott, and H. Shang, *Geothermal energy recovery from underground mines.* Renewable and Sustainable Energy Reviews, 2011. **15**(2): p. 916-924.
3. Ghoreishi-Madiseh, S.A., et al., *Performance evaluation of large scale rock-pit seasonal thermal energy storage for application in underground mine ventilation.* Applied Energy, 2017. **185**: p. 1940-1947.
4. NRCan. *Table 3: Secondary energy use and ghg emissions by industry – including electricity-related emissions*. Available from: https://oee.nrcan.gc.ca/corporate/statistics/neud/dpa/showTable.cfm?type=CP&sector=agg&juris=ca&rn=3&page=4&CFID=7421311&CFTOKEN=cf40a8b159987159-3954B80B-05C3-E781-307F91FA4024283F.
5. Chu, Z., et al., *Mine-oriented low-enthalpy geothermal exploitation: A review from spatio-temporal perspective.* Energy Conversion and Management, 2021. **237**: p. 114123.
6. Sarbu, I. and C. Sebarchievici, *General review of ground-source heat pump systems for heating and cooling of buildings.* Energy and Buildings, 2014. **70**: p. 441-454.
7. Narsilio, G.A. and L. Aye, *Shallow geothermal energy: an emerging technology*, in *Low Carbon Energy Supply*. 2018, Springer. p. 387-411.
8. NRCan. *Heating and cooling with a heat pump*. 2022 [cited 2023 July 07]; Available from: https://natural-resources.canada.ca/energy-efficiency/energy-star-canada/about/energy-star-announcements/publications/heating-and-cooling-heat-pump/6817#o.

9. Raymond, J., et al. *Direct utilization of geothermal energy from coast to coast: a review of current applications and research in Canada*. in *Proceedings, World Geothermal Congress*. 2015.

10. Li, M. and A.C.K. Lai, *Review of analytical models for heat transfer by vertical ground heat exchangers (GHEs): A perspective of time and space scales.* Applied Energy, 2015. **151**(Supplement C): p. 178-191.

11. Gehlin, S., *11 - Borehole thermal energy storage*, in *Advances in Ground-Source Heat Pump Systems*, S.J. Rees, Editor. 2016, Woodhead Publishing. p. 295-327.

12. Erol, S. and B. François, *Efficiency of various grouting materials for borehole heat exchangers.* Applied Thermal Engineering, 2014. **70**(1): p. 788-799.

13. Beier, R.A., M.D. Smith, and J.D. Spitler, *Reference data sets for vertical borehole ground heat exchanger models and thermal response test analysis.* Geothermics, 2011. **40**(1): p. 79-85.

14. Kavanaugh, S.P., et al., *Geothermal heating and cooling : Design of ground-source heat pump systems*. 2014, Atlanta: ASHRAE.

15. Bernier, M.A., *Closed-loop ground-coupled heat pump systems.* Ashrae Journal, 2006. **48**(9): p. 12.

16. American Society of Heating, R. and I. Air-Conditioning Engineers, *2019 ASHRAE® Handbook Heating, Ventilating, and Air-Conditioning Applications (S-I Edition)*. American Society of Heating, Refrigerating and Air-Conditioning Engineers, Inc. (ASHRAE).

17. Javed, S. and J. Spitler, *Accuracy of borehole thermal resistance calculation methods for grouted single U-tube ground heat exchangers.* Applied Energy, 2017. **187**: p. 790-806.

18. Dalla Santa, G., et al., *Modified compressibility of cohesive sediments induced by thermal anomalies due to a borehole heat exchanger.* Engineering Geology, 2016. **202**: p. 143-152.

19. Spitler, J.D. *GLHEPRO-A design tool for commercial building ground loop heat exchangers*. in *Proceedings of the fourth international heat pumps in cold climates conference*. 2000. Citeseer.

20. Hellström, G. and B. Sanner, *Earth energy designer.* User's Manual, version, 2000. **2**.

21. Liu, X. and G. Hellstrom, *Enhancements of an integrated simulation tool for ground-source heat pump system design and energy analysis.* Proceedings of Ecostock, 2006.

22. Crawley, D.B., et al., *EnergyPlus: creating a new-generation building energy simulation program.* Energy and Buildings, 2001. **33**(4): p. 319-331.

23. Eskilson, P., *Thermal analysis of heat extraction boreholes.* 1987.

24. Zhang, C., et al., *Computational methods for ground thermal response of multiple borehole heat exchangers: A review.* Renewable Energy, 2018. **127**: p. 461-473.

25. Geothermal, G., *Ground Loop Design™ Premier 2016 User's Guide*. 2016: USA.

26. Bandos, T.V., et al., *Finite line-source model for borehole heat exchangers: effect of vertical temperature variations.* Geothermics, 2009. **38**(2): p. 263-270.

27. Zeng, H.Y., N.R. Diao, and Z.H. Fang, *A finite line-source model for boreholes in geothermal heat exchangers.* Heat Transfer—Asian Research, 2002. **31**(7): p. 558-567.

28. Lamarche, L. and B. Beauchamp, *A new contribution to the finite line-source model for geothermal boreholes.* Energy and Buildings, 2007. **39**(2): p. 188-198.

29. Claesson, J. and S. Javed. *An analytical method to calculate borehole fluid temperatures for time-scales from minutes to decades*. in *ASHRAE Transactions*. 2011.

30. Thomson, W., *Compendium of the Fourier mathematics for the conduction of heat in solids, and the mathematically allied physical studies of diffusion of fluids and transmission of electric signals through submarine cables (based on articles prepared for the Encyclopaedia Britannica in 1880 and the Quarterly Journal of Mathematics in 1856)*. 1884, Cambridge University Press. p. 41-60.

31. Carslaw, H. and J. Jaeger, *Heat in solids*. Vol. 1. 1959: Clarendon Press, Oxford.

32. Beck, J.V., B. Blackwell, and C.R.S. Clair Jr, *Inverse heat conduction: Ill-posed problems*. 1985: James Beck.

33. Lamarche, L., S. Kajl, and B. Beauchamp, *A review of methods to evaluate borehole thermal resistances in geothermal heat-pump systems.* Geothermics, 2010. **39**(2): p. 187-200.

34. Spitler, J.D. and M. Bernier, *2 - Vertical borehole ground heat exchanger design methods*, in *Advances in Ground-Source Heat Pump Systems*, S.J. Rees, Editor. 2016, Woodhead Publishing. p. 29-61.

35. Molina-Giraldo, N., et al., *A moving finite line source model to simulate borehole heat exchangers with groundwater advection.* International Journal of Thermal Sciences, 2011. **50**(12): p. 2506-2513.

36. Tye-Gingras, M. and L. Gosselin, *Generic ground response functions for ground exchangers in the presence of groundwater flow.* Renewable Energy, 2014. **72**: p. 354-366.

37. Dalla Santa, G., et al., *Relevance of computing freeze-thaw effects for borehole heat exchanger modelling: A comparative case study.* Geothermics, 2019. **79**: p. 164-175.

38. Cimmino, M., M. Bernier, and F. Adams, *A contribution towards the determination of g-functions using the finite line source.* Applied Thermal Engineering, 2013. **51**(1-2): p. 401-412.

39. Bandos, T.V., et al., *Finite cylinder-source model for energy pile heat exchangers: Effect of buried depth and heat load cyclic variations.* Applied Thermal Engineering, 2016. **96**: p. 130-136.

40. Guo, Y., et al., *Considering buried depth in the moving finite line source model for vertical borehole heat exchangers—a new solution.* Energy and Buildings, 2020: p. 109859.

41. Gehlin, S., *Thermal response test: method development and evaluation*. 2002, Luleå tekniska universitet.

42. Angelotti, A., et al., *Energy performance and thermal impact of a Borehole Heat Exchanger in a sandy aquifer: Influence of the groundwater velocity.* Energy Conversion and Management, 2014. **77**: p. 700-708.

43. Capozza, A., M. De Carli, and A. Zarrella, *Investigations on the influence of aquifers on the ground temperature in ground-source heat pump operation.* Applied Energy, 2013. **107**: p. 350-363.

44. Fan, R., et al., *A study on the performance of a geothermal heat exchanger under coupled heat conduction and groundwater advection.* Energy, 2007. **32**(11): p. 2199-2209.

45. Chiasson, A.D., S.J. Rees, and J.D. Spitler, *A preliminary assessment of the effects of groundwater flow on closed-loop ground source heat pump systems*. 2000, Oklahoma State Univ., Stillwater, OK (US).

46. Fujii, H., et al., *Optimizing the design of large-scale ground-coupled heat pump systems using groundwater and heat transport modeling.* Geothermics, 2005. **34**(3): p. 347-364.

47. Wang, H., et al., *Thermal performance of borehole heat exchanger under groundwater flow: A case study from Baoding.* Energy and Buildings, 2009. **41**(12): p. 1368-1373.

48. Sutton, M.G., D.W. Nutter, and R.J. Couvillion, *A ground resistance for vertical bore heat exchangers with groundwater flow.* Journal of Energy Resources Technology, 2003. **125**(3): p. 183-189.

49. Diao, N.R., Q.Y. Li, and Z.H. Fang, *Heat transfer in ground heat exchangers with groundwater advection.* International Journal of Thermal Sciences, 2004. **43**(12): p. 1203-1211.

50. Rivera, J.A., P. Blum, and P. Bayer, *A finite line source model with Cauchy-type top boundary conditions for simulating near surface effects on borehole heat exchangers.* Energy, 2016. **98**: p. 50-63.

51. Rivera, J.A., P. Blum, and P. Bayer, *Influence of spatially variable ground heat flux on closed-loop geothermal systems: Line source model with nonhomogeneous Cauchy-type top boundary conditions.* Applied Energy, 2016. **180**: p. 572-585.

52. Zhou, Y., Z. Zheng, and G. Zhao, *Analytical models for heat transfer around a single ground heat exchanger in the presence of both horizontal and vertical groundwater flow considering a convective boundary condition.* Energy, 2022. **245**: p. 123159.

53. Zhou, Y., Z.-h. Wu, and K. Wang, *An analytical model for heat transfer outside a single borehole heat exchanger considering convection at ground surface and advection of vertical water flow.* Renewable Energy, 2021. **172**: p. 1046-1062.

54. Luo, J., et al., *A review of ground investigations for ground source heat pump (GSHP) systems.* Energy and Buildings, 2016. **117**: p. 160-175.

55. Di Sipio, E., et al., *Subsurface thermal conductivity assessment in Calabria (southern Italy): a regional case study.* Environmental Earth Sciences, 2014. **72**(5): p. 1383-1401.

56. Grobe, M., et al., *Importance of geoscience information in the implementation of closed-loop, ground-source heat pump systems (Geoexchange) in Alberta.* Energy Resources Conservation Board, Alberta Geological Survey ERCB/AGS Open File Report, 2009. **9**.

57. Perego, R., et al., *Sustainability evaluation of a medium scale GSHP system in a layered alluvial setting using 3D modeling suite.* Geothermics, 2016. **59**: p. 14-26.

58. Abdelaziz, S.L., et al., *Multilayer finite line source model for vertical heat exchangers.* Geothermics, 2014. **51**: p. 406-416.

59. Pan, A., et al., *A novel analytical multilayer cylindrical heat source model for vertical ground heat exchangers installed in layered ground.* Energy, 2020. **200**: p. 117545.

60. Zhou, G., Y. Zhou, and D. Zhang, *Analytical solutions for two pile foundation heat exchanger models in a double-layered ground.* Energy, 2016. **112**: p. 655-668.

61. Hu, J., *An improved analytical model for vertical borehole ground heat exchanger with multiple-layer substrates and groundwater flow.* Applied Energy, 2017. **202**(Supplement C): p. 537-549.

62. Jin, G., et al., *Thermal performance analysis of multiple borehole heat exchangers in multilayer geotechnical media.* Energy, 2020. **209**: p. 118236.

63. Luo, Y., T. Yan, and J. Yu, *Integrated analytical modeling of transient heat transfer inside and outside U-tube ground heat exchanger: A new angle from composite-medium method.* International Journal of Heat and Mass Transfer, 2020. **162**: p. 120373.

64. Erol, S. and B. François, *Multilayer analytical model for vertical ground heat exchanger with groundwater flow.* Geothermics, 2018. **71**(Supplement C): p. 294-305.

65. Luo, Y., G. Xu, and N. Cheng, *Proposing stratified segmented finite line source (SS-FLS) method for dynamic simulation of medium-deep coaxial borehole heat exchanger in multiple ground layers.* Renewable Energy, 2021. **179**: p. 604-624.

66. Zhang, D., et al., *Heat transfer analysis of a borehole heat exchanger array in a layered subsurface.* Applied Thermal Engineering, 2022. **216**: p. 119076.

67. Jia, L., et al., *Analytical heat transfer model for coaxial heat exchangers based on varied heat flux with borehole depth.* Applied Thermal Engineering, 2023. **218**: p. 119317.

68. Cimmino, M., *The effects of borehole thermal resistances and fluid flow rate on the g-functions of geothermal bore fields.* International Journal of Heat and Mass Transfer, 2015. **91**: p. 1119-1127.

69. Deng, Y. and C. B. Fedler, *Multi-layered soil effects on vertical ground-coupled heat pump design.* Transactions of the ASAE, 1992. **35**(2): p. 687-694.

70. Luo, J., et al., *Analysis on performance of borehole heat exchanger in a layered subsurface.* Applied Energy, 2014. **123**: p. 55-65.

71. Li, W., et al., *Effect of the heat load distribution on thermal performance predictions of ground heat exchangers in a stratified subsurface.* Renewable Energy, 2019. **141**: p. 340-348.

72. Guo, Y., G. Huang, and W.V. Liu, *A new semi-analytical solution addressing varying heat transfer rates for U-shaped vertical borehole heat exchangers in multilayered ground.* Energy, 2023. **274**: p. 127373.

73. Bidarmaghz, A., et al., *The importance of surface air temperature fluctuations on long-term performance of vertical ground heat exchangers.* Geomechanics for Energy and the Environment, 2016. **6**: p. 35-44.

74. Li, C., et al., *Influence of ground surface boundary conditions on horizontal ground source heat pump systems.* Applied Thermal Engineering, 2019. **152**: p. 160-168.

75. Bortoloni, M., M. Bottarelli, and Y. Su, *A study on the effect of ground surface boundary conditions in modelling shallow ground heat exchangers.* Applied Thermal Engineering, 2017. **111**: p. 1371-1377.

76. Zhou, K., et al., *Comparative study on thermal performance of horizontal ground source heat pump systems with Dirichlet and Robin boundary conditions on ground surface.* Energy Conversion and Management, 2020. **225**: p. 113469.

77. Liu, Q., et al., *Parametric optimization of a spiral ground heat exchanger by response surface methodology and multi-objective genetic algorithm.* Applied Thermal Engineering, 2023. **221**: p. 119824.

78. Larwa, B. and K. Kupiec, *Heat transfer in the ground with a horizontal heat exchanger installed–Long-term thermal effects.* Applied Thermal Engineering, 2020. **164**: p. 114539.

79. Krarti, M., et al., *Analytical model to predict annual soil surface temperature variation.* Journal of Solar Energy Engineering, 1995. **117**(2): p. 91-99.

80. Badache, M., et al., *A new modeling approach for improved ground temperature profile determination.* Renewable Energy, 2016. **85**: p. 436-444.

81. Khatry, A., M. Sodha, and M. Malik, *Periodic variation of ground temperature with depth.* Solar Energy, 1978. **20**(5): p. 425-427.

82. Pan, A., L. Lu, and Y. Tian, *A new analytical model for short vertical ground heat exchangers with Neumann and Robin boundary conditions on ground surface.* International Journal of Thermal Sciences, 2020. **152**: p. 106326.

83. Chiasson, A.D., *Geothermal heat pump and heat engine systems: Theory and practice*. 2016: John Wiley & Sons.

84. Ahmadi, M.H., et al., *Ground source heat pump carbon emissions and ground-source heat pump systems for heating and cooling of buildings: A review.* Environmental Progress & Sustainable Energy, 2017.

85. Lund, J.W. and T.L. Boyd, *Direct utilization of geothermal energy 2015 worldwide review.* Geothermics, 2016. **60**: p. 66-93.

86. Yang, H., P. Cui, and Z. Fang, *Vertical-borehole ground-coupled heat pumps: A review of models and systems.* Applied Energy, 2010. **87**(1): p. 16-27.

87. Beck, M., et al., *Geometric arrangement and operation mode adjustment in low-enthalpy geothermal borehole fields for heating.* Energy, 2013. **49**: p. 434-443.

88. Miglani, S., K. Orehounig, and J. Carmeliet, *A methodology to calculate long-term shallow geothermal energy potential for an urban neighbourhood.* Energy and Buildings, 2018. **159**: p. 462-473.

89. Monzó, P., et al., *Numerical modeling of ground thermal response with borehole heat exchangers connected in parallel.* Energy and Buildings, 2018. **172**: p. 371-384.

90. Fossa, M., *The temperature penalty approach to the design of borehole heat exchangers for heat pump applications.* Energy and Buildings, 2011. **43**(6): p. 1473-1479.

91. Malayappan, V. and J.D. Spitler. *Limitations of using uniform heat flux assumptions in sizing vertical borehole heat exchanger fields*. in *Proceedings of Clima*. 2013.

92. Huang, B. and V. Mauerhofer, *Life cycle sustainability assessment of ground source heat pump in Shanghai, China.* Journal of Cleaner Production, 2016. **119**: p. 207-214.

93. Bayer, P., M. de Paly, and M. Beck, *Strategic optimization of borehole heat exchanger field for seasonal geothermal heating and cooling.* Applied Energy, 2014. **136**: p. 445-453.

94. Priarone, A. and M. Fossa, *Modelling the ground volume for numerically generating single borehole heat exchanger response factors according to the cylindrical source approach.* Geothermics, 2015. **58**: p. 32-38.

95. ASHRAE, *34 Geothermal energy*, in *2015 ASHRAE Handbook - Heating, Ventilating, and Air-Conditioning Applications (SI Edition)*. 2015, American Society of Heating, Refrigerating and Air-Conditioning Engineers, Inc.

96. Cimmino, M. and M. Bernier, *A semi-analytical method to generate g-functions for geothermal bore fields.* International Journal of Heat and Mass Transfer, 2014. **70**: p. 641-650.

97. Komar, J., *Thermal conductivity test report*. 2014, rEvolve Engineering Inc.

98. Naldi, C. and E. Zanchini, *A new numerical method to determine isothermal g-functions of borehole heat exchanger fields.* Geothermics, 2019. **77**: p. 278-287.

99. Sanner, B., et al. *Thermal response test–current status and world-wide application*. in *Proceedings world geothermal congress*. 2005. International Geothermal Association.

100. Wang, H., et al., *Improved method and case study of thermal response test for borehole heat exchangers of ground source heat pump system.* Renewable Energy, 2010. **35**(3): p. 727-733.

101. Faghri, A. and Y. Zhang, *4 - Generalized governing equations for multiphase systems: averaging formulations*, in *Transport Phenomena in Multiphase Systems*, A. Faghri and Y. Zhang, Editors. 2006, Academic Press: Boston. p. 238-330.

102. Zhang, X., W. Liu, and Z. Liu, *Criterion for local thermal equilibrium in forced convection flow through porous media.* 2009. **12**(11): p. 1103-1111.

103. Fossa, M., O. Cauret, and M. Bernier. *Comparing the thermal performance of ground heat exchangers of various lengths*. in *Proceedings from the 11th International Conference on Energy Storage, EFFSTOCK*. 2009.

104. Lamarche, L., *g-function generation using a piecewise-linear profile applied to ground heat exchangers.* International Journal of Heat and Mass Transfer, 2017. **115**: p. 354-360.

105. Claesson, J. and S. Javed, *A load-aggregation method to calculate extraction temperatures of borehole heat exchangers.* ASHRAE Transactions, 2012. **118**(1): p. 530-539.

106. Lazzarotto, A., *A network-based methodology for the simulation of borehole heat storage systems.* Renewable Energy, 2014. **62**: p. 265-275.

107. Marcotte, D. and P. Pasquier, *Fast fluid and ground temperature computation for geothermal ground-loop heat exchanger systems.* Geothermics, 2008. **37**(6): p. 651-665.

108. Chaparro, L. and A. Akan, *Signals and systems using MATLAB*. 2018: Academic Press.

109. Monzó, P., et al., *A novel numerical approach for imposing a temperature boundary condition at the borehole wall in borehole fields.* Geothermics, 2015. **56**: p. 35-44.

110. Geng, S., et al., *Evaluation of thermal anomalies in multi-boreholes field considering the effects of groundwater flow.* Sustainability, 2016. **8**(6): p. 577.

111. Piller, M. and A. Liuzzo Scorpo, *Numerical investigation of forced convection from vertical boreholes.* Geothermics, 2013. **45**: p. 41-56.

112. Zanchini, E., S. Lazzari, and A. Priarone, *Long-term performance of large borehole heat exchanger fields with unbalanced seasonal loads and groundwater flow.* Energy, 2012. **38**(1): p. 66-77.

113. Gashti, E.H.N., M. Malaska, and K. Kujala, *Analysis of thermo-active pile structures and their performance under groundwater flow conditions.* Energy and Buildings, 2015. **105**: p. 1-8.

114. Javed, S. and J. Claesson, *New analytical and numerical solutions for the short-term analysis of vertical ground heat exchangers.* ASHRAE Transactions, 2011. **117**(1): p. 3.

115. Lamarche, L. and B. Beauchamp, *New solutions for the short-time analysis of geothermal vertical boreholes.* International Journal of Heat and Mass Transfer, 2007. **50**(7): p. 1408-1419.

116. Bandyopadhyay, G., W. Gosnold, and M. Mann, *Analytical and semi-analytical solutions for short-time transient response of ground heat exchangers.* Energy and Buildings, 2008. **40**(10): p. 1816-1824.

117. Perez, R. and T.E. Hoff, *Chapter 10 - Solar anywhere forecasting*, in *Solar Energy Forecasting and Resource Assessment*, J. Kleissl, Editor. 2013, Academic Press: Boston. p. 233-265.

118. Zhang, C., et al., *A review on thermal response test of ground-coupled heat pump systems.* Renewable and Sustainable Energy Reviews, 2014. **40**: p. 851-867.

119. Gultekin, A., M. Aydin, and A. Sisman, *Effects of arrangement geometry and number of boreholes on thermal interaction coefficient of multi-borehole heat exchangers.* Applied Energy, 2019. **237**: p. 163-170.

120. Boehm, S., et al., *State of climate action 2021: systems transformations required to limit global warming to 1.5 °C.* 2021.

121. Benli, H. and A. Durmuş, *Evaluation of ground-source heat pump combined latent heat storage system performance in greenhouse heating.* Energy and Buildings, 2009. **41**(2): p. 220-228.

122. Li, H., et al., *Evaluating the performance of a large borehole ground source heat pump for greenhouses in northern Japan.* Energy, 2013. **63**: p. 387-399.

123. Hu, J., *An improved analytical model for vertical borehole ground heat exchanger with multiple-layer substrates and groundwater flow.* Applied Energy, 2017. **202**: p. 537-549.

124. Marcotte, D. and P. Pasquier, *On the estimation of thermal resistance in borehole thermal conductivity test.* Renewable Energy, 2008. **33**(11): p. 2407-2415.

125. BniLam, N. and R. Al-Khoury, *A spectral element model for nonhomogeneous heat flow in shallow geothermal systems.* International Journal of Heat and Mass Transfer, 2017. **104**: p. 703-717.

126. Man, Y., et al., *A new model and analytical solutions for borehole and pile ground heat exchangers.* International Journal of Heat and Mass Transfer, 2010. **53**(13): p. 2593-2601.

127. Bauer, D., et al., *Thermal resistance and capacity models for borehole heat exchangers.* International Journal of Energy Research, 2011. **35**(4): p. 312-320.

128. Hellstrom, G., *Ground heat storage: thermal analysis of duct storage systems: Part I Theory.* University of Lund, Lund, 1991.

129. Hahn, D.W. and M.N. Özisik, *Heat conduction*. 2012: John Wiley & Sons.

130. Hillel, D., *Soil Physics*, in *Encyclopedia of Physical Science and Technology (Third Edition)*, R.A. Meyers, Editor. 2003, Academic Press: New York. p. 77-97.

131. Wang, J., et al., *A new approach to modelling the effective thermal conductivity of heterogeneous materials.* International journal of heat and mass transfer, 2006. **49**(17-18): p. 3075-3083.

132. Robertson, E.C., *Thermal properties of rocks.* 1988.

133. Schimmel Jr, W., J. Beck, and A. Donaldson, *Effective thermal diffusivity for a multimaterial composite laminate.* 1977.

134. Zeng, H.Y., N.R. Diao, and Z.H. Fang, *A finite line-source model for boreholes in geothermal heat exchangers.* Heat Transfer—Asian Research, 2002. **31**(7): p. 558-567.

135. *Heat conduction using Green's functions*, K.D. Cole, Editor. 2011, CRC Press: Boca Raton :.

136. Eskilson, P. and J. Claesson, *Simulation model for thermally interacting heat extraction boreholes.* Numerical heat transfer, 1988. **13**(2): p. 149-165.

137. Diersch, H.J.G., et al., *Finite element modeling of borehole heat exchanger systems: Part 2. Numerical simulation.* Computers & Geosciences, 2011. **37**(8): p. 1136-1147.

138. Li, W., et al., *Experimental and numerical investigations on heat transfer in stratified subsurface materials.* Applied Thermal Engineering, 2018. **135**: p. 228-237.

139. Yang, W., P. Lu, and Y. Chen, *Laboratory investigations of the thermal performance of an energy pile with spiral coil ground heat exchanger.* Energy and Buildings, 2016. **128**: p. 491-502.

140. Beier, R.A., *Transient heat transfer in a U-tube borehole heat exchanger.* Applied Thermal Engineering, 2014. **62**(1): p. 256-266.

141. Launder, B.E. and D.B. Spalding, *The numerical computation of turbulent flows.* Computer Methods in Applied Mechanics and Engineering, 1974. **3**(2): p. 269-289.

142. Li, M. and A.C.K. Lai, *Analytical model for short-time responses of ground heat exchangers with U-shaped tubes: Model development and validation.* Applied Energy, 2013. **104**: p. 510-516.

143. Lurie, M.V., *Modeling of oil product and gas pipeline transportation*, in *Modeling of Oil Product and Gas Pipeline Transportation*. 2009. p. 1-214.

144. de Myttenaere, A., et al., *Mean absolute percentage error for regression models.* Neurocomputing, 2016. **192**: p. 38-48.

145. Incropera, F.P., et al., *Fundamentals of heat and mass transfer*. Vol. 6. 1996: Wiley New York.

146. Chiasson, A.D., *Geothermal Heat Pump and Heat Engine Systems : Theory and Practice*. 2016, Hoboken, UNITED KINGDOM: John Wiley & Sons, Incorporated.

147. American Society of Heating, R. and I. Air-Conditioning Engineers, *35. Geothermal Energy*, in *2019 ASHRAE® Handbook Heating, Ventilating, and Air-Conditioning Applications (S-I Edition)*. American Society of Heating, Refrigerating and Air-Conditioning Engineers, Inc. (ASHRAE).

148. Guo, Y., et al., *Considering buried depth for vertical borehole heat exchangers in a borehole field with groundwater flow—An extended solution.* Energy and Buildings, 2021. **235**: p. 110722.

149. Bennet, J., J. Claesson, and G. Hellström, *Multipole method to compute the conductive heat flows to and between pipes in a composite cylinder*. 1987: Husbyggnadsteknik, Tekniska högsk.

150. Gnielinski, V., *New equations for heat and mass transfer in turbulent pipe and channel flow.* Int. Chem. Eng., 1976. **16**(2): p. 359-368.

151. Sonnad, J.R. and C.T. Goudar, *Turbulent flow friction factor calculation using a mathematically exact alternative to the Colebrook–White equation.* Journal of Hydraulic Engineering, 2006. **132**(8): p. 863-867.

152. Levine, A., G. Rhodes, and A. Kvien, *Mining gold (geothermal opportunities leveraged through data): Exploring synergies between the geothermal and mining industries*. 2022, National Renewable Energy Lab.(NREL), Golden, CO (United States).

153. Zeng, H., N. Diao, and Z. Fang, *Heat transfer analysis of boreholes in vertical ground heat exchangers.* International journal of heat and mass transfer, 2003. **46**(23): p. 4467-4481.

154. Mandelis, A., *Green functions of one-dimensional thermal-wave fields*, in *Diffusion-wave fields: Mathematical methods and Green functions*, A. Mandelis, Editor. 2001, Springer New York: New York, NY. p. 22-84.

155. Cole, K.D., *Analysis of photothermal characterization of layered materials–design of optimal experiments.* International journal of thermophysics, 2004. **25**(5): p. 1567-1584.

156. de Monte, F., J.V. Beck, and D.E. Amos, *A heat-flux based "building block" approach for solving heat conduction problems.* International Journal of Heat and Mass Transfer, 2011. **54**(13): p. 2789-2800.

157. Čermák, V. and L. Rybach, *Thermal conductivity and specific heat of minerals and rocks.* Landolt-Börnstein: Numerical Data and Functional Relationships in Science and Technology, New Series, Group V (Geophysics and Space Research), Volume Ia,(Physical Properties of Rocks), edited by G. Angenheister, Springer, Berlin-Heidelberg, 1982: p. 305-343.

158. Zhang, L., Q. Zhang, and G. Huang, *A transient quasi-3D entire time scale line source model for the fluid and ground temperature prediction of vertical ground heat exchangers (GHEs).* Applied Energy, 2016. **170**: p. 65-75.

159. Kavanaugh, S., *An instruction guide for using a design tool for vertical ground-coupled.* Groundwater and Surface Water Heat Pumps Systems-Ground Source Heat Pump System Designer, GshpCalc Version, 2010. **5**.

160. Cui, P., et al., *Simulation modelling and design optimization of vertical ground heat exchanger-GEOSTAR program.* Procedia Engineering, 2015. **121**: p. 906-914.

161. Hecht-Méndez, J., et al., *Optimization of energy extraction for vertical closed-loop geothermal systems considering groundwater flow.* Energy Conversion and Management, 2013. **66**: p. 1-10.

162. de Paly, M., et al., *Optimization of energy extraction for closed shallow geothermal systems using linear programming.* Geothermics, 2012. **43**: p. 57-65.

163. IEA, *Renewables 2021: Analysis and forecasts to 2026*. 2021, International Energy Agency: Paris.

164. IEA, *Heating without global warming*. 2014, International Energy Agency: Paris.

165. IEA, *The future of heat pumps*. 2022, International Energy Agency: Paris.

166. *Current and Historical Alberta Weather Station Data Viewer*. [cited 2023 Nov. 30]; Available from: https://acis.alberta.ca/acis/weather-data-viewer.jsp.

167. Oosterkamp, A., T. Ytrehus, and S.T. Galtung, *Effect of the choice of boundary conditions on modelling ambient to soil heat transfer near a buried pipeline.* Applied Thermal Engineering, 2016. **100**: p. 367-377.

168. Mihalakakou, G., *On estimating soil surface temperature profiles.* Energy and Buildings, 2002. **34**(3): p. 251-259.

169. Aguareles, M., et al., *A mathematical model for the energy stored in green roofs.* Applied Mathematical Modelling, 2023. **115**: p. 513-540.

170. Keltner, N.R. and J.V. Beck, *Unsteady surface element method.* Journal of Heat Transfer, 1981. **103**(4): p. 759-764.

171. Sauer, T.J., et al., *Measurement of heat and vapor transfer coefficients at the soil surface beneath a maize canopy using source plates.* Agricultural and Forest Meteorology, 1995. **75**(1): p. 161-189.

172. Ham, J.M. and G.J. Kluitenberg, *Positional variation in the soil energy balance beneath a row-crop canopy.* Agricultural and Forest Meteorology, 1993. **63**(1): p. 73-92.

173. Ling, F. and T. Zhang, *A numerical model for surface energy balance and thermal regime of the active layer and permafrost containing unfrozen water.* Cold Regions Science and Technology, 2004. **38**(1): p. 1-15.

174. Zhang, T., *Influence of the seasonal snow cover on the ground thermal regime: An overview.* Reviews of Geophysics, 2005. **43**(4).

175. Schmidt, T., D. Mangold, and H. Müller-Steinhagen, *Central solar heating plants with seasonal storage in Germany.* Solar Energy, 2004. **76**(1): p. 165-174.

176. Hesaraki, A., S. Holmberg, and F. Haghighat, *Seasonal thermal energy storage with heat pumps and low temperatures in building projects—A comparative review.* Renewable and Sustainable Energy Reviews, 2015. **43**: p. 1199-1213.

177. Reuss, M., *6 - The use of borehole thermal energy storage systems*, in *Advances in Thermal Energy Storage Systems (Second Edition)*, L.F. Cabeza, Editor. 2021, Woodhead Publishing. p. 139-171.

178. Sibbitt, B., et al., *The Performance of a High Solar Fraction Seasonal Storage District Heating System – Five Years of Operation.* Energy Procedia, 2012. **30**: p. 856-865.

179. Berardi, U. and M. Naldi, *The impact of the temperature dependent thermal conductivity of insulating materials on the effective building envelope performance.* Energy and Buildings, 2017. **144**: p. 262-275.

180. Lachenbruch, A.H., *Periodic heat flow in a stratified medium, with application to permafrost problems*. 1959: US Government Printing Office.

181. Hwang, C., *Predictions and observations on the behaviour of a warm gas pipeline on permafrost.* Canadian Geotechnical Journal, 1976. **13**(4): p. 452-480.

182. Rad, F.M., A.S. Fung, and W.H. Leong, *Feasibility of combined solar thermal and ground source heat pump systems in cold climate, Canada.* Energy and Buildings, 2013. **61**: p. 224-232.

183. Lund, J.W. and A.N. Toth, *Direct utilization of geothermal energy 2020 worldwide review.* Geothermics, 2021. **90**: p. 101915.

184. Hu, X., et al., *Effects of temperature-dependent property variations on the output capacity prediction of a deep coaxial borehole heat exchanger.* Renewable Energy, 2021. **165**: p. 334-349.

185. Hu, X., et al., *Utilizing geothermal energy from enhanced geothermal systems as a heat source for oil sands separation: A numerical evaluation.* Energy, 2022. **238**: p. 121676.

186. Ingersoll, L. and H. Plass, *Theory of the ground pipe source for the heat pump.* ASHVE Trans, 1948. **54**(3): p. 339-348.

187. Association, I.G.S.H.P. *Software*. [cited 2023 Oct. 15]; Available from: https://igshpa.org/software/.

188. Diersch, H.J.G., et al., *Finite element modeling of borehole heat exchanger systems: Part 1. Fundamentals.* Computers & Geosciences, 2011. **37**(8): p. 1122-1135.

189. Al-Khoury, R. and P.G. Bonnier, *Efficient finite element formulation for geothermal heating systems. Part II: transient.* International Journal for Numerical Methods in Engineering, 2006. **67**(5): p. 725-745.

190. Tang, F. and H. Nowamooz, *Factors influencing the performance of shallow Borehole Heat Exchanger.* Energy Conversion and Management, 2019. **181**: p. 571-583.

191. Hein, P., et al., *A numerical study on the sustainability and efficiency of borehole heat exchanger coupled ground source heat pump systems.* Applied Thermal Engineering, 2016. **100**: p. 421-433.

192. Casasso, A. and R. Sethi, *Efficiency of closed loop geothermal heat pumps: A sensitivity analysis.* Renewable Energy, 2014. **62**: p. 737-746.

193. BOSCH. *CDi Series SM Rev C – Engineering Submittal Sheet*. Available from: https://www.bosch-homecomfort.com/us/media/country_pool/documents/engineering-submittal-sheets/water-to-air-water-source-heat-pumps/btc760108305g_greensource_sm_revc_ess_10.2022.pdf.

194. Zarrella, A. and P. Pasquier, *Effect of axial heat transfer and atmospheric conditions on the energy performance of GSHP systems: A simulation-based analysis.* Applied Thermal Engineering, 2015. **78**: p. 591-604.

195. *Emission Factors and Reference Values*, E.a.C.C. Canada, Editor. 2023: Gatineau QC.

196. Shah, N.N., M.J. Huang, and N.J. Hewitt, *Performance analysis of diesel engine heat pump incorporated with heat recovery.* Applied Thermal Engineering, 2016. **108**: p. 181-191.

197. Hepbasli, A., et al., *A review of gas engine driven heat pumps (GEHPs) for residential and industrial applications.* Renewable and Sustainable Energy Reviews, 2009. **13**(1): p. 85-99.

198. Wang, M., Y. Chen, and Q. Liu, *Experimental study on the gas engine speed control and heating performance of a gas Engine-driven heat pump.* Energy and Buildings, 2018. **178**: p. 84-93.

199. Liu, F.-G., et al., *Experimental investigation of a gas engine-driven heat pump system for cooling and heating operation.* International Journal of Refrigeration, 2018. **86**: p. 196-202.

200. Görgülü, K., et al., *Influences of uniaxial stress and moisture content on the thermal conductivity of rocks.* International Journal of Rock Mechanics and Mining Sciences, 2008. **45**(8): p. 1439-1445.

201. Fujii, H., et al., *An improved thermal response test for U-tube ground heat exchanger based on optical fiber thermometers.* Geothermics, 2009. **38**(4): p. 399-406.

202. Zhao, P., et al., *Stratified thermal response test measurement and analysis.* Energy and Buildings, 2020. **215**: p. 109865.

203. Bakirci, K., et al., *Energy analysis of a solar-ground source heat pump system with vertical closed-loop for heating applications.* Energy, 2011. **36**(5): p. 3224-3232.

204. Li, Y., et al., *Analysis of the soil heat balance of a solar-ground source absorption heat pump with the soil-based energy storage in the transition season.* Energy, 2023. **264**: p. 126394.

205. Sazon, T.A., Q. Zhang, and H. Nikpey, *Comparison of different configurations of a solar-assisted ground-source CO2 heat pump system for space and water heating using Taguchi-Grey Relational analysis.* Energy Conversion and Management, 2024. **300**: p. 117881.

206. Ma, Z.D., et al., *Analysis on variations of ground temperature field and thermal radius caused by ground heat exchanger crossing an aquifer layer.* Applied Energy, 2020. **276**: p. 115453.

207. Claesson, J. and G. Hellström, *Multipole method to calculate borehole thermal resistances in a borehole heat exchanger.* Hvac&R Research, 2011. **17**(6): p. 895-911.

208. Templeton, J.D., et al., *Abandoned petroleum wells as sustainable sources of geothermal energy.* Energy, 2014. **70**: p. 366-373.

209. Wight, N.M. and N.S. Bennett, *Geothermal energy from abandoned oil and gas wells using water in combination with a closed wellbore.* Applied Thermal Engineering, 2015. **89**: p. 908-915.

210. Chen, K., et al., *Study on long-term performance sustainability of medium deep borehole heat exchanger based on simplified one-dimensional well model.* Applied Thermal Engineering, 2023. **230**: p. 120820.

211. Wang, G., et al., *A robust numerical method for modeling multiple wells in city-scale geothermal field based on simplified one-dimensional well model.* Renewable Energy, 2019. **139**: p. 873-894.

212. Saeid, S., R. Al-Khoury, and F. Barends, *An efficient computational model for deep low-enthalpy geothermal systems.* Computers & Geosciences, 2013. **51**: p. 400-409.